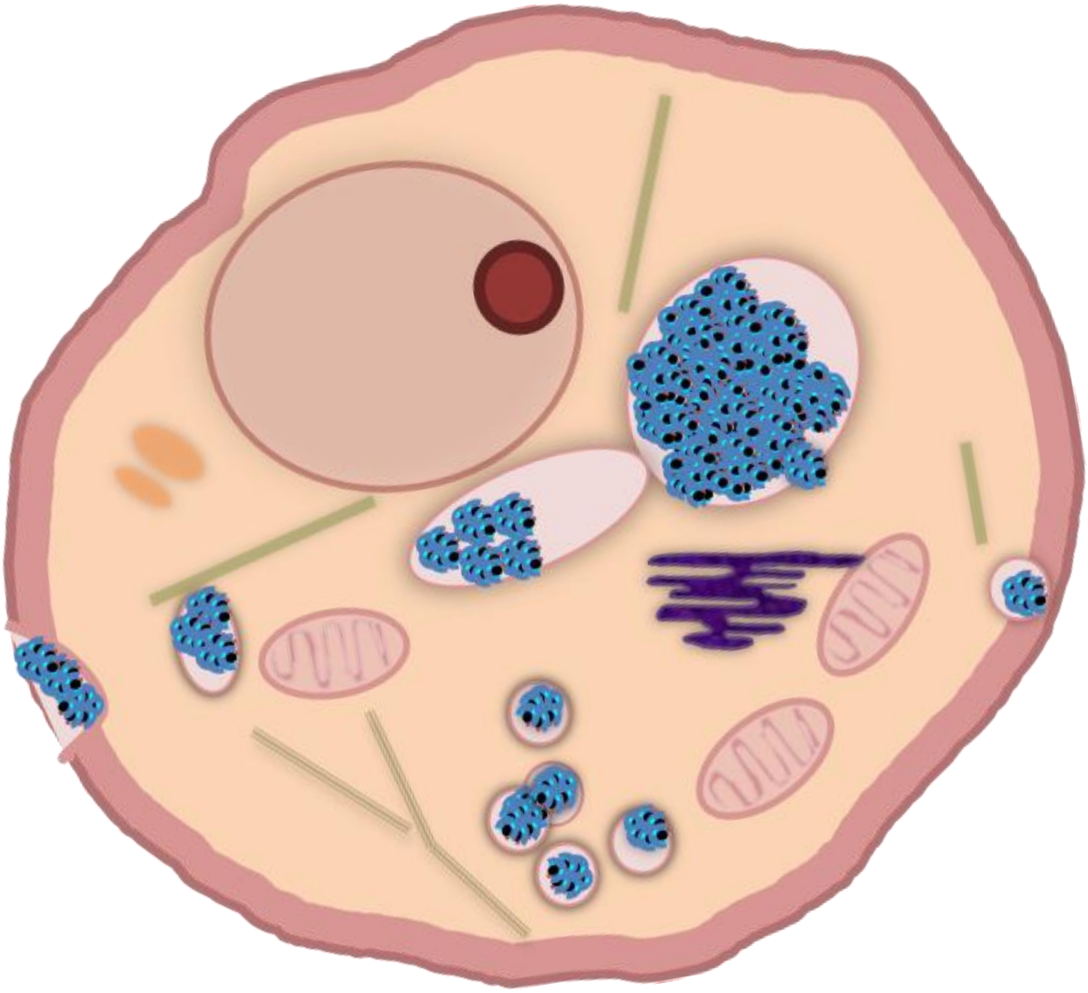

ADDRESSING THE DYNAMICAL MAGNETIC RESPONSE OF MAGNETIC NANOPARTICLES AFTER INTERACTING WITH BIOLOGICAL ENTITIES

DISERTACIÓN PRESENTADA POR DAVID CABRERA CARRASCO PARA OPTAR AL GRADO DE DOCTOR POR LA UNIVERSIDAD AUTÓNOMA DE MADRID

DIRECTOR: FRANCISCO JOSÉ TERÁN GARCINUÑO
TUTOR ACADÉMICO: JULIO CAMARERO DE DIEGO

A mi familia y amigos

Contents

Aknowledgments **I**

Abstract – Resumen **II**

Motivation **IV**

1. Fundamentals **2**

1.1. Introduction 2

1.2. Magnetic properties of materials 3

1.3. MNPs microstructure and composition 10

1.4. MNPs in colloidal dispersion 12

1.5. Magnetic characterization techniques for MNPs 16

1.6. Non-magnetic characterization techniques of MNPs 24

1.7. Cell culture and MNPs 26

2. Development of an AC magnetometer for advance magnetic measurements **34**

2.1. Introduction 34

2.2. Prototype development 35

2.3. AMF calibration 41

2.4. Reproducibility and error estimation 45

2.5. Software development 46

2.6. AC hysteresis measurements 49

2.7. Conclusions 52

3. Influence of magnetic dipolar interactions on the dynamical magnetic response of IONPs **54**

3.1. Introduction 54

3.2. Inter- and Intra-aggregates dipolar interactions 55

3.3. Influence of extrinsic and intrinsic parameters on magnetic dipolar interactions 71

3.4. Conclusions 76

3.5. Methods 78

4. Viscosity effects on the dynamical magnetic response of magnetic nanoparticles 81

4.1. Introduction ____ 81

4.2. Viscosity effects on the magnetism of the MNPs ____ 82

4.3 Conclusions ____ 95

4.4. Methods ____ 96

5. Dynamical magnetic response of IONPs in live cells ____ 101

5.1. Introduction ____ 101

5.2. Dynamical magnetic response of IONPs in live cells ____ 103

5.3. Influence of viscosity on the dynamical magnetic response of IONPs ____ 111

5.4. Influence of aggregation on the dynamical magnetic response of IONP ____ 116

5.5. Conclusions ____ 126

5.6. Methods ____ 127

6. Influence of MNP-biomolecules interaction on the dynamical magnetic response of MNPs ____ 133

6.1. Introduction ____ 133

6.2. MNPs colloidal properties in biological fluids ____ 134

6.3. Unveiling specific MNP-biomolecule interaction by AC magnetometry: towards a biosensing platform ____ 140

6.4. Conclusions ____ 159

6.5. Methods ____ 160

***7.* General conclusions - *Conclusiones generales* ____ 165**

ANNEX I – Magnetic nanoparticles samples ____ 171

References ____ 180

List of publications ____ 189

Aknowledgments

The writing and completion of this dissertation would not have been possible without the support and guidance of few special people. I would like to express the deepest appreciation to:

- *Francisco J. Terán for all the support and guidance provided during these intense years. For his constant fights to find funding to sustain my PhD, his backing that usually went beyond the general tasks of a PhD supervisor, and all his generous advices that made this dissertation and a fruitful research activity possible.*
- *Julio Camarero for introducing me into the group and transmit me important doses of optimism and willingness at work.*
- *Emilio Artés and Daniel Ortega for all their technical, scientific and personal support during all these years. Without them, certainly this work will not be achieved.*
- *Our collaborators Takashi Yoshida, Julian Carrey, Teresa Pellegrino, Aitziber L. Cortajarena, Neil Telling, Gorka Salas and Luc Dupre, as well as all their technicians, PhD student and postdocs that deeply enriched this work: Maria Elena Materia, Aidin Lak, Antonio Aires, Kaarjel Kauslya, Leonor de la Cueva and Rebeca Amaro, Jonathan Leliaert, Annelies Coene.*
- *Adriana Arnáiz for cell training.*
- *Eva Céspedes, for giving to me the opportunity to go to Keele.*
- *Institute for Science and Technology, Keele University, all people from Guy Hilton Research, and especially Neil Telling for helping and hosting me in a such a warm manner during six months. An experience that will be difficult to forget.*
- *Ingrid Hilger for hosting me during one month at Jena, where I had the opportunity learning novel techniques on cell culture.*
- *IMDEA Nanoscience for giving to me the opportunity of carrying out this research.*
- *All my family and friends, which transmitted me all the willingness not to desist in this long but satisfactory path.*

Abstract – Resumen

Heat dissipation due to hysteresis losses in magnetic materials generally constitutes a difficult issue to circumvent. But in magnetic nanoparticles (MNPs) instead, their ability to release heat when subjected to external alternating magnetic fields (AMF) is currently being exploited for treating solid tumors in the so-called magnetic hyperthermia (MH) therapy. In those therapies, the preservation of the MNPs magnetic response after interacting with biological entities (biomolecules, cells and/or tissues) and their related heat dissipation is crucial for their use in biomedical applications. However, recent studies point out that the interactions of MNPs with cells, tissues or proteins strongly modifies their intrinsic magnetic properties. Among the underlying reasons behind such variation of magnetic properties of IONPs, enhancement of environmental viscosity, IONPs clustering and protein adsorption are pointed as the main causes.

Here, we evaluated the dynamical magnetic response of a wide set of MNP under biological-mimicking and directly when they interact with live cells and biomolecules. In biological-mimicking medium, we examined on one hand the impact of inter and intra-aggregate magnetic dipolar interactions on the MNPs magnetic response, observing different phenomena related to both types of magnetic dipolar interactions. On the other hand, we evaluated the role of the environmental viscosity on the dynamical magnetic response of MNPs colloids.
Later, we investigated how the interaction of MNPs with live cells and biomolecules affects the MNPs nanomagnetism. First, we investigated the influence of IONP cell internalization on their dynamical magnetic response by AC magnetometry and susceptometry, finding that intracellular MNPs clustering provides the major contribution to the changes of the studied MNPs magnetic response. Finally, we assessed the effects of dispersing MNPs in biological fluids on their magnetic response, demonstrating the ability of AC magnetometry to unveil unspecific and specific MNPs-biomolecule interaction.

The know-how outcome of this thesis work will allow the design of novel nanostructures whose magnetic losses (i.e. magnetic hyperthermia efficiency) will remain non-influenced by viscosity and aggregation effects related to biological environments. Moreover, our findings encourage further investigation towards the engineering of more complex functionalized MNPs which, ultimately, will allow conception of an effective biomarkers sensing platform based on the use of AC magnetometer.

La disipación de calor debido a fenómenos de histéresis en materiales magnéticos generalmente constituye un problema difícil de abordar. En las nanopartículas magnéticas (NPM) sin embargo, su capacidad de liberar calor cuando son expuestas a campos magnéticos alternos externos (CME) es explotanda actualmente para tratar tumores sólidos en la llamada terapia de hipertermia magnética (HM). En tales terapias, la preservación de la respuesta magnética de las NPM y su disipación de calor después de interactuar con entidades biológicas (biomoléculas, células y / o tejidos) es crucial para su uso en aplicaciones biomédicas. Sin embargo, estudios recientes señalan que las interacciones de las NPM con células, tejidos o proteínas modifican fuertemente sus propiedades magnéticas intrínsecas. Entre las posibles razones subyacentes detrás de dicha variación podemos encontrar el incremento de la viscosidad del entorno de las NPM, su agregación y la adsorción de proteínas sobre su superficie.

En este trabajo hemos evaluado la respuesta magnética dinámica de un amplio conjunto de NPM dispersas en medios que imitan las condiciones de distintas matrices biológicas, así como en interacción directa con células vivas y biomoléculas. En primer lugar, examinamos el impacto de las interacciones dipolares magnéticas inter e intra-agregados en la respuesta magnética de NPM, observando diferentes fenómenos relacionados con ambos tipos de interacciones dipolares magnéticas. Por otro lado, evaluamos el papel de la viscosidad del medio de dispersión en la respuesta magnética dinámica de los coloides de NPM, usando medios de dispersión de viscosidad creciente.

Posteriormente, hemos investigado cómo la interacción de las NPM con células vivas y biomoléculas afecta el nanomagnetismo de las NPM. Primero, investigamos la influencia de la internalización células de las NPM en su respuesta magnética dinámica mediante magnetometría y susceptometría de corriente alterna (CA), encontrando que la agregación de NPM proporciona la mayor contribución a los cambios en su respuesta magnética. Finalmente, evaluamos los efectos de la dispersión de NPM en fluidos biológicos sobre su respuesta magnética, demostrando la capacidad de la magnetometría de CA para revelar interacciones inespecíficas y específicas entre NPM y biomoléculas.

Los resultados de este trabajo de tesis permitirán el diseño de nuevas nanoestructuras cuyas pérdidas magnéticas (es decir, la eficiencia de la hipertermia magnética) no se verán influenciadas por la viscosidad y los efectos de agregación relacionados con la interacción con entornos biológicos. Además, nuestros hallazgos alientan una mayor investigación hacia funcionalizaciones de NPM más complejas que, en última instancia, permitirán la concepción de una plataforma de detección de biomarcadores efectiva basada en el uso de magnetómetro de CA.

Motivation

Heat dissipation due to hysteresis losses in magnetic materials generally constitutes a difficult issue to circumvent. But in magnetic nanoparticles (MNPs) instead, their ability to release heat when subjected to external alternating magnetic fields (AMF) is currently being exploited for treating solid tumors in the so-called magnetic hyperthermia (MH) therapy.[12] The heat dissipated by MNPs is exchanged with their surroundings, leading to a local temperature raise -ideally up to 43ºC-, which eventually destroy malignant tissues.[13,14] Indeed, recent clinical trials have successfully proved the efficacy of this proof-of-concept on distinct cancer types.[13,14]

Among different chemical compositions, iron oxide nanoparticles (IONPs) have attracted most of attention by scientific community due to the precise control on their synthesis, their suitable magnetic properties,[15-17] and negligible toxicity drawbacks[18].[15,16,19,20] The preservation of the IONP magnetic response after interacting with biological entities (biomolecules, cells and/or tissues) is, therefore, crucial for their use in biomedical applications acting as nanocarriers[21], imaging tracers[22], hyperthermia mediators[13] or transducers[23]. However, recent studies points out that the interactions of IONPs with cells, tissues or proteins strongly modifies their intrinsic contrast signal,[24,25] magnetic heating losses,[1,16,26] or magnetic trapping properties.[27] Such experimental evidences call into to question the reliability of exploiting the magnetic properties of IONPs for providing a given heat exposure or contrast signal into biological environments. Amid the underlying reasons behind such variation of magnetic properties of IONPs, some authors point out the enhancement of IONP environmental viscosity,[1] which occurs inside cell vesicles[2], brings drastic reductions of MNPs heating efficiency[28]. Other authors correlate these changes of the magnetic response to the increase of IONPs clustering[3,4] when nanoparticles internalize into cells as a consequence of their intracellular transit[5]. Also, the protein adsorption by nanoparticle surface alters their magnetic properties[6-11]. However, the net contribution of both parameters (i.e. MNPs aggregation and environmental viscosity enhancement), have not been yet fully quantified.

Besides, most of those experimental studies have been majorly based on calorimetric measurements when MNPs are subjected to an external AMF to date. Such experiments certainly provide useful preliminary information about the thermal performance of MNPs that can be expected once placed in different biological structures. Nonetheless, they offer scarce details about the dynamical magnetic properties of MNPs, hindering direct analysis of the IONP thermal underperformance into biological matrices. In addition, calorimetric-based methods present important inconveniences regarding the inaccuracy of heat losses quantification, and the need of determining physical constants for calculating heat losses into cells, which risk the cellular integrity.

Alternatively, some authors addressed those experimental studies exclusively by magnetic means: AC susceptometry,[29] Field Cooling-Zero Field Cooling (FC-ZFC) and relaxativity have been employed for determining how the magnetic properties of the MNPs are modified when located in the biological matrix.. However, the magnetic response under AMF conditions has not been deeply probed, unless at the MH conditions. Hence, we stress that a deeper understanding on how the interactions of MNPs with biological entities modifies the dynamical magnetic response of IONP is mandatory for using MNPs in clinics. That would require suitable methodologies that allow to characterize MH conditions under the right AMF and MNPs environmental conditions.

Here we present a set of studies on the role of MNPs intrinsic (i.e. size[15,17], composition) and extrinsic parameters (concentration, aggregation, viscosity, biological environment), including those related with IONPs-biological entities on the dynamical magnetic response of IONPs. Without detriment of using also well-established calorimetric (SAR measurements) and magnetic techniques (AC susceptometry), we systematically employed a self-designed AC magnetometer – an approach that allows to monitor the MNPs dynamical magnetic response under near-MH AMF conditions when found in any liquid solution (including biological fluids) and directly in live cells.

Initially, we will address the study of the MNPs dynamical magnetic response when dispersed in diverse liquid medium that mimics, somehow, the effects that can be awaited in biological entities. In **Chapter 3**, we will study the influence of the inter- and intra-aggregate magnetic dipolar interactions on the dynamical magnetic response of the MNPs, inducing the aggregative and local MNP concentration increase effects that nanoparticles suffer when internalized in cells or after exposed to biological fluids. Later, we will evaluate the role of the environmental viscosity on the dynamical magnetic response of a MNPs in **Chapter 4**, unveiling how the nanoparticle composition and size, as well as AMF conditions, assume a central role in the sensitivity of nanoparticles thermal response to medium viscosity.

After the studies carried out under biological-mimicking conditions, we will assess how the dynamical magnetic response of MNPs is altered when located in two biological different-nature biological matrices: cancer cell cultures and biological fluids. **Chapter 5** address the study of the dynamical magnetic response of IONPs when internalized inside live MCF-7 cells. Together with AC magnetometry and susceptometry studies of IONPs internalized in live cells, we also performed those magnetic studies under the previously employed biological-mimicking conditions (i.e. IONPs aggregation increase and environmental viscosity enhancement). In this manner, we expected a better clarification about the biological influencing effects on the nanoparticles dynamical magnetic response.

Subsequently**,** we will address the study on how the dispersion of MNPs in biological media (Phosphate Buffer Saline and Human Blood Serum) affects the colloidal properties of IONPs in chapter **Chapter 6** and how, indirectly, those changes are manifested in their AC hysteresis loops. Finally, we will explore the possibility of using AC magnetometry to unveil specific protein adsorption onto MNPs surface in the last part of the chapter. Such findings would imply promising applications of this magnetic-based method towards the detection of strategic biomarkers related to human pathological and/or physiological conditions.

Our results and conclusions intend to provide new guidelines for the analysis of the influence of the biological matrix on the magnetism of IONPs which, ultimately, will ease the translation of MNPs-based technology into clinics.

Fundamentals

1

Chapter

1. Fundamentals

1.1. Introduction

In this chapter, the fundamental concepts are set to provide a fertile background to understand this thesis dissertation. Hence, the basis on the magnetism of MNPs are mentioned, starting with the generalities of magnetic materials to the particular magnetic behaviour of MNPs, including interaction phenomena. The most widely employed techniques for structural, colloidal and magnetic characterization of MNPs. Finally, the general aspects of cell cancer culture, and the optical techniques, methods and protocols for assessing cell viability and structural aspects, which have been used in Chapter 5.

1.2. Magnetic properties of materials

The origin of magnetic properties of materials immersed its root in quantum mechanics phenomena, which are determined by their composition and the crystal lattice organization. Several classifications of diverse complexity and criteria have been proposed, although the most common attends to the presence of magnetic order in absence of external magnetic field ***H***. According to this criterium, the magnetic materials can be divided in two groups:[30]

a) Absence of magnetic order:
   a. Diamagnetic
   b. Paramagnetic
b) Permanent magnetic order:
   a. Ferromagnetic
   b. Antiferromagnetic
   c. Ferrimagnetic

Among magnetic materials lacking magnetic order in absence of an external magnetic field, we can distinguish diamagnetic and paramagnetic materials. Diamagnets are materials whose magnetic moments oppose to external magnetic fields. Thus, an applied magnetic field creates an induced magnetic field in them in the opposite direction, causing a repulsive force. Contrarily, the opposite behavior (i.e. attraction to external magnetic field) is showed by paramagnetic materials, i.e. the generation of and induced magnetic field with the same direction of H field, creating a magnetic order subjected to the presence of the external magnetic field.

Among magnetic materials having a permanent magnetic order in absence of an external magnetic field, we can distinguish ferromagnetic, ferrimagnetic and antiferromagnetic materials, schematically described in Figure 1.1. Ferromagnetic materials are characterized by the high magnetization values in absence of an applied magnetic field. This is due to the conservation of a spontaneous magnetic order where magnetic moments are aligned in a preferential direction. In the case of antiferromagnetics, magnetic moments are aligned antiparallel and with the same magnitude, resulting in a null net magnetic moment in absence of magnetic field.

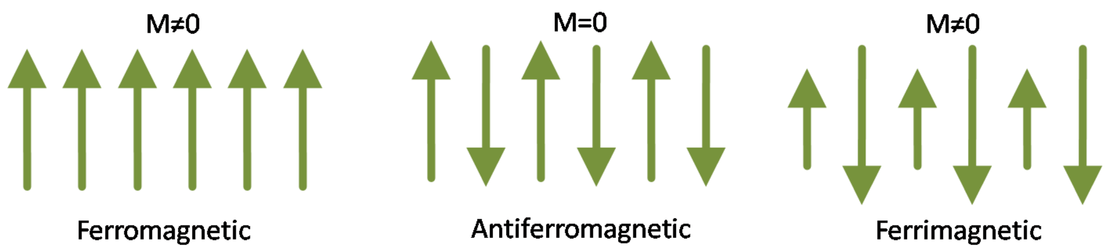

Figure 1.1. Schematic representation of coupling of different magnetic materials in absence of external magnetic field.[31]

Last, ferrimagnetic materials have similar macroscopical magnetic properties to the ferromagnetic. The main difference is the origin of magnetic moment as in ferrimagnets, magnetic coupling between adjacent and different magnetic moments can be parallel as well as antiparallel. However, different modulus of the magnetic moments provides a net total permanent magnetic moment.

Generally, the magnetic response under an external magnetic field **H** is characterized by magnetization loops. Thus, ferro and ferrimagnetic materials exhibit an hysteretic behavior characterized by the following magnetic parameters (Figure 1.2):

- **Remanent magnetization or remanence** (M_R), the value of magnetization in absence of an external magnetic field.
- **Saturation magnetization** (M_S), or maximum magnetization value that material achieves under the influence of an external magnetic field.
- **Coercitive field** (H_C), magnetic field value at which the magnetization value is zero.

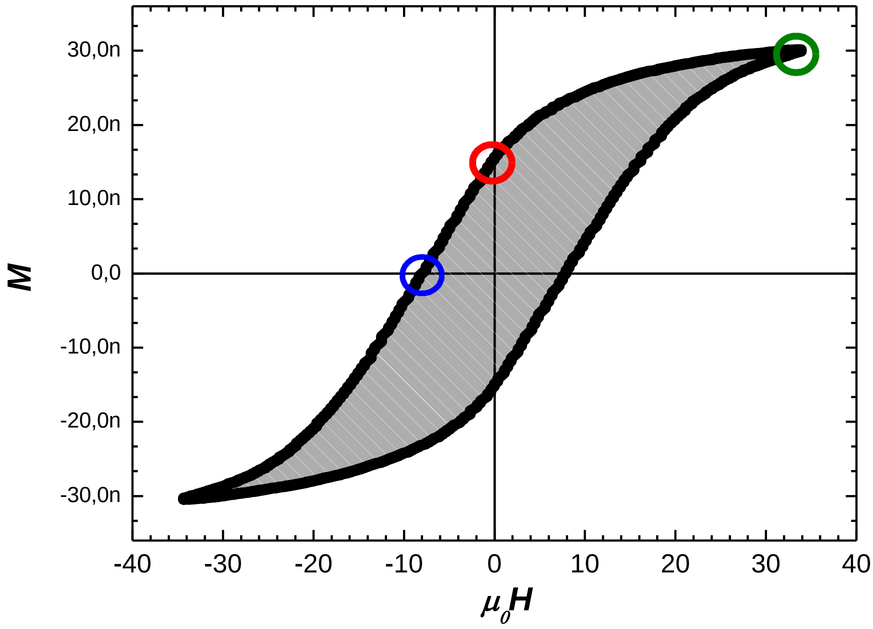

Figure 1.2. Magnetic hysteresis loop. Red circle: Remanent magnetization e. Green circle: Saturation magnetization. Blue circle: Coercive field.

Although hysteresis loop provides important information about the magnetic properties of a magnetic material, the study of magnetic hysteresis loop becomes of great importance not only from the magnetic properties point of view but from thermal properties of a material. For this case, it is important to note that the area enclosed inside the magnetic hysteresis loop also quantifies the energy dissipation of a magnetic material under certain field conditions:

$$Area = E_h = \int \mu_0 M(H) dH \text{ (J)} \qquad \text{(eq. 1.1)}$$

Where M denotes the magnetization component and H the applied external field. When alternating magnetic field is applied, this energy is multiplied by the frequency f**,** with the resultant work or heating power:

$$W_h = E_h \cdot f \text{ (W)} \qquad \text{(eq. 1.2)}$$

Under determined field conditions and normalized to magnetic mass of the sample, magnitude receives the denomination of **Specific Absorption Rate** (SAR)[12]:

$$SAR = \frac{Absortion\ power}{magnetic\ Mass}\ (\text{W/g}) \qquad \text{(eq. 1.3)}$$

In permanent magnets, several mechanisms govern the inversion of the magnetization when they are exposed to an external magnetic field. Whereas ferro/ferrimagnetic materials present multidomain structures at the macro scale as it is the case of particles of micrometer sizes (Fig. 1.3a), this domain organization varies below a critical particle size, resulting in monodomain structures. IN that case, Hc start to be comparable to anisotropic field Hk=2K/Ms, where K represent the magnetic anisotropy (Fig. 1.3b).

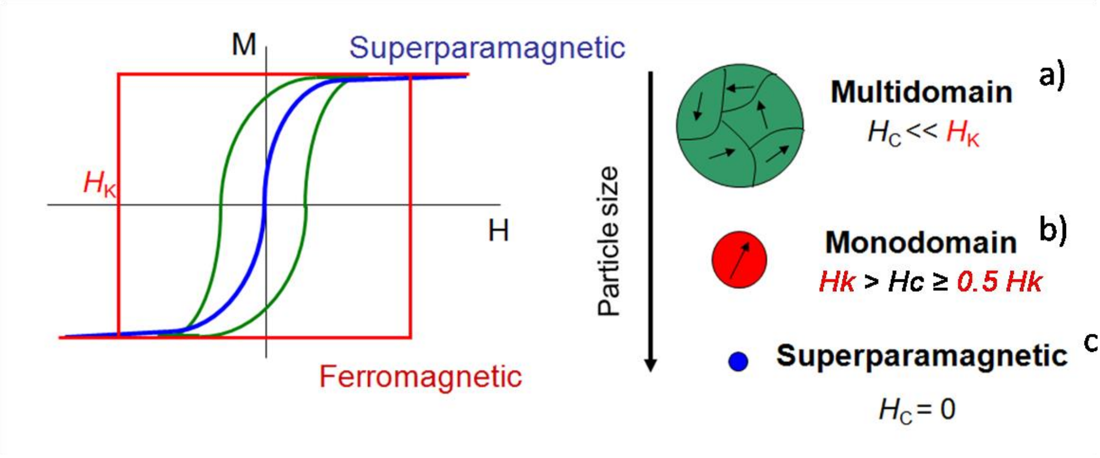

Figure 1.3. Schematic representation of magnetic structure and behavior of magnetic nanoparticles with size. Green: Multidomain structure; Red: Monodomain structure; Blue: Superparamagnetic behavior regime.

Composition, shape, presence of dopants and surface effects determine this critical size value related to the reduction of magnetostatic energy. For instance, in iron oxide, the most common compound used in MNPs for biomedical purposes, monodomain structure appears below 50 nm. Then, magnetic moment rest on an equilibrium preferential orientation, separated from the other one (in uniaxial anisotropy case) by an energy barrier that explains the spontaneous magnetization and hysteretic phenomena (Figure 1.4). According to the Stoner-Wohlfarth model,[32] which describes the magnetization phenomena of single-domain magnets, external field modify energy well levels, forcing a jump between energy wells when field amplitude takes a certain value and activating coherent rotation mechanisms. Ultimately, activation of inversion mechanism induces a heat release leading to hyperthermia response.

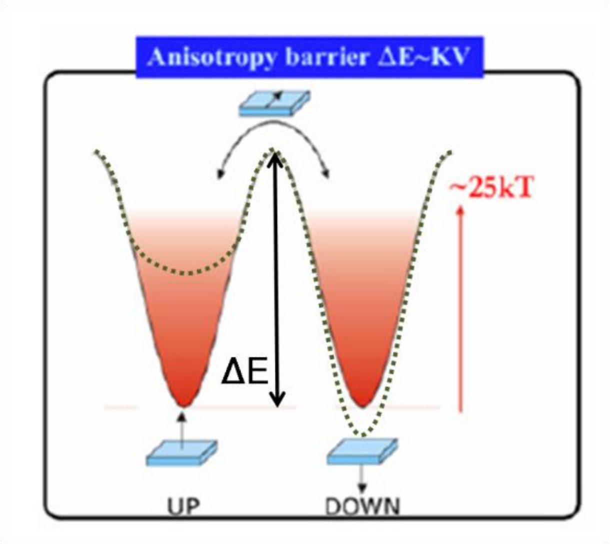

Figure 1.4. Scheme of energy barrier between the two preferential orientations of magnetization. Green line denotes effect of external magnetic field in energy wells.

Further decrease of magnetic particles size below the typical monodomain region (< 25 nm for iron oxide nanoparticles), leads magnetic frustration since thermal fluctuations generates a flipping of the magnetic moment between the possible states across the barrier of magnetic energy. [33] Such behavior is known as ***superparamagnetism.***

1.2.1. Magnetic relaxation mechanisms of MNPs

Typically, the time required to flip the magnetic moment over the magnetic barrier is called Néel Relaxation Time. In absence of magnetic field, energy barrier $\Delta E=KV$ where K is the magnetic anisotropy and V the nanoparticle size. Such relaxation time follows an Arrhenius Law: [34,35]

$$\tau_N = \tau_0 e^{KV/k_b T} \qquad \text{(eq. 1.4)}$$

where $\tau_0=10^{-9}$, k_b the Boltzmann constant and T the temperature.

However, this is not the unique MNPs heat mechanisms present at the nanoscale. When MNPs are liquid dispersed, another magnetic relaxation mechanisms can arise. This phenomenon is due to thermally driven reorientation of the particle (i.e., physical rotation of the particle) and its respective relaxation time in absence of external magnetic field is given by:

$$\tau_B = \frac{3\eta V_H}{k_B T} \qquad \text{(eq. 1.5)}$$

Where η is the dynamic media viscosity and V_H the hydrodynamic volume. The Effective Relaxation Time is given by the following expression:

$$\tau_{eff} = \frac{\tau_N \, \tau_B}{\tau_N + \tau_B} \qquad \text{(eq. 1.6)}$$

In general, both Néel and Brown relaxation processes coexist while their related relaxation time values are comparable. When one of relaxation mechanisms is much faster (i.e. high relaxation rates), it dominates.

In typical superparamagnetic nanoparticles, under quasi-static magnetic field conditions (that is $f < 1\ Hz$), relaxation time of the particle will be much faster than the applied field, obtaining an average zero magnetization value in absence of external magnetic field; i.e. close magnetization loop. Consequently, no heat dissipation is released. Statistical equations from mechanical models, like Langevin equation, allow to accurately describe this behavior. In contrast, the magnetization loops of the MNPs become hysteretic when H_{AC} frequency is comparable with $1/\tau_{eff}$ (Figure 1.5).

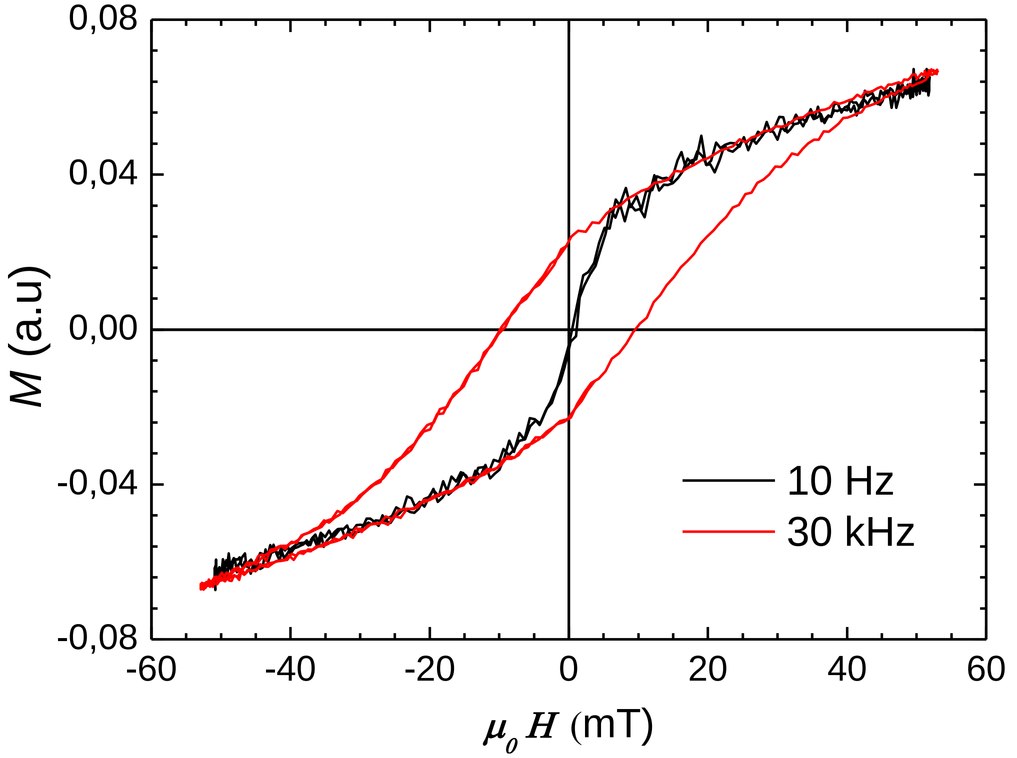

Figure 1.5. AC hysteresis loops measurement of 15nm IONP sample obtained by magneto-optical Magnetometer based on Faraday effect. Black curve corresponds to AC field whose f=10Hz, whereas in red one f=30kHz.

In first approach, Dynamic Linear Response Theory (DLRT) is a well-accepted theoretical model to describe the hysteresis loop under alternating magnetic fields at low intensity values. [36] Essentially, the main equation of DLRT describe hysteresis loop as ellipses which expand in a linear manner with the external alternating magnetic field:

$$M\big(H(t)\big) = H_0(\chi' \cos(2\pi f\ t) + \chi''\sin\,(2\pi f\ t) \qquad \text{(eq. 1.6)}$$

Where χ’ and χ’’ represents the phase and the out of phase components of magnetic susceptibility. However, it is important to note that this approach is only valid when H is near to 0. In contrast, magnetic fields in magnetic hyperthermia are sometimes comparable to the anisotropy field of the MNPs ($H_k = K/2M_{saturation}$), leading to the invalidity of DLRT premises (Figure 1.6). [37]

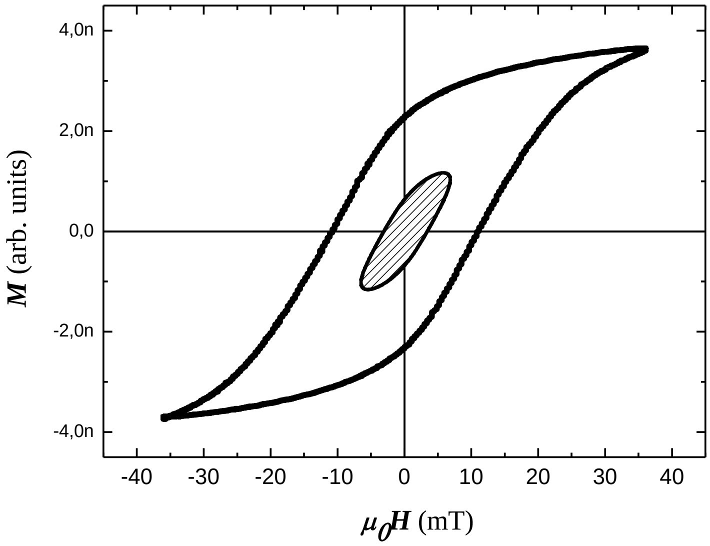

Figure 1.6. Experimental measurements of AC hysteresis loops at 100 kHz for 19nm IONP dispersed in water measured by an induction magnetometer. Dashed cycle: linear response region. Solid cycle: out-of-linear response region.

Large external magnetic fields lead to different phenomena related to its interaction with the internal MNP magnetic moment.[38] The external field alter the dynamical magnetic response of IONPs due to the appearance of a magnetic torque and the activation of magnetic inversion mechanisms, modulating the relaxation times. Hence, micromagnetic models based on modified Landau-Liftshit-Gilbert equation have been extensively explored for simulating the AC hysteresis loops and consequently, the assessment of the magnetic losses.[39-42]

1.3. MNPs microstructure and composition

Among the different compositions of MNPs, iron oxides have focused most of the scientific community's attention so far, being employed in technology issues for long time. Their biocompatibility, ease and moderate cost of synthesis and moderate turning together with the accumulated experience in the use of these compounds, turn iron oxide nanoparticles (IONPs) into the reference material for biomedical applications nowadays.

1.3.1. Structural properties IONPs

The chemical composition of the magnetic IONP is magnetite (Fe_3O_4), with a face cubic centered structure and Fe^{2+} and Fe^{3+} cations; and maghemite, also with FCC cell that only contains Fe^{3+}. In the first allotropic, Fe^{3+} in tetrahedral and octahedral site couple antiferromagnetically (in same direction and opposite sense) via oxygen atom. That implies a net magnetic moment only from Fe^{2+} cations (Figure 1.7a). In maghemite case, Fe^{2+} vacancies are randomly distributed in octahedral sites, whereas Fe^{3+} occupies octahedral and tetrahedral spaces (Figure 1.7b). In both cases, the presence of antiparallel spins in the lattices and the spontaneous magnetization of them categorize both as ferrimagnetic.

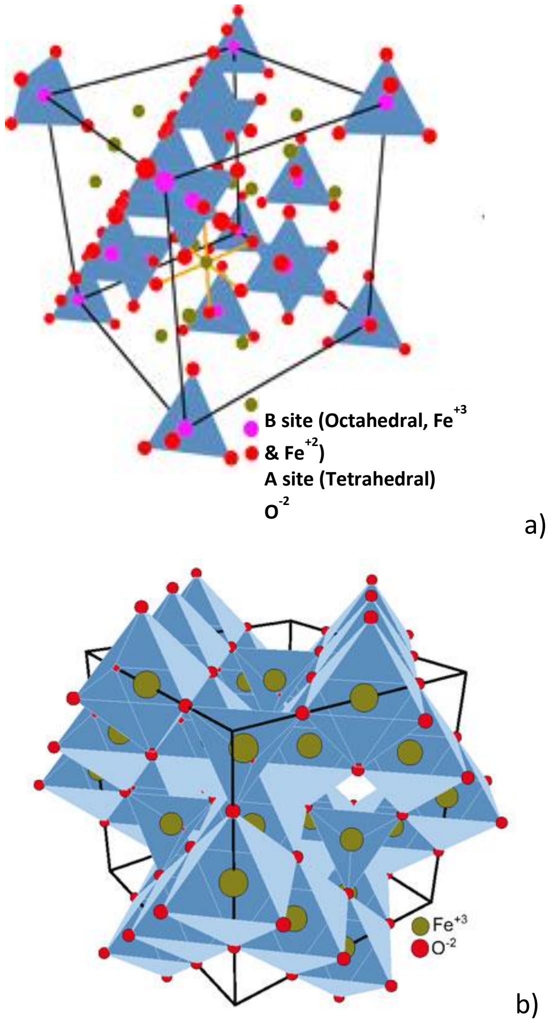

Figure 1.7. Representation of crystalline structure of a)magnetite and b)maghemite[43]

1.3.2. Transition metal doping of IONPs

Maghemite and magnetite oxides, phases from which usually IONPs are made of, present magnetic anisotropy values around 4.6 kJ m^{-3} and 11-14 kJ m^{-3} respectively. IONPs composition and crystal lattice essentially dictates the magnitude of their magnetic anisotropy (K). Hence, despite the shape and surface defects can play a role tuning IONPs magnetic anisotropy, their composition essentially disables the raising of

K far beyond the above-mentioned values, limiting their heat capability. For the sake of overcoming these *K* thresholds, several authors have purposed the IONPs doping with transition metals (such as Mn or Co), modifying the crystal structure of the system. These elements, thanks to their similar Fe atomic radius, can substitute iron positions in the lattice, reaching K values up to 220 kJ m^{-3} depending on the doping level and in principle, enhancing their thermal features. However, it is important to note that although this approach have demonstrated to increase MNPs SAR under certain AMF conditions, the magnetic heat release may be highly determined by Brownian relaxation process (i.e. sensitive to viscosity), leading to unsuitable capabilities to act as intracellular hyperthermia mediators.

1.4. MNPs in colloidal dispersion

Magnetic nanoparticles solubilization and stabilization in a colloidal dispersion become a crucial point in biomedical application[44]. The ability of keeping MNPs stable in liquid phases for long periods of times (generally, months) is a prerequisite for the translation of this technology into clinics. However, MNPs counts with a considerable surface energy when dispersed in a colloid. Also, MNPs experiment inter-particle attractive forces due to their magnetic nature. Such confluence of attractive force lead to the apparition of aggregation and agglomeration phenomena and eventually, the destabilization of the MNPs colloidal dispersion. Hence, nanoparticles surface engineering becomes mandatory to compensate these MNPs aggregative phenomena.

Proper coatings supply colloidal stability of MNPs for a given liquid dispersion, which tightly depends on the polarity of the solvent. In general, coating material are expected to avoid their agglomeration into the colloidal dispersion thanks to their ability to generate inter-particle electrostatic and/or steric repulsion forces (Figure 1.8), maintaining the MNPs aggregates size below < 0.2 µm.

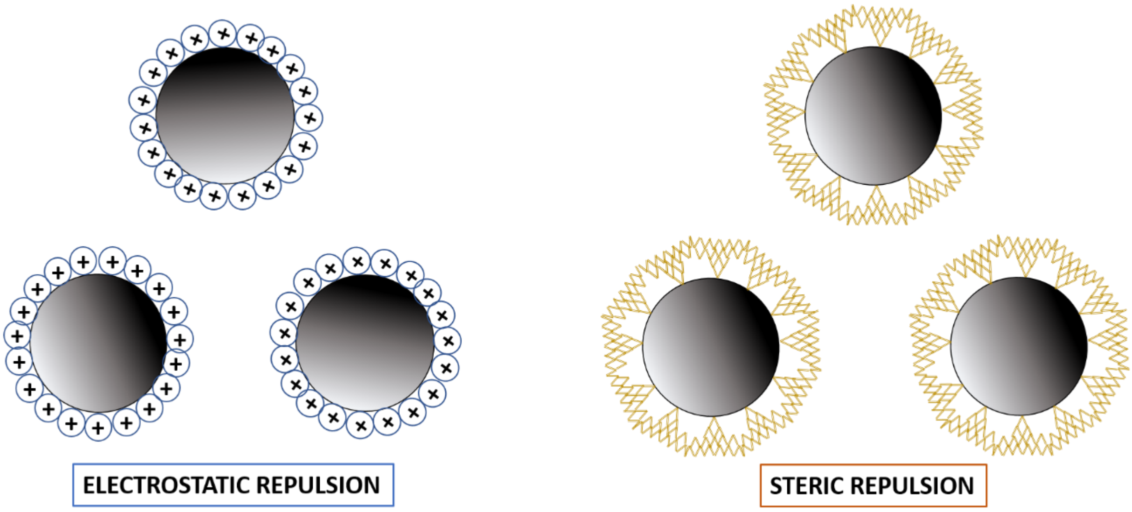

Figure 1.8. Schemes of MNPs colloidal stabilization strategies based on electrostatic repulsion (left) and steric (right graph) repulsion.

The existent variety of compositions used for MNP coating enables to confer stability to MNPs in the most diverse solvents. In a general manner, hydrophiles will be compatible with polar solvents (H_2O) and hydrophobes with apolar solvents (toluene, hexane). The latter are commonly found as surfactants (i.e. oleic acid) in thermal decomposition synthesis methods, providing not only stability to the dispersion via steric repulsion among particles, but also taking an active role in the reaction as nucleation control agents. However, as a prerequisite for biomedical applications, MNPs need to be solubilized in aqueous dispersion, i.e. polar solvent. For that purpose, we can find coatings made of PMAO[16], aminopropilsilane (APTES), polyetilene glycol (PEG)[45], dimercaptosuccinic acid (DMSA)[46] or polyvinylpyrrolidone (PVP)[47], among others. Also, citrates have been widely reported as together to stabilize MNPs and are considered to be MNPs cell internalization enhancement agent.[48]

1.4.1 MNPs dispersed in biological fluids

When nanoparticles enter a biological fluid, such as blood or plasma, MNPs surface may be rapidly bind by biomolecules. These interactions eventually lead to the formation of a dynamic protein corona and in some cases, the particle-particle aggregation. In addition, the natural presence of ions in the physiological fluids modifies the interaction between MNPs surface charges and solvent with the diluted molecules. Nanoparticles surface properties, such as hydrophilicity and net surface charge, dictates the extent and specificity of protein binding and the affinity with the solvent and consequently, the stability of MNPs in physiological conditions (Figure 1.9).

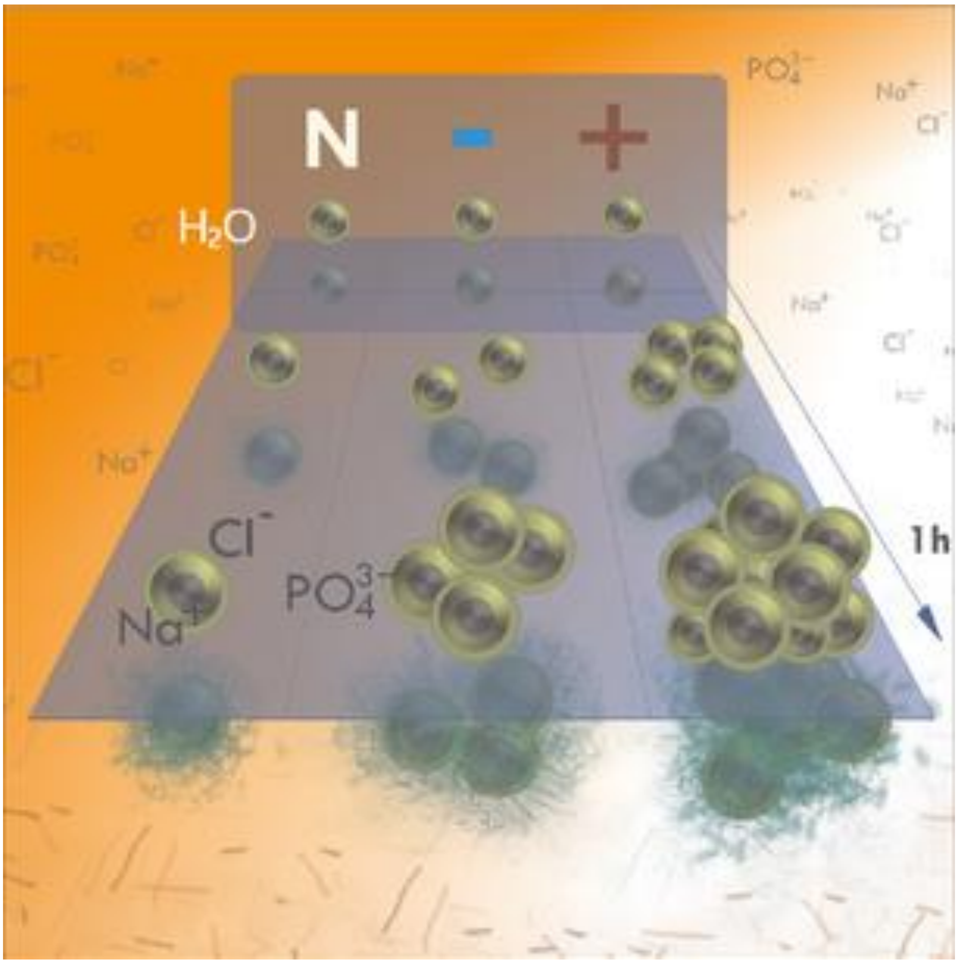

Figure 1.9. Illustration of the different effects on the colloidal stability of MNP produced by the presence of biomolecules and salts in the dispersion medium. Reproduced from ref.[49]

Remarkably, MNP-biomolecule interactions can lead to changes into the dynamical magnetic response since Brown and Neel magnetic relaxation mechanisms are modified, mainly due to changes in the hydrodynamic volume (V_H) and the effective anisotropy (K_{eff}) of the particles (Figure 1.10).

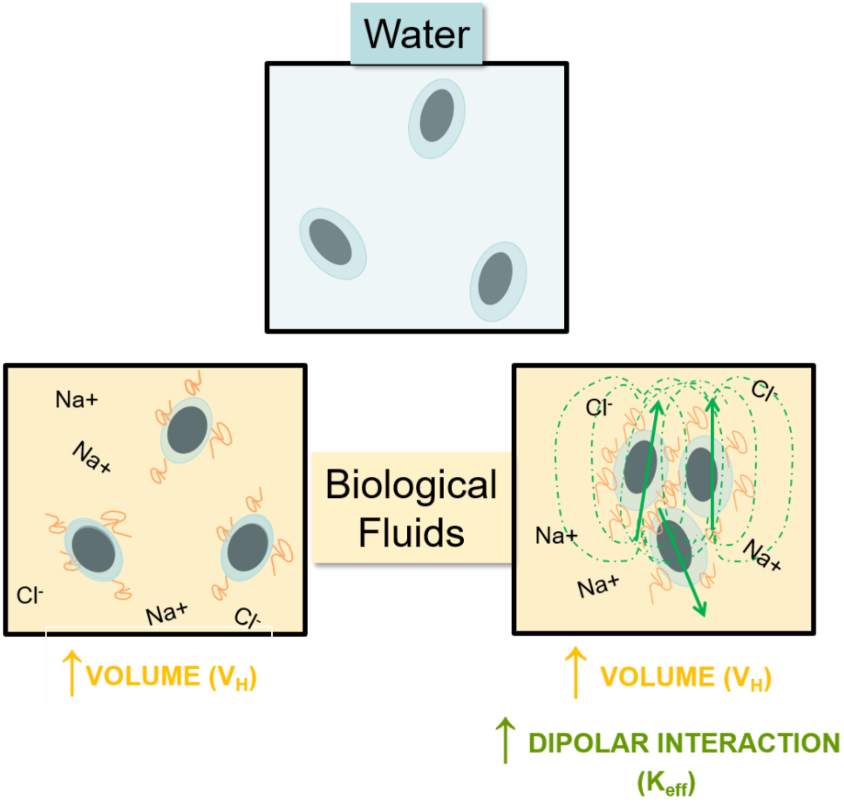

Figure 1.10. Schematic representation of the variations in VH and Keff induced by MNPs-proteins interaction and the presence of dilluted ions.

All this phenomenology is even enhanced when MNPs interact with more complex biological entities. Following a cell internalization paths, MNPs suffer a remarkable agglomeration inside cell vesicles which, in some cases, overcomes in one decade the hydrodynamic volume measured in water dispersion (Figure 1.11). In addition, accordingly to *Kuimova et al.*[50], MNPs would face a partial immobilization due to the high viscosity values (η) present in cell vesicles (~10-80 η_{Water}). The evaluation of the dynamical magnetic response of MNPs inside cells requires therefore the consideration not only of V_H and K_{eff}, but also the environmental viscosity which presumably will alter the Brownian relaxation mechanism.

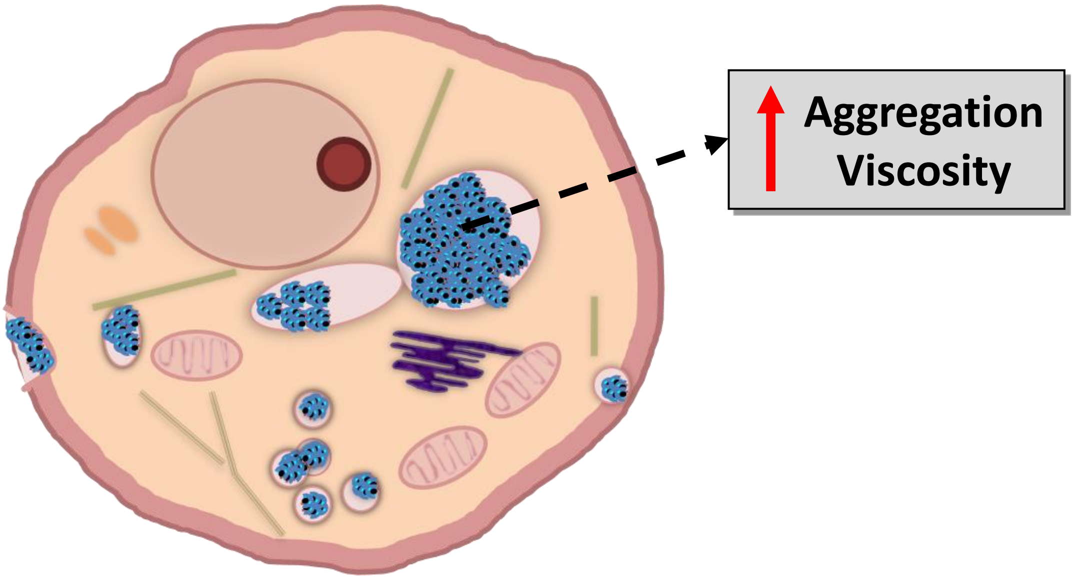

Figure 1.11. Scheme of the influence of cell internalization into the colloidal properties of MNPs.[49]

1.5. Magnetic characterization techniques for MNPs

1.5.1. Calorimetry under alternating magnetic field conditions

The magnetic heat release of MNPs when subjected to an AMF is a relevant physical parameter related to determine the suitability of its dynamical magnetic response of MNPs for MH hyperthermia studies. Diverse methods and parameters for the heat losses characterization have been purpose, although the most reported physical magnitude is the Specific Absorption Rate (SAR), defined in equation 1.3.

For measuring SAR, MNPs are generally dispersed in liquid medium. Once the MNPs dispersion is in thermal equilibrium with the environment, AMF is activated, producing a heat dissipation that will be transfer to the dispersion media. Parallel, this temperature rise is monitored with an optic fiber probe immersed in the colloidal dispersion (Figure 1.12).

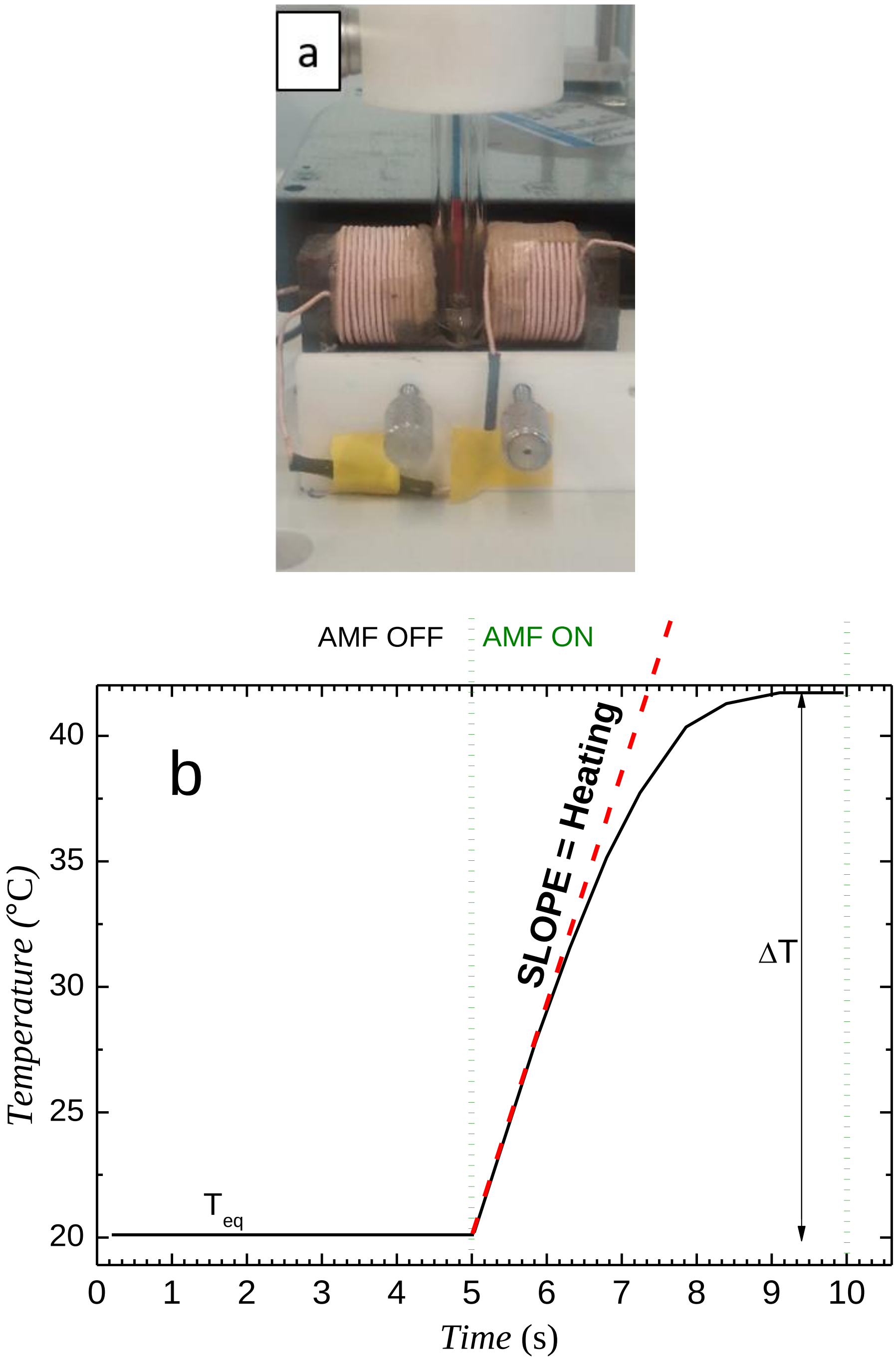

Figure 1.12. a) Photography of an SAR measurement equipment. b)Temperature raise in time of MNPs sample dispersed in water during a SAR measurement.

Afterwards, SAR is calculated as follows:

$$SAR = \frac{Cd\, m_d}{m_{MNP}} \left.\frac{dT}{dt}\right|_{max} \qquad \text{(eq. 1.7)}$$

Where Cd is the dispersion specific heat, $m_d$is the mass of the dispersion, m_{MNP} is MNPs mass and $\left.\frac{dT}{dt}\right|_{max}$ is the initial slope of the curve temperature versus time.

Ideally, these measurements should be performed under adiabatic conditions. Nevertheless, this thermodynamic regime strongly hinders the design of the equipment and the measurement protocol[51]. In consequence, practically all reported SAR measurements are performed under non-adiabatic conditions, although heat losses can be reduced attending to the different heat transmission mechanisms: i) small volumes of colloidal dispersions (tens of µL) are used to avoid radiative heat losses; ii) vacuum shield surrounding the sample holder minimises conductive losses; iii) convection losses are diminished reducing the aperture for introducing the temperature probe into the sample volume.

1.5.2. Magnetic characterisation

Induction techniques

Induction magnetic characterization techniques are traditionally the most developed techniques since it is probably the only one that can be built with relatively low-cost requirements. Generally, detection system of these apparatus is based on the so-called pick-up coils, whose transfer function $V_{EMF} = f(B)$ derives from the Faraday's Electromagnetic Law of Induction:

$$V_{EMF} = -n\frac{d\Phi}{dt} = -n \cdot A \cdot \frac{dB}{dt} \qquad \text{(eq. 1.8)}$$

Where n is the number of is turns of the pick-up coil, Φ is the magnetic flux that pass through the pick-up coil, A is the area enclosed inside the pick-up coil and B is the magnetic induction field.

In the context of the magnetic characterization of MNPs, the time scale in which the magnetic measurement is performed charges special relevance since dynamical effects on the magnetization of the MNPs (Néel and Brown relaxation mechanisms) arises in magnetic hyperthermia condition. Generally, this frontier between the quasi-static and alternating regime is imposed in the 1-10 seconds.

AC Techniques

AC Magnetometer

AC magnetometer enables the measurement of hysteresis loops of a magnetic material under AMF conditions. The main attractive of is technique relies on the possibility of measuring the magnetization loop of MNPs in AMF conditions which are near to these used in magnetic hyperthermia treatments[13]. in comparison with calorimetric methods, their main advantages are, on one hand, the measurement of the hysteresis loop, which provides information that goes beyond the SAR – identification and quantification of hysteresis loop parameters, i.e. remanence, coercivity, saturation and shape, providing quite profitable information about MNP magnetic relaxation mechanisms, magnetization reversal and the particle-particle magnetic dipolar interactions[15]. On the other hand, the measurement of the AC hysteresis loops is not influenced by the media where MNPs are dispersed, since generally MNPs magnetic contribution to the induced electromotive force (EMF) is several orders of magnitude larger that these generated by the dispersion media. Such AC magnetometer characteristic enables one of his main features: the performance of AC measurement of MNPs which are in biological matrices. AC magnetometer plays a main role in the present work as it is systematically employed in each study presented here, leading us to develop our own prototypes for advanced magnetic measurements of MNPs. Thus, the present dissertation reserves a chapter (Chapter 2) in where the technical and operative aspects about development of an AC magnetometer prototype is addressed.

AC Susceptometer

AC susceptometer measures the magnetic response of MNPs in terms of complex susceptibility (Figure 1.13). This instrument share with AC magnetometer common hardware features mostly regarding to the excitation and detection coils, although their electronic and software design is oriented for different magnetic excitation and detection windows.

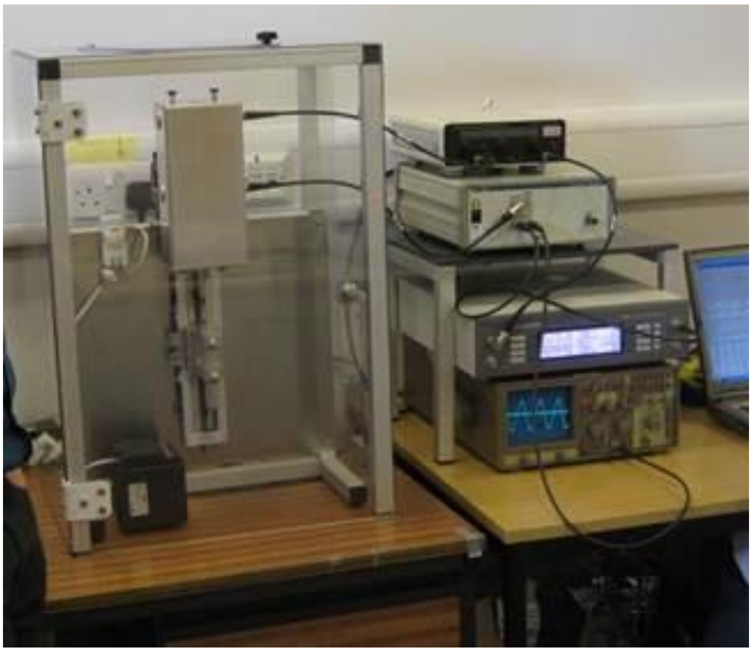

Figure 1.13. AC susceptometer at Institute for Science and Technology in Medicine, Keele University, UK. Reproduced with permission.

Usually, AC susceptometer cover a wide range of field frequencies (from mHz to MHz) while the magnetic field amplitude (H_0) is limited to dozen of A m^{-1}. At this low fields, the sample magnetic behaviour is enclosed in the linear response regime and the magnetization of the studied sample is described in terms of complex magnetic susceptibility:

$$M(t) = H_0(\chi' cos\omega t + i\chi'' sin\omega t) \qquad \text{(eq. 1.9)}$$

Where $\chi'$is the in-phase or real component, χ'' the out-of-phase or imaginary component of the susceptibility and $\omega = f/2\pi$. Since the measurement protocol usually contemplates an initial subtraction of the background signal produced by defects in the compensation of the detection coils circuit, as well as delay artefacts provoked by electronics, the induced voltage can be deduced from:

$$V_{sample}(t) = -\mu_0 n\, S_{sample} \frac{dM(t)}{dt} \qquad \text{(eq. 1.10)}$$

Substituting $M(t)$ (eq. 1.9) into into V_{sample}, we obtain:

$$V_{sample}(t) = \mu_0 n\, S_{sample} \omega H_0 \left(\chi' sin\omega t + i\chi'' cos\omega t\right) \qquad \text{(eq. 1.11)}$$

On the other hand, relaxation times relates to the complex susceptibility (χ_{ac}) as follows:

$$\chi_{ac} = \chi' + i\chi'' \qquad \text{(eq. 1.12)}$$

$$\chi' = \chi_0 \frac{1}{\left(1 + \left(\omega\, \tau_{eff}\right)^2\right)} \qquad \text{(eq. 1.13)}$$

$$\chi'' = \chi_0 \frac{\omega\, \tau_{eff}}{\left(1 + \left(\omega\, \tau_{eff}\right)^2\right)} \qquad \text{(eq. 1.14)}$$

Where τ_{eff} is effective relaxation time, showed in equation 1.6. Thanks to this relation among magnetic relaxation mechanisms and the complex susceptibility (χ_{ac}), AC susceptometer provides direct information about the magnetic relaxation mechanisms of MNP when dispersed in liquid media and similarly to the AC magnetometry, its suitability for measuring the MNPs magnetic response in biological entities have been accomplished.[29,52]

DC Techniques

Inductive sensor, such as pick-up coils, can only measure magnetic fields (B) that change in time. For the nature of these techniques, AC magnetometer and susceptometer work on the base of alternating magnetic field generation. However, it is possible measuring also the B-field under quasi-static conditions if a change in the magnetic flux, which crosses the detection coil, is generated by other means beyond an alternating current.

Vibrating Sample Magnetometer (VSM)

The vibrating sample magnetometer (VSM) is a good example of this procedure. In this instrument, the magnetic sample is placed in a stick joint to a mechanic resonator and located in a homogeneous constant magnetic field (Figure 1.14). The sample that is eventually magnetized generates a magnetic field. This field receive the name of magnetic stray field. As the sample is vibrating, the magnetic flux from the magnetic stray field collected by the secondary coils will vary in time, resulting in an induced electromotive force (ε_{sec}).

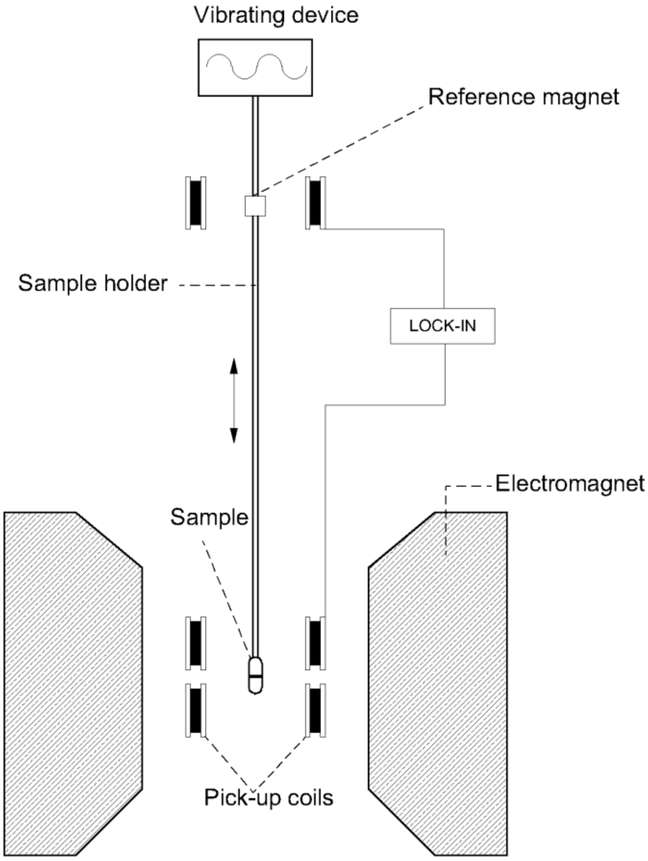

Figure 1.14. Schematic representation of a Vibrating Sample magnetometer. Figure based on ref. [53]

The vibration of the mechanical resonator is used as reference by a Lock-in amplifier that filters all the frequencies that do not corresponds with the mechanical resonator, obtaining the contribution of the magnetic moment of the sample. A distinguished characteristic of VSM is the large magnetic field that can apply: common commercial models work in a range of 1-5 T – more than enough for reaching the saturation in most of ferro-ferrimagnetic material.

Quantum techniques

Superconducting Quantum Interference Device Magnetometer (SQUID)

Superconducting Quantum Interference Device (SQUID) Magnetometer are equipment able to measure magnetic flux variations through the use of superconducting technology. It consists of two superconductors separated by two thin insulators to create two parallel Josephson junctions (Figure 1.15).

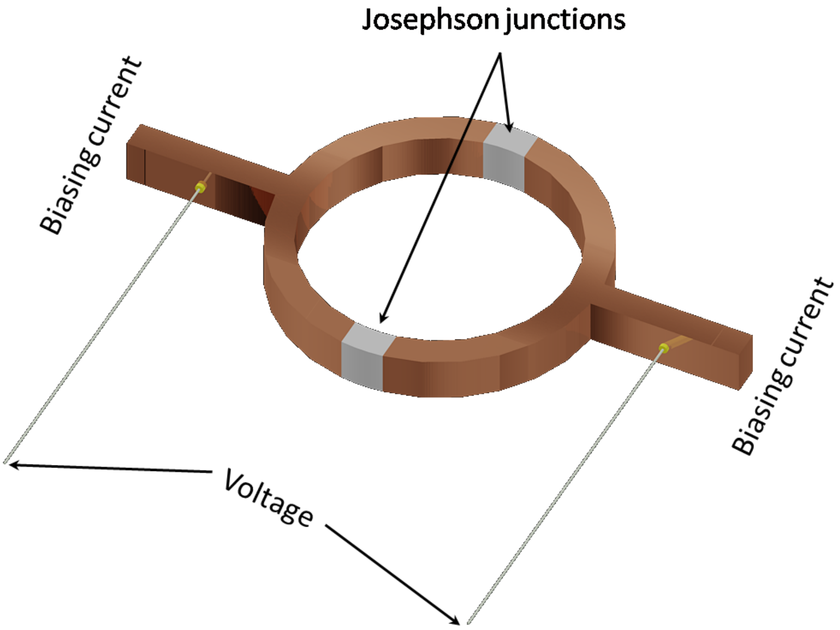

Figure 1.15. Schematic representation of a SQUID detector. Based on ref. [54]

If certainly SQUIDs can reach magnetic fields as large as these of VSM, its most important feature is a great sensitivity associated to the fundamentals of its detection system. The magnetic flux that penetrates the ring is quantized and is an integer number of the flux quantum. In consequence, minimum detectable magnetic flux can be calculated as follows:

$$\phi_0 = \frac{2\pi\hbar}{2e} \cong 2.0678 \cdot 10^{-15} \; (T\,m^2) \qquad \text{(eq. 1.15)}$$

The running of the dispositive is based on the injection of a constant biasing current through the superconducting ring. Thus, when the magnetic flux enclosed by this ring changes, the measured voltage suffers oscillations that ultimately are translated in quantum of ϕ_0.

1.6. Non-magnetic characterization techniques of MNPs

1.5.1 Colloidal Characterisation

Dynamic Light Scattering (DLS) and Electrophoretic Light Scattering (ELS)

Dynamic Light Scattering is among the most popular techniques for determining the hydrodynamic size of particles down to 1 nm. The basic principle is the following: a laser beam is projected through the sample, producing a scattered light that is detected at a previously known angle.

The light scattered by the nanoparticles provides information about their Brownian random motion in the dispersant, as they present characteristic patterns in the fluctuations of its intensity in time $I_s(t)$. Computing this data in form of a correlation function, one can obtain the diffusion coefficient of the nanoparticles D that is related with the radius of the particles R on this manner:

$$R = \frac{k_B T}{6\pi \eta D} \qquad \text{(eq. 1.16)}$$

Where k_B is the Boltzmann constant, T is the temperature and η is the dispersion medium viscosity. The validity of this formula is limited to low nanoparticles concentrations rates (bellow 0.05 g/L) where multiple scattering of light will not occur.

An analogous technique, Electrophoretic Light Scattering (ELS) is used for determining the potential difference between the liquid medium and layer of fluid attached to the nanoparticles (ζ-potential). In this case, an oscillating electric field is injected in the dispersion, producing a migration of particles. The particle is irradiated by a laser beam and scattering light causes a Doppler shift due to the electrophoretic mobility of the particles. Ultimately, ζ-potential can be calculated from the latter using the Smoluchowski equation:

$$\zeta = \frac{\eta U}{\varepsilon_0 \varepsilon_r} \qquad \text{(eq. 1.17)}$$

Where η is the media viscosity, U the nanoparticles electrophoretic mobility, E the electric field, $\varepsilon_0$the permittivity in vacuum and ε_r the permittivity of the dispersion medium.

Both hydrodynamic size and ζ-potential are known to affect the colloidal stability. Thus, a systematic evaluation on them in the used samples become mandatory in order to prevent undesirable agglomeration phenomena and in consequence, destabilization.

1.6.2. Elementary analysis

Inductively Coupled Plasma Mass Spectrometry (ICP-MS/OES)

Inductively Coupled Plasma-Mass Spectrometry is an analytical technique used for elemental quantification, from which schematic representation of the is shown in Figure 1.16. This technique basis on the combination of a Inductive Coupled Plasma (ICP) source with an mass spectrometer detector. The ICP ionizes the target atoms of the sample in ions that afterward are selectively separated and detected in the mass spectrometer (MS). Argon gas is made to flow inside the ICP torch zone and a spark is applied, stripping off electrons from the argon atoms and forming ions. These ions are contained with a coil connected to a radio-frequency generator, producing the collision and ionization with other argon atoms and later a plasma.

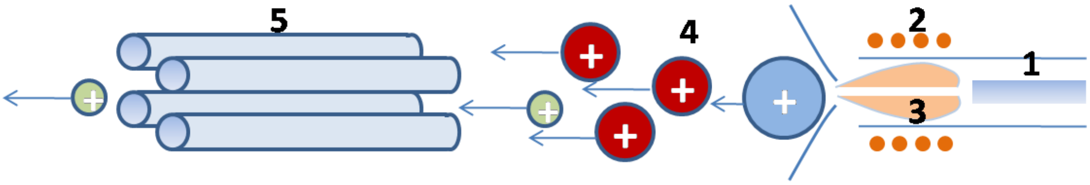

Figure 1.16. Schematic representation of an ICP-MS. 1. Sample nebulizer 2. RF coil 3. Argon plasma. 4. Sample ions. 5.Mass spectrometer. Based on PerkinElmer, Inc. image.

The sample is introduced into the argon plasma as an aerosol and the elements are desolvated, turned into gas phase and eventually ionized. Finally, the ions of the target sample are transported to a low-pressure zone of the instrument (<10^{-5} Torr) and focused via electrostatic lenses into the mass spectrometer (commonly a quadrupole mass filter), filtering them accordingly their mass/charge ratio and providing an associated characteristic spectrum. One of the most important advantages of this technique is their detection limits (around ppm), which renders a suitable technique for a precise elementary quantification of the compounds used in the present work.

1.7. Cell culture and MNPs

Cell culture has become a useful and omnipresent tool in nanomedical research. This term strictly refers to the extraction of cells from an animal or plant for their later growth and alive maintenance under suitable artificial conditions. Once disaggregated from their original tissue, cells receive the name of primary culture which in last term, after subsequent passages, become a **cell line.** Culture of cells extracted directly from tumors have become relatively common nowadays. However, most of *in-vitro* experiments are carried out with well-established human cancer cells lines, such as HeLa or MCF-7 cancer cells. These cell line, defined as continuous due to their ability to proliferate without passage limit, are widely employed by the research community and easily available, facilitating also the repeatability of the experiments and the reproducibility between different laboratories.

The prerequisites for cell culture, now relatively common in any research institution with biology research programs, are mainly a well-ventilated laboratory with a laminar flow hood (Class II), CO_2 incubator, centrifuge, optical microscope, plastic ware such flasks, tubes and dishes and supply of supplemented cell culture medium (DMEM, Serum) for the growth, manipulation and storage of cells are located. These facilities and supplies provide a sufficient environment for a safe, sterile working with cells (Figure 1.17).

Figure 1.17. Typical view of a cell culture laboratory. IMDEA Nanoscience cell culture laboratory.

Protocols and materials for the growth a preservation of a concrete cell line are variable. The composition of the culture medium or the diverse culture manipulation operation (centrifugation, trypsinization) which cells can stand strongly dependent on the used line. In our case, as it will be shown in their correspondent chapter, MCF-7 cell line was used for in-vitro experiments with MNPs. The important amount of research in nanomedicine accomplished with these cells and more concretely, their suitability for the implementation of effective MNPs internalization protocols, essential for the obtaining of a magnetic characterization of vesicularized MNPs, raised as the main reasons behind this election. MCF-7 are adherent cells, growing as a monolayer over the supporting material. Also, they are sensitive to the enzymatic action of trypsin, allowing the detaching from the growing support employing biochemical means when the confluency of cells in the culture flask/dishes overcome the 80% and the passage is needed, or when the experiments demand the detachment of cells.

1.7.1. MNPs internalization in cells

In literature, a wide variety of MNPs internalization and labelling methods into cells can be found. In general terms, we can distinguish two main groups: mechanical guided (MG) and direct incubation (DI) methods. In the first group (i.e. mechanically directed methods), the MNPs are physically guided to the cell membrane or cytoplasm using centrifugation or external magnetic field gradients. In DI methods, the interaction between MNPs and cells are not mechanically forced. Such interaction appears spontaneously instead, thanks to the natural cells internalization mechanisms , i.e. Claritin/caveolar mediated endocytosis, pinocytosis, micropinocytosis and phagocytosis,[55,56] represented in Figure 1.18. Briefly, DI methods consist on the following: MNPs, usually sterilized by microfiltration, autoclave or UV exposition, are dispersed in cell culture medium in final concentrations below 0.5 g/L. Then, cell medium of a previously growth cell culture is substituted by MNPs loaded medium, after which cells are kept in incubation at 37°C from 8 to 72 h. Finally, non-internalized MNPs are retired through the extraction of the supernatant and rinse of the culture with PBS or another cell compatible medium.

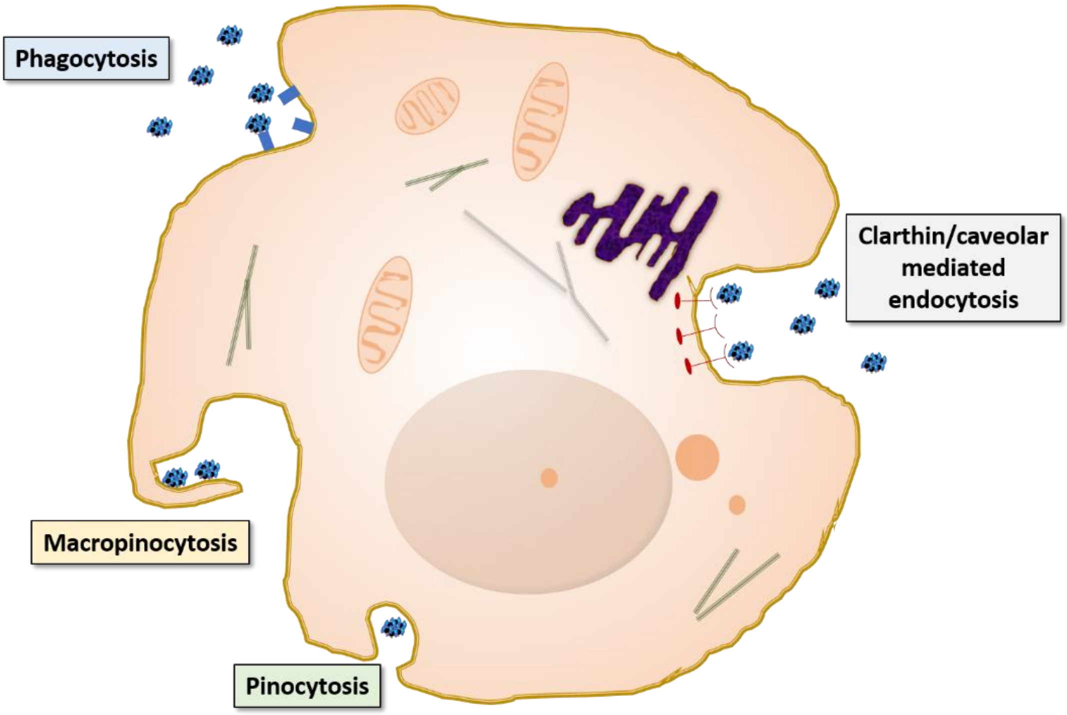

Figure 1.18. Schematic representation of different cell internalization mechanisms. Figure based on ref. [56]

MG methods have reported larger MNPs internalization rates, and authors claims their suitability for their easy transability among laboratories[57]. However, DI methods are traditionally the most employed[1,58] and consequently, the best characterized in terms of toxicity and safety[59]. Also, DI methods yield can be improved with the inclusion of cell starvation steps[48], MNPs surface engineering (both, coating and functionalization) and the stabilization of MNPs in cell culture medium with the formation of a protein corona onto the MNPs surface. These improvements, together with its easy implementation, turn DI into our selected method for all the cell studies presented in this work.

1.7.2. Microscopy techniques employed in cell culture

Microscopy techniques are employed in cell culture according to cell maintenance and experimental requirements. Optical microscopy is widely employed for the control of the different stages implied in cell culture works, such as the detachment, cell counting, seeding and control of cell confluency and morphology (Figure 1.19). However, the use of optical microscopy is not only limited to cell culture tasks, but also to different studies if effective image resolution needed do not go further to microns, such as a preliminary visualization of the MNPs in cell cultures.

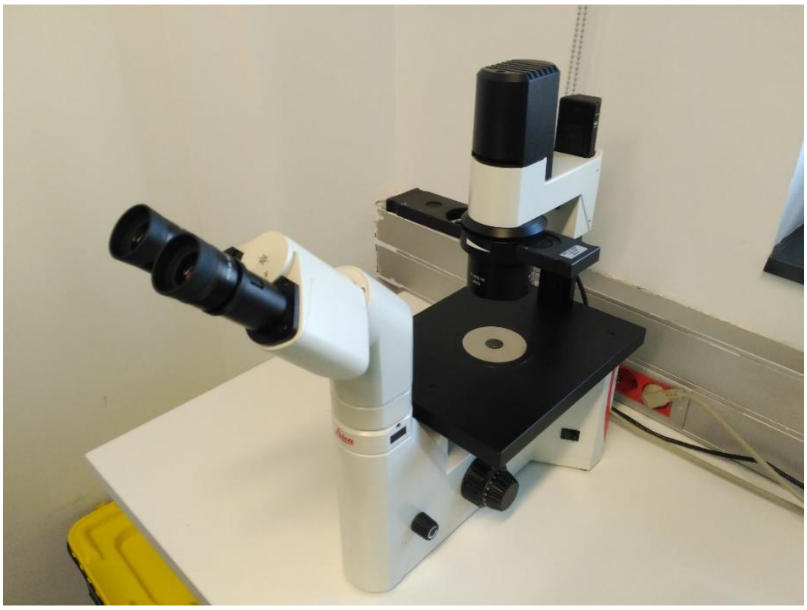

Figure 1.19. Optical microscope employed for cell culture maintenance tasks.

For a better visualization of the intracellular components and the location of MNP in cells, the utilization of more advanced microscopes is quite convenient instead. Confocal microscope provides a system, based on the illumination of the sample with lasers, which correct aberrations of optical microscopy. Such corrections enable the capture of tomographic planes along the cells and more interestingly, a further 3D reconstruction of the images with special-purpose software.

Also, Transmission Electron Microscopy (TEM) critically overcome the resolution of optical microscopes. Hence, using suitable pre-treatment of cell culture for the sake of make them visible to the electron beam, we can obtain tomographic sections with magnifications around 20k to 50k, making it at excellence technique to trace the path of the magnetic nanoparticles along the intracellular matrix. The complementation of the above-mentioned microscopy techniques with diverse cell and MNPs staining procedures, which selectively colour a target structure or react upon the presence of biological processes, turn these techniques in interesting tools for the monitor of the interaction between MNPs and cell cultures, showing the MNPs exact location in cells and how MNPs can affects the cell culture in terms of viability and morphology.

1.7.3. Stains and assay

Prussian Blue

Prussian Blue is a traditional and well-extended stain in histology and cell culture fields. Mainly, it is used for detecting an excess of iron in the spleen and bone marrow, conditions related to pathologies such as hemochromatosis and hemosiderosis. In our case, this staining protocol results quite useful as its implementation is simple, and the results can be visualized in an optic microscope. Its mechanisms of action basis on the combination of a ferric ion (+3) present in iron-based MNPs with ferrocyanides. Such combination leads to the formation of a bright blue pigment called Prussian Blue, observable under optical microscope set-up in bright field configuration. This approach does not provide rigorous data of MNPs in cells in terms of 3D development for the necessity of using optical microscopy for the visualization of the stained sample. However, as mentioned before, its cheapness and easy-to-use characteristics turns Prussian Blue Staining in a magnificent assistance in the optimization of a MNPs internalization protocol, as shown in Figure 1.20, where we can observe how two different MNPs cell uptake protocols lead to totally distinct results. In Figure 1.20a, MNPs appears equally in the surroundings of the cells, covering the nucleus of the cell, and attached. Figure 1.20b instead shows the ideal scenario regarding an efficient MNPs internalization in cells: blue perinuclear demi-lune halos, which indicates an effective MNP internalisation in cells, together with a lack of precipitation of the particles onto the growth surface.

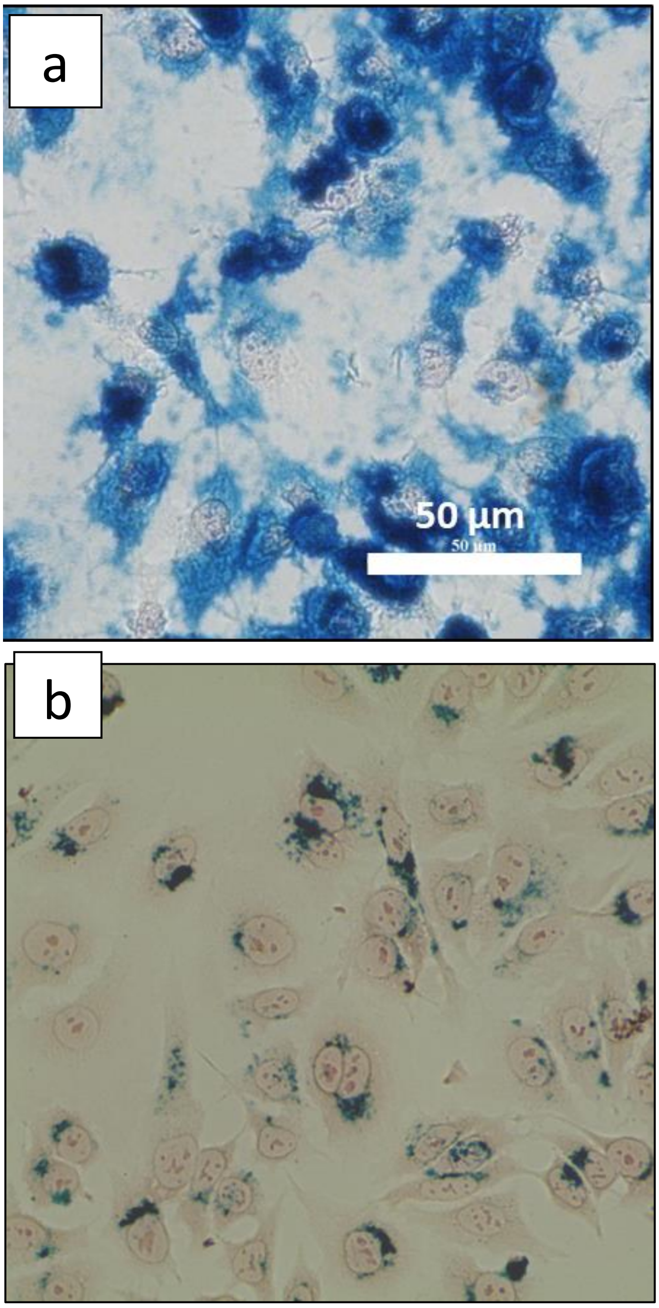

Figure 1.20. Bright field images of Prussian Blue stained MCF-7 cells after an a) failed and b) effective MNPs internalization process.

ActinRed™ 555

ActinRed™ 555 test (ReadyProbes®) allows the visualization of the cytoskeleton through its illumination with a fluorophore. The dye, tetramethylrhodamine isothiocyanate (TRITC), penetrates through the membrane of the cell and attach to F-actin with a high-affinity rate. After the actin binding, TRITC shows a brilliant fluorescent emission (Ex/Em: ~540/565 nm), permitting the assessment of cell morphology after in-vitro MNPs magnetic characterization experiments in a detailed manner.

Calcein AM and Ethidium homodimer LIVE/DEAD® test

Live/Dead® test allows the assessment of cell viability employing fluorescence and confocal microscopes. This assay basis on the use of two-color fluorescence components that simultaneously are added to the cells object of the study. Calcein AM reacts in presence of the intracellular esterase activity, proper of live active cells, producing a strong green fluorescence in viable cells (excitation/emission ~495nm/~515nm). Ethidium homodimer (EthD-1) instead, penetrates damage cell membranes, strongly enhancing their light emission features upon binding to nucleic acids. Such binding generates bright red fluorescence emission in the nucleus of cells if their membrane integrity has been compromised (ex/em ~495 nm/~635 nm). The combined use of both compounds enables us to determine how the employed MNPs and the different magnetic characterization techniques used in this work affects the integrity of the cells cultures.

Development of an AC magnetometer for advance magnetic measurements

2

Chapter

2. Development of an AC magnetometer for advance magnetic measurements

2.1. Introduction

In the present chapter, we describe the development of an AC magnetometer for measuring the dynamical magnetic response of MNPs under AMF conditions. Considering that the shape of the hysteresis loops varies with frequency and the area enclosed inside the loop represents mainly the energy dissipated by the magnetic nanomaterials[42], the present instrument entails the development of a methodology highly relevant for the AC magnetic characterization of MNPs. Among the main advantages of using an AC magnetometer for MNPs magnetic response characterisation, we can highlight that i) the measurements are performed under the same AMF conditions than in Magnetic Hyperthermia,[13] ii) AC hysteresis loop contains much more information than just the area enclosed inside: magnetic interaction,[60] aggregation of MNPs[49], nature of the relaxation mechanisms[61] or changes in magnetic anisotropy studies can be addressed, iii) measurement times are sensibly shorter than in calorimetric measurements. Whereas the AC magnetometry measurements are performed in much less than a minute, longer times and values of physical parameters (specific heat of dispersion medium) are needed in calorimetric equipment mainly due to experimental requirements related to non-adiabatic conditions[62], iv) the medium where MNPs are dispersed negligibly contributes to the input signal of the AC magnetometer. This, together with short time exposition of the samples to AMF conditions needed for the measurement, opens the possibility of measuring AC hysteresis loops of MNPs not only in aqueous media, but also in biological media and live cells.

2.2. Prototype development

Our main aims in the development of the AC magnetometer have been the construction of a low-cost, friendly-use and versatile equipment for measuring the AC hysteresis loops of MNPs dispersed in aqueous, biological media and placed in live cells. Since we tried to minimise the fabrication costs of the magnetometer without sacrificing the measurement reliability, its conception pivoted over three main principles:

- Use of lab electronic instruments.
- Use of low-cost materials and easy to handle.
- The establishment of a reliable methodology and data analysis protocol, providing good sensibitivity and reproducibility rates.

In Figure 2.1, an image of the AC magnetometer together with a set-up scheme is shown. According to their functionality, this apparatus is divided in three well distinguishable components. First, an AMF generator, made by a Litz wire solenoid-type coil integrated in a resonant electronic circuit (LCR), capable of generating AC magnetic fields up to H_{MAX} = 30 kA m^{-1} and f = 150 kHz. Secondly, a detection system based on pick-up or secondary coils connected to an oscilloscope (Tektronix) finally, a central processing/control unit, which in our case refers to PC with a special-purpose programmed software. Further details about all the above-mentioned components are provided in the following sections.

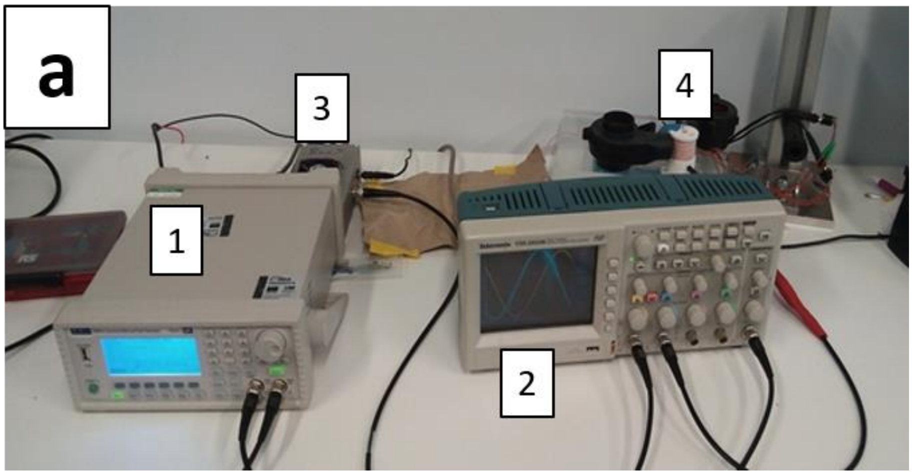

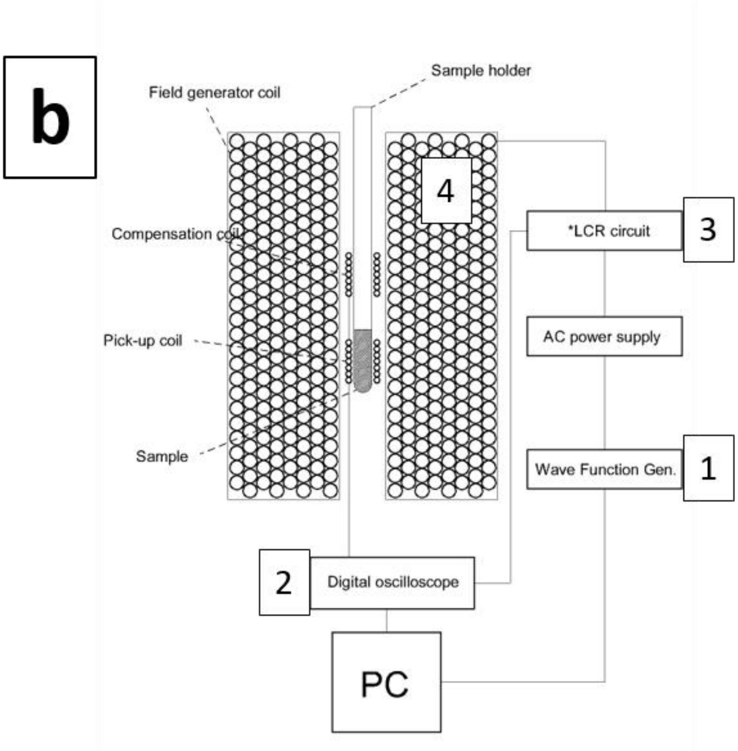

Figure 2.1. a) Image of the AC magnetometer set-up. b) General components scheme of the AC magnetometer.

2.2.1. LCR circuit

The AMF generator electronics consist of a LCR resonant circuit widely exploited in the magnetic hyperthermia equipment (Figure 2.2). This LCR circuit, from which the AMF generator coil corresponds to the inductive component (L), is fed by an AC power supplier (x10 gain in the frequency range from DC to 1 MHz) driven by a wave function generator (Aim-TTi TG5011). The principle of operation of this electronic configuration is establishing discrete resonant frequencies of the AC current which are related to the capacitor value (C). Hence, this resonant set-up can inject larger electric power loads from the AC power supplier to the AMF generation coil resulting in AC currents of few amps (peak value), which generates extreme AMF conditions (f and H_{MAX}).

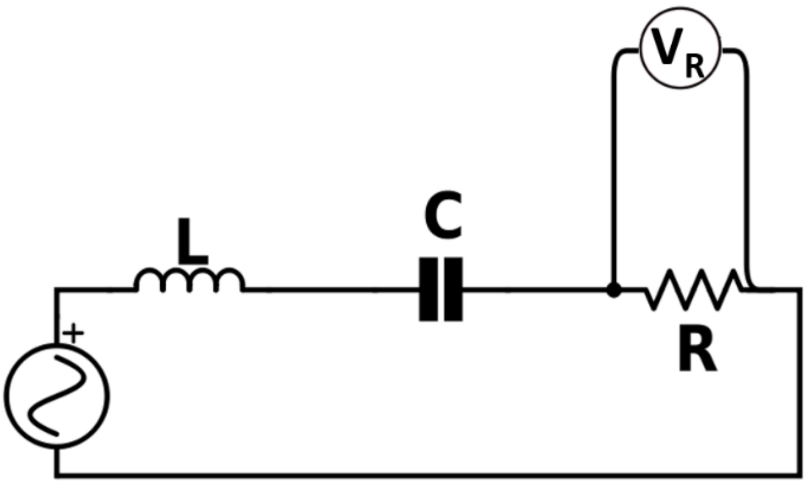

Figure 2.2. Scheme of the LCR resonant circuit employed for AMF generation.

Considering that the resonant frequency (f_0) of a LCR circuit is given by the following equation:

$$f_0 = \frac{1}{2\pi\sqrt{LC_0}} \qquad \text{(eq. 2.1)}$$

where L is the inductance and C is the capacitance; we can preestablish a needed capacity value (C_0) for a target AMF frequency (f_0). For setting the frequencies available for the AC magnetometer, different capacitors (C) were manually switched providing distinct capacity values to the LCR circuit. However, it is important to note that the solution f_0 of this equation requires the previous knowledge of the capacity and inductance of the circuit. In our case, this represents an added difficulty due to, as explained in following sections, the home-made characteristics of the AMF generator coil. Hence, we accomplished another methodology, which excludes the necessity of explicitly knowing the AMF generation coil inductance, for calculating LCR resonant frequencies. First, we needed to find a pair of f_0 and C_0 capacity values where the LCR resonates manually tuning the system. In this regard, previously LCR derived V_R signal (Figure 2.2) results a suitable control parameter for establishing the resonance parameters, as it reaches its maximum value when the resonant frequency (f_0) is set into the wave function generator. Once this $C_0 f_0$ pair was set up, $C_n f_n$ new pairs can be calculated equalling L component in both equations:

$$\frac{1}{2\pi {f_n}^2 C_n} = L = \frac{1}{2\pi {f_0}^2 C_0} \qquad \text{(eq. 2.2)}$$

Rearranging the terms:

$${f_0}^2 C_0 = {f_n}^2 C_n \qquad \text{(eq. 2.3)}$$

In Table 2.1, theoretical and empirical f and C capacity values employed in AC magnetometry measurements are shown. There, a good agreement between calculated and measured values are found.

Table 2.1. Theoretical and empirical values of C capacity and their resonant frequencies (*f*) counterparts.

Theoretical *C* (nF)	Empirical *C* (nF)	Theoretical *f* (kHz)	Empirical *f* (kHz)
	20 (*C₀*)		**101 (*C₀*)**
326	**320**	**25**	**25**
126	**120**	**40**	**40**
81	**80**	**50**	**51**
29	**27**	**85**	**87**
9.6	**9.7**	**150**	**145**

2.2.2. AMF generation coil

The field generation coil (primary coil) is composed by Litz wires wounded in a non-electric conductive support, resulting in a solenoid geometry. This type of wires counts with the main feature of reducing the skin effect associated to the transport of high frequency currents in an electrical conductor, diminishing the coil impedance and Joule effect-associated heat losses as much as possible. The efficiency of the coil is sufficiently optimised in order to only use a pair of low voltage fans for its cooling. Also, in comparison with pipe-type conductors employed in other reported set-ups[63], Litz wires are easy to handle and wound, reducing the complexity of constructing an efficient home-made type AMF generator coil.

2.2.3. Detection system

The detection system consists of two identical contrary-wise pick-up coils connected in series (Figure 2.1b) and derived to the oscilloscope. The lower pick-up coil, where sample holders are placed during the measurement, captures the EMF that corresponds to the studied MNPs. The upper one instead takes the role of compensation coil, reducing the contribution of the AMF to the EMF. The pick-up coils are wound on the same support than the main coil and are properly isolated from it with isolating tap.

Measurement fundamentals and protocol

We designed a measurement process inspired on the so-called differential method, reported in other AC magnetometer designs[63,64]. The main advantage of this approach is the significant reduction of background signals, related to the sole contribution of the AMF into EMF. For the measurement of the AC hysteresis loops of MNPs, we proceeded as follows: first, without the presence of the sample inside the measurement area, the AMF is activated, and the induced EMF is acquired. This signal, named as background signal (V_{back}), arises from the fact that the detection coils are not fully compensated (Figure 2.3a-black line). Indeed, they are not totally identical in terms of shape, conductivity and placement into the AMF. Secondly, after V_{back} have been acquired, the sample is set into the lower pick-up coil and the EMF signal is acquired again (V_{back} + V_{sample}). Changes that the introduction of sample produces on the acquired EMF signals can be appreciated in Figure 2.3. In this example, V_{back} signal (Figure 2.3a-green line) presents a sinusoidal shape which incorporates well defined peaks when the sample stands inside the detection coil (Figure 2.3a-black line).

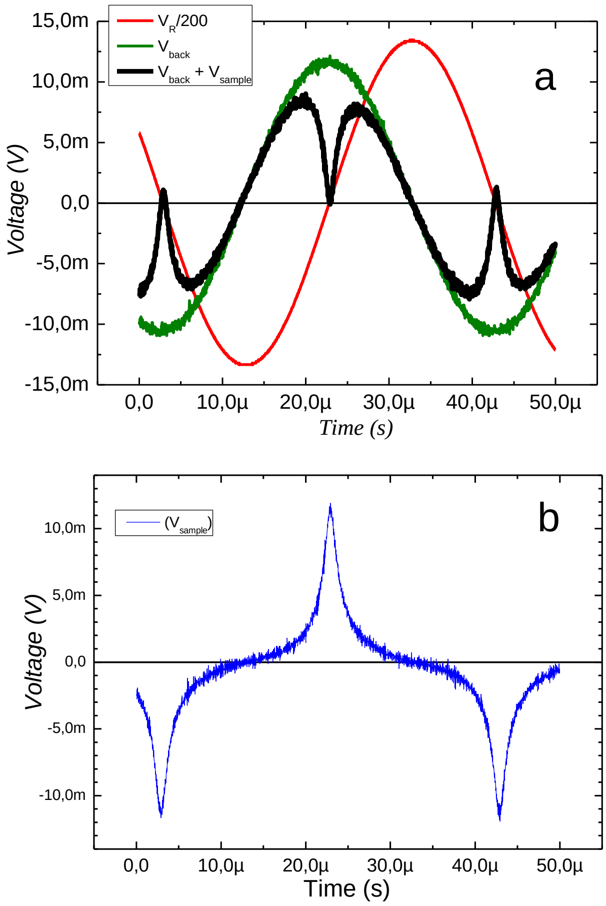

Figure 2.3. Acquired signals during the measurement procedure. **a)** Red line: Signal parallel to the resistances of the LCR circuit (V_R). Green line: background EMF signal induced by the AMF (V_{back}). Black line: induced EMF by the EMF and the sample contribution (V_{back} + V_{sample}). **b)** Contribution to the EMF of the measured sample (V_{sample}).

After the acquisition process is finished, the background signal V_{back} (i.e. the signal without sample) is subtracted from the EMF induced by the field plus the sample (V_{back}+V_{sample}), resulting in the calculation of the sole contribution of the sample to the EMF (Figure 2.3b). Afterwards, in order to calculate the magnetization per unit of mass, V_{sample} is numerically integrated respect to time as follows:

$$M(t) = \frac{1}{\mu_0 n \rho A_{sample} \phi} \int V_{sample}\, dt \qquad \text{(eq. 2.4)}$$

Where $M(t)$ is the time dependant magnetization per unit of mass of magnetic materials, n the number of turns of the pick-up coil, A_{sample} the surface of an infinitesimal section of the sample, and ρ the density of the magnetic material and ϕ the volume concentration of the sample. Parallelly to the acquisition of V_{back} + V_{sample}, V_R signal from LCR circuit (Figure 2.3a-red line) is also acquired as reference of the AMF (the validity of

V_R as reference signal of the AMF will be discussed in the following section). Finally, we proceed to plot the hysteresis loops tracing M versus H, as shown in Figure 2.4.

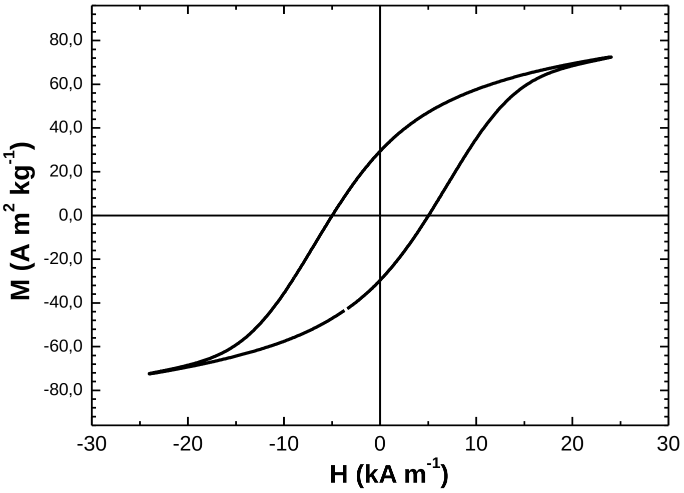

Figure 2.4. Example of AC Hysteresis loops of MNPs dispersed in water at 100 kHz and 24 kA m^{-1}.

2.3. AMF calibration

We used two distinct approaches to calibrate the maximum magnetic field intensity (H_{MAX}). In first approach, we employed a commercial Gauss/Teslameter (FH-55, Magnet-Physik, Figure 2.5) for the quantification of H_{MAX} inside the AC magnetometer measurement region, setting up a longitudinal Hall probe whose dimensions allows its placement inside the detection coil. Using this method, the H_{MAX} values along the sample placement area showed variations below 1%, ensuring the placement of the sample under almost homogeneous AMF conditions. However, it is important to note that the range of measurement of this Gauss/Teslameter is limited to a maximum frequency of 20 kHz. Thus, a complementary approach for calibrating H_{MAX} at larger frequencies was needed. To carry out a calibration of H_{MAX} in a wider frequency range, we employed a home-made AMF detector, consisting of a single pick-up coil of a given surface (S) and connected to an oscilloscope to read the voltage induced by the AMF. Considering that the expression Vind=nSHf, where V_{ind} is measured, and N,f,and S (surface of the coil) are known parameters, we can extract the peak value of H.

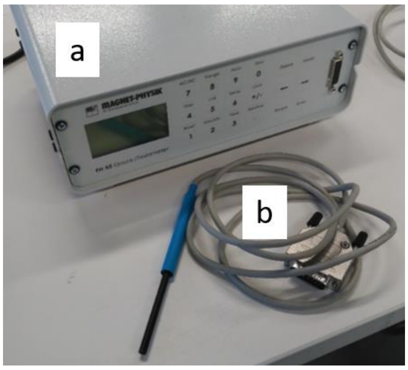

Figure 2.5. Commercial Gauss/Teslameter (FH-55, Magnet-Physik) employed for the calibration of H_{MAX} field at low frequencies ($f < 20$ kHz). **a)** acquisition and processing unit. **b)** longitudinal Hall probe.

Using both calibration methods, we could assess that i) both approaches (i.e. Gauss/Teslameter and pick-up coil based) reports similar H_{MAX} value in the AMF conditions where their working range overlap (f = 20kHz), ii) the existence of a well-defined linear behavior beyond 20 kHz, discarding undesirable effects, such as an unexpected fall of H_{MAX} values at larger frequencies (Figure 2.6a). Interestingly, we also assessed that V_R signal (See Figure 2.3) is linearly correlated with the H_{MAX} measured values, turning this LCR derived voltage signal into an appropriate parameter for monitoring AMF conditions during the AC hysteresis loops measurements (Figure 2.6b).

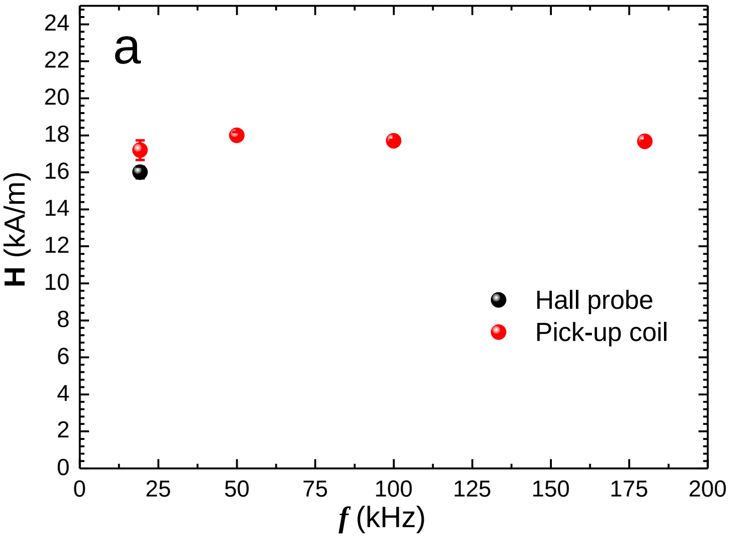

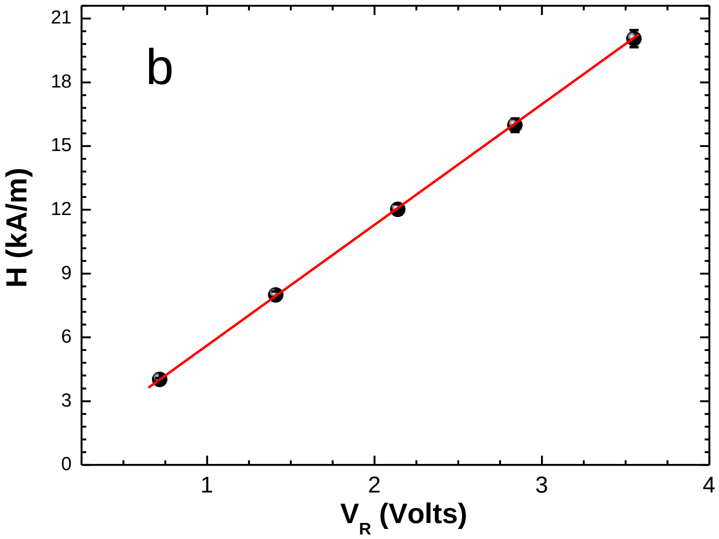

Figure 2.6. Calibration measurements of H field. a) H field measured with a Hall probe (black dot) and a pick up coil (red dot) at different frequencies. B) H fields measured with Hall probe at different V_R voltages. $f = 10$ Hz

2.3.1. Calibration of mass magnetisation (M)

Mass magnetization (*M*) magnitude can be directly calculated applying the equation 4. However, it is important to note that this equation limits to describe ideal pick-up coils. Hence, diverse events which could influence the EMF induction phenomena, such as tiny deformations of the detection coils due to heat-related dilatation phenomena or the degradation of the detection pick-up coils in time, are not accounted in this equation at all. We employed therefore a *M* calibration process supported by the measurement of pattern samples. This kind of approaches, which are also commonly used in commercial magnetometry equipment, provides an empirical input for calibrating the magnetization units, correcting possible deviations on the *M* values related to abovementioned causes (pick-up coil degradation/deformation).

For implementing this M calibration methodology in our instrument, we measured two different IONPs water dispersed samples (G31 and R26) in the AC magnetometer and VSM (i.e. DC conditions) at room temperature, using the same sample and holder for measuring the DC and AC magnetization. The choice of the pattern samples was based on their different dynamical magnetic response (i.e. opening of the AC hysteresis loop under similar AMF conditions), as we can appreciate in Figure 2.7 (red lines). G31 sample showed an almost superparamagnetic-like magnetization loop at $H_{MAX} = 30$ kA/m and $f = 25$ kHz. R26 presented a noticeably hysteretic behavior under similar AMF conditions instead. In contrast, one can appreciate that both IONPs samples showed a non-hysteretic behavior under DC conditions at room temperature (Figure 2.7-black lines). After we measured each sample with the AC magnetometer and VSM, the largest magnetization values (M_{MAX}) of the AC and DC loops were matched. Finally, we calculated two conversion factors based on these M_{MAX} equalization operation which, ultimately, were used for calibrating the mass magnetization values of the AC magnetic measurements performed in this work.

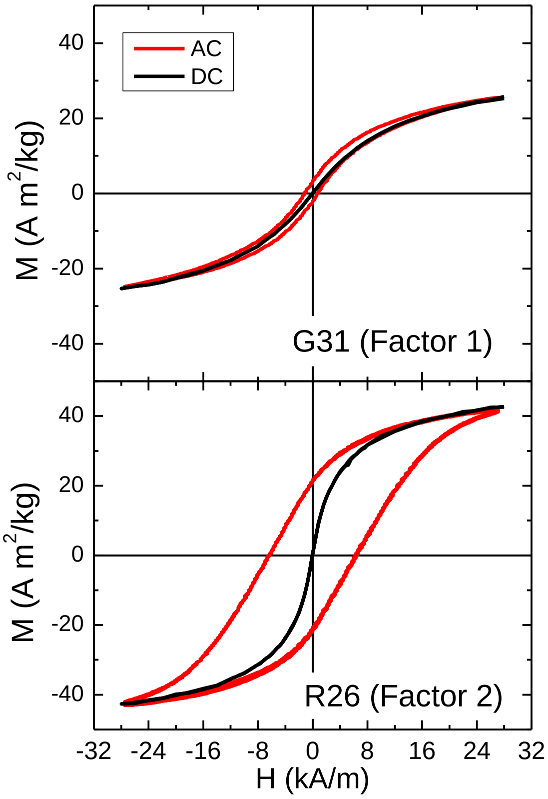

Figure 2.7. DC (black line) and AC (red line) magnetisation loops of G31 and R26 samples dispersed in water at [Fe] = 11 and 9 g_{Fe}/L, respectively. f_{AC} = 100 kHz.

In order to assess the congruency of the exposed *M* calibration method, we applied both calibrating factors (i.e. related to G31 and R26 samples) to the AC hysteresis loops of another sample (G54), which is totally independent from the calibration process. Figure 2.7 shows AC hysteresis loops of G54 sample dispersed in water at [Fe] = 10 g_{Fe}/L, measured at 100 kHz, and whose mass magnetization (M) have been calibrated accordingly G31-related calibration factor (black line) and R26-related calibration factor (red line). Noticeably, both calibrated loops are perfectly overlapped, showing a good agreement despite the different dynamical magnetic response of G31 and R26 sample under similar AMF conditions (Figure 2.8).

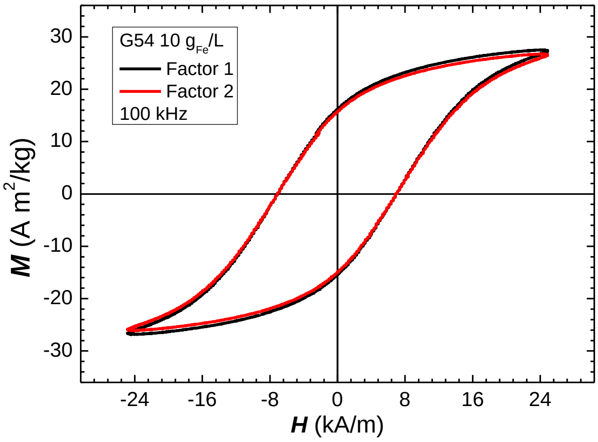

Figure 2.8. AC hysteresis loops measurements of G54 sample dispersed in water at [Fe] = $10 g_{Fe}$/L. Mass magnetisation (M) calibrated according to factor 1 (black line) and factor 2 (red line). f = 100 kHz.

In addition, we also compared both M-calibrated AC hysteresis loops of G54 water dispersed sample with its major DC hysteresis loop measured in VSM. As shown in Figure 2.9-inset, both dynamical M-calibrated hysteresis loops are consistent with their G54 quasi-static magnetization cycle counterpart.

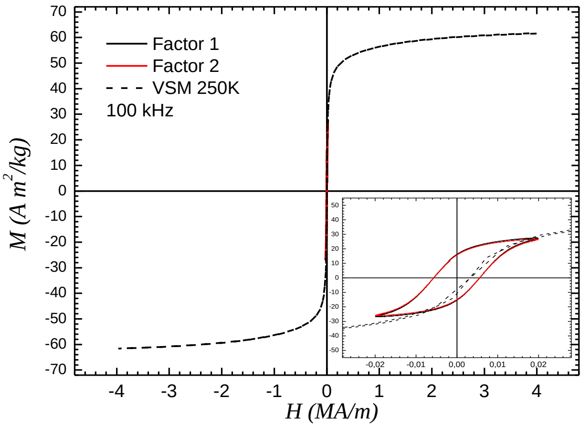

Figure 2.9. VSM measurement of G54 sample dispersed in water at 10 g_{Fe}/L, performed at 250 K. Inset: Fitting between DC (dashed lines) and AC (straight lines, f = 100 kHz) magnetisation loops of G54 samples dispersed in water at 10 g_{Fe}/L.

2.4. Reproducibility and error estimation

We assessed the quality of the AC hysteresis loops measurements for every studied MNPs sample in a systematical way, repeating the measurement process at least three times for each sample and AMF condition (Figure 2.10). This procedure allowed us the estimation of an error associated to the characteristic magnetic parameters of the magnetization loops (the hysteretic area (A), coercive field (H_C), maximum magnetization (M_{MAX}) and remanence (M_R)), calculating the standard deviation of their values.

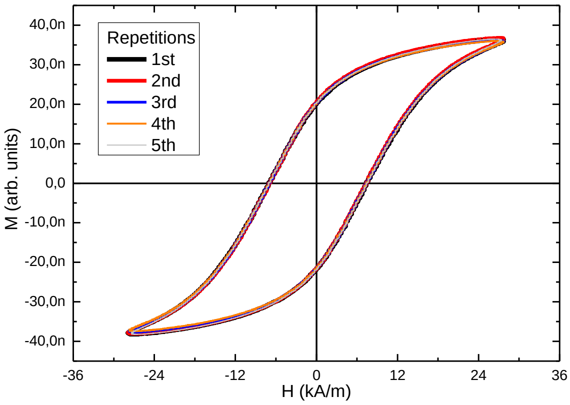

Figure 2.10. AC hysteresis loops of G54 sample dispersed in water at [Fe]=15 g_{Fe}/L. f = 100 kHz. The measurement was repeated five times in this case.

Generally, the magnetic samples studied in this PhD work found good reproducibility providing that [Fe] > 0.5 g_{Fe}/L.

2.5. Software development

2.5.1. Model of programming

For the control of the measurement and acquisition process, we programmed an special-purpose application on LabView software development environment. LabView provides a platform highly oriented to the control of measurement apparatus and its interface is quite optimized for engineering and scientific programming. In this regard, the use of a visual based development environment, almost similar to a flux diagram structure, simplifies the task of implementing a control software for our instrument. Certainly, the high level of this language generates difficulties on the depuration and optimization of the code, making it inappropriate for applications that need to be developed at lower computational levels. However, we considered LabView as a suitable tool due to the simple control and acquisition tasks that the software has to follow to perform the AC hysteresis loops measurements.

2.5.2. Software design

Regarding the basic operations that the software must accomplish, we designed the flux diagram presented in Figure 2.11. The developed application implemented diverse control and data acquisition steps, classified as acquisition, wave generator orders and internal software operations. Also, some stages of the measurement were based on the software/user interaction, as the operator addresses the task of introducing and extracting the sample into detection coil according to the measurement requirements. In Figure 2.12, the general aspect of the developed software is shown. The application allowed, on the one hand, the control of the wave generator and so, the activation/deactivation of the AC magnetic field. On the other hand, the program managed the acquisition of the targeted signals (i.e. V_R and pick-up coils'). Hence, for the sake of communicating with the laboratory equipment employed in the AC magnetometer fabrication (i.e. wave function generator and oscilloscope), we employed NI-VISA communication protocol libraries, incorporated in the LabView package and which allows a plug-and-play type USB connection. Finally, once the acquisition of the different signals was finished, the software saved the acquired data into a preselected *.dat file for its further data analysis.

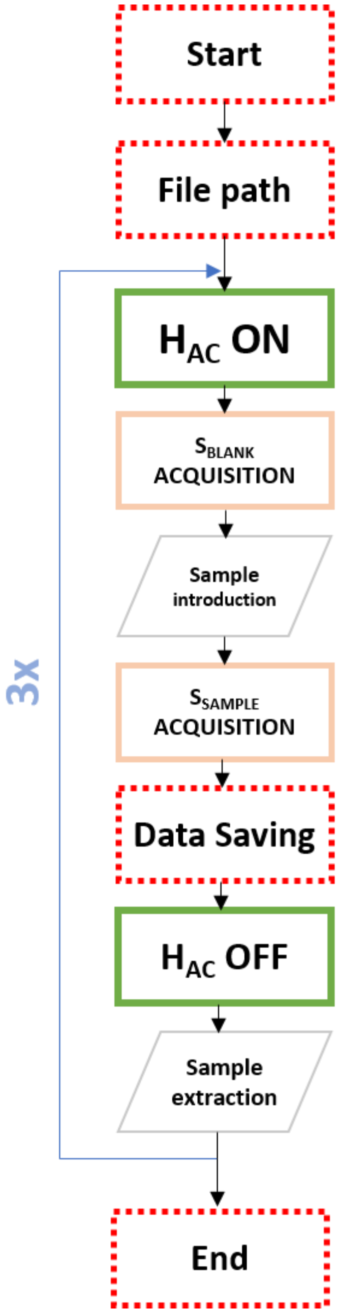

Figure 2.11. Flux diagram of the control and acquisition program. The blocks are classified accordingly their functionality: AMF activation/deactivation (green straight line), acquisition orders (salmon line), actions of software (red dashed line) and human actuations (rhomboidal blocks).

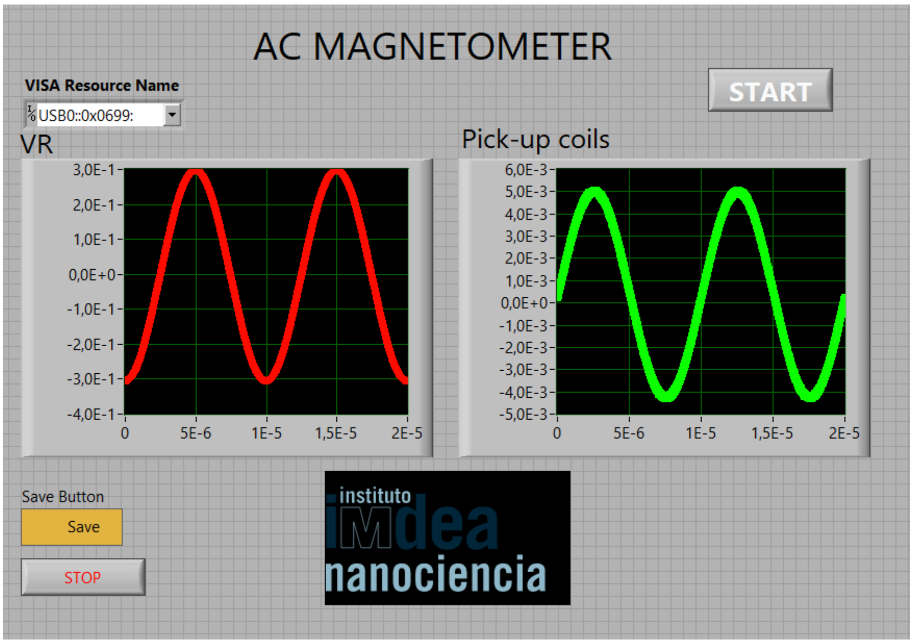

VISA Resource Name
USB0::0x0699:

Figure 2.12. General view of the programmed software for the control and acquisition of the measurement.

It is important to note that this first version of the software offered a low automatization rate. Among others, frequency tuning needed to be manually set up in the wave function generator. Also, all the data treatment (e.g. signals averaging, integration and plotting AC hysteresis loop) was mandatorily carried out by the user with data analysis software. These drawbacks were overcome in next prototypes versions although.

2.6. AC hysteresis measurements

AC magnetometer entails a versatile MNP characterisation equipment, which allows to measure the magnetic response of MNPs under near hyperthermia AMF conditions, providing quite useful information inside this field. Among its advantages, we can remark the low acquisition times needed for the measurement of a hysteresis loop (less than 5 s), low-cost requirements for its manufacturing and a remarkable range of work (20–180 kHz, 5–30 kA m^{-1}). However, its main advantage in comparison with calorimetric methods probably relies on the low signal that MNPs dispersion media induce into the AC magnetometer detection system. Such characteristic allows the direct measurement of the MNPs magnetic response regardless of the environment where they are dispersed, as long as this environment does not provide a strong ferro-ferrimagnetic contribution.

As we will show in the experimental chapters, the AC magnetometer acquire a central role in this dissertation, as for the achievement of our aims, we systematically measured the MNPs magnetic response in a wide variety of biological and non-biological dispersion media, and directly in live cells. However, it is important to note that the utility of this technique goes further to the results presented in this work. It can comprise other tasks, such as providing information about the colloidal state of the MNPs[65] or acting as a biosensor display platform, as we will explore in Chapter 6. Finally, due also to the important amount of information that AC hysteresis loops provides on the magnetism of MNPs, other authors have also suggested other functionalities to this technique, highlighting its use for MPI related applications or as an intrinsic MNPs temperature control[66].

2.6.1. Advance Instrumentation Unit

All the knowledge collected during the design of the AC magnetometer presented in this work have contributed to the creation of more advances prototypes (AC Hyster series, IMDEA Nanociencia). These new AC magnetometers are more compacted, highly automatized and count with a friendly-use software platform. The measurement software includes functionalities related to data analysis, strongly facilitating the measurement procedure to non-experienced operators. AMF conditions were also extended to a range from 4 to 40 kA m^{-1} in H_{MAX} and frequencies from 10 kHz up to 300 kHz (Figure 2.13) thanks to important improvements of the cooling system.

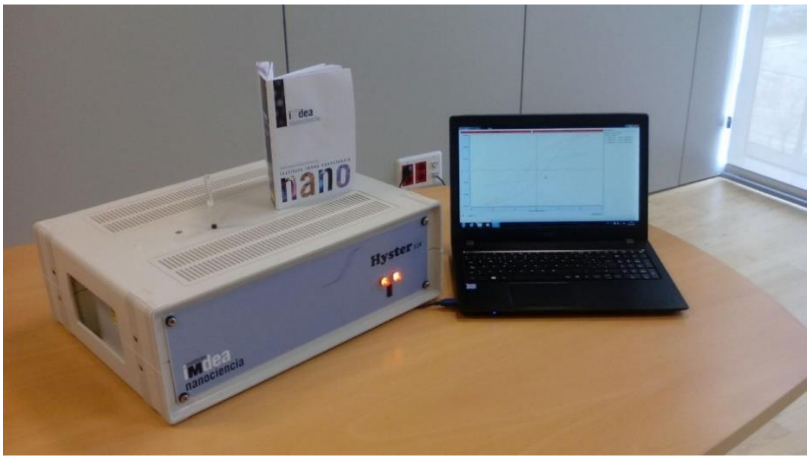

Figure 2.13. Current versions of the AC magnetometer (AC Hyster 1.3).

Finally, the last models opened also the possibility of using AC magnetometers not only as a AC magnetic characterisation equipment but also in other interesting applications, such as biomarkers detection. In this regard, the last prototypes take part in a new fast and portable biomarkers detection method, which is currently under patenting procedures (**patente Europea nº EP17382758.5**).

2.7. Conclusions

We have developed a home-made AC magnetometer capable of measuring magnetization loops under AMF from MNPs dispersed in aqueous solution and/or placed in biological fluids and entities. For the main coil we employed Litz wire, enabling to generate AMF conditions in a range from f = 25 – 150 kHz and H_{MAX} = 4 – 30 kA m^{-1}, requiring electric power due to its reduced skin effect and Joule effect-related heat losses. Two contrary-wise pick-up coils connected to a commercial oscilloscope controlled by a PC with a special-purpose software make up the detection system. Details about the calibration protocols of the H-magnetic field, mass magnetisation (M), measurement quality and reproducibility are also provided. This set-up postulates as a powerful tool for the characterisation of the AC magnetic response of MNPs, strongly complementing the traditional calorimetric methods thanks its versatility, low-cost, wide range of work, compatibility with biological fluids and entities and fast measurement times.

Influence of magnetic dipolar interactions on the dynamical magnetic response of IONPs

3

Chapter

3. Influence of magnetic dipolar interactions on the dynamical magnetic response of IONPs

3.1. Introduction

In this chapter, we will address the study of the influence of the magnetic dipolar interaction in the dynamical magnetic response of IONPs. Experimental evidences call into question the reliability of IONPs for giving a controlled heat exposure or contrast signal in any biological environment, a concern that affects at the root of their biomedical applications. Therefore, it is crucial to deepen in understanding how the biological processing of IONPs influences the response of IONPs under H_{AC} conditions. Accordingly previous works,[9] agglomeration of nanoparticles is favored when are cell internalized or dispersed in biological media. In consequence, the magnetic response of MNPs can be highly modified[3,24]. This clustering, which can be seen either as an increase of MNPs aggregation or local concentration, favors magnetic dipolar interactions that remarkably alters their magnetic response under external magnetic field[6,7]. In order to influence of interacting phenomena on the magnetism of MNPs, the role of different parameters such as particle size,[15,16] aggregation[9], concentration[20,67,68] and size polydispersity[46] have been studied under different experimental conditions. However, and this is perhaps the main concern, data reported so far do not show an overall picture in relation to the effects of some parameters on the heating performance. It is not clear how **AC hysteresis loops** evolve when interacting phenomena dominate, and how such evolution determines the magnetic heat dissipation. Understanding the role of magnetic interaction phenomena on the MNPs heat dissipation is mandatory for controlling their heat release.

In the current chapter, we report on an experimental study of the influence of magnetic dipolar interactions on the dynamic magnetic response of IONPs. First, we assessed the role of inter- and intra-aggregates i) by increasing the IONPs concentration of the colloidal dispersion, and ii) by increasing the size of IONPs aggregates at constant IONP concentration respectively. Secondly, we presented and discussed about other external and internal parameters, such as external magnetic field intensity (H_{MAX}) and particle size. These experimental evidences were compare with current models on magnetic dipolar interactions.

For the abovementioned studies, we employ three IONPs with different sizes and polydispersity: G54, R26 and G31. First, this chapter presents the intra- and inter-aggregates interactive phenomena experiments. Secondly, we study the influence of H_{MAX} and particle size on magnetic dipolar interactions by selecting two different core size samples: R26 and G31. (See Annex I for sample details).

3.2. Inter- and Intra-aggregates dipolar interactions

The influence of magnetic interacting phenomena on the magnetic response of IONPs has been explored by means of two distinct approaches on G54 sample. On one hand, inter-aggregates interactions (i.e. long-range interactions) have been explored by varying nanoparticle concentration without intentionally altering the primary aggregation state (i.e. assuming D_H does not vary) (Figure 3.1a). On the other hand, intra-aggregate interactions (i.e. short-range interactions) have been probed increasing the hydrodynamic size at a given IONPs concentration (2 g_{Fe} L^{-1}), augmenting the number of interacting nanoparticles in the aggregate (Figure 3.1b) (See methods section).

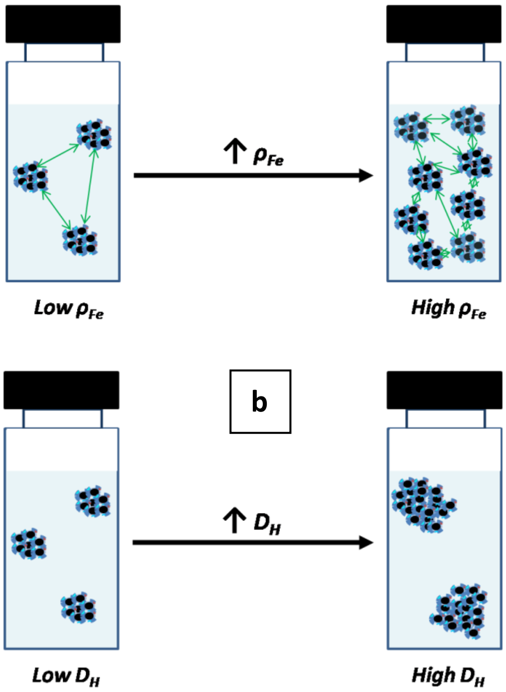

Figure 3.1. Schematic representation of IONPs dispersion at increasing a) Iron concentration and b) hydrodynamic size. Green arrows represent magnetic dipolar interactions.

3.2.1. Inter-aggregate interactions

The influence of magnetic dipolar inter-aggregate interactions on the dynamical magnetic response of IONPs was firstly studied by assessing the evolution of *SAR* with the IONPs concentration. A first consequence of increasing the IONPs concentration is the reduction of the proximity between IONPs aggregates (d). Since the magnetic dipolar interactions (H_{dip}) are proportional to the magnetic moment of the particles (m) and inversely proportional to d, d increase leads to strength the IONPs dipole-dipole interaction. To scale the proximity between nanoparticles, the dispersion volume fraction (ϕ_d) is extensively used[20,69]. It is defined as the proportion between the volume occupied by the IONPs in the dispersion ($V_{IONP,d}$) and the total dispersion volume (V_d). In addition, ϕ_d is a parameter widely employed to link the experimental results obtained from concentration dependence studies with theoretical models.[68] Considering the mixed chemical composition between maghemite and magnetite of our IONPs, we calculate the largest ϕ_d assuming γ-Fe_2O_3 as the main chemical composition of the studied IONPs as follows:

$$\phi_d(\%) = \frac{V_{IONP,d}}{V_d} \approx \frac{[Fe]\cdot 1.4\cdot 100}{\rho_{\gamma-Fe_2O_3}} \qquad \text{(eq. 3. 1)}$$

where *[Fe]* is the Fe concentration in the dispersion, and $\rho_{\gamma-Fe2O3}$ is the bulk density of maghemite (4.9 g cm^{-3}). Higher values for ϕ_d implies closer inter-aggregates separation distance and so, stronger magnetic dipolar interactions are expected. In Figure 3.2, one can appreciate the Fe concentration dependence of *SAR* at given H_{AC} conditions (100 kHz and 40 kAm^{-1}). At a first glance, the *SAR* dependence shows a non-monotonic behaviour: an initial decay occurs at very low concentrations ([Fe] ≤ 1 g_{Fe} L^{-1}) where SAR decreases to values 50% smaller than the one at the lowest [Fe]. Then, SAR value is maintained constant along an intermediate concentration range (1 $g_{Fe}L^{-1}$≤ [Fe] ≤ 5 $g_{Fe}L^{-1}$) before SAR values begin to progressively increase around 50 % when reaching a local maximum around [Fe]=10 g_{Fe} L^{-1}. Further increase of Fe concentration leads to a slight decrease of heating efficiency till the highest concentration value studied ([Fe]=15 g_{Fe} L^{-1}).

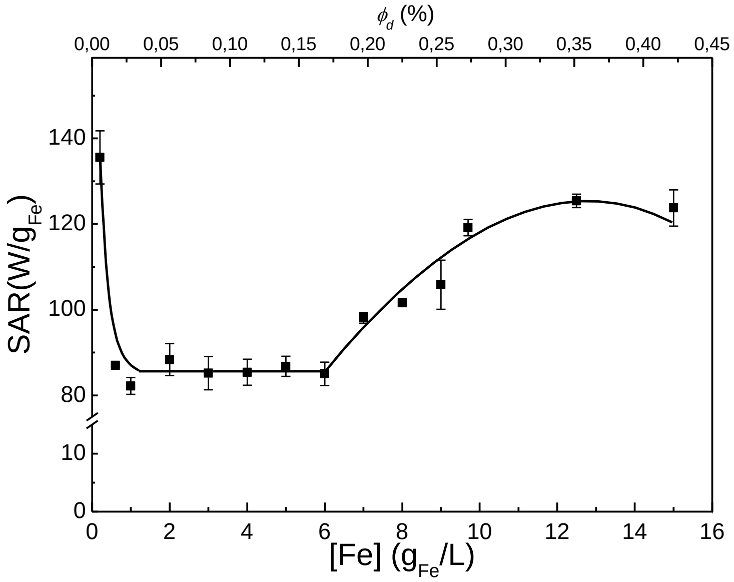

Figure 3.2. [Fe] dependence of SAR values from IONP dispersed in water under given HAC conditions (105 kHz and 40kAm-1). The upper x-axis presents □d calculated by Equation 2. Solid line is a guide to the eye.

The non-monotonic behaviour shown in Figure 3.2 is associated to the increase of ϕ_d as previously reported experimentally[68,70,71] and theoretically[20,68,69,72,73]. This can be understood in terms of magnetic dipolar interactions accounting for both the intrinsic magnetic features of the particles (anisotropy, magnetisation)[20] and experimental conditions (concentration, magnetic field intensity).[68,69,73] The initial drop of SAR values is related to the reduction of the energy barrier by magnetic interactions at low IONPs concentration.[68,72] The observation of the subsequent increase and decrease of the SAR values with [Fe] has been assigned to the opening of hysteresis losses, which is tightly related to magnetic dipolar energy and field conditions. As shown in Fig. 3.2, the experimental value ϕ_d for which SAR is maximum corresponds to $\phi_d \sim 0.32\%$, similar to previous predictions[73]. Considering that $SAR = A \cdot f$, where A is the area of the hysteresis loop, and f is the magnetic field frequency, one can expect that magnetization cycles would vary with IONPs concentration. To assess this point, we have measured hysteresis loops under AC magnetic field conditions (100 kHz and 26 kA m^{-1}). It is important to note that two different magnetic field conditions in calorimetric (100 kHz and 40 kA m^{-1}) and magnetic measurements (100 kHz and 26 kA m^{-1}) were used, due to technical limitations of the AC magnetometer to reach larger magnetic field intensities. Hence, we measured SAR of G54 sample at three different iron concentrations ([Fe]= 2, 10 and 15 g_{Fe} L^{-1}) and nine magnetic field intensities were to evaluate the comparability of both magnetic field conditions. In Figure 3.3, calorimetric measurements under the abovementioned conditions are presented. For the studied Fe concentrations, SAR displays similar values beyond H~28 kA m^{-1}.

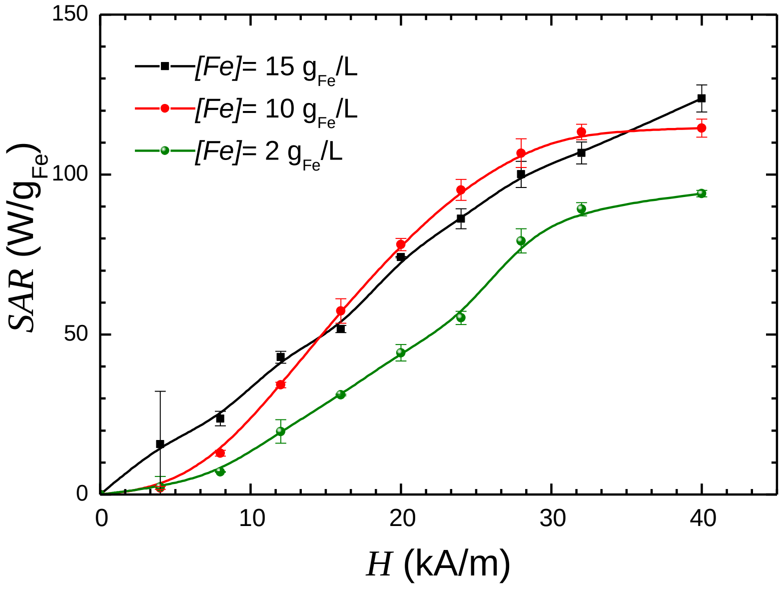

Figure 3.3.(a) AC magnetisation loops dispersed at different iron concentration. On the left, loops normalised to magnetic mass. On the right, loops normalised to maximum magnetisation value (M_{Max}). (b)(c) Loops at different [Fe] (3, 10 and 15 g L^{-1}) normalised to magnetic mass and M_{Max} resepectively. f = 100 kHz.

Thus, we can asseverate that H_{ac} conditions used in AC magnetometry measurements allows to probe comparable data with the ones the ones assessed in the calorimetric - measurements.

Figure 3.4 shows hysteresis loops of IONPs at different concentrations under H_{AC} conditions (100 kHz and 26 kA m^{-1}). As different loops strongly overlap on each other, we highlighted the most representative ones in Figure 3.4bc. At a first glance, the increase of *[Fe]* enhances the opening of the hysteresis loops via the raise of magnetization values

(*M_R* and *M_{MAX}*) but not due to variations of *H_C*. Indeed, *H_C* keeps constants when *[Fe]* increases, as clearly seen when AC hysteresis loops are *M_{MAX}* normalized (see Figure 3.4c).

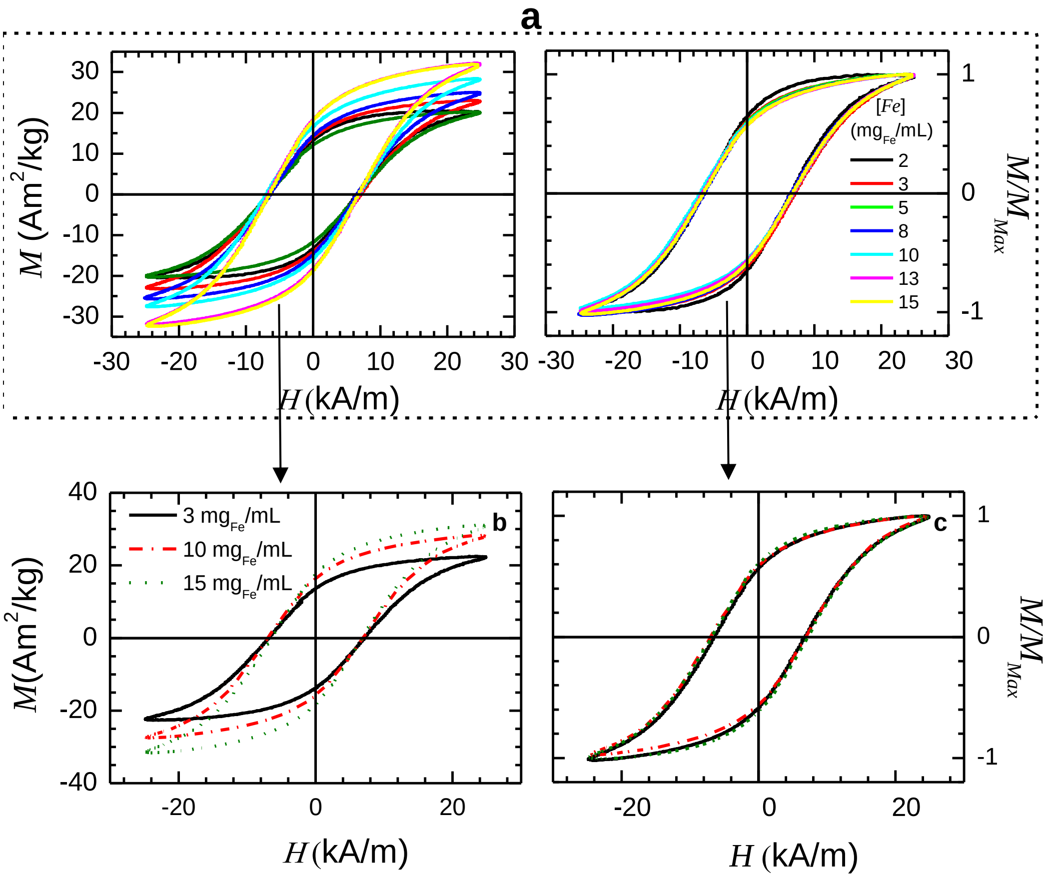

Figure 3.4.(a) AC magnetisation loops dispersed at different iron concentration. On the left, loops normalised to magnetic mass. On the right, loops normalised to maximum magnetisation value (M_{Max}). (b)(c) Loops at different [Fe] (3, 10 and 15 g L^{-1}) normalised to magnetic mass and M_{Max}, resepectively. Magnetic field frequency: 100 kHz.

To appreciate the effects of long distance magnetic dipolar interactions on the hysteresis loops, the main magnetic parameters (*A*, *M_R*, *M_{MAX}* and *H_C*) of the measured AC magnetization loops were quantified and plotted in Figure 3.5. One may notice that the area enclosed the hysteresis loop (*A*), the remanence (*M_R*) and the magnetization values at maximal applied field intensity (*M_{MAX}*) behave in a similar way than the *[Fe]* dependence of *SAR*, although the field intensities are slightly different. As mentioned before, *H_C* keeps constant along the studied *[Fe]* range.

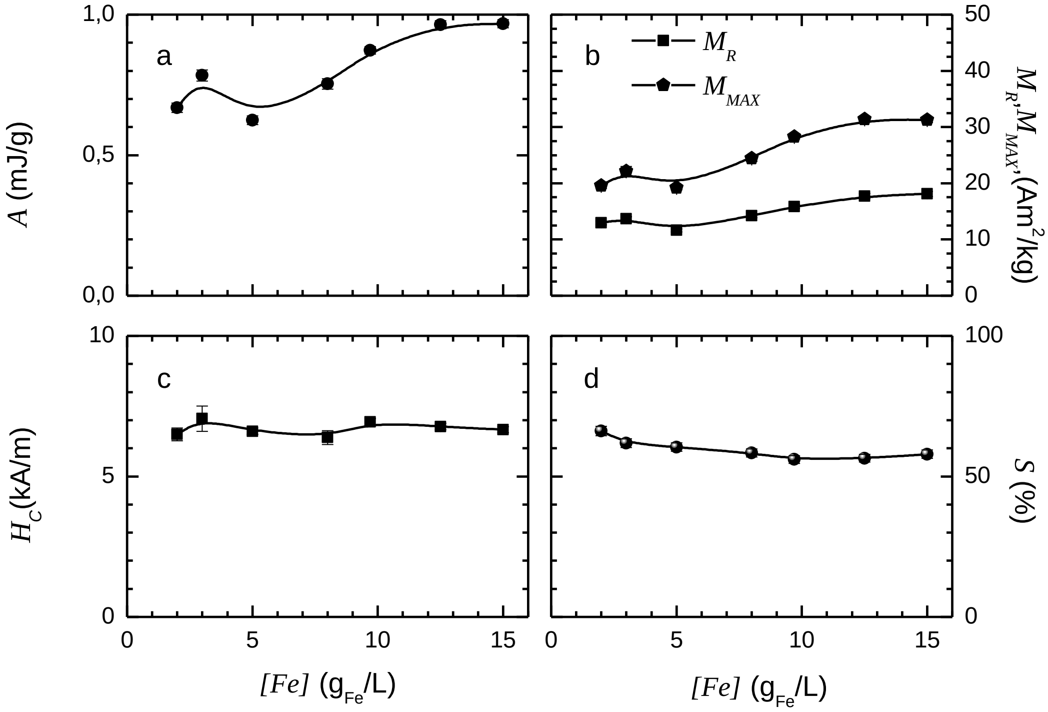

Figure 3.5. [Fe] dependences of IONP hysteresis loops parameters (A, MR, MMAX, and HC) obtained from Fig. 8a. Solid lines are a guide to the eye. Magnetic field frequency: 100 kHz.

Besides, the squareness of the AC hysteresis loops (*S*), understood as $S = M_R/M_{MAX}$, shows a progressive reduction from 70% to 60% in the studied *[Fe]* range. Hence, the trend of the different magnetic parameters extracted from the hysteresis loops shows that the *[Fe]* dependence of magnetic heat losses is mainly due to the rising of the magnetization values (i.e., M_R and M_{MAX}) and not to variations of H_C.

3.2.2. Intra-aggregate interactions

The other possibility to go further in the study of magnetic dipolar interactions is by increasing the aggregation degree, i.e. D_H (See methods section). For this purpose, our approach is to intentionally vary D_H at low IONPs concentration, since interacting inter-aggregate phenomena are less significant. As SAR value keeps constant in the concentration range between 1 and 6 g L^{-1} (See Figure 3.2), a concentration of 2 g_{Fe} L^{-1} was established for these experiments. Before varying D_H, we have checked the magnetic response from individual IONPs dispersed in organic media where D_H = 20 nm, like the average IONPs core size presented in the sample annex (Annex I). Second, we have compared the magnetic measurements from individual IONPs with the one obtained from primary aggregates (D_H~50nm) formed after ligand exchange process and suspension in water (Fig. 3.6a).

Finally, aggregate size was further increased by varying pH or by dispersing IONPs in saline buffer solution and the AC magnetic measurements were performed (See methods section). These two different methodologies provide different hydrodynamic size ranges and polydispersity, whose influence on the magnetic heating losses is probed. Table 3.1 collects the colloidal parameters in organic and aqueous media after inducing the different aggregation states of IONPs under pH variation and saline buffer solution. Whereas the variation of dispersion pH leads to D_H with low PDI (< 0.2), the IONPs dispersion in saline buffers leads to higher PDI values (> 0.2).

Dispersant	*pH*	*Time(h)*	ζ V(mV)	D_H (nm)	PDI
Toluene	-		-	20	0.20
Water	7	24	-37.7	56	0.13
	4.1	24	-17.6	92	0.15
	4.0	24	-16.2	138	0.2
	3.9	24	-14.7	220	0.24
Buffer Saline	7	0.5	-	91	0,22
	7	1	-	119	0,25
	7	2	-	155	0,29
	7	3	-	198	0,40
	7	4	-	255	0,47
	7	5.5	-	356	0,52

Table 3.1. Summary of IONP colloidal parameters at different pH and buffer saline conditions.

In this manner, we can check the influence of the PDI on the magnetic response of IONPs aggregates. Figure 3.6 shows the dependence of SAR with IONPs aggregation (i.e. SAR vs D_H). At first glance, SAR values drop with aggregation but in a different manner depending on the PDI. On one hand, SAR values between aggregates of low PDI slightly increases at small values of D_H (< 100 nm), before to significantly fall (~ 25%) for D_H=139 nm. On the other hand, larger PDI lead to progressive but smooth (~10%) reduction of SAR values when D_H varies from 56 to 356 nm.

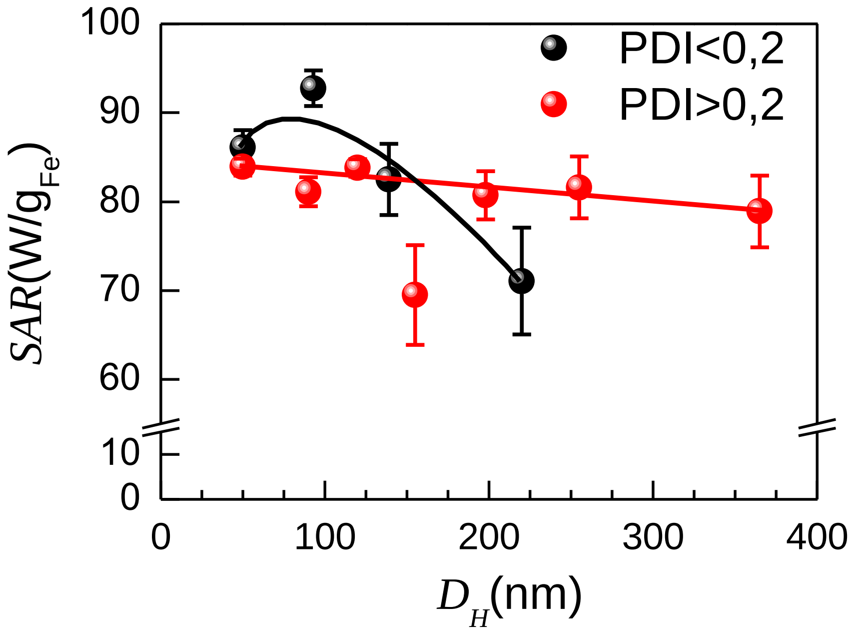

Figure 3.6. Aggregation size dependence of *SAR* values from IONP dispersions with different PDI (< 0.2, black dots and > 0.2 red dots) obtained under given H_{AC} conditions (105 kHz and 40 kA/m) and [*Fe*] = 2 mg_{Fe}/mL.

For the sake of a better understanding on the different effects related to short-distance magnetic dipolar interactions, we measured dynamic hysteresis loops for different hydrodynamic size (Figure 3.7). First, one may notice a strong variation of the hysteresis opening and shape while increasing D_H: hysteresis loops become more leaned upon increasing D_H, independently of PDI value. Apparently, this is related to the increase of H_C and not due to any variations of S, as revealed.

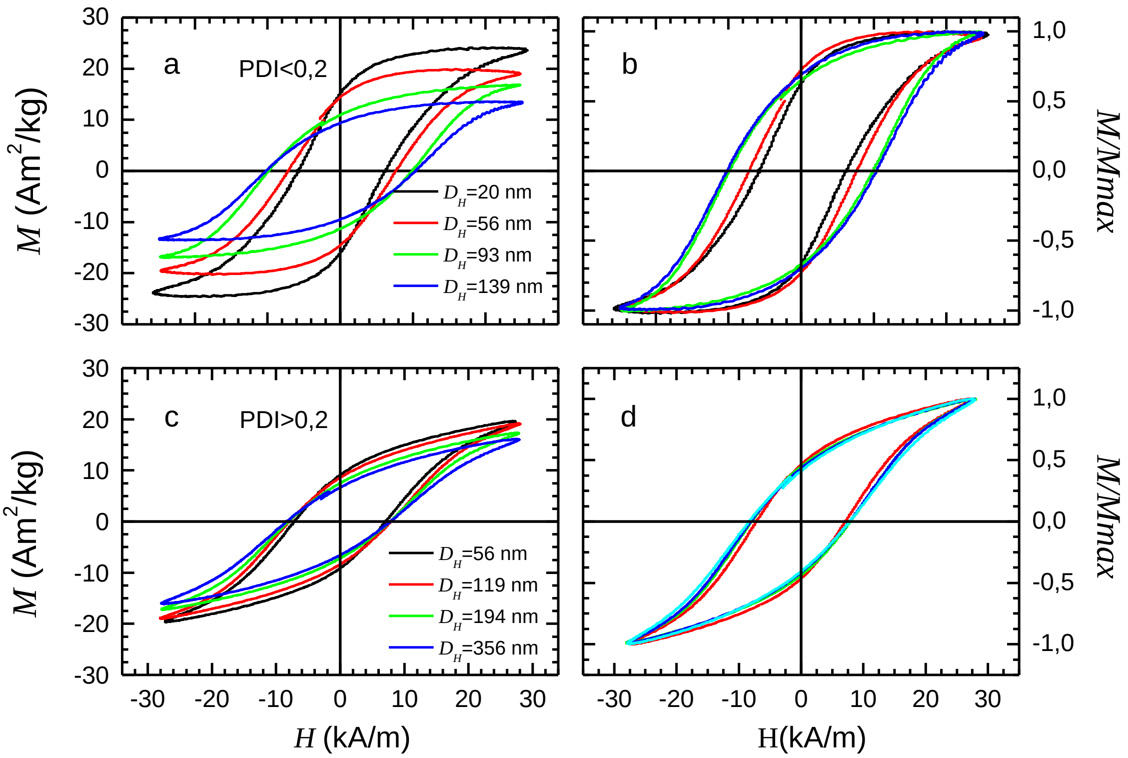

Figure 3.7. Dynamic hysteresis loops obtained at different D_H (a,c) at 100 KHz and [*Fe*]= 2 mg_{Fe}/mL and normalized to each respective maximum magnetization value (b,d) for distinct PDI values.

A careful analysis of the magnetization loops parameters, showed in Figure 3.8, reveals that the variation of A, H_c, M_{MAX}, M_R and S with D_H is tightly related to the PDI. The magnetization cycle variations are more pronounced for PDI <0 .2 than for PDI > 0.2 (see Fig. 3.7) in general. Particularly, A, M_{MAX} and M_R behave similarly with D_H variation showing a significant reduction, whose relative variations depend on the PDI. In contrast, H_C remarkably increases (up to 66%) with D_H raise, reaching a saturation value beyond 100 nm. Finally, S shows a progressive reduction from 50% to 40% in the studied D_H range. Interestingly, all these physical parameters behave in a different manner with D_H (i.e. short-distance dipolar interactions) than with respect to *[Fe]* (i.e. long-distance dipolar interactions):

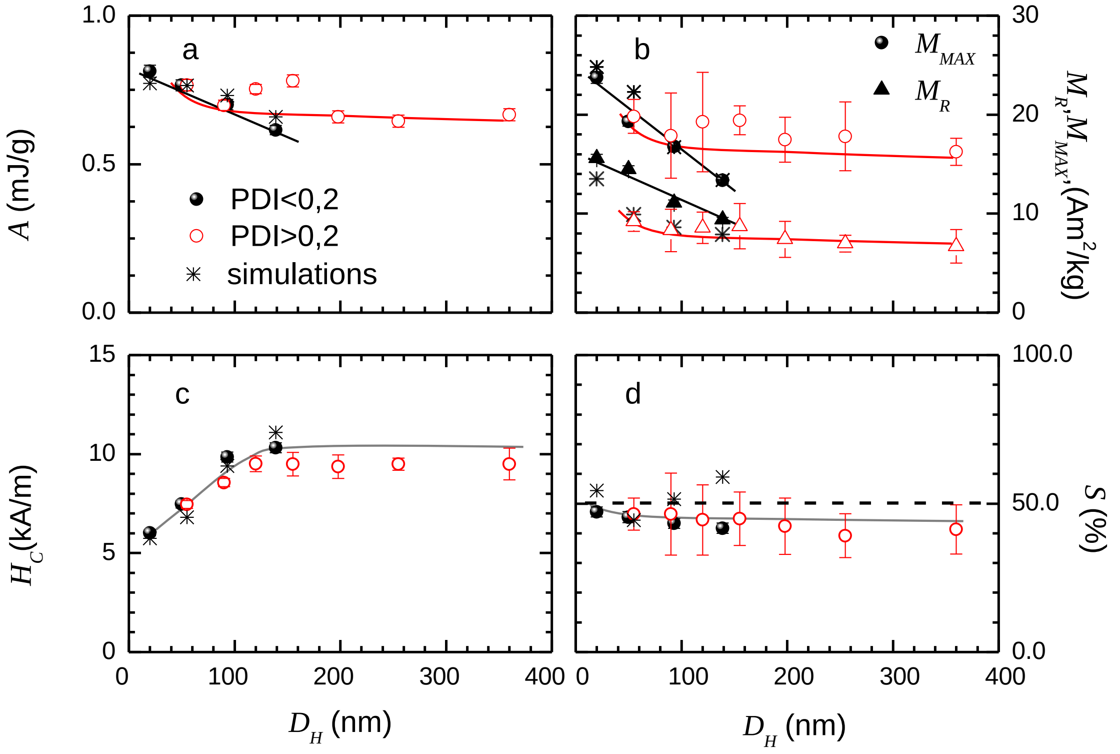

Figure 3.8. Aggregation size dependence of hysteresis loops magnetic parameters (A,M_R,M_{MAX}, and H_C) obtained from Fig. 10. Solid and dash lines are guides to the eye.

i) H_C increases with D_H while it remains constant with [Fe], ii) A, M_{MAX}, M_R decrease with D_H, while behaves non-monotonically with [Fe], iii) S value keeps below (above) 50% when varying D_H ([Fe]). Contrary to the case of increasing [Fe], the variation with D_H of the magnetic parameters (M_{MAX}, M_R, S and H_C) shown in Figure 3.8 hampers its correlation SAR trends with D_H.

For a better understanding of the presented experimental phenomena, numerical simulations were performed by Dr. Julian Carrey at INSA in Toulouse, France. Numerical simulations of hysteresis loops when magnetic interactions were neglected were performed using an algorithm implemented under MATLAB®, as described in ref. [42]. Simulations of interacting nanoparticles were performed using the C language program, as described in ref.[73]. When IONP size distribution effects were included in the simulations, the IONP size distribution, provided in Annex I, was discretized by using a step of 1 nm. Then hysteresis loops were computed for these various diameters, and a weighted averaged hysteresis loop was calculated. Experimental results shown in Figure 3.7 are in qualitative good agreement with kinetic Monte-Carlo simulations where the influence of magnetic interactions in isotropic disordered aggregates was evaluated. The aggregate volume fraction was used to find the IONPs occupation degree within a spherical hydrodynamic volume of an aggregate (V_H) of diameter D_H:

$$\phi_a(\%) = \frac{N \cdot V_p \cdot 100}{V_H} \tag{eq. 3.2}$$

where N is the number of IONP into the aggregate, and V_p is the volume of an individual IONP. The magnetic field conditions (100 kHz and 24 kAm^{-1}), and the volume fraction ϕ_d=0.038% (corresponding to 2 $gFeL^{-1}$), are similar to those used in the experiments (See ref. [60] for ulterior modelling details). The magnetization loops were fitted for distinct D_H values, focusing on the set of data with PDI < 0.2. Figure 3.9 shows the best fit for each hysteresis loop and Table 3.2 summarizes N and ϕ_a value used in the simulations. The reduction of M_S and the increment of the ellipticity observed in the empirical data of the cycles are also corroborated by the simulations shown in Figure 3.9. The magnetic parameters (A, M_{MAX}, M_R, H_C) extracted from these simulations are in good agreement with the experimental data (included in Fig. 3.8).

Table 3.2. Summary of number of nanoparticles (N) and volume fraction (ϕd and ϕa) employed in the simulations for each $D_H$value.

D_H	*Number of nanoparticles, N*	*Volume fraction*
20 nm	2000	Φ_d =0.038%
50 nm	4	Φ_a =30.9%
90 nm	18	Φ_a =23.8%
139 nm	57	Φ_a =20.5%

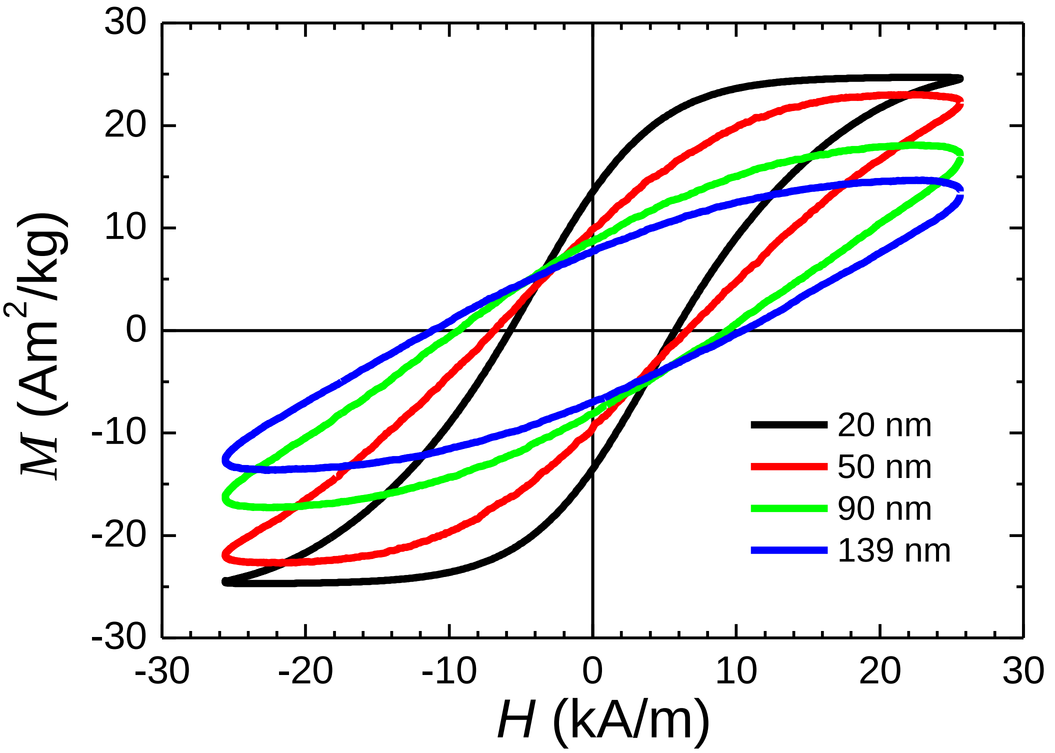

Figure 3.9. Numerical simulations of hysteresis loops of individual and aggregated IONP for different D_H in the range from 20 to 139 nm. Magnetic interactions are considered, with parameters given in Table 2.

It is worth to notice that ϕ_a value decreases when D_H increases, pointing that large aggregates are less compact than small ones (Fig. 3.10a). The number of interacting IONPs per aggregate is smaller than the number of particles which may fill the IONPs aggregate volume associated with D_H. This might be the sign of a fractal-like structure with several branches as reported in ref. [9] (Fig. 3.10b). In addition, all the main features of the experimental data on the intra-aggregate interactions can be fitted assuming these aggregates are composed of spatially disordered IONPs within a sphere, whose easy axis is oriented in the magnetic field direction and with a reduced value of ϕ_a.

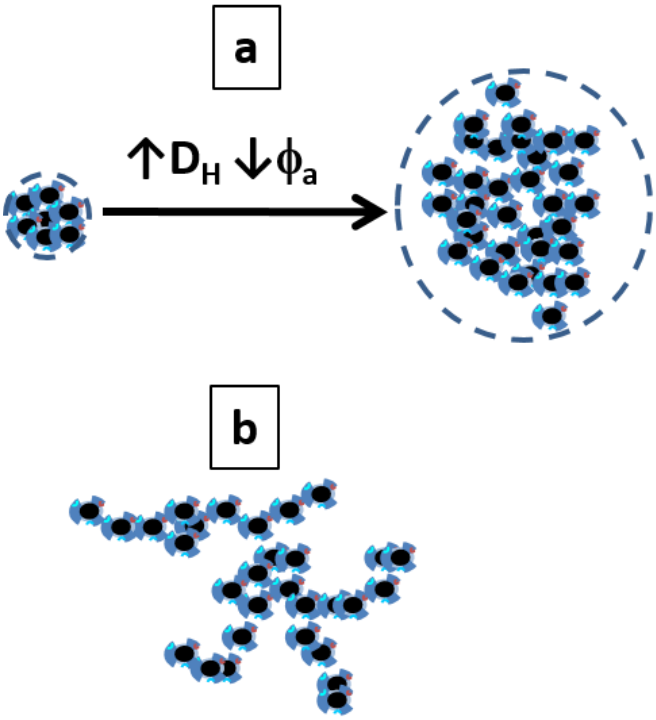

Figure 3.10. Schematic representation of a) Increase of hydrodynamic size (D_H) with decrease of aggregate compacity (ϕ_a) b) Fractal-like structure aggregate.

Figure 3.6 shows that the intentional increase of D_H results in a reduction of *SAR* values due to magnetic dipolar interactions. These interacting effects are significantly observed on the AC magnetization loops in the transition from individual IONPs (D_H=20 nm) to primary IONPs aggregates in water (D_H=56 nm) (Fig. 3.7). Indeed, the variations Hc (i.e. increase) and M_{MAX} (i.e. decrease) are highly appreciable (~25 and ~20%, respectively), despite the variation of A is smaller than 10%. Recent studies[7,9] have similarly probed that the dipolar interactions related to IONPs clustering negatively affects to their heat dissipation under H_{AC} with respect to individual IONPs. This is because intra-aggregate interactions efficiently alter the magnetic properties of IONPs colloids due to short-distances between IONPs in the aggregates. Considering that $SAR= A\cdot f$[42], *A* is defined by few magnetic parameters (M_r, M_{MAX},H_C and *S*), differently influenced by magnetic dipolar interactions as shown in Fig. 3.2 and 3.6. Therefore, the complex relationship between *SAR* and magnetic dipolar interactions can be simplified with the magnetic parameters extracted from AC magnetization loops, probing that hysteresis loops is more suitable for a better understanding of the nature and origin of the intra-aggregate interacting phenomena.

On one hand, magnetic nanoparticle aggregation result from the competition between attractive (dipolar and Van der Waals) and repulsive (electro-steric) interactions, leading to nanoparticle colloids with spatially disorder arrangement[9]. Considering the experimental results shown in Fig. 3.8, where M_{MAX}, M_{R}, and A decreases while D_H is intentionally increased, we stress the average demagnetizing effect associated to intra-aggregate dipolar interactions. Moreover, the spatial arrangement of IONP requires stronger external magnetic fields to reverse the magnetization while D_H increases, as shown in Fig. 3.7. Such demagnetizing effects related to intra-aggregate dipolar interactions are a consequence of the physic-chemical laws involved into the formation of IONP aggregates[74]. Short-range magnetic dipolar interactions could explain the acute reduction of *SAR* when IONPs are found inside cells, in addition to environmental viscosity could alter the contribution from magnetic relaxation processes (i.e. Brown or Néel) to heating mechanisms[28]. This aspect has relation with an issue that will be shown in Chapter 5. Indeed, clustering formation after cell uptake favors intra-aggregate dipolar interactions, resulting in the reduction of *SAR* values of the IONPs.

On the other hand, the data set related to long-distance dipolar interactions (i.e. inter-aggregate interactions) shows totally different behavior under similar H_{AC} conditions. First, no variation of coercivity (i.e. H_C) was shown although the concentration varied in a large range of *[Fe]* from 2 to 15 g_{Fe} L^{-1}. Previous theoretical[68,73] and experimental[75] works have vaguely shown the concentration dependencies of SAR and H_c, M_R and M_{MAX} for an individual IONP. However, we can find common features such as a progressive reduction on H_c, M_R and M_{MAX} values. Furthermore, the enhancement of *SAR* with *[Fe]* tightly relies on the 100% (40%) increase of M_{MAX} (M_R). Considering the anisotropic nature of magnetic dipolar interactions among IONP, changes in effective anisotropy mediated by dipolar interaction are highly determined by the spatial arrangement of magnetic dipoles.[76,77] Hence, we hypothesize that the remarkable increase of magnetization parameters (i.e. M_R and M_{MAX}) with *[Fe]* could be explained by considering magnetically-ordered spatial arrangements of magnetic dipoles (nanoparticles or aggregates). This leads to averaged magnetizing effects with no variation of coercivity, contrary to the case when D_H was intentional varied. Finally, it is worth nothing that SAR and AC hysteresis loops dependencies on [Fe] and D_H (Fig. 6, 8-

10, 12) associated with inter- and intra- aggregate dipolar interactions, are strongly related to structural and colloidal parameters (average size and shape of individual and aggregated IONPs). Therefore, different behaviors of SAR and hysteresis loops with [Fe] and D_H would be expected in case nanoparticle and/or aggregate size and/or their morphology would differ. In any case, further theoretical studies are needed to describe such conditions and their consequences. For this purpose, the dynamic hysteresis loops (see in Fig. 3.4 and 3.7) and their related magnetic parameter (see Fig. 3.5 and 3.8) stand for a solid set of data, which could be employed by numerical simulations to probe different hypothesis.

Another important point to remark is the effect of size distribution on the strength of the magnetic dipolar interactions. In the last 10 years, the influence of PDI related to IONPs size was widely studied on the magnetic properties of IONP. Recent works underline that IONPs synthesized by thermal decomposition with narrow size distributions leads to the observation of larger *SAR* values with respect to the case of larger PDI values of IONPs size.[10,46] The reason behind these findings can be related to the fact that thermal decomposition methods generally lead to IONPs with narrow size distribution, uniform morphology and improved surface (i.e. reduced defects). On one hand, low IONPs surface defects result in the increase of magnetic permeability and consequently, the increase of *SAR*[46,78]. On the other hand, uniform IONPs size and shape also contribute to larger *SAR*[10,46] in comparison to polydisperse IONPs. Indeed, different sizes and morphologies distinctly contribute to the overall magnetic heating of the IONPs ensemble. Thus, we can expect that larger PDI of D_H would result in IONP aggregates composed by different number of IONP and consequently, the interacting phenomena would result in nanoparticle aggregates exposed to different effective magnetic fields. According to our findings, the magnetic response of an ensemble of IONP colloids with large PDI for D_H results slightly different: while H_C behaves in a similar manner independently of PDI, M_R and M_{MAX} are more sensitive to PDI value, varying stronger (weaker) for low (high) PDI values (Fig. 3.8). In overall, narrow (wide) D_H distribution leads to a strong (weak) magnetic variation. However, we have no microscopic explanation to propose in order to totally describe such behavior so far.

Regarding the simulations, the values of M_S and K_{eff} employed in the calculations are much lower than the ones observed or expected. The fact that the M_S values measured in high-frequency hysteresis loops are much lower than expected has been previously reported[79,80] revealing a general feature of hyperthermia experiments. On one hand, this could be related to the fact that the effective temperature of IONP is larger than the one of the surrounding. This would give rise to lower values of M_S and K_{eff}. It would be also possible that the need of using low values of M_S in the numerical simulations could be since a two-level approximation is used. In that case, intra-well excitations are neglected, leading to a low effective magnetization at low magnetic fields. On the other hand, the need of low K_{eff} value agrees with the observation of a negligible influence of the dispersion viscosity on the *SAR* values (see Fig. 3.10).[28]

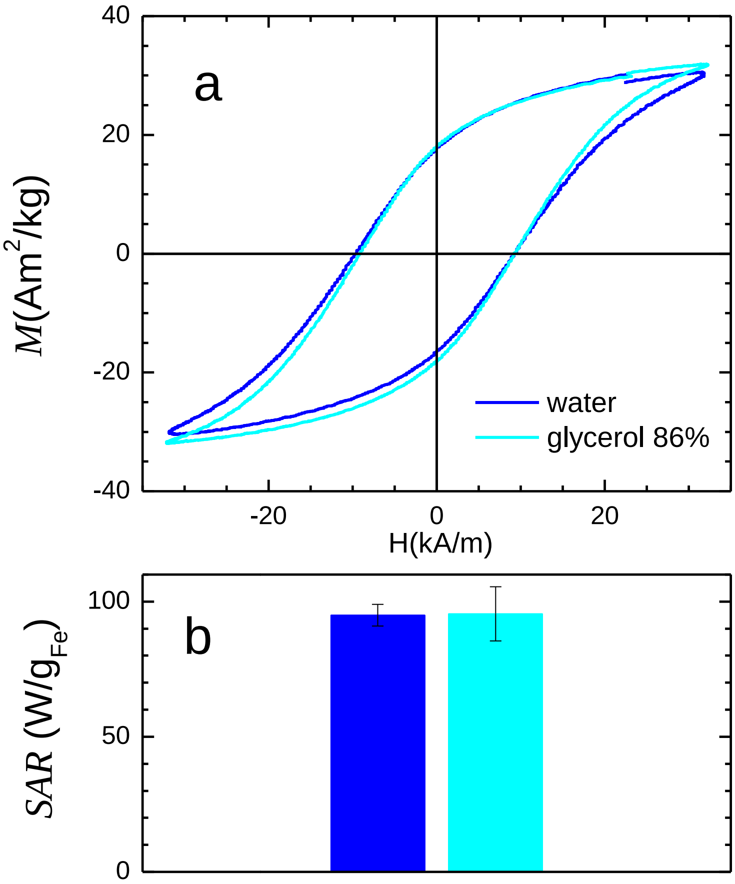

Figure 3.10. Numerical simulations of hysteresis loops of individual and aggregated IONPs for different D_H in the range from 20 to 139 nm. Magnetic interactions are taken into account, with parameters given in Table 2. Size distribution is included. Anisotropy axis are oriented in the direction of the applied magnetic field.

In addition, the dependences of *SAR* values with H_{AC} intensity at different *[Fe]* shown in Figure 3.6 reveal that *SAR* reaches a constant value beyond 32 kA/m.[81] This is an indication of the low values of the anisotropy fields (~45 kA/m) resulting in K_{eff} values around $1 \cdot 10^4$ Jm^{-3}.

3.3. Influence of extrinsic and intrinsic parameters on magnetic dipolar interactions

Although the results presented in the present chapter are related to the influence of the magnetic dipolar interactions on the magnetic behavior of IONPs mostly from an experimental perspective, we cannot obviate that magnetic dipole-dipole interactions field in IONPs is complex and extensive. Proof of this is the important number of parameters that can participate in these phenomena. In first approach, we could classify them as and IONPs extrinsic –external magnetic field, inter-IONP distances– and IONPs intrinsic –size, polydispersity, composition, anisotropy, shape–. Addressing all them certainly entails a titanic task that was not intended to be addressed in the present work. However, on a representative manner and for opening research topics, we studied the influence on the magnetic dipolar interaction of two additional parameters, representatives of IONPs extrinsic – Magnetic field intensity, $\boldsymbol{H_{MAX}}$ – and intrinsic – IONP particle volume, $\boldsymbol{V}$ –.

3.3.1. Magnetic field intensity (H_{MAX}) effects on IONP magnetic dipolar interactions

Accordingly to previous theoretical studies[39], H_{MAX} determines the apparition of different magnetic heating modes on MNPs liquid dispersions. Regarding the magnetic dipolar interactions, H_{MAX} would play a relevant role modulating the MNPs interacting effects. When MNPs are found under blocked regime (i.e. when $f >> 1/\tau_{\mathrm{eff}}$), the relation between maximum field intensity and magnetic anisotropy field (H_{MAX}/H_K) determines capacity of H_{ac} for reversing the magnetic moment of MNPs, and consequently the apparition of hysteresis and heating release. Moreover, when magnetic losses are computationally studied at different MNPs concentration, distinct H_{MAX}/H_K ratios results in a variation of the peak described in Figure 3.2, both on the concentration in where it arises and the sharpness

To assess these predictions as well as limitations of these Stoner-Wohlfarth based models in MH conditions, where the magnetic blockade of the MNPs are assumed, we performed calorimetric measurements on R26 sample dispersed in water at different iron concentration ([Fe]) under AC magnetic field (100 kHz) at three different H_{MAX} values (4, 8 and 40 kA m^{-1}). In Figure 3.11, the iron concentration dependence of SAR is shown. Similarly to the case of Figure 3.2, the non-monotonic behavior of the magnetic heating rate is observed when [Fe] is varied. This reveals the presence of magnetic dipole-dipole interactions mediated by the inter-aggregates distances under all H_{ac} used conditions. However, the H_{MAX} value changes the overall trend. At a first glance, the results obtained at 40 and 8 kA m^{-1} show a decreasing trend of SAR from 0.5 to 2 g_{Fe} L^{-1}. Moreover, all curves present a peak on intermediate iron concentration values (i.e. between 3 and 10 g_{Fe} L^{-1}), after which they show a decreasing tendency toward the highest studied iron concentration.

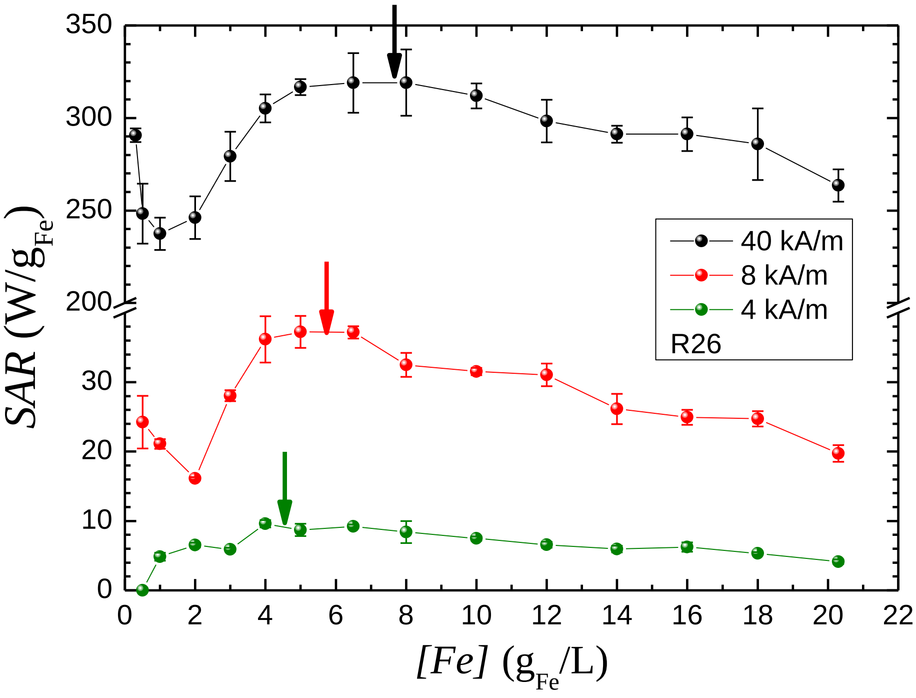

Figure 3.11. SAR measurements of R26 IONPs at different [Fe] and H_{MAX} (H_{MAX}= 4, 8, 40 kA m^{-1}). f = 100 kHz.

However, the SAR maximum peak clearly shifts to lower concentrations when reducing the external field intensity, from ~6 g_{Fe} L^{-1} at H_{MAX} = 8 kA m^{-1} to ~4 g_{Fe} L^{-1} at H_{MAX} = 4 kA m^{-1}. Moreover, the peak becomes less pronounced when H_{MAX} decreases. Recent theoretical models[10] explain these evidences as a consequence of the ratio H_{MAX} /H_K (Figure 3.12). One can identify our experimental evidences when the theoretical ratio H_{MAX}/H_K vary from 10 to 6 or smaller values.

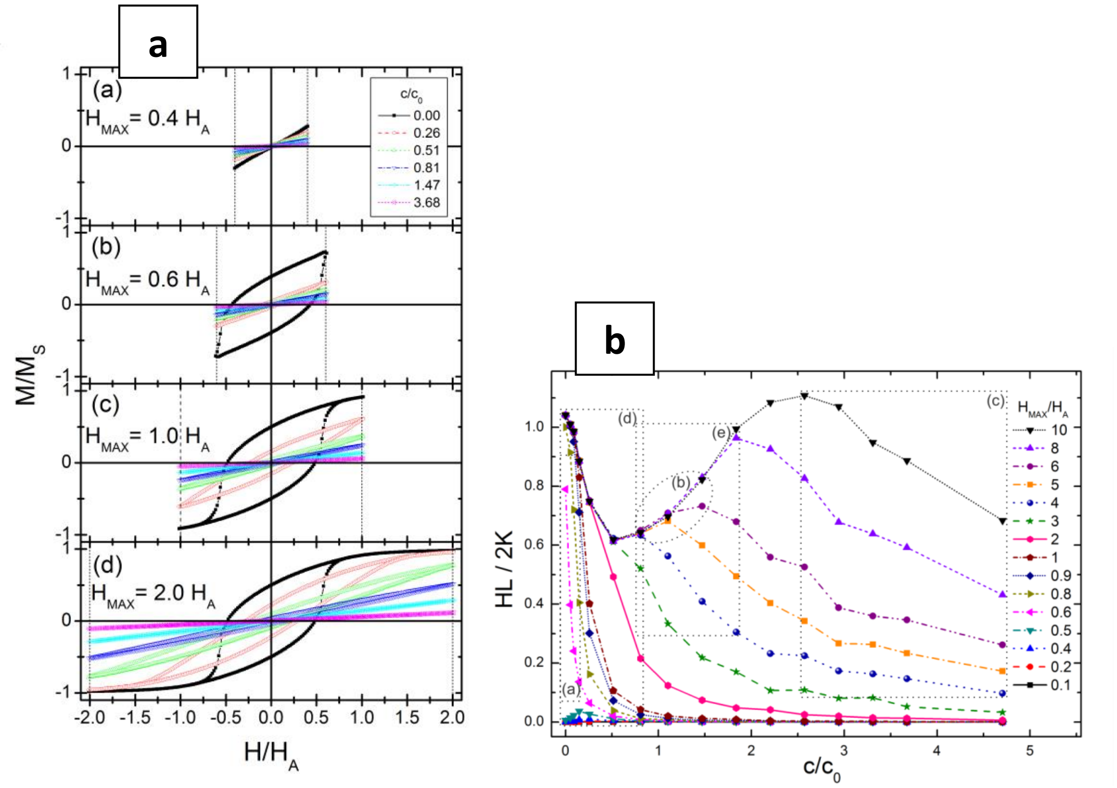

Figure 3.12. a) Influence of interaction conditions (depicted as increasing c/ c0 values) on hysteresis losses for different field amplitudes HMAX (see text for details). Stoner−Wohlfarth noninteracting particles are represented by the case c/c0 = 0. b) Dimensionless magnetic−hyperthermia scenario. Computation results of heating efficiency (HL/2K) vs sample concentration (c/c0) for different field amplitudes (H_{MAX}/H_A). Extracted from ref. [68]

However, it is important to remember that these predictions are strictly valid if MNPs are magnetically blocked. To asses this point, we performed AC magnetometry measurements of R26 particles at similar frequency (100 kHz) and comparable magnetic fields than the ones used in SAR measurements at a representative concentration. AC hysteresis loops of R26 sample under three H_{MAX} (4, 8, 30 kA m^{-1}) and fixed frequency (100 kHz) conditions are shown in Figure 18 ([Fe]=4 g_{Fe} L^{-1}). For the largest field intensity (H_{MAX} = 30 kA m^{-1}), AC magnetization loops present an appreciable hysteretic behavior

(Figure 3.13, black curve), something predictable from the considerable values obtained in SAR measurements at similar concentration (SAR = 330 W g_{Fe}^{-1}).

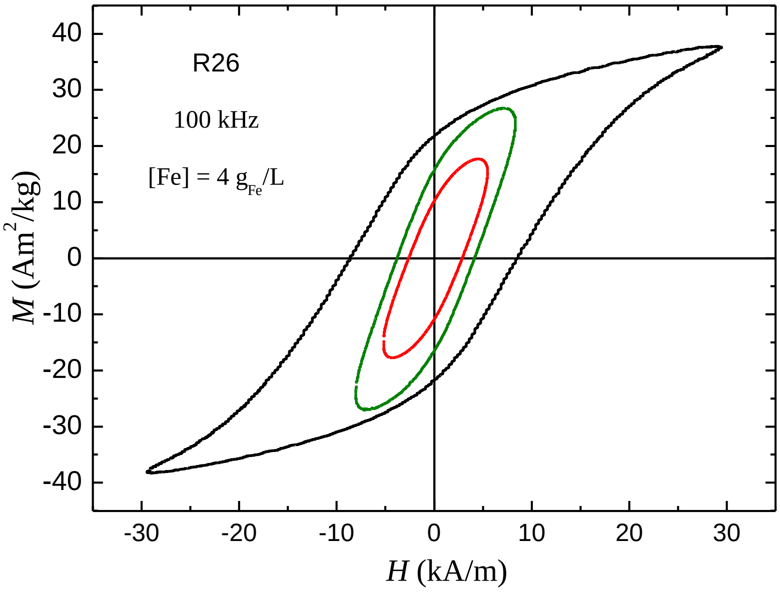

Figure 3.13. AC magnetometry measurements of R26 samples at different H_{MAX} (30, 8 and 4 kA/m). f = 100 kHz.

Besides, the hysteretic behavior begins to disappear when lower H_{MAX} are applied to the particles (Fig. 3.13, green and red lines). Outstandingly, the magnetization loops converge to an ellipsoidal shape at lower fields (i.e. 8 and 4 kA m^{-1}). According to *Carrey et al.*[42], the apparition of ellipsoids in AC magnetometries implies the mediation of dynamic relaxation mechanism (i.e. Néel and/or Brown). Furthermore, lowest employed fields ($H_{MAX} = 4$ *kA* m^{-1}) are probably under $0.5H_K$ value. This would lead, according to the theoretical model exposed in Figure 3.12a, to the vanishing of the hysteretic behavior, something not appreciated in the experimental data, and which is presumably related to the dynamic contributions to the magnetization of the IONPs.

3.3.2. Particle volume (*V*) on IONPs dipolar interactions

In similar manner to the abovementioned parameters, **particle volume** (*V*) can play an important role on the magnetic dipole-dipole interaction. The magnitude of the MNPs internal magnetic moment is given by the following expression:

$$|m| = V \cdot M_s \qquad \text{(eq. 3. 3)}$$

where M_s is saturation magnetization and V is particle size. Thus, larger V values implies larger magnetic moments of the MNPs and in consequence, stronger interacting regimes. In order to experimentally show this effect, we performed SAR measurements of two different particle volume IONPs with similar M_s values at different concentration. In this manner, we can marginalize M_s contribution to the magnetic dipolar interaction. Figure 3.14 show SAR measurements for R26 and G31 samples (i.e. V equal to 19 and 12 nm, respectively) dispersed in water at diverse iron concentration ([Fe]) and similar magnetic field intensity and frequency (H_{ac}=100 kHz and 40 kA m^{-1}). Analogously to the behavior observed in R26 samples, SAR of the smaller nanoparticles (i.e. G31) shows exponential decreasing tendency from the lowest Fe concentration (1 g_{Fe} L^{-1}) up to 4.5 g_{Fe} L^{-1}. Curiously, no peak emerges in the studied concentration range, showing an almost constant SAR value from 4.5 g_{Fe} L^{-1} to 18.5 g_{Fe} L^{-1}.

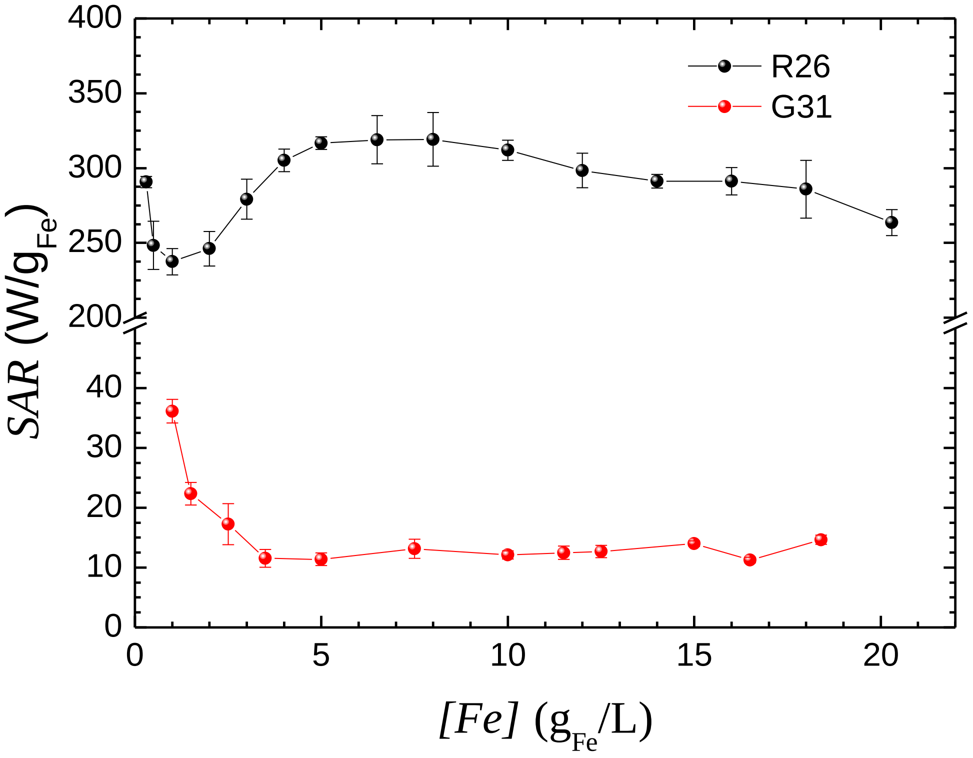

Figure 3.14. SAR measurements of R26 and G31 IONPs at different [Fe] and H_{MAX} (H_{MAX}= 4, 8, 40 kA m^{-1}). f = 100 kHz.

As both particles present comparable saturation magnetization values (M_s) (Annex I), it can be assumed R26 nanoparticles present larger magnetic dipolar moment, which could explain the apparition of stronger dipolar interacting effects observed in SAR measurements. The variation of the nanoparticle size also leads to variation on the effective magnetic anisotropy[15], being larger K_{eff} values at smaller particle size. Consequently, smaller H_K values are expected for larger IONP sizes. So, this explains that the concentration dependence of the larger size resembles the theoretical curve at $H_{MAX}/H_K=10$, when $H_{MAX} = 40$ kA m^{-1}. In case of smaller sizes, the related concentration dependence resembles the theoretical curve at $0.6 < H_{MAX}/H_K \leq 2$.

However, the use of two different particle volume (V) for this study necessarily implies considerations on the dynamical magnetic relaxation mechanism. Considering that the IONPs have similar hydrodynamic size in water (see Annex I) and viscosity media (η) are similar in both dispersions, particle volume strongly determines the effective relaxation time (τ_{eff}) via Néel relaxation mechanism contribution (τ_{Neel}), highly dependent on particle volume (V). In consequence, the time scale of the performed measurements (i.e. relation between $1/\tau_{eff}$ and the magnetic field frequency f) for each IONPs was different, hindering an immediate understanding of the exposed results.

3.4. Conclusions

In this chapter, we have probed interacting phenomena by AC magnetic and calorimetry studies on IONPs synthesized by thermal decomposition. First, we have studied the influence of inter and intra-aggregate magnetic dipolar interactions on the *SAR* values and AC hysteresis loops by i) increasing the IONPs concentration and ii) increasing hydrodynamic aggregate size. We have observed different effects associated with both kinds of dipolar interactions. On one hand, the increase of the nanoparticle concentration leads to a non-monotonic behavior of *SAR* related to magnetizing effects mediated by inter-aggregate dipolar interactions (i.e. increase of M_R and M_{MAX}). On the other hand, the enhancement of IONPs aggregate size leads to a progressive reduction of *SAR* values related to demagnetizing effects mediated by intra-aggregate dipolar interactions (i.e. reduction of M_R and M_{MAX}). Variations of H_C have been only observed in the latter case. Finally, we experimentally exposed the existence of other effects that modulate the dipolar interactions in MNPs colloids, such as the external field intensity and the particle volume. These results provide an important hint to understand the different effects mediated by magnetic dipolar interactions providing new approach to understand the dynamic magnetic response of IONPs after cell processing. At the same, encourages to the improvement to the current theoretical model to predict the complex scenario that the dipolar interaction purpose in the MH mediated by MNPs working beyond the magnetically blocked regime.

3.5. Methods

Variation of hydrodynamic size

Dynamic Light Scattering (DLS) was employed to measure the aggregation degree expressed by the hydrodynamic size (D_H). The ζ potential was tested at 25 °C by using a DLS Zetasizer Nano-ZS instrument (Malvern, U.K.) with laser light wavelength of 659nm. Zeta potential (ζ) is the parameter used to probe the IONPs surface charge under certain conditions of pH and ionic strength of the dispersion media. Two methodologies were emplyed to increase the hydrodynamic size of IONP:

i) The pH variation of the IONPs aqueous dispersion: To increase the D_H of the IONP colloids, pH was adjusted by dispersing IONPs in a buffer solution of potassium hydrogen phthalate with anionic strength of 10^{-2} M. The D_H variation induced with pH was tracked by using < 0.5 g_{Fe} L^{-1} suspensions into a standard cuvette at given pH. Tampons of pH 3.9 and 4.0 were obtained by mixing 50 ml of potassium hydrogen phthalate 0.1 M with 1.4ml and 0.1 ml of HCl 0.1M respectively, while for pH 4.1, it was mixed with 1.3 ml of NaOH 0.1M. Tampon solutions were diluted 10 times to reach the ionic strength used in Z-potential measurements (10^{-2} M) and pH deviations readjusted with HCl and NaOH addition. To induce the aggregation, 100 µl of concentrated IONP (6 mg_{Fe}/ml) were diluted on 200 µl of each tampon solution and allowed to sit overnight on the refrigerator (4ºC). The precipitated IONPs were immersed in a vigorous ultrasound bath during 30 min. Hydrodynamic size of each sample were measured before and after each calorimetric measurement and AC magnetization cycle.

ii) The dispersion of IONPs into saline buffer solution: An alternative method, based on the time variation of D_H after the IONPs dispersion in an ionic modified media, was performed to increase D_H from 56 to 356 nm. For that purpose, a concentrated IONPs sample (14.5 g_{Fe} L^{-1}) was diluted in a homemade PBS buffer solution (150 mNaCl and 50 mM Na_2HPO_4), reaching a final IONP concentration of 2 g_{Fe} L^{-1} and salt molarities of 15 mMNaCl and 5 mM Na_2HPO_4. IONP dispersed in such buffer solution shows an evolution of D_H with time. In a period of 5.5 hours, the colloidal stability of IONPs aggregates is strongly altered, allowing the increase of D_H up to 356 nm. For the sake of monitoring the suitable values of D_H in order to perform the magnetic measurements, the evolution of D_H was tracked by DLS measurements at different incubation times up to 5.5 hours (see **Table 3.1**). DLS measurements were performed in <0.5 g_{Fe} L^{-1} suspensions into a standard cuvette with the employed saline buffer suspension (15 mMNaCl and 5 mM Na_2HPO_4). Beyond 5.5 hours, the IONPs dispersion becomes colloidal unstable and precipitates. Sonication of the colloids is avoided during the experiment in order not to interfering with the aggregation dynamics.

Iron quantification in IONPs dispersions

The iron concentration (*[Fe]*) of water colloidal dispersions was determined in mg of iron per mL of dispersion volume by Inductively Coupled Plasma Atomic Emission Spectroscopy (Perkin Elmer OPTIMA 2100 DV) after acid digestion 1h at 60ºC (mixture of ¼ 65% HNO_3 and ¾ 37% HCl) at Instituto de Ciencia de Materiales de Madrid-CSIC.

Viscosity effects on the dynamical magnetic response of magnetic nanoparticles

4

Chapter

4. Viscosity effects on the dynamical magnetic response of magnetic nanoparticles

4.1. Introduction

In this chapter, we will address the study of the viscosity effects on the dynamical magnetic response of MNPs. Aiming to prepare magnetic nanostructures as suitable agents for in vivo magnetic hyperthermia or magnetic particle imaging, it is mandatory to assess all physical parameters controlling the dynamical magnetic response at the nanoscale. In this regard, viscosity (η) is one of them which still requires additional studies for a full understanding on how magnetic relaxation processes modulate the nanoparticle heating efficiency.[67,82] Fortin et al. presented one of the few comprehensive experimental studies considering the influence of the medium viscosity, and found a strong decrease of heat dissipation while increasing the viscosity of the medium.[28] Hence, it is crucial to unveil what determines those viscosity effects to predict any derived underperformance and choose the right MNP design strategy.

Calorimetry measurements are currently employed to quantify the MNP heat dissipation [41,42,60,68,73,83], in spite of the potential error sources in measuring and determining SAR values, which are difficult to keep under control. [84,85] In contrast, hysteresis loop measurement under AMF is the most direct and accurate tool to probe magnetic heat losses as a function of different extrinsic or intrinsic parameters such as particle aggregation,[60] or concentration.[60,75] At the same time, AC hysteresis loops is the experimental result which can be directly compared with theoretical models.[60] Concerning how medium viscosity influences the AC hysteresis loops of MNPs is still an open question, which requires to be properly addressed.

The present chapter merges the choice of bespoke nanoparticle systems, consisting in a set of cobalt ferrite and iron oxide nanocubes with increasing magnetic anisotropy, featuring distinct considerations to best explain the actual role of viscosity on the dynamical magnetic response of MNPs. The role of nanoparticle size, size distribution, chemical composition, and magnetic field conditions in rendering the dynamical magnetic response sensitive to medium viscosity is studied.

4.2. Viscosity effects on the magnetism of the MNPs

In order to probe the role of the above mentioned intrinsic and extrinsic parameters on the viscosity effects, we studied iron oxide nanoparticles (IONPs) of edge size 14±2 nm (M195) and 24±4 nm (M223), and cobalt ferrite nanoparticles (CoFeNPs) of edge size21 ± 2nm (SA94)(see Annex I for sample details). This set of MNPs allows one to probe the viscosity effects while progressively increasing KV by changing either size (i.e. V ranging from 1.4x10-24 to 2.7x10-23 m^3) or MNP chemical composition[86] (cobalt ferrite K=290 kJ/m^3, magnetite K=-13 kJ/m^3). The magnetization cycles of the studied MNPs at 260 K show different magnetic behavior under quasi-static conditions (See Annex I-Sample set): pronounced hysteretic behavior for SA94, superparamagnetic behavior for M195, and intermediate for M223. Such different magnetic properties of MNPs under quasi-static conditions agree with the expected trend of the KV values for the studied MNPs (See Annex I). Furthermore, similar tendency will be also observed in the dynamical magnetization response, including magnetic heating efficiency that clearly varies with chemical composition (i.e. K) and size (i.e. V).[28] Additionally, MNPs shape[87], surface defects, coating or core/shell nanostructure also influence the K value, and therefore, modulate the magnetic heating efficiency.

SAR values are commonly determined to appraise effects on the dynamical magnetic response of MNPs. Considering that SAR = A·f, one may expect that any variation of SAR values with η will be translated into variations of shape and area of the corresponding AC hysteresis loops. In order to verify this point, we have measured hysteresis loops at different viscosity values ranging from 0.9 to 153.5 m·Pas and under AMF conditions (100 kHz and H_{MAX}=24 kA/m), which are very close to the ones currently employed in magnetic hyperthermia treatments.[13]

Figures 4.1ac shows the representative viscosity dependence of the AC hysteresis loops for the studied MNPs. As expected, the opening of the AC hysteresis loops under the same conditions significantly depends on MNPs, and hence the KV value.

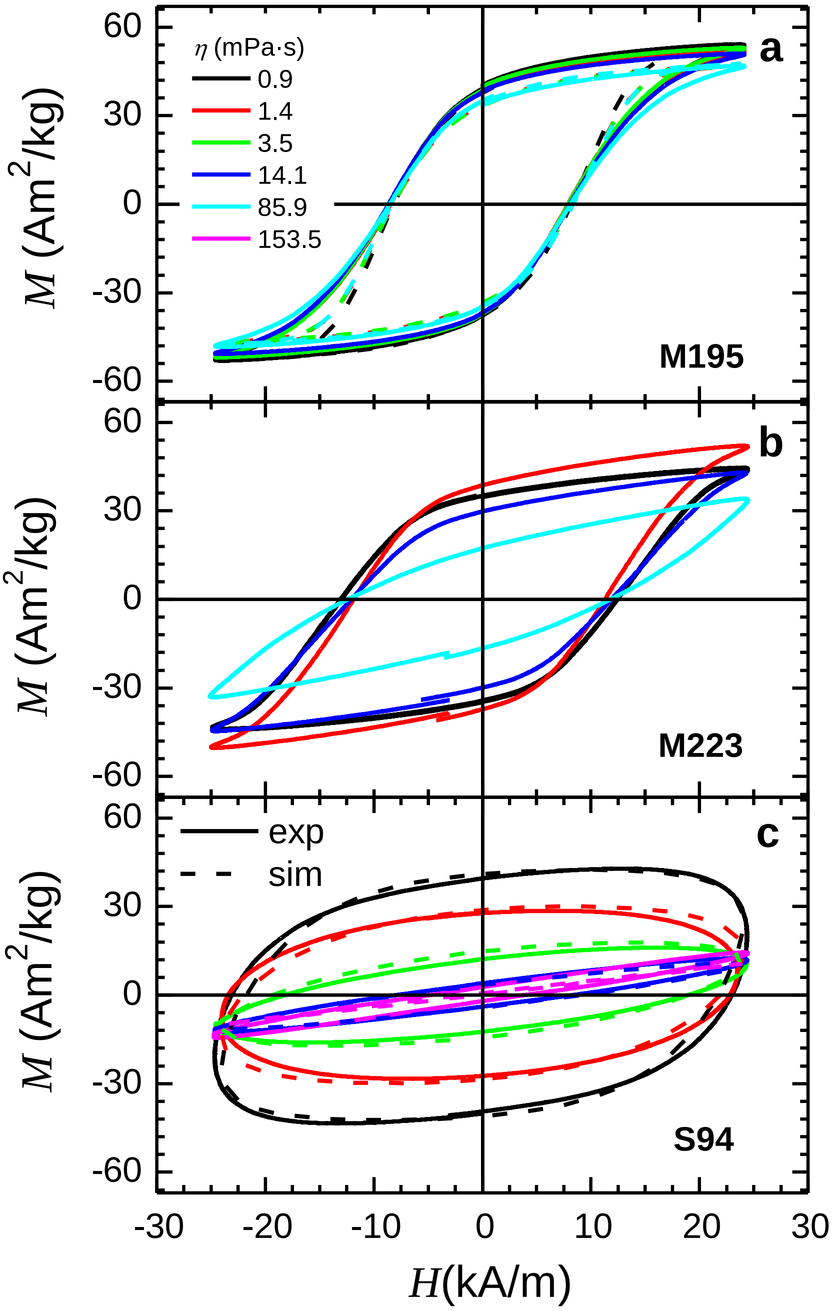

Figure 4.1. Viscosity dependence of AC hysteresis loops under AMF (100 kHz and 24 kA/m) for a) M195, B) M223, C) SA94 at 1g$_{Fe}$/L. Solid lines are experimental values, dashed lines are numerical simulations described in Material and Methods.

Indeed, the AC hysteresis loops are less opened in case of IONPs (i.e. M195 and M223) than in case of CoFeNPs (SA94). The latter is also highly sensitive to η in comparison to IONPs, whose viscosity effects diminishes with particle size. Such behavior is consequently observed for SAR values obtained by calorimetric measurements under similar experimental conditions, as observed in Figure 4.2.

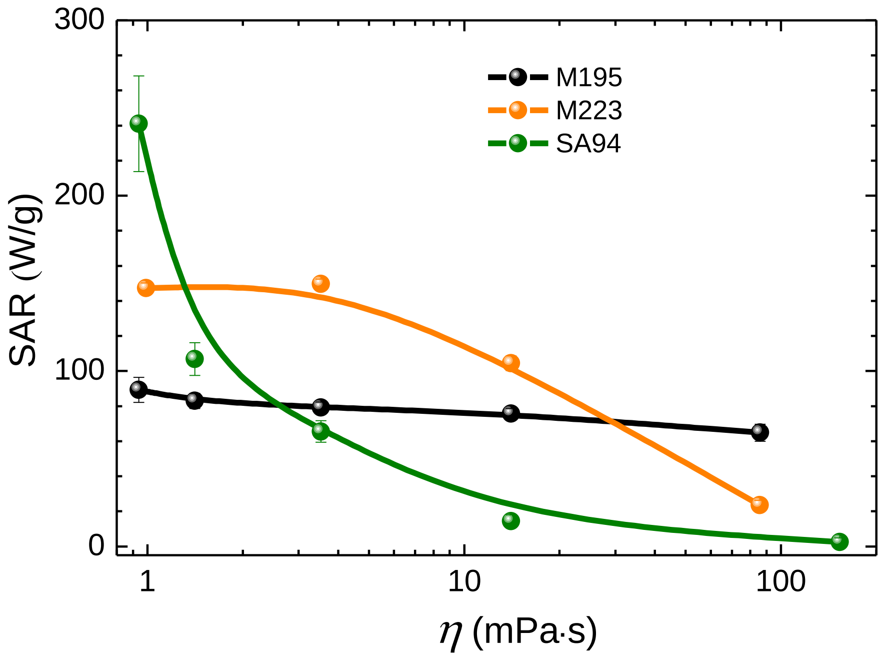

Figure 4.2. Viscosity dependence of SAR for M195 (black dots) and M223 (red dots) IONCs and SA94 (green dots) under AMF (100 kHz and 24 kA/m) at $1g_{Fe}/L$. Lines are a guide to the eye.

Indeed, SAR values of CoFeNPs are twice larger than those of IONPs (SA94 : 440 W/g; M223 : 205 W/g; M195 : 120 W/g for η= 0.9 mPa·s) as expected due to the different KV values. By increasing η the SAR values of CoFeNPs shows an exponential decrease down to 4 W/g. Contrarily, the SAR behavior depends on IONC size. While large IONCs display a progressive reduction of SAR values down to 38 W/g when increasing η, the small ones show slight reduction down to 98 W/g.

As shown in Chapter 3, analogue magnetic phenomena could result from MNPs aggregation. In order to assess whether glycerol induces aggregation on the studied MNP dispersions, we performed DLS measurements of MNPs dispersed in water and mixed aqueous medium (i.e. water and glycerol) up to the largest glycerol fraction (36% v/v_W glycerol) to check their D_H values. Figure 4.3 shows number weighted hydrodynamic size histograms of IONPs and CoFeNPs dispersed in water and glycerol/water mixed medium. Mean D_H and PDI values, collected in Table 4.1, do not significantly differ when determined in both used solutions.

Table 4.1. Mean number weighted hydrodynamic sizes (D_H) and polydispersity index (PDI) of the studied MNPs dispersed in water and 36% glycerol.

	Water dispersion		**36% Glycerol dispersion**	
MNP	D_H (nm)	PDI	D_H (nm)	PDI
M195	28	0.15	29	0.21
M223	42	0.12	43	0.15
SA94	32	0.21	33	0.16

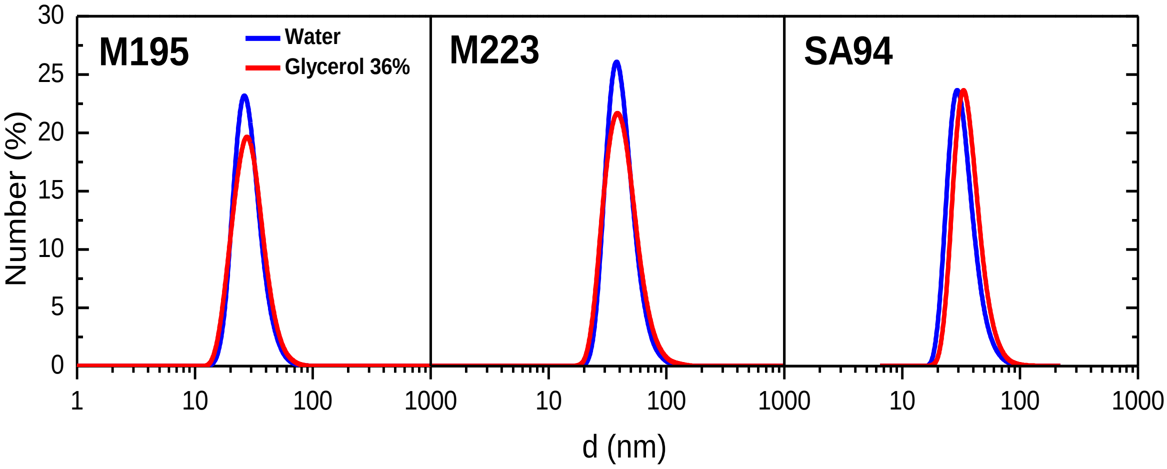

Figure 4.3. Number weighted hydrodynamic size histograms of M195, M223 and SA94 measured in water (blue curves) and in 36% glycerol solution (red curves). Mean values and polydispersity index are shown inside graphs.

Moreover, further analysis of the AC hysteresis loops evidences the related effects with the MNPs environmental viscosity. On the one hand, AC hysteresis loops of CoFeNPs feature a reduction of all characteristic hysteresis parameters (i.e. coercive field (H_C), remanence (*M_R*), and maximum magnetization (*M_{MAX}*) when increasing the viscosity of the medium, as shown in Figure 4.4.

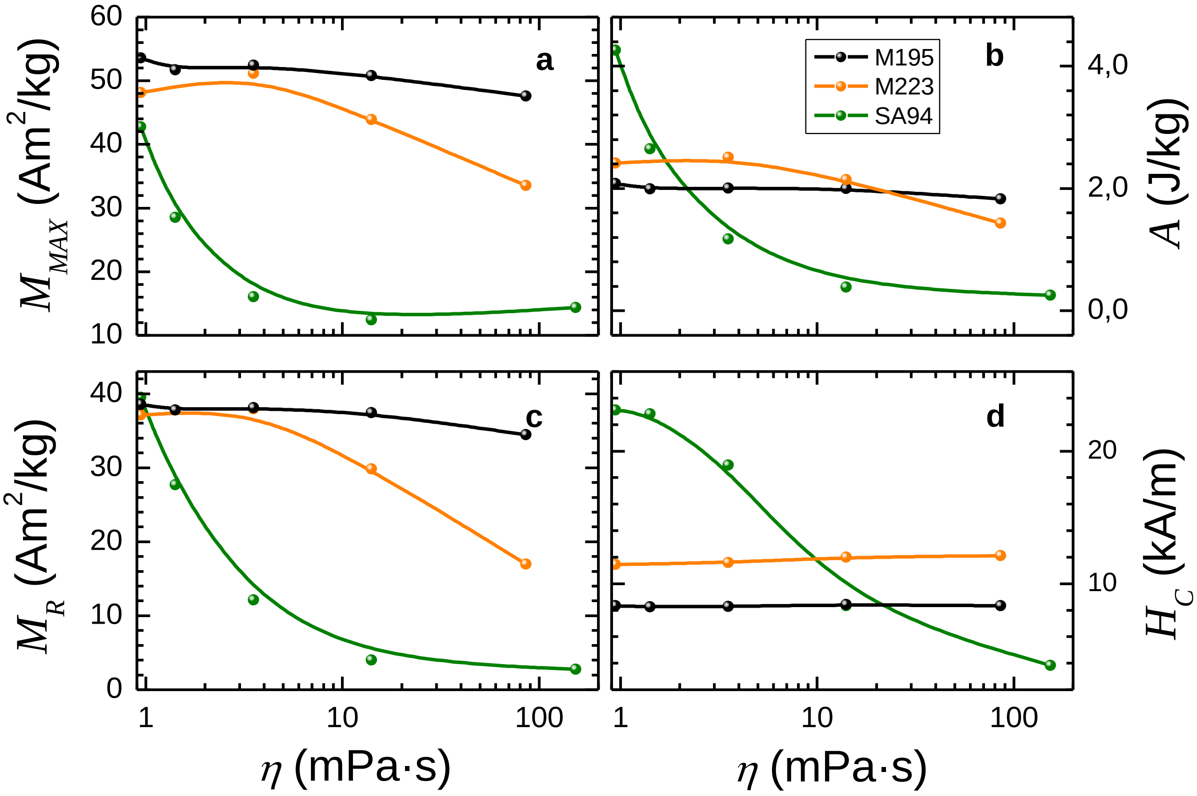

Figure 4.4. Viscosity dependence of MR, MMAX, HC, and A extracted from Fig.2 for SA94 (blue dots) , M223 (red dots) and M195 (black dots) IONCs under AMF (100 kHz and 24 kA/m). Lines are a guide to the eye.

On the other hand, the changes of shape and the area of AC hysteresis loops for IONPs (i.e. M195 and M223) at increasing η depend on particle size. Whereas M_R and M_{MAX} decrease for both IONPs sizes, but in a more pronounced manner for the larger size, H_C does not vary with viscosity for any size (see Figure 4.4d). Hence, the shape and area of the AC hysteresis loops for the larger IONPs behave differently with η similarly to those of CoFeNPs. Furthermore, the variation of *A* with η (Figure 4.4b) matches the respective SAR dependence (Figures 4.1 and 4.2). As revealed in Figures 4.4bc, the viscosity dependence of *A* is intimately associated with demagnetizing effects, i.e. reduction of M_R, and M_{MAX}, depending on the considered MNP. However, the role of H_C on the determination the viscosity dependence of *A* values is not straightforward due to the complex interplay between different parameters involved in the MNPs magnetization dynamics (mainly, *K*, H_{MAX}, and size distribution). Whereas H_C shows a progressive decrease with η for CoFeNPs, it remains constant for IONPs. According to the correlation of the viscosity dependences of SAR and *A*, the variation of AC hysteresis loops with η seems to be related to changes in the magnetic relaxation mechanisms, as originally proposed by Fortin et al[28]. In order to confirm this hypothesis, we analyzed the magnetic relaxation processes by AC susceptibility (ACS) measurements on the most and least sensitive MNPs to η. At a first glance, Figure 5.5 shows that the Brownian mechanism dominates the relaxation processes for those MNPs whose dynamical magnetic response is sensitive to viscosity (i.e. SA94) under the applied AMF conditions (i.e. 100 kHz, see dotted line in Figure 4.4). The contrary applies for the Néel mechanism (i.e. M195). For CoFeNPs, the real (χ') and imaginary (χ'') parts of AC susceptibility clearly reflect the sole contribution of the Brownian relaxation.

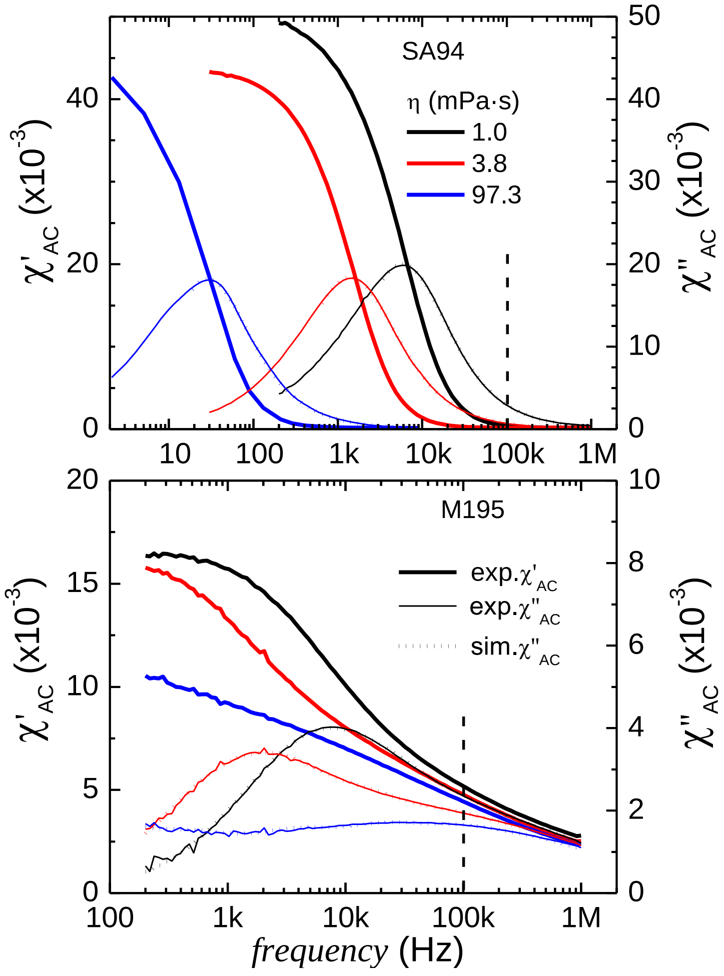

Figure 4.5. Frequency dependence of χ' (thick lines) and χ'' (thin lines) for SA94 (upper figure) and M195 (lower figure) samples dispersed in different viscous media. Dotted lines indicates simulated curves according to Debye model. Dashed lines indicate the AMF frequency experimentally employed in SAR and AC magnetization measurements.

χ' decays down to zero at high frequencies and χ'' exhibits a pronounced maximum that shifts towards lower frequencies when increasing η. It is worth noting that from the variation of χ'' values at a frequency of 100 kHz for different viscosities, we can qualitatively describe the viscosity dependences of *A* (i.e. SAR) despite the strong differences of the field intensity values (H_{MAX}= 24 kA/m and 0.07 kA/m for AC hysteresis loop and ACS measurements, respectively). χ'' at 100 kHz reaches zero when increasing η for SA94, similarly to the viscosity dependences observed for A and SAR values. In contrast, both Brownian and Néel relaxation processes coexist in M195 sample. Whereas the Brownian peak shifts towards lower frequencies when increasing η, a less pronounced maximum is observed around 60 kHz within the frequency range associated with Néel relaxation. However, for the M195 χ'' does not reach zero at high frequencies even for the highest η because a broad Néel relaxation maximum peaked around 60 kHz is observed for η = 97.3 mPa·s. It is important to note that AC susceptibility measurements were performed at rather low field amplitudes (i.e. 0.07 kA/m), so that the zero-field expressions hold for τ_B and τ_N. In spite of the recently reported influence of H_{MAX} on magnetic dynamics[88], Néel relaxation prevails for M195 at the AMF conditions employed in SAR and AC hysteresis loop measurements (i.e. 100 kHz and 24 kA/m).

In order to shed light in our experimental observation, Dr. Aidin Lak performed numerical simulations of AC susceptometry measurements. The curve-fitting of ACS measurements was performed using a least-squares fit routine to solve Debye equations and written in MATLAB. The routine uses the Levenberg-Marquardt algorithm which is a powerful scheme for non-linear problems. These simulations can describe the AC susceptibility response of the studied MNPs in good agreement with the experimental results, as shown in Figure 4.5 (dotted lines). In this regard, the values of fitting parameters were comparable to experimental ones (Table 4.2 and 4.3). In addition, simulations confirm the prevalence of magnetic relaxation processes on the studied samples. Thus, relaxation mechanisms of M195 sample are characterized by the coexistence of Néel and Brownian processes. However, only Brownian process prevails for SA94 in the studied frequency range. The coexistence of Néel and Brownian mechanisms for M195 has significant consequences for determining the influence of viscosity on its dynamical magnetic response. Indeed, field conditions (mainly frequency but also intensity) will strongly define such viscosity sensitivity as it will be shown later.

Table 4.2. Results obtained from the best fits to the ACS imaginary part for M195.

M195	0% glycerol dispersion	36% glycerol dispersion	81% glycerol dispersion
η (mPa.s)	1	4.33	70
D_H (nm)	38	38	38
σ_H	0.3	0.3	0.3
K (kJ/m^3)	11.3	11.3	11.3
σ_C	0.17	0.17	0.15

Table 4.3. Results obtained from the best fits to the ACS imaginary part for SA94.

SA94	0% glycerol dispersion	36% glycerol dispersion	86% glycerol dispersion
η (mPa.s)	1	4.16	200
D_H (nm)	33.7	33.7	33.7
σ_H	0.17	0.17	0.17

Concerning the overall understanding of viscosity effects on AC hysteresis loops, Dr. Takashi Yoshida, from Kyushu University, performed numerical simulations based on the stochastic Landau–Lifshitz–Gilbert (LLG) model. Thus, the viscosity dependencies of AC hysteresis loops can be directly related to the prevalence of different relaxation mechanisms as extracted from Figure 4.6. For high KV values (i.e., SA94 and M223), AC hysteresis loops are highly sensitive to medium viscosity due to the prevalence of Brownian relaxation when field intensity is considered. On the contrary, low KV values (i.e. M195) lead to a decrease of the viscosity influence when the Néel relaxation times

(τ_{Neff}) are shorter than τ_{Beff} (Figure 4.6EG).

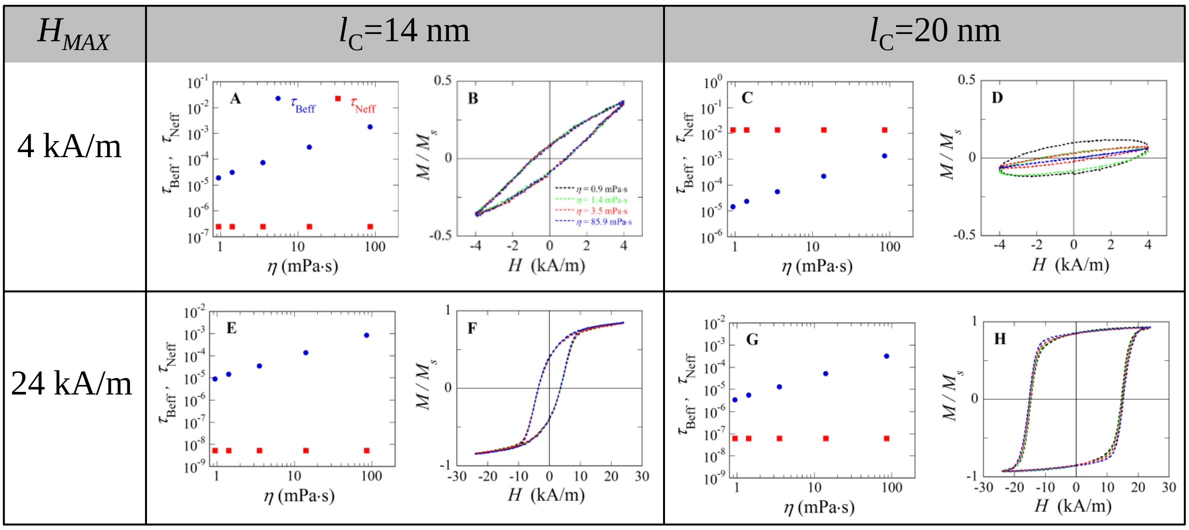

Figure 4.6. Viscosity dependences of the field-dependent relaxation times and AC normalized *M-H* curves calculated for IONCs under *AMF* (100kHz) and different values of l_c and H_{MAX} A),B) l_c = 14 nm and H_{MAX} =4 kA/m, C) , D) l_c = 20 nm and H_{MAX} = 4 kA/m, E) , F) l_c = 14 nm and H_{MAX} = 24 kA/m, and G),H) l_c = 20 nm and H_{MAX} = 24 kA/m.

Hence, AC hysteresis loops of SA94 are highly sensitive to viscosity (Figure 4.6B) because τ_{Beff} is much smaller than τ_{Neff} (Figure 4.6A). Unlikely, M195 present different viscosity effects on depending on AMF conditions. In particular, no viscosity effects are observed on the dynamical magnetic response when τ_{Neff} are shorter than τ_{Beff} (Figure 4.6E-H). The consideration of these different magnetic dynamics in the LLG equations provides a suitable theoretical framework to simulate AC hysteresis loops (dotted lines in Figure 4.1), resulting in good agreement with the experimental results (solid lines in Figure 4.1). The values of fitting parameter K leading to the best fitting were K = 28.6 kJ m^{-3} for SA94 and K = 10.6 kJ m^{-3} for M195. The slight discrepancies between experimental and theoretical results can be related to the hydrodynamic size distribution or dipolar interactions not considered by the model, or small differences of the K values. Note that K values in the simulations reasonably agree with those obtained from ACS. These parameters were kept constant in the numerical simulations for different viscosities.

To determine the role of AMF conditions in the medium-related viscous effects, AC magnetization measurements of M195 were performed under different medium viscosities (η = 0.9, 1.5, 85.9), field frequencies (*f* = 24, 51 and 96 kHz) and maximum field intensities (H_{MAX} = 4, 8, 16 and 24 kA/m) conditions (Figure 4.7). At first glance, clear patterns in the AC magnetic behavior of the sample are distinguished at different η values. Concerning field frequency, AC magnetic response exhibit a stronger sensibility to the viscosity of the dispersion medium at lower frequencies (f = 24 and 51kHz), showing important changes in curves shape and a A decrease when η increases. Contrarily, this magnetic response variability is just slightly displayed when field frequency increases up to 96 kHz. A plausible reason of the observed phenomenology lays on the contribution of Brown relaxation observed in AC susceptibility measurements for M195 sample. Indeed, the well pronounced Brown-related χ''peak observed at f ~ 9 kHz (Fig.4.5) establish that when the value of AMF frequency is close to this maximum, the AC hysteresis loop will be highly sensitive to viscosity than at much higher frequencies where Néel relaxation prevails. In addition, field intensity plays also a relevant role on the viscosity effects on the AC hysteresis loops.

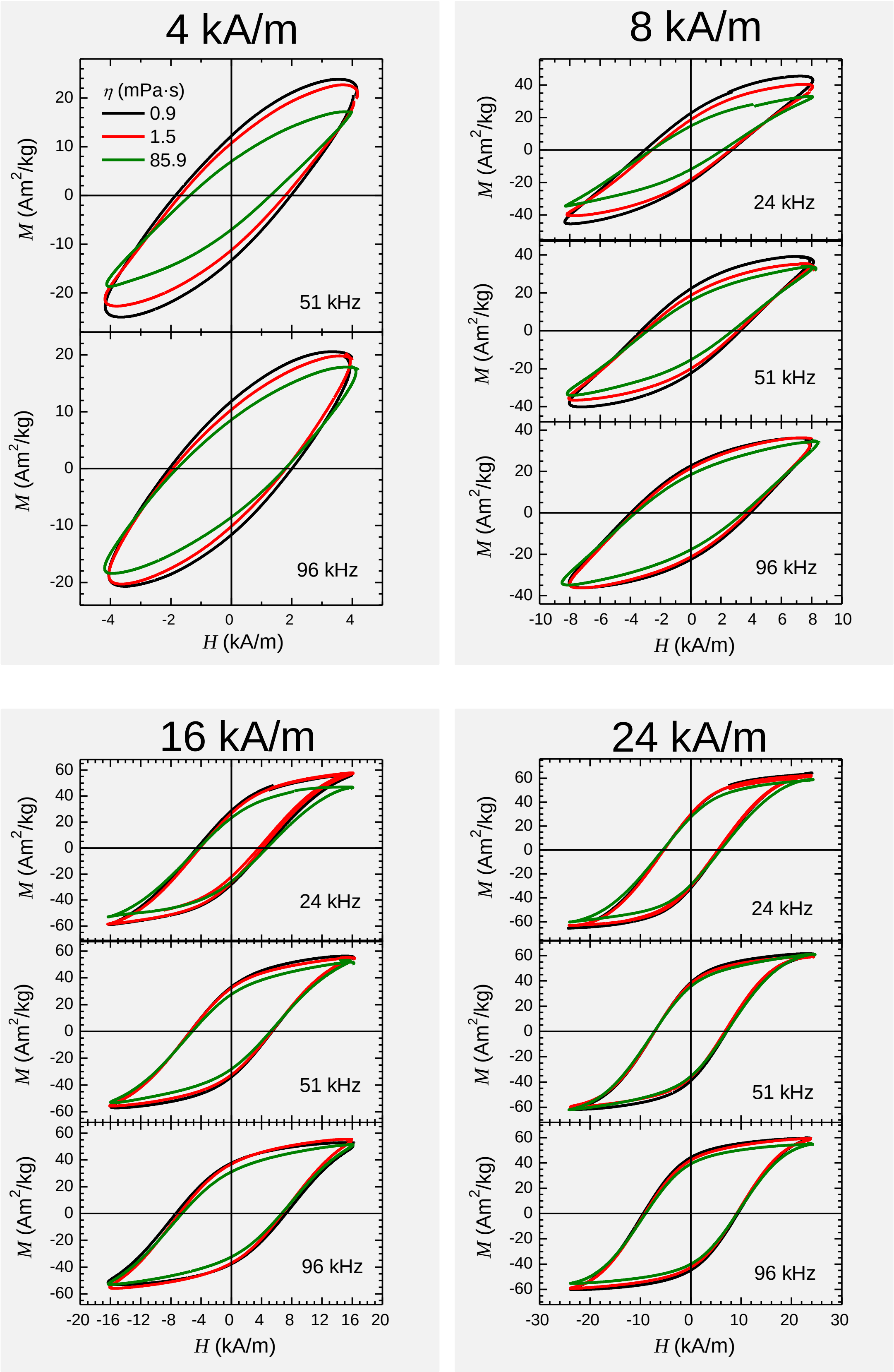

Figure 4.7. Mass-normalized AC hysteresis loops of M195 dispersed in distinct viscosity media (black line 0.9 mPa s, red line 3.5 mPa s, green line 85.9 mPa s) and under different AMF conditions (grouped by field intensity).

Thus, despite AC hysteresis loops at 24 kA/m are slightly influenced by large η, independently of the AMF frequency, lower magnetic field intensities ($\leq$ 8 kA/m) favors the sensitivity of AC hysteresis loops to viscosity of the dispersion medium, which is distinctly pronounced depending on frequency. On the whole, lower field intensities and frequencies render AC hysteresis loops more sensible to viscosity. The explanation is related to the field dependence of relaxation times and the relevance of the MNP magnetic torque. Indeed, H_{MAX} values of 4 kA/m are enough to appreciate significant variations of the shape and A of the AC hysteresis loops (i.e. H_C, M_R, M_{MAX}) when η = 3.5 m·Pas. Such behavior is ascribed to the capability of the external AC magnetic field ($\overrightarrow{\mathrm{H_{ex}}}$) to generate magnetic torques. Magnetic torques, already introduced in recent studies, are manifested in two different ways: as an internal rotation of the magnetic moment $\vec{\mathrm{m}}$ of the MNPs and as a physical rotation of the MNPs in a liquid medium. Consequently, the dependence on H_{MAX} of such coexistent phenomena influences the Néel and Brownian rotational mechanisms, determining the τ_{Beff} and τ_{Neff} values, respectively (Figures 4.6CG). The variation of the prevalent effective relaxation time (from τ_{Neff} to τ_{Beff}) with H_{MAX} (4 and 24 kA/m) partially explains why AC hysteresis loops of M195 are so sensitive to η at 4kA/m. However, the key parameter required to explain such observations is the particle size distribution. Figures 4.6A-D show that l_C -which defines V and consequently the anisotropy energy barrier- leads to the raise of the τ_{Neff} values. Hence, the crossover between τ_{Neff} and τ_{Beff} regimes is favored by the size distribution (i.e. large values of Δl_C). Therefore, when the dynamical magnetic contribution of MNPs of a given l_C is weighted according to the related size histogram (See Annex I), AC hysteresis loops are differently sensitive to viscosity depending on H_{MAX} (as shown in Figures 4.6BDFH). Finally, the concomitant influence of H_{MAX} and size distribution on τ_{Neff} and τ_{Beff} is required to fully understand the experimental results at low field intensities. The balance between several parameters determining τ_{Neff} and τ_{Beff}, namely size distribution, η, H_{MAX} and K eventually define the effective relaxation mechanism. Thus, AC hysteresis loops of M195 at H_{MAX} = 24 kA/m present no viscosity effects (Figure 4.1c) because the Néel relaxation is dominant for l_C values due to the stronger field-dependence of τ_{Neff} in comparison with τ_{Beff},[88] as opposed to the observations at 4 kA/m (Figures 4.6E-H). Moreover, the implicit consideration of both τ_{Neff} and τ_{Beff} results in an overall good agreement between experimental and theoretical hysteresis loops under the different extreme H_{MAX} experimental conditions (i.e. 4 and 24 kA/m) (Figure 4.8).

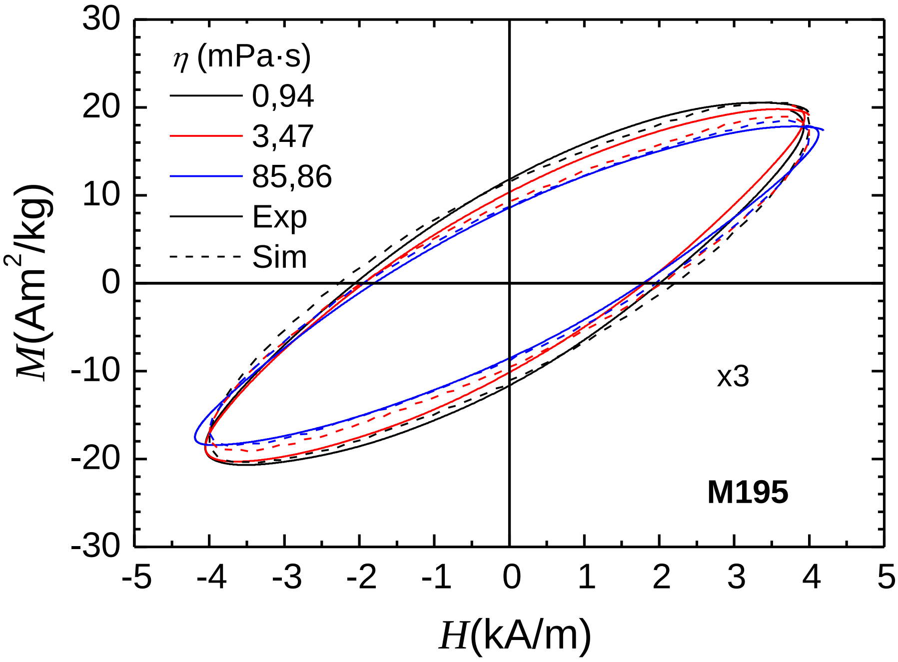

Figure 4.8. Viscosity dependence of AC hysteresis loops under AMF (100 kHz and 4 kA/m) for IONCs at $1g_{Fe}/L$. Solid lines are experimental values, dashed lines are numerical simulations. For the sake of clarity, magnetization values are increased 3-fold.

The presented study stresses the fact that the viscosity effects are not only related to MNP size and *K* favor Brownian relaxation process, but also to field conditions (i.e. values of H_{MAX}, field frequency). In a first approach, MNP size and *K* define the crossover between Néel and Brownian mechanisms, resulting in magnetic dynamics that are sensitive to viscosity for large MNP sizes and *K* values. Secondly, H_{MAX} and field, and MNPs size distribution play also a critical role in the dynamic magnetic response, as both parameters strongly influence relaxation mechanisms.

4.3 Conclusions

We have demonstrated the convenience of AC hysteresis loop measurements to determine the influence of viscosity on the dynamical magnetic response of MNPs. AC hysteresis loops from selected MNPs of different anisotropy constants dispersed in increasingly viscous media provide conclusive evidences on: i) the balance between those parameters determining the dominant magnetic relaxation process -namely size, size distribution, H_{MAX}, f and K- eventually define the viscosity sensitivity of the dynamical magnetic response of MNPs, ii) the viscosity dependence of the AC hysteresis area is correlated to that of the SAR, due to demagnetization effects related to changes in the magnetization dynamics when viscosity increases, iii) size distributions and field-effective relaxation times precisely reproduce the hysteresis loops in most of the considered cases, and iv) the election of field conditions (field frequency and intensity) allows to select the relaxation mechanisms resulting in the modulation of the viscosity sensitivity degree of the MNPs. Our reported results encourage further exploration of the viscosity influence on the magnetization dynamics of MNPs, from dissipating the very slight discrepancies found between experiments and theory, to broadening the KV range explored by selecting suitable MNPs. Understanding which parameters determine the sensitivity of dynamical MNP magnetic response to viscosity is of great importance towards engineering MNPs with invariable magnetic heat losses and selecting the convenient AMF conditions for magnetic hyperthermia.

4.4. Methods

Calorimetry measurements

The volumetric specific heat constants considered for Milli-Q water (CDDW) and different glycerol dispersions in water (C%glycerol) used were: CDDW=4.20±0.02 J/g˚C, C15%=4.03 ±0.01 J/g˚C, C36%=3.55 ±0.03 J/g˚C, C60%=3.07 ±0.03 J/g˚C, C81%=2.66 ±0.01 J/g˚C, C86%=2.33 ±0.01 J/g˚C.. These values were obtained by Discovery Differential Scanning Calorimeter (TA Instruments) at Servicio Interdepartamental de Investigación at the Universidad Autónoma de Madrid.

Viscosity measurements

Viscosity measurements were peformed by Dr. Maria Elena Materia, working at Dr. Teresa Pellegrino's group (Genoa, Italy). The rheological properties of the different media (12 mL volume of 0%, 15%, 36%, 60%, 81% and 86% Glycerol in double distillated water) were characterized by means of viscosity measurements (DH-2 rheometer, TA Instruments, Delaware, USA) under both controlled shear and temperature conditions. The rheometer is equipped with a double gap cylinder chamber and cylindrical geometry rotating in between, in order to grant high precision measurement with low viscosity fluids. Table 4 shows the average viscosity values (two repetitions) for the different media studied by using a temperature ramp mode: specific shear rate (50 s^{-1}), the temperature range (15 and 35 °C) and rate (2 °C/min).

Table 4.4: Mean viscosity values and related standard deviations at 22º and 24ºC.

Glycerol fraction (%)	Mean viscosity values at 297 K (mPa·s)	Mean viscosity values at 295 K (mPa·s)
0	0.9 ± 0,1	1.0 ± 0,1
15	1.4 ± 0,1	1.5 ± 0,2
36	3.5 ± 0,1	3.8 ± 0,2
60	14.1 ± 0,10	15.4 ± 0,3
81	85.9 ± 0,1	97.3 ± 0,3
86	153.5 ± 0,3	176.2 ± 0,3

Complex ac-susceptibility measurements

The complex AC-susceptibility (ACS) measurements were carried out by Dr. Frank Ludwig at Technische Universität Braunschweig using two setups operating from 10 Hz to 10 kHz and 1 kHz to 1 MHz at magnetic field amplitudes of 0.46 kA/m and 0.07 kA/m, respectively. The ACS measurements at lower frequencies (2 Hz to 9 kHz) were performed using a fluxgate-based rotating magnetic field setup at 0.16 kA/m magnetic field amplitude.[89] The ACS measurements were carried out at 295 K in a volume of 150 µL of MNP dispersions with different glycerol fractions (0%, 36%, 81%, and 86%) but at fixed iron concentration of 2gFe/L.

Numerical simulations

Numerical simulations of ACS measurements were performed using a least-squares fit routine to solve Debye equations (eq. 1.13-15) and written in MATLAB. The routine uses the Levenberg-Marquardt algorithm which is a powerful scheme for non-linear problems.

Numerical simulations of AC hysteresis loops were based on calculating modified stochastic LLG equation describing the dynamics of the magnetic moments $\underset{\mathrm{m}}{\rightarrow}$:

$$\frac{d\vec{m}}{dt} = \frac{\mu_0}{2\tau_0 KV}\left[\frac{m}{\lambda}\vec{m} \times \left(\overrightarrow{H_{eff}} + \overrightarrow{H_{th}}\right) - \vec{m} \times \vec{m} \times \left(\overrightarrow{H_{eff}} + \overrightarrow{H_{th}}\right)\right] \qquad \text{(eq. 4.1)}$$

where τ_0, which is given by $\tau_0 = m/2\gamma\lambda KV_c$, is the attempt frequency, m is the magnitude of the magnetic moment, γ is the gyromagnetic ratio, λ is a dimensionless damping coefficient, K is the magnetic anisotropy constant, and V is the individual MNP volume. The effective magnetic field $\overrightarrow{H_{eff}}$ has been calculated assuming a uniaxial magnetic anisotropy and neglecting magnetic dipolar interactions; thus:

$$\chi\overrightarrow{H_{eff}} = \overrightarrow{H_{ex}} + \overrightarrow{H_K} \qquad \text{(eq. 4.2)}$$

where $\overrightarrow{H_K} = \frac{2KV}{\mu_0 m}\frac{\vec{m}\cdot\vec{n}}{m}\vec{n}$, and $\vec{n}$ is unit vector along the easy axis. Thermal fluctuations have been taken into account in the form of a random torque (as described in ESI). The influence of the applied field on the Néel and Brownian relaxation times as well as their relative contribution to their relaxation processes have been computed through the following set of equations:

$$\tau_{Beff} = \frac{\tau_B}{\sqrt{1 + 0.07\xi^2}} \qquad \text{(eq. 4.3)}$$

$$\tau_{\mathrm{Neff}} = \tau_{\mathrm{N}} \frac{\exp(\sigma h^2)}{(1 - h^2)(\cosh \xi - h \sinh \xi)} \qquad \text{(eq. 4.4)}$$

where $\sigma = \frac{KV}{k_B T}$, $\xi = \frac{\mu_0 M_S V H_{ac}}{k_B T}$, $h = \frac{\xi}{2\sigma}$, τ_N and τ_B are Néel and Brown relaxation times in the absence of an external field. For more realistic results, the experimental nanoparticle size distributions were inserted in the relevant equations. The algorithm was developed in C++ with CUDA running on a graphics processing unit (NVIDIA Tesla C2075).

Dynamical magnetic response of iron oxide nanoparticles in live cells

5

Chapter

5. Dynamical magnetic response of IONPs in live cells

5.1. Introduction

In this chapter, we will study the dynamical magnetic response of IONPs nanoparticles inside live cells.

Concerning the magnetic heat release in cellular environments, several studies report a significant reduction between 70 and 90%, depending on nanoparticle size, chemical composition, and/or aggregation degree.[1,90] However, these experimental results were mainly obtained in fixed cells (i.e. cells with a generalized protein cross-linking), which could lead to an additional source of variation of the dynamical magnetic response with respect to live cells.

Soukup et al.[29] reported on how magnetization relaxation processes, probed by AC susceptibility (ACS) measurements, varied when MNPs are located in live cells, with respect to colloidal dispersion. Similar results were obtained by *Moise et al.*[52] when the magnetic anisotropy constant of the IONPs was directly varied by doping either with zinc or cobalt. Although ACS measurements provide extremely useful insights into the dynamic response of MNPs in biological environments, the typical field intensity values employed in these measurements (< 0.04 kA/m) are far from those used in magnetic hyperthermia[13] or MPI. It is therefore difficult to extract general conclusions from ACS measurements alone, since relaxation times and magnetization reversals are strongly modulated by the external field intensity.[88]

The dynamical magnetic response of MNPs under AMF is generally described by the specific absorption rate (SAR), which represents the heat loss per second per gram of magnetic material. SAR is mainly measured using calorimetric methods which allow the quantification of MNP heat dissipation losses considering different extrinsic and intrinsic MNP parameters.[15,16,60,68] However, calorimetry measurements for determining SAR [82] are inaccurate and difficult to standardize. At the same time, the calorimetry method requires parameters such as specific heat which are difficult to be determined in biological entities without affecting their integrity. Contrary, AC magnetometry (ACM)[64] affords a direct and accurate method to probe and quantify heat related to magnetic losses.

In the present chapter, a magnetic study supported on ACM and ACS measurements of IONPs internalized in live cells is presented. We studied the influence of the cell internalization in two different core size commercial citric acid coated IONPs (11nm and 21 nm) with distinct dominating magnetic relaxation mechanisms (Néel and Brownian, respectively). We assessed the AC susceptibility (up to 40 kHz) and AC hysteresis loops (100 kHz, ±20 kA/m) by measuring the same sample of IONPs dispersed in aqueous solutions as well as in live cells. In order to better understand the behavior of the MNPs in live cells, we assessed the dynamical magnetic response of IONPs when varying environmental viscosity and nanoparticle aggregation. Understanding the underlying reasons behind the changes of dynamical magnetic behavior in biological matrices is of great importance to design novel MNPs nanostructures whose heating efficiency and/or MPI signal remains unaffected by biological environments.

5.2. Dynamical magnetic response of IONPs in live cells

We performed ACS and ACM studies of IONPs dispersed either in double distillated water (ddH_2O) at $1g_{Fe}/L$, or internalized within live cells to determine the prevailing magnetic relaxation mechanism, and the magnetic heat losses. Figure 5.1 shows the dynamic magnetic measurements of 11nm ± 4 nm (FM-CT2 sample) and 21 ± 6 nm (DC7 sample) IONPs dispersed in water (solid lines) at $\rho_{Fe} = 1\ g_{Fe}/L$ (See Annex I for IONPs TEM images and core size histograms). The ACS measurements of the smaller (FM-CT2) IONP dispersed in ddH_2O (Figure 5.1a, solid black curves), show a constant value of real ACS component (χ') from 10 Hz up to ~2 kHz, and then a progressive decrease towards larger frequencies. Since the ACS real component (χ') dominates within the measured frequencies, a Néel peak is predicted at higher frequencies above the measurable range (i.e. >>500 kHz), whilst the imaginary component (χ'') shows a broad peak around 9 kHz.

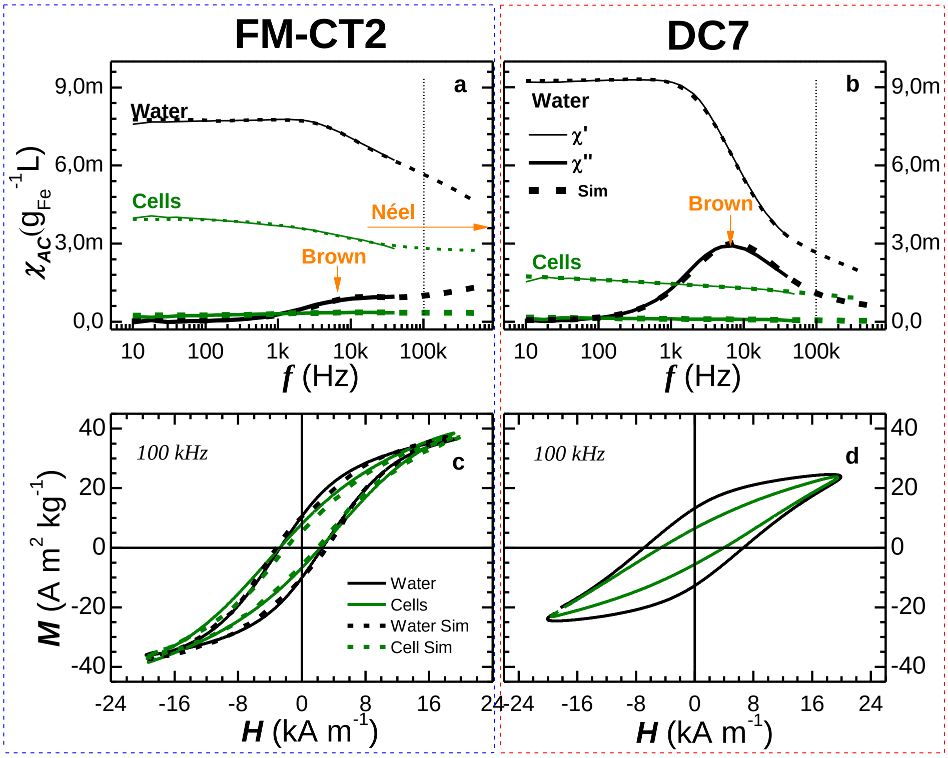

Figure 5.1. Experimental (solid lines) and simulated (dashed lines) AC susceptibility for a) FM-CT2 (11 nm core), b) DC7 (21 nm core) dispersed in water (black line) and inside live cell (green line) and AC hysteresis curves at HAC=100 kHz and 20 kA/m c) FM-CT2, d) DC7 IONPs dispersed in water (black line) and inside live cell (green line). The iron content was 1mgFe/mL for all data, except for DC7 IONPs inside live cell (0.7gFe/L). Dotted lines in a) and b) indicate the HAC frequency employed in AC hysteresis loops measurements.

These features are representative of the coexistence of Brownian and Néel relaxation processes in these IONPs dispersed in water. [91] Indeed, the less pronounced χ'' peak observed at f= 9 kHz is related to the Brownian relaxation process as confirmed later in the viscosity study, residual in comparison to the Néel contribution in any case. Such coexistence of both Brownian and Néel relaxation processes in FM-CT2 sample could be assigned to the large size distribution of the cores, which is asymmetric towards large sizes (see Annex I for TEM images and size distribution). Typically, IONPs of larger sizes will have sufficient anisotropy energy to be magnetically blocked around the f = 9 kHz region, allowing the observation of a weak Brownian contribution. The prevalence of the Néel relaxation mechanism indicates that the majority of the IONPs have Néel relaxation times shorter than the AC field cycle time within the frequency range studied. Besides, ACS measurements of the DC7 samples dispersed in ddH$_2$O (Figure 5.1 b –solid black curve) show an entirely different scenario. On one hand, the χ' component shows constant value from 10 Hz up to 1 kHz but a more progressive decrease towards large frequencies. On the other hand, χ'' shows a well pronounced, (Brownian related) peak at 9 kHz and a much weaker high-frequency (Néel related) component, revealing the prevalence of Brownian relaxation in the studied frequency range for the larger IONPs (DC7). This is consistent with a large proportion of IONPs whose internal magnetic moment remains aligned to the AC field during the AC field cycle, and indicates that these particles have higher anisotropy energy barrier than the FM-CT2 particles.

ACM measurements were performed under AMF conditions close to those currently employed in magnetic hyperthermia treatments[13] and therefore, with magnetic field intensities orders of magnitude greater than those employed for ACS measurements. Figures 5.1cd (solid black lines) show distinct hysteretic behavior of both IONPs dispersed in ddH$_2$O. While the values of magnetization at the maximum field intensity (M_{MAX}) or remanence (M_R) are larger for FM-CT2 than for DC7 sample, the area is evidently larger for the DC7 sample due to larger coercivity (H_C) values. ACM measurements were performed under AMF conditions close to those currently employed in magnetic hyperthermia treatments[13] and therefore, with magnetic field intensities orders of magnitude greater than those employed for ACS measurements. Figures 5.1cd (solid black lines) show distinct hysteretic behavior of both IONPs

dispersed in ddH_2O. While the values of magnetization at the maximum field intensity (M_{MAX}) or remanence (M_R) are larger for FM-CT2 than for DC7 sample, the area is evidently larger for DC7 sample due to higher coercivity (H_C) values. Assuming that hysteresis area is related to magnetic heating losses, we determine the SAR values measured for FM-CT2 and DC7 samples dispersed in water solutions are 40 ± 2 and 76 ± 4 W/g, respectively. These different SAR values depending on particle size can be understood in terms of IONP volume (V)[61], or in another words: different magnetic anisotropy energy barrier KV, where K is the magnetic anisotropy.[61]

In order to assess the dynamical magnetic response of the same IONPs in live cells, we incubated IONPs with a breast cancer cell line (MCF-7), following a IONP cell uptake protocol[59] (see methods section). After 24 hours of incubation, the IONPs loaded cells were detached from the cell culture flask. Immediately after, we performed ACS and ACM measurements on the live cell suspensions.

Dynamical magnetic response of IONPs inside cells in comparison with the ones dispersed in water reflects strong differences. In ACS (Figure 5.1ab – solid green lines), the absolute values of χ' dramatically drops for both IONPs after cell internalization across all the measured frequency range, but to a different extent but to a different extent being more pronounced for the larger IONPs – DC7. In contrast, χ'' shows a flat signal with values near zero across the overall measured frequency range independently of IONP size.

In addition, ACM curves of IONPs (Figure 5.1cd) internalized in cells significantly vary their sigmoidal shape and the opening (lowering coercivity and remanence) in comparison to the curves of IONPs obtained in water dispersion. Note that the variation of the loop areas for IONP dispersed in water compared to the ones inside cells is more pronounced for the larger nanoparticles size (DC7). This is clearly reflected in the magnetic SAR values obtained from the AC hysteresis loops, which change from 40 ± 2 W/g in ddH_2O to 36 ± 1 W/g in cells for FM-CT2 sample (i.e. 10% reduction), and from 76 ± 4 W/g in ddH_2O to 38 ± 1W/g in cells for DC7 sample (49% reduction). Thus, the larger nanoparticles (i.e. DC7) show a more remarkable reduction of the magnetic heat losses, while the smaller particles size (FM-CT2) almost maintain their SAR value.

Noticeably, the ability to dissipate heat of both IONPs in the cellular environment is preserved.

Recent works report on experiments with cells cultures where negligible macroscopic temperature rises were observed.[48,92,93] This limited temperature enhancement raises fundamental questions as to whether MNPs should be discounted as an efficient source of thermal stress in live cells, despite the observation of a significant reduction of cell viability. Different apoptotic inductive phenomena, such as lysosome and or/cell membrane permeabilization or mechanical stimulation have been suggested as alternative mechanisms for cell death instead of thermal stress.[94] By measuring the AC magnetization loops of IONPs under magnetic hyperthermia field conditions, our results reveal the existence of IONP magnetic losses and hence, heat dissipation inside the cells. Hence, the observation of no temperature rise in cell cultures could be related to their specific experimental conditions in these previous studies rather than to the removal of the intrinsic magnetic heating losses of IONPs inside cells[92]. For example, a very low IONPs concentration in the overall cell media volume, or strong thermal losses of the experimental set-up may hinder the observation of a significant temperature rise.

In order to monitor the IONPs internalization and conditions of the cells after the magnetic measurements, we reseeded one fifth of the cells employed in the magnetic measurements, recovering adherence after 12 hours. Immediately after, the cells were subjected to fixation, preparation and/or dying procedures, and visualized under suitable microscopy techniques (See methods section). Figure 5.2 shows a representative image set of the reseeded cells. In Prussian Blue images, we can observe characteristic perinuclear demilune halos around the cell nucleus in both IONP sizes incubated cultures, pointing to an intra-cytoplasmic internalization of nanoparticles and discounting appreciable IONPs precipitation phenomena (Figure 5.2ad).

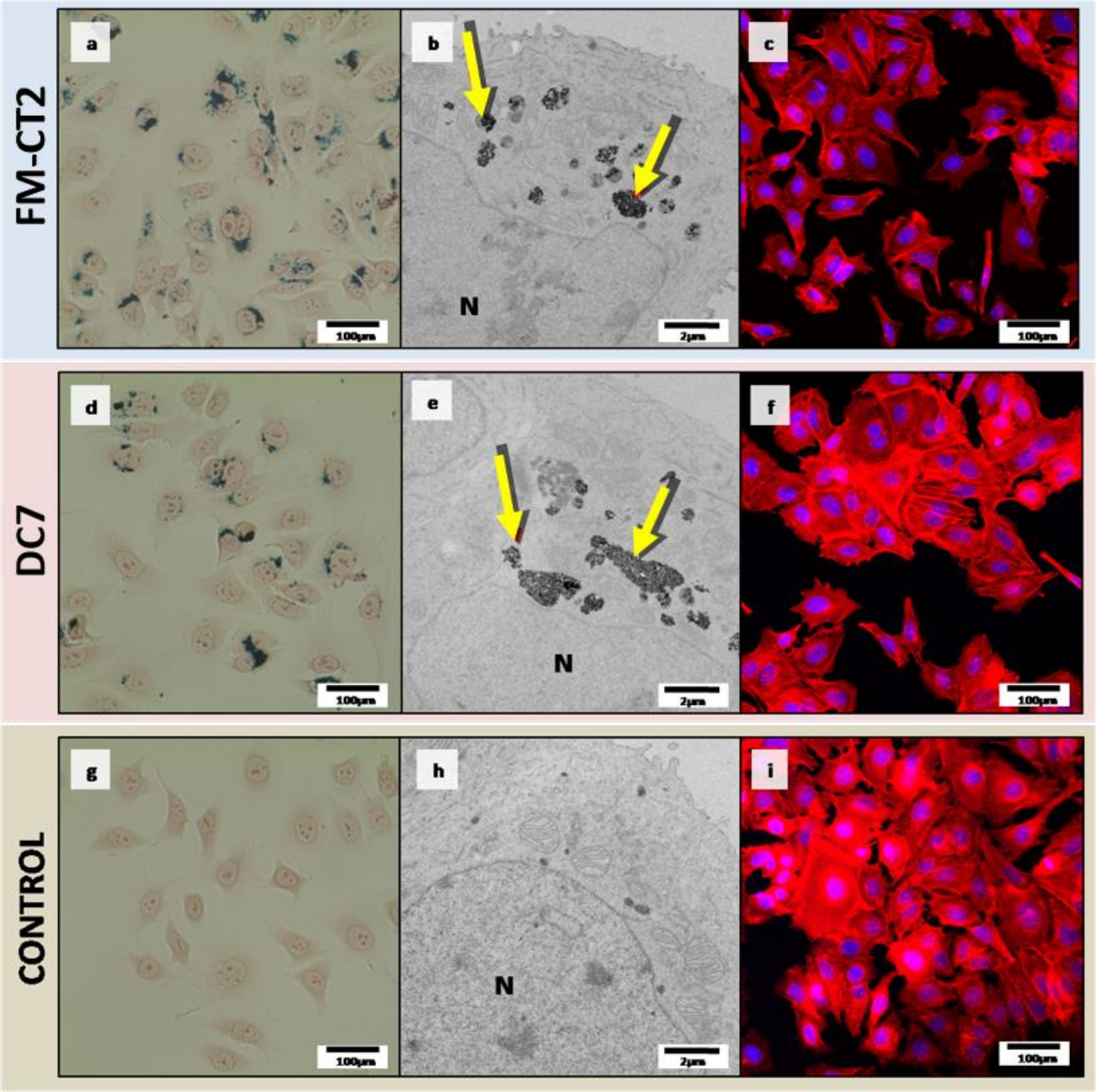

Figure 5.2**.** Representative micrographics of reseeded cells 12 h after AC magnetic measurements. ***a)d)g)*** Bright field images of Prussian Blue stained cells; scale bars 100 mm, ***b)e)h)*** Cells TEM section images; scale bars 2 mm; red arrows indicate the location of IONP. ***c)f)i)*** Cell 3D reconstructed confocal images ; scale bars 100 mm. Cells were stained with DAPI (blue) for nucleus staining, and ActinRed© for actin staining.

Quantitatively assessed by ICP-MS on the non-reseeded cells fraction, both incubation cultures yielded comparable values of IONP internalization for both nanoparticle size: 28 pg_{Fe}/cell for 11 nm IONPs and 21 pg_{Fe}/cell for 21nm IONPs (See methods section). In cell TEM images (Figure 5.2bh), IONPs are mostly found in intra-cellular vesicles, confirming that the measured ACS and ACM signal do not arise from IONPs located outside of cells. In particular, images evidences massive aggregation of IONPs in the cell vesicles, as also reported elsewhere.[1] The typical sizes of subcellular vesicles (several hundreds of nanometers) where IONPs are located reflect the clustering effects when IONPs transit across the cytoplasm. Such cluster sizes represent a huge increase in the degree of aggregation with respect to the IONP clusters formed in water which have hydrodynamic sizes (D_H) of 50 nm and 67 nm for FM-CT2 and DC7, respectively (See Annex I). Finally, we evaluated the cell morphology by using 4',6-diamidino-2-phenylindole (DAPI) and ActinRed© dying for visualization under confocal microscopy (Figure 5.2ci); as well as staining-free under bright field microscopy (Figure 5.3). Images show well-spread cells which are free from morphology aberrations, whilst live/dead staining confirmed cell viability (Figure 5.4). In this regard, cells are kept at room temperature (25ºC) for 5 minutes and exposed to magnetic hyperthermia field during a short period of time during the AC hysteresis loops measurements (< 5 s) for the sake of preserving cell viability.

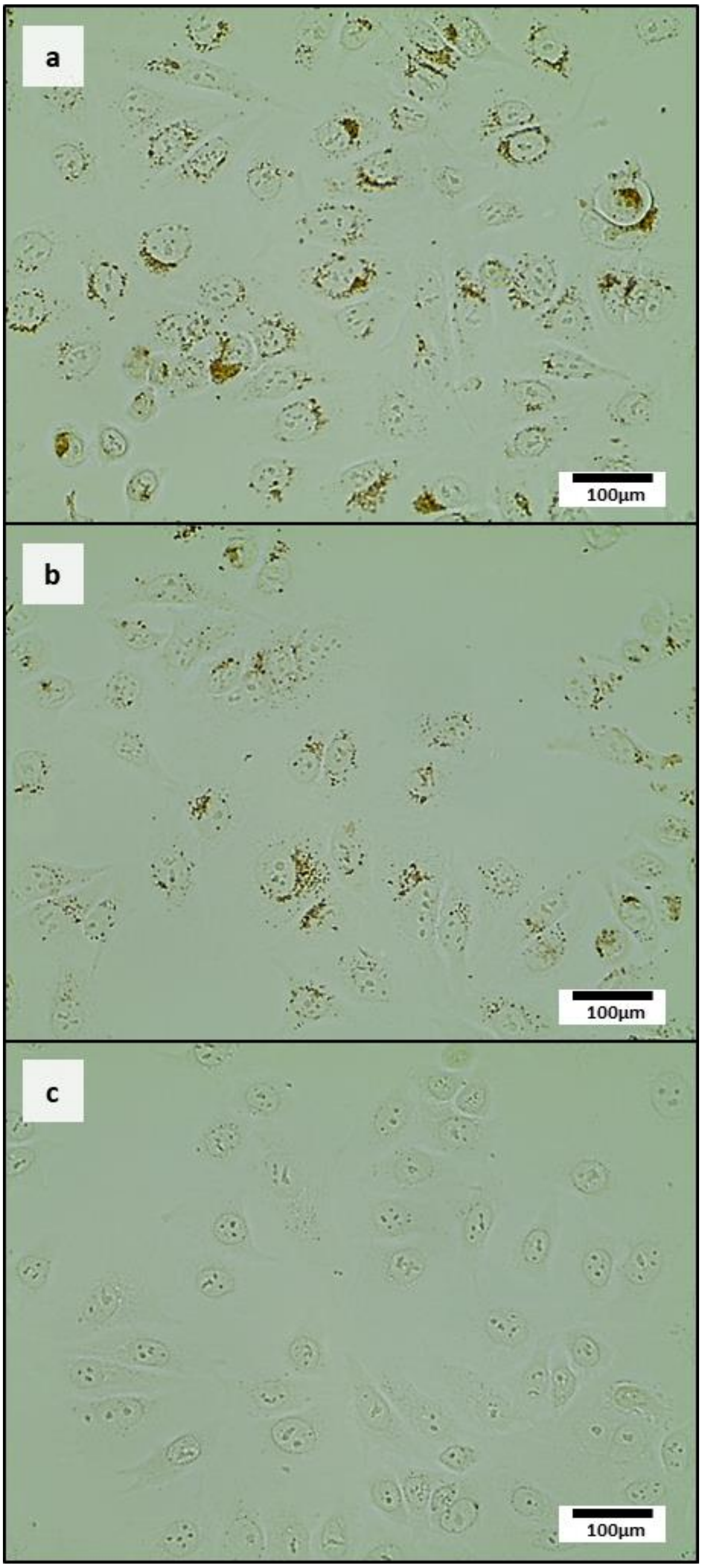

Figure 5.3. Bright field images of fixed MCF-7 cells; scale bar 100 mm. **a)** FM-CT2 IONPs incubated cells, **b)** DC7 IONPs incubated cells. **c)** Cells with no particles.

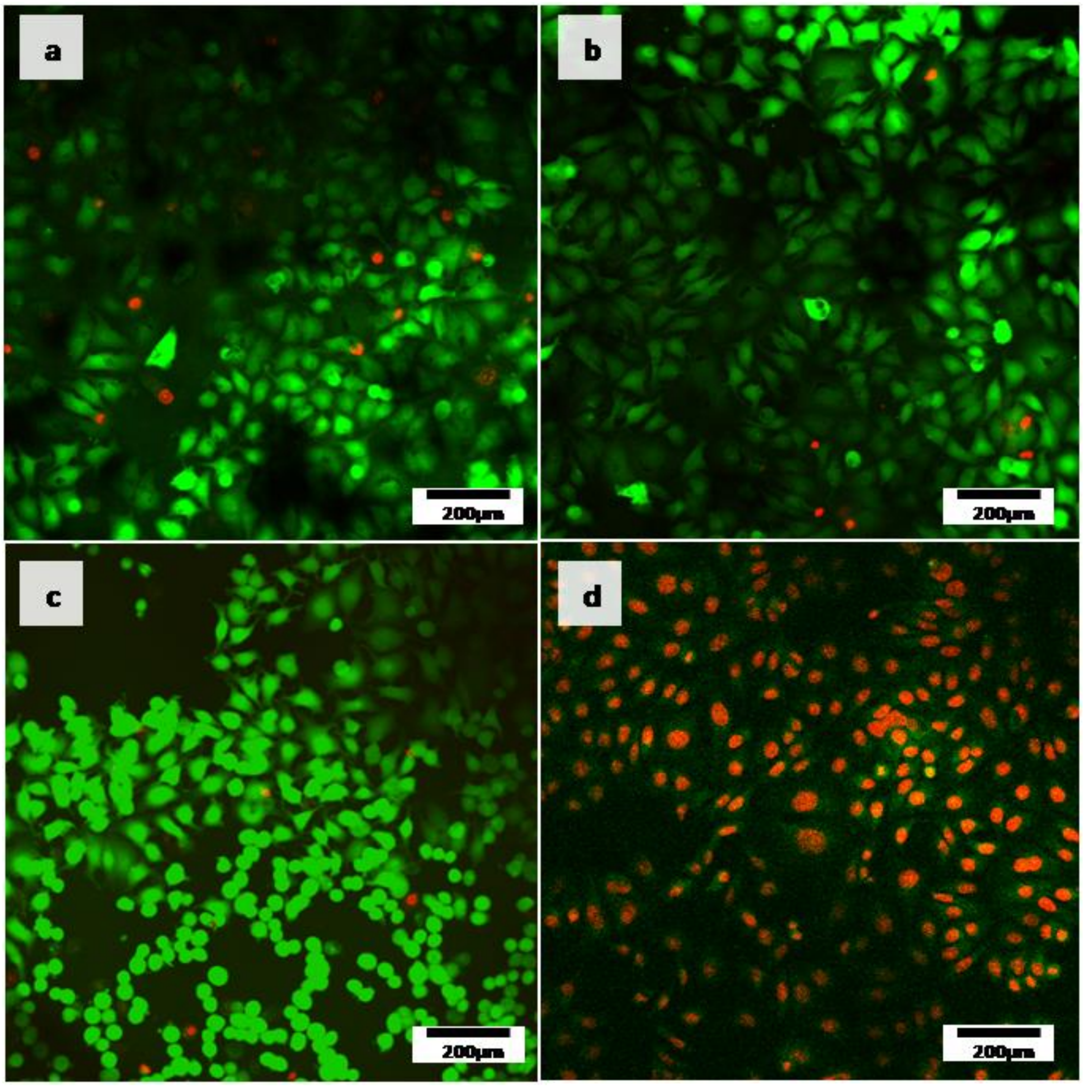

Figure 5.4. LIVE/DEAD® viability/cytotoxicity (calcein AM/ethidium homodimer-1) test microscopies under confocal microscopy; scale bar 200 mm, 12h after the magnetic measurements and their reseed. Red colour indicates membrane permeabilization and cell damage. a) FM-CT2 incubated cells. b)DC7 incubated cells. c) cells with no particles. d) cells intentionally attacked with methanol as positive control.

The results described above indicate that the influence of the cellular environment on the dynamical magnetization response of IONPs has a common effect on ACM and ACS, whilst being more pronounced for the larger IONPs size (DC7). These observations suggest that similar underlying mechanisms are responsible for the variation of the magnetization dynamics after the IONPs internalization in live cells. Therefore, to better understand such effects on the dynamic magnetic response of IONPs, we developed a methodology aiming to determine the effects of cell internalization on the magnetic heat losses of magnetic nanoparticles. This methodology is based on the assessment of the dispersion medium viscosity and IONPS aggregation effects on the ACM and ACS measurements of MNPs dispersed in aqueous solutions.

5.3. Influence of viscosity on the dynamical magnetic response of IONPs

To assess the environmental viscosity effects on the dynamical magnetic response of the studied IONPs, we performed ACM and ACS measurements of IONPs dispersed in aqueous media with an increasing glycerol fraction for raising viscosity (η). The highest η value of the used viscous dispersions is comparable to that determined inside intracellular vesicles according to recent studies (Table 5.1). [2,95]

Table 5.1. Glycerol/water mixed media employed for the viscosity studies of the IONP dynamical magnetic response. The experimental viscosity values at 37ºC were extrapolated from *Viscosity of Glycerol and Its Aqueous Solutions. Industrial and Engineering Chemistry. 43, 9. 2119.*

Glycerol	**Viscosity (MPa s)**	
(% v_{Gly}/v)	**25 ºC**	**37 ºC**
0	0.9	0.7
15	1.3	0.9
36	2.7	1.2
60	14	3.2
81	47	31

Prior to the magnetic characterization of the different IONPs dispersions, we assessed, in a similar manner than in Chapter 4, the possible aggregation phenomena on the IONPs induced by the addition of glycerol to the dispersion media. Figure 5.5 shows the hydrodynamic size distribution in water and at the maximum allowed glycerol fraction in DLS measurements (36% v_{Gly}/v) are presented for both IONPs sizes. Here, D_H distributions do not show significant variations when glycerol is added to the dispersion when compared to their water dispersion counterparts.

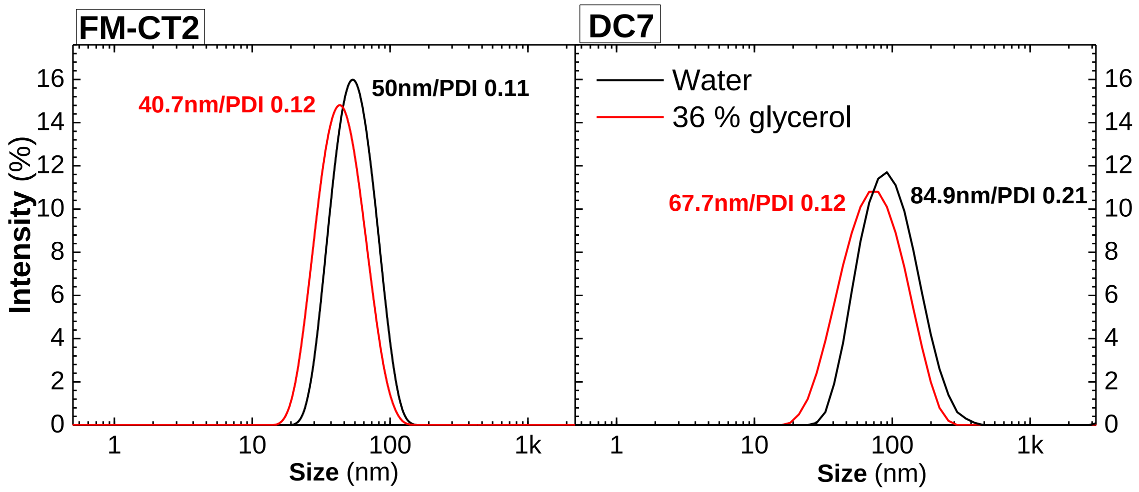

Figure 5.5. Hydrodynamic size distribution suspensions for FM-CT2 and DC7 dispersed in water and 36% glycerol (v_{Gly}/v). Z-average and PDI values are included inside the graphs.

Figure 5.6 shows ACM and ACS measurements of FM-CT2 and DC7 IONPs dispersed in media with different viscosity. AC hysteresis loops of FM-CT2 IONPs (Fig. 5.6a) present no significant variation when increasing medium viscosity, maintaining the hysteretic area (A) along the studied viscosity range (Figure 5.7a).

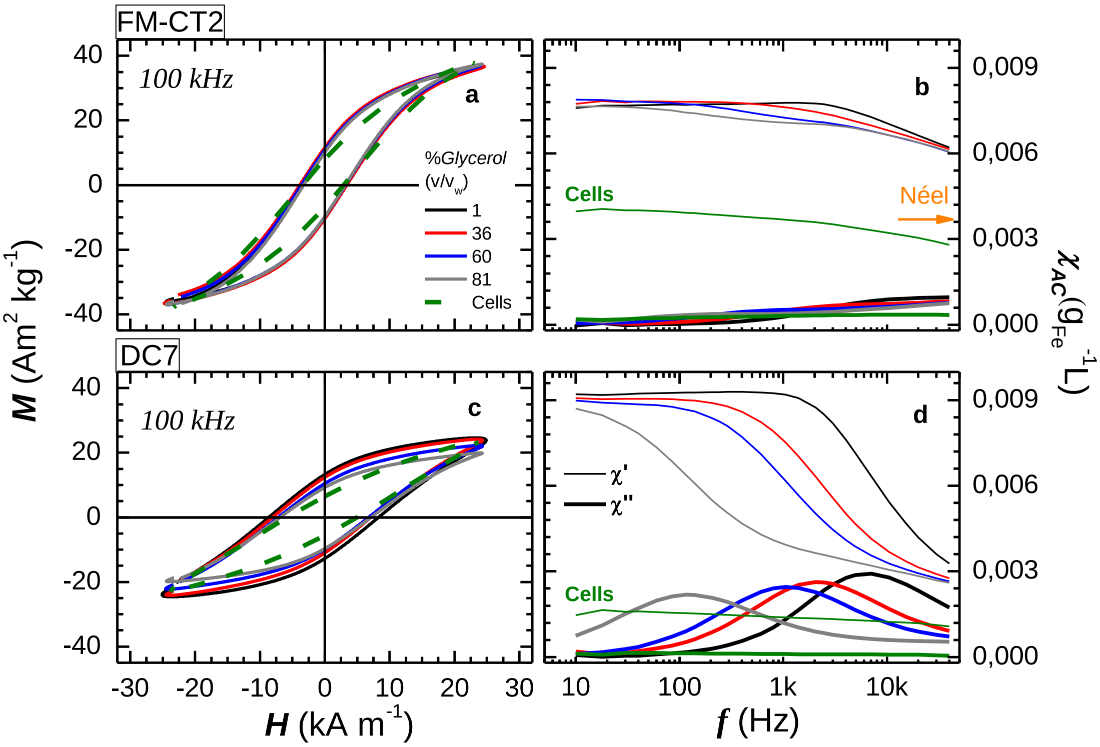

Figure 5.6. Viscosity dependence of AC hysteresis loops under H_{AC} 100 kHz and 20 kA/m of **a)**FM-CT2 (11nm core), **c)**DC7 (21nm core); viscosity dependence of AC susceptometry of **b)**FM-CT, **d)**DC7. Green lines correspond to magnetic measurement performed on IONPs inside live cell. The iron content was $1g_{Fe}/L$ for all data, except for DC7 IONPs inside live cell ($0.7g_{Fe}/L$).

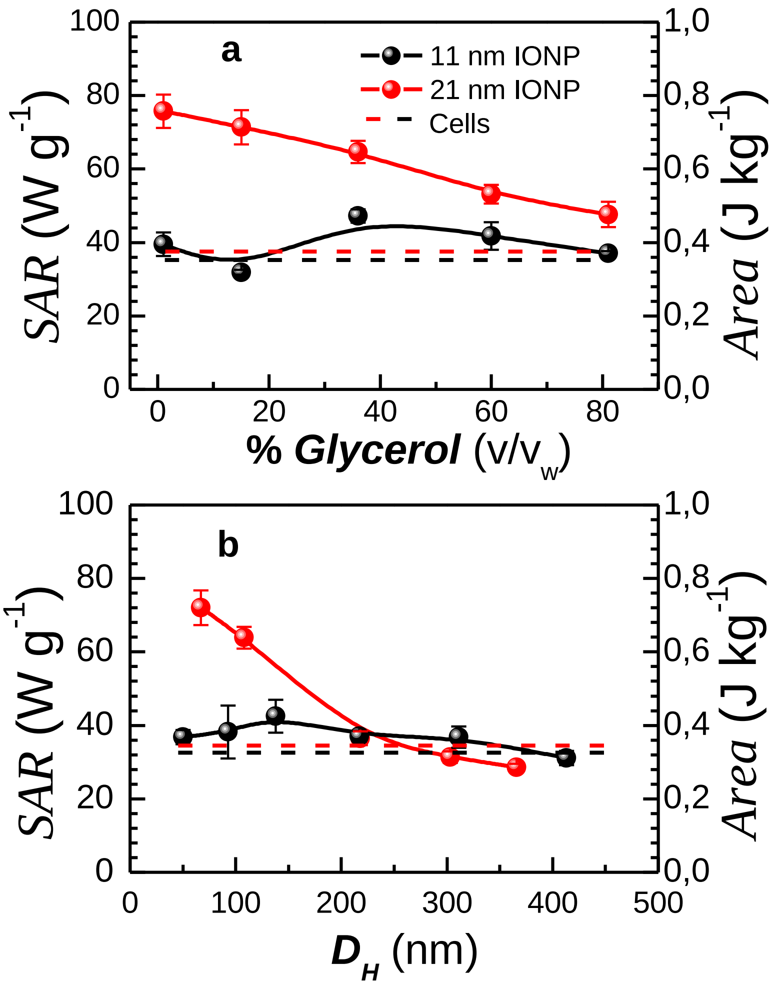

Figure 5.7. Specific Absorption Rate (SAR) and hysteresis loops area (A) dependence versus a) glycerol fraction (v/v$_w$), b) IONP hydrodynamic size (D_H). Dashed lines corresponds to the measurements of IONPs inside live cell. The iron content was 1g$_{Fe}$/L for all data, except for 21nm IONPs inside live cell (0.7g$_{Fe}$/L).

In addition, ACS measurements show little changes for FM-CT2 sample when medium viscosity increases (Figure 5.6b). We assign such independence from the environmental viscosity of the dynamical magnetic response of FM-CT2 to the predominance of the Néel relaxation mechanism in this sample.

Conversely, the dynamical magnetic response of 21 nm IONPs (DC7) is submitted to a stronger influence of medium viscosity. Figure 5.6c shows AC magnetization loops, where the loop of the area (A) reduces up to 37% of the loop area (A) when viscosity has values comparable to those reported into cell vesicles.[2] Consequently, heating losses (i.e. SAR values) similarly shrink from 76 ± 4 to 48 ± 3 W/g when η increases (Fig. 5.7a). Simultaneously, ACS measurements (Fig. 5.7d) show a shift towards lower frequencies for the χ'' peak (f = 9 kHz in water) with increasing medium viscosity. We understand such experimental magnetic behavior in terms of the prevalence of Brownian relaxation process for the larger nanoparticles (DC7) in the range of studied viscosity values. Another interesting aspect of this set of ACS and ACM measurements is their distinct sensitivity to viscosity. ACS measurements are more sensitive to medium viscosity than ACM, an effect which can be assigned to the role of field intensity on the magnetization dynamics[61,88]. In fact, maximum field intensity (H_{MAX}), which differs by more than two decades in the case of ACS and ACM measurements ($H_{MAX} \sim 0.04$kA/m and in 20kA/m, respectively), modulates the dynamical magnetic response of IONPs, mostly due to the appearance of a magnetic torques [40,61,88] and the competition between different modes (magnetic or viscous) of heat losses depending on the H_{max}/H_K ratio (where H_K is the anisotropy field)[39] on which the measurements are performed.

In any case, it is worth noting that the trend observed in the ACM and ACS measurements at different η are significantly far from the results observed in live cells for both IONPs. In Figure 5.8, the characteristic magnetic parameters of hysteresis loops (i.e. A, M_R, H_C and M_{MAX}) extracted from Figure 5.6ac are shown. Here, we can appreciate strong differences from the same parameters obtained in cell internalized IONPs for 21 nm nanoparticles (DC7) and to a lesser extent for the 11 nm nanoparticles. (FM-CT2).

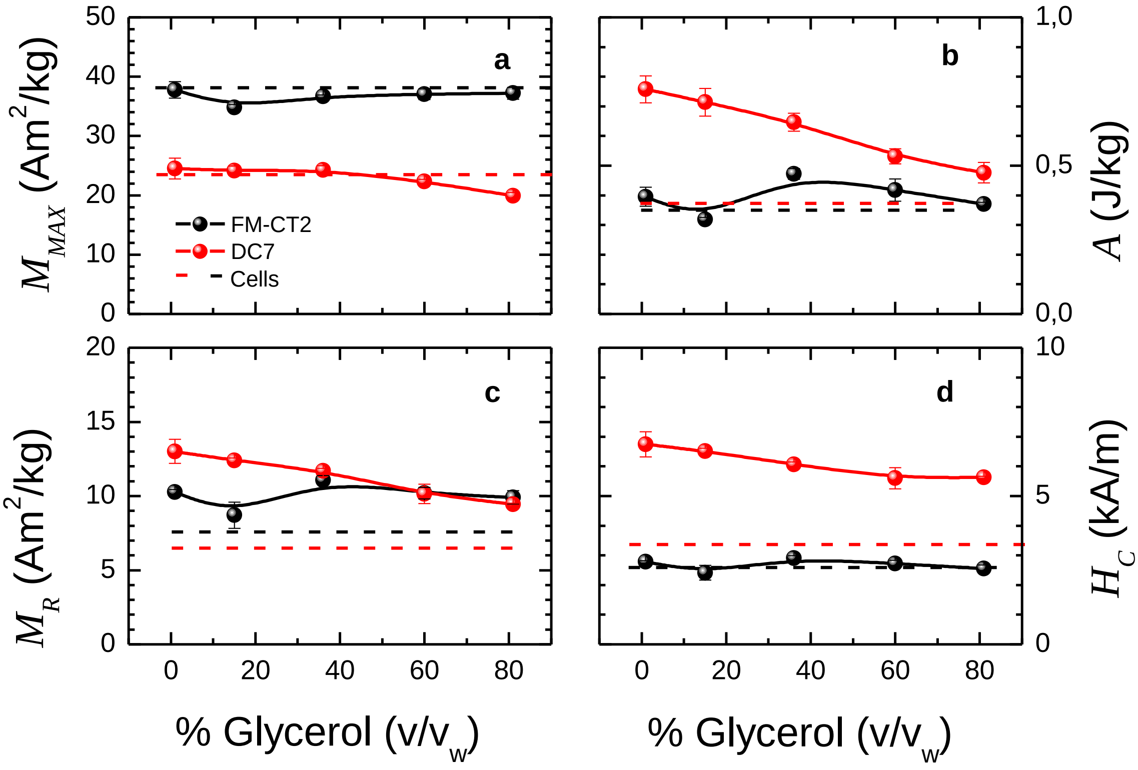

Figure 5.8. Viscosity dependende of magnetic parameters obtained from Figure 3 for FM-CT2 (11nm core) and DC7 (21nm core) at increasing glycerol fraction (%v/v$_w$) a) M_{MAX}, b) A c) M_R , d) H_c. Red and black dashed lines are the corresponding values extracted from magnetic measurements inside cells from Figures 1ac.

Analogously, ACS measurements clearly show significant discrepancies with respect to measurements of IONPs in live cells at the highest medium viscosity values. The real part values of the susceptibility (χ') measured for both IONPs sizes at the highest medium viscosity (η) are far from those measured when internalized in cells, although the maximum η values are comparable to the ones reported in cell vesicles.[50] Regarding the imaginary part of the susceptibility (χ''), measurements of IONPs at the largest medium viscosity value and inside cells seem to be far from overlapped, especially inside the ~5-50kHz range. In the case of the larger nanoparticles instead, we can clearly observe that the Brownian peak, displaced to ~100Hz due to the enhancement of medium viscosity, is far from reaching a flat profile shown for IONPs inside cells. Thus, although the variations of η leads to modifications on the dynamical magnetic response of the studied IONPs, such viscosity increase do not qualitatively replicate the magnetic response measured in cells. Hence, we alternatively assessed the effects of increasing nanoparticles aggregation on the dynamical magnetic response of IONPs.

5.4. Influence of aggregation on the dynamical magnetic response of IONP

In order to probe the role of nanoparticle aggregation on the dynamical magnetic response, we carried out ACM and ACS measurements of IONPs with hydrodynamic sizes (D_H) up to 400 nm in aqueous dispersions (protocol is described in methods section). The IONP hydrodynamic size (D_H) values of the studied IONP aggregates are in the range of the vesicle sizes where MNPs are located following their transit across the cytoplasm after cell uptake.[5] Figure 5.9 shows ACM and ACS measurements performed for aqueous dispersions of FM-CT2 (11nm core) and DC7 (21nm core) IONPs at different D_H sizes. Here, we can corroborate that the AC magnetic response is significantly tuned by the IONP aggregation, in agreement with recent observations which shows the effects of magnetic dipolar interactions on altering the AC hysteresis loops.[60]

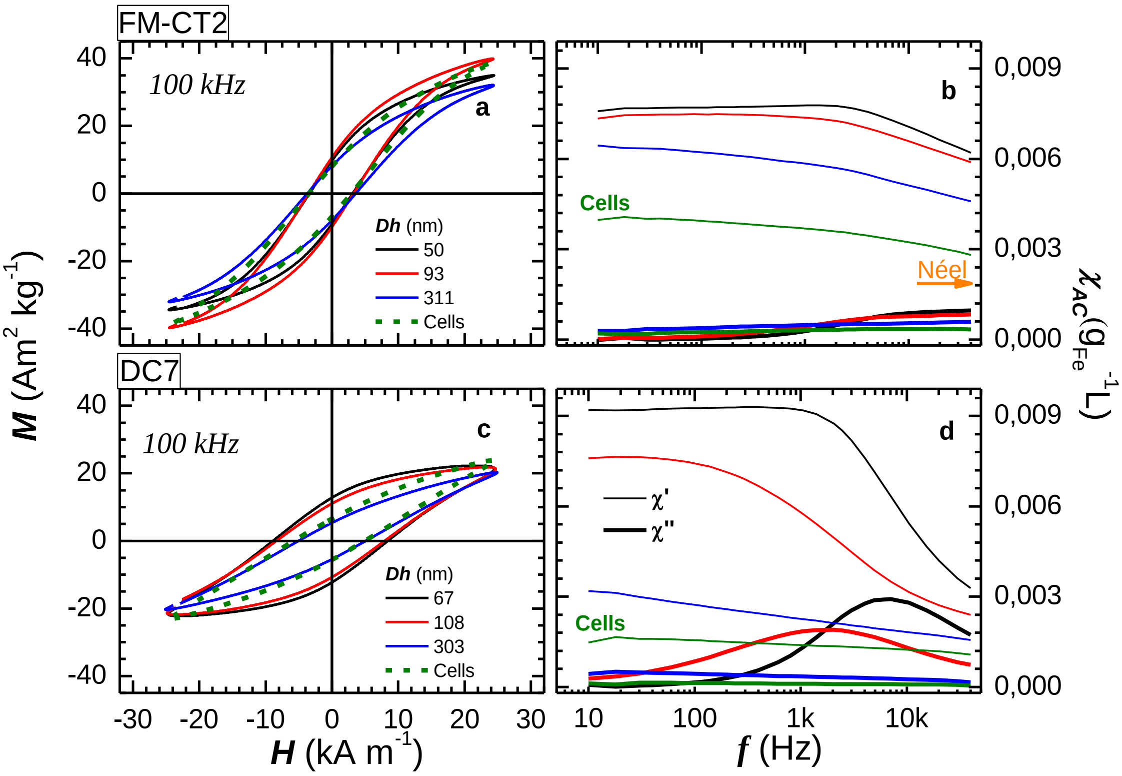

Figure 5.9. Aggregation dependence of AC hysteresis loops under H_{AC} 100 kHz and 20 kA/m of **a)** FM-CT2 (11 nm core), **c)** DC7 (21 nm core) dispersed in ddH$_2$O. Aggregation dependence of AC susceptometry curves of **b)** FM-CT2, **d)**DC7 dispersed in water at different hydrodynamic size. Green lines correspond to the magnetic measurement performed in IONPs inside live cell. The iron content was *1*g$_{Fe}$/L for all data, except for DC7 inside live cell (0.7g$_{Fe}$/L). Dashed lines in **b)** and **d)** indicate the H_{AC} frequency employed in AC hysteresis loops measurements.

Indeed, considering the trend obtained in ACM and specially ACS measurements for both IONPs, a convergence towards the measurements in cells can be found. Figures 9ac shows that the AC hysteresis loops of FM-CT2 and DC7 IONPs significantly vary in shape with increasing D_H, although to a different extent depending on particle size. The changes are again more pronounced for the larger IONPs (DC7). This phenomenology is even more evident when the AC hysteresis loops are M_{MAX} normalized (Figure 5.10).

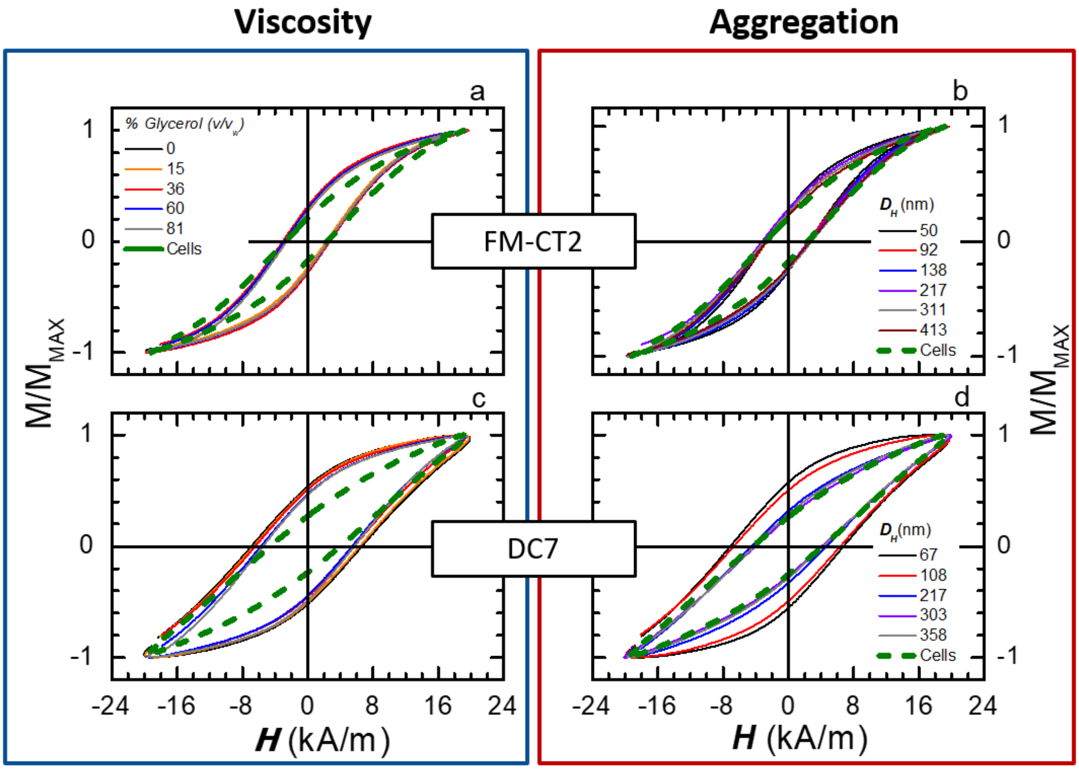

Figure 5.10. Viscosity (blue frame) and aggregation (red frame) dependence of normalized AC magnetization loops at 100 kHz and 18 kA/m. a)b) FM-CT2 (11nm core). c)d) DC7 (21 nm core). Green lines correspond to the magnetic measurement performed in IONPs inside live cells. The iron content was 1g_{Fe}/L for all data, except for DC7 inside live cells (0.7g_{Fe}/L).

Whereas the increase of the medium viscosity does not lead to important variations into the AC hysteresis loops measured in cells (Figure 10-blue frame), IONPs aggregation increase provoke the apparition of loops with similar shape than these ones measured in cells (Figure 5.10-red frame). Regarding SAR, the corresponding reduction of values is lower than 10% for the smaller IONPs (FM-CT2): from 40 ± 2 W/g at D_H=50 nm to 37 ± 3W/g at D_H=311 nm. Indeed, magnetic heat losses remain roughly constant for the 11 nm IONPs in the studied D_H size range (Fig. 5.7b). However, SAR values of larger IONPs (DC7) significantly shrink ~60% from 76 ± 4 W/g at D_H=67 nm to 31± 2 W/g at D_H=303 nm. This reduction is considerably larger than the one obtained when varying viscosity. As shown in Figure 5.11, the underlying reason for such reduction in loop area and consequently SAR lies in a generalized decrease of M_R and H_C in the magnetization loops, and to a lesser extent of M_{MAX}. Most significantly, all characteristic features of the AC hysteresis loops (i.e. *A*, M_R, M_{MAX}, and H_C) achieve values close to those observed in live cells at the largest D_H values.

All characteristic features of the AC hysteresis loops (i.e. *A*, M_R, M_{MAX}, and H_C) achieve values close to those observed in live cells at the largest D_H values (Figure 5.11). The increase of intra-aggregate magnetic dipolar interactions while increasing D_H can explain such magnetic behavior , as recently reported.[60]

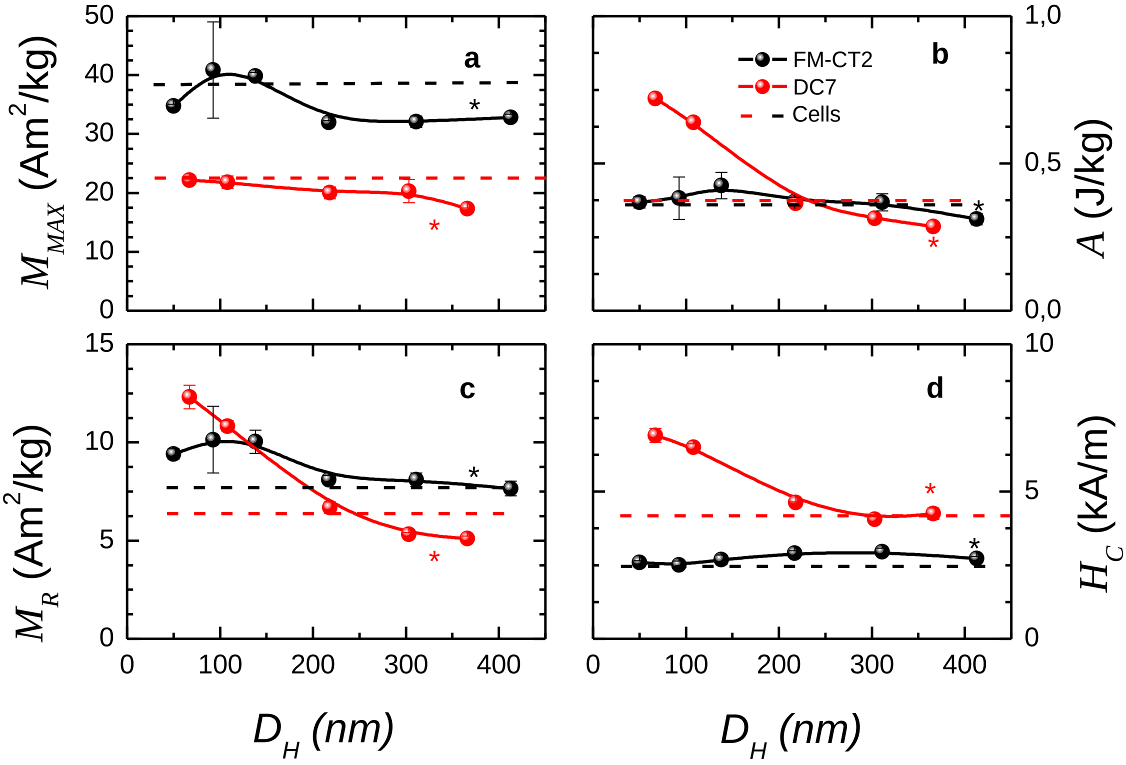

Figure 5.11. Aggregation dependende of magnetic parameters obtained from Figure 9 for FM-CT2 (11nm core) and DC7 (21 core) at different viscosities. a) M_{MAX}, b) A c) M_R , d) H_c. Red and black dashed lines are the corresponding values extracted from magnetic measurements inside cells from Figures 1ac. *Values obtained under unstable colloidal conditions.

In addition, ACS measurements significantly change when increasing D_H. Figure 9b shows that for FM-CT2, the Brownian peak on the ACS imaginary part shifts towards lower frequencies when increasing D_H, similarly to the case of increasing η. We understand this behavior in terms of the variation of the hydrodynamic volume, which modulates Brownian relaxation time in a similar way to η. However, in contrast to the small changes observed with increasing viscosity, noticeable changes of the ACS real part are observed when increasing D_H. In particular, the decrease of χ' values resembles the ACS results measured for IONPs inside live cells (Figure 5.9b –solid green lines). Similar effects are observed for the larger IONPs (DC7), where the ACS imaginary part shows a progressive broadening and shift of the Brownian peak at 9 kHz towards lower frequencies when D_H increases (Figure 5.9d). Again, χ' and χ'' show a trend with D_H that matches the observation in live cells (solid green line), suggesting that both studied phenomena (i.e. IONPs aggregation and cell internalization) lead to similar effects on the dynamical magnetic response of the IONPs.

In order to quantify the experimental observations discussed above, Dr. Annelies Coenne, Dr. Jonathan Leliaert and Dr. Luc Dupré performed numerical simulations based on: i)a least-squares fit routine to match generalized Debye equations to ACS measurements using a trust region reflective algorithm, ii) micromagnetic simulations of the AC hysteresis loops, by solving the stochastic Landau–Lifshitz–Gilbert (LLG) equations using Vinamax software.[96] Both numerical models included the magnetic dipolar interactions among IONPs for describing the dynamical magnetic response of IONPs when increasing aggregate size, but using different approaches (see methods section).

Simulations precisely and quantitively reproduce the ACS measurements of IONPs dispersed in water (see dotted lines in Figures 5.1ab) by using fitting parameters whose values are close to experimental ones. The effective anisotropy values (K_{eff}) equal to 4.7 kJ/ m^3 for 11nm and 21 nm are much lower than in bulk iron oxides (Table 5.2 and 5.3), but close to the values estimated from the K_{eff} value derived from the Stoner-Wohlfarth model ($K_{eff} = H_C \cdot M_S/2$) using experimental SQUID measurements (Figure 5.12) at low temperatures (10 K): $K_{eff} = 4.7$ and 4.2kJ/m^3 for for FM-CT2 and DC7, respectively.

Table 5.2. Fitting viscosity (η) and effective anisotropy (K_{eff}) values employed in AC susceptibility simulations of the viscosity ACS measurements.

11 nm core size IONPs

Glycerol (%v_{Gly}/v)	η (mPa s)	K_{eff} (J m^{-3})
0	0.7	4.7
15	2	4.9
36	4.5	4.6
60	14.6	4.7
81	55.8	4.8

21 nm core size IONPs

Glycerol (%v_{Gly}/v)	η (mPa s)	K_{eff} (J m^{-3})
0	0.7	4.7
15	1.2	4.7
36	2.7	5.1
60	5.4	5.2
81	45	5.3

Table 5.3. Experimental values (FBS fraction, z-average, number D_H and PDI) and adjusted parameters (number D_H, effective anisotropy (K_{eff}) and PDI) employed in AC susceptibility simulations of the viscosity ACS measurements.

11 nm core size IONPs

FBS (% v_{FBS}/v)	z-average (nm)	Number DH (nm)	Simulated Number D_H (nm)	PDI	Simulated PDI	Simulated Keff (kJ m-3)
0	50	34	25	0.1	0.1	4.7
2	93	93	60	0.3	0.2	4.3
6	138	185	92	0.6	0.3	4.3
12	217	209	112	0.8	0.3	3.4
24	311	245	120	0.9	0.3	3.4
47	413	254	115	1*	0.3	3.4
CELLS			262		0.3	2.9

21 nm core size IONPs						
FBS ($\%v_{FBS}/v$)	**z-average (nm)**	**Number D_H (nm)**	**Simulated Number D_H (nm)**	**PDI**	**Simulated PDI**	**Simulated K_{eff} ($kJ\ m^{-3}$)**
0	67	33	40	0.2	0.3	4.7
3	108	40	75	0.4	0.3	5
8	218	94	91	0.5	0.4	4.9
15	303	265	187	0.7	0.5	2.4
31	358	252	170	1*	0.5	2.1
CELLS			206		0.5	1.8

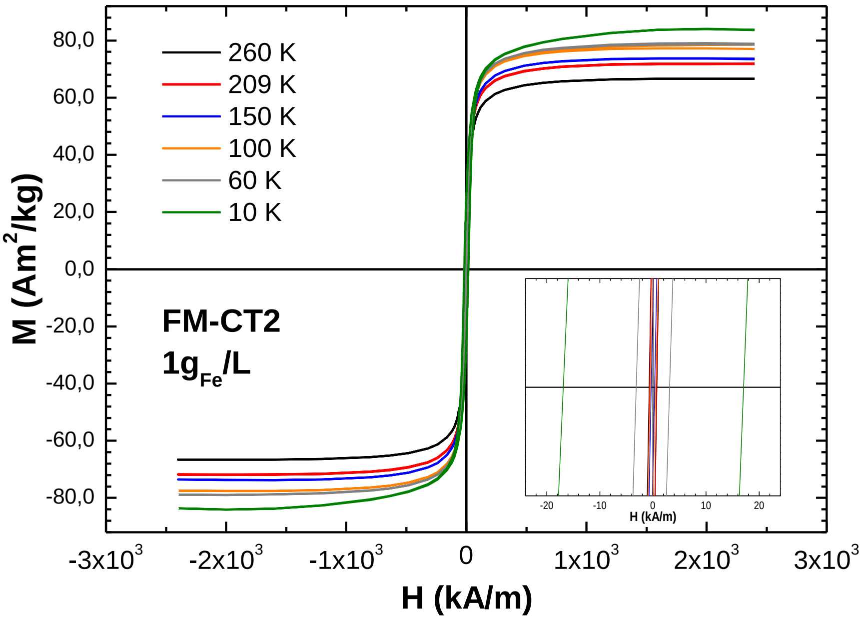

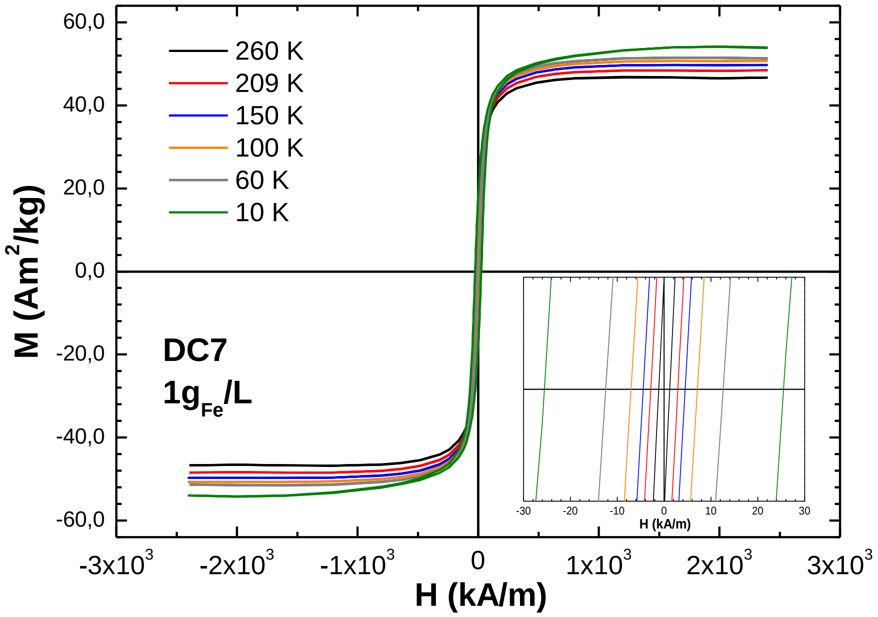

Figure 5.12. SQUID measurements of 11nm and 21nm IONPs dispersed in water solutions at $1g_{Fe}$/L at different temperatures. Inset: Zoom area in the low field region.

They agree with recently reported K_{eff} values of similar magnetic nanoparticle samples under AC magnetic field conditions[97-99]. Furthermore, the slight particle aggregation already existing in water dispersions for both IONP sizes (Z- average hydrodynamic sizes = 50 and 67 nm for 11and 21 nm, respectively) could also explain the low K_{eff} values in comparison to bulk maghemite. In cells, ACS fits obtained for the same IONPs indicate that K_{eff} values noticeably diminish to from 4.7 to 2.9 kJ/m^3 for 11 nm and from 4.1 to 1.8 kJ/m^3 for 21 nm IONPs. Hence, the influence of cell uptake on the ACS response is to drastically reduce K_{eff} values, independently of nanoparticle size. In addition, the AC hysteresis loops of FM-CT2 sample in water dispersion and inside cells were also simulated (Figure 5.1c). Interestingly, the K_{eff} reduction observed when IONPs are inside cells is in good agreement with the simulation of the AC magnetization loops, since micromagnetic fitting requires a reduction of K_{eff} from 3.4 kJ/m^3 (in water) to 2.9 kJ/m^3 (inside live cells).

To understand the underlying mechanisms behind the suppression of K_{eff}, we performed ACS simulations considering variations of medium viscosity and IONPs aggregation (and in consequence, magnetic dipolar interactions) (Figure 5.13). From the modelling of the viscosity data set, the fitting parameters of IONPs extracted from water ACS data (Table

5.2) were tested. Additionally, the fit of IONPs aggregation ACS data set provides significant information for understanding the influence of cell uptake on the dynamical magnetic response of the studied IONPs, as shown in Figure 5.14. The ACS and ACM aggregation data series show a trend that merges to the IONP results measured in cells, for both IONPs size. In this case, the numerical simulation of the ACS measurements describes a decreasing tendency of K_{eff} concomitantly related to the increase of D_H and polydispersity (Table 5.3). On one hand, the increase of D_H implies larger hydrodynamic volume (V_H), which modulates the Brownian relaxation time ($\tau_B = \frac{3\eta V_H}{k_B T}$), and therefore shifts the Brownian peak of χ'' to lower frequencies. On the other hand, the increase of aggregation degree favor the magnetic dipole-dipole interactions, which can be simplified as resulting in the influence of the K_{eff} value, and consequently, the Néel relaxation time ($\tau_N = \frac{\sqrt{\pi}}{2\sqrt{K_{eff}V/k_B T}}\tau_0 e^{-K_{eff}V/k_B T}$).[60]

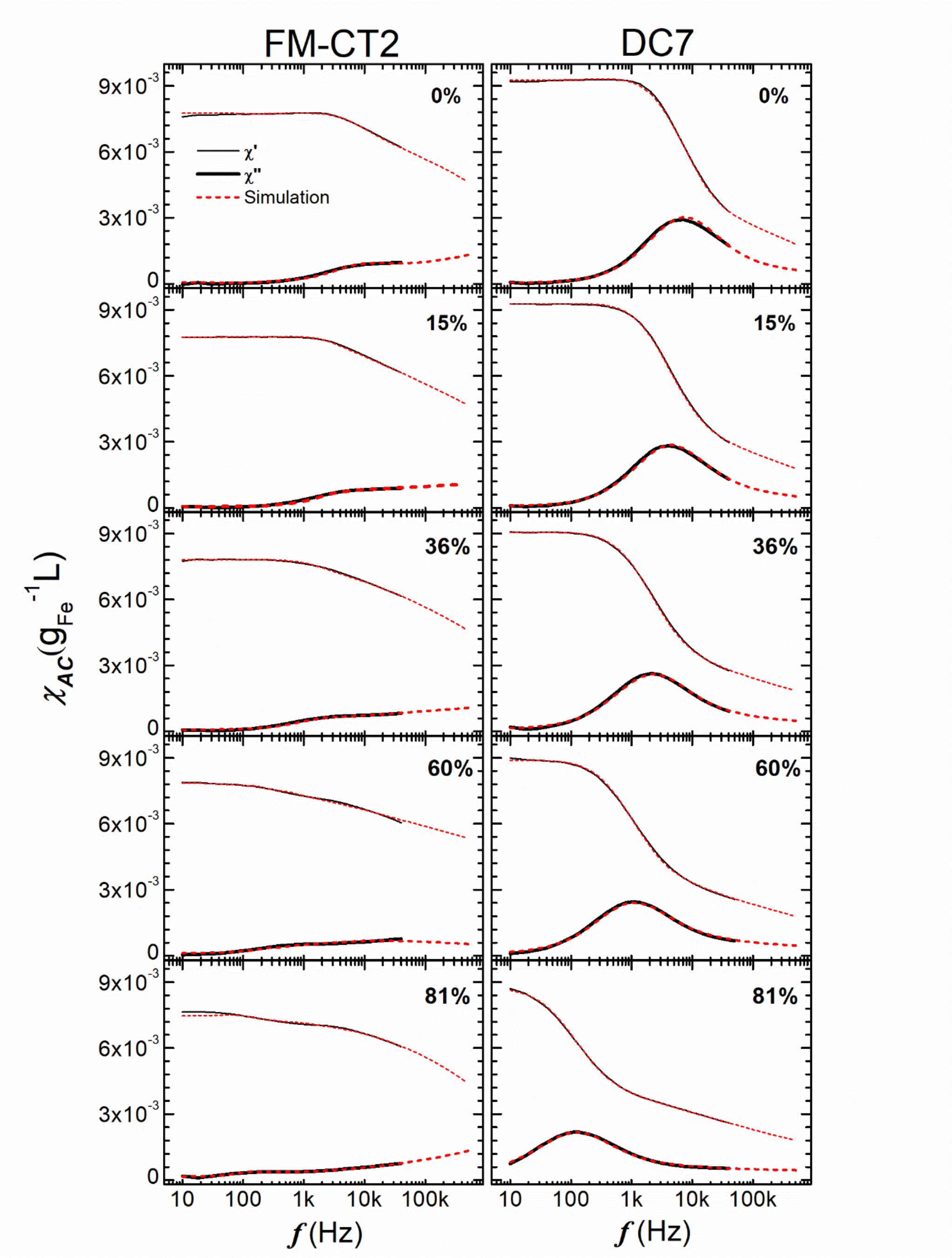

Figure 5.13. Extended experimental and simulated AC susceptibility data at different glycerol fractions (% v/v$_w$) of FM-CT2 and DC7 samples. Percentage correspond to the glycerol fraction (% v/v$_w$) used in the dispersion.

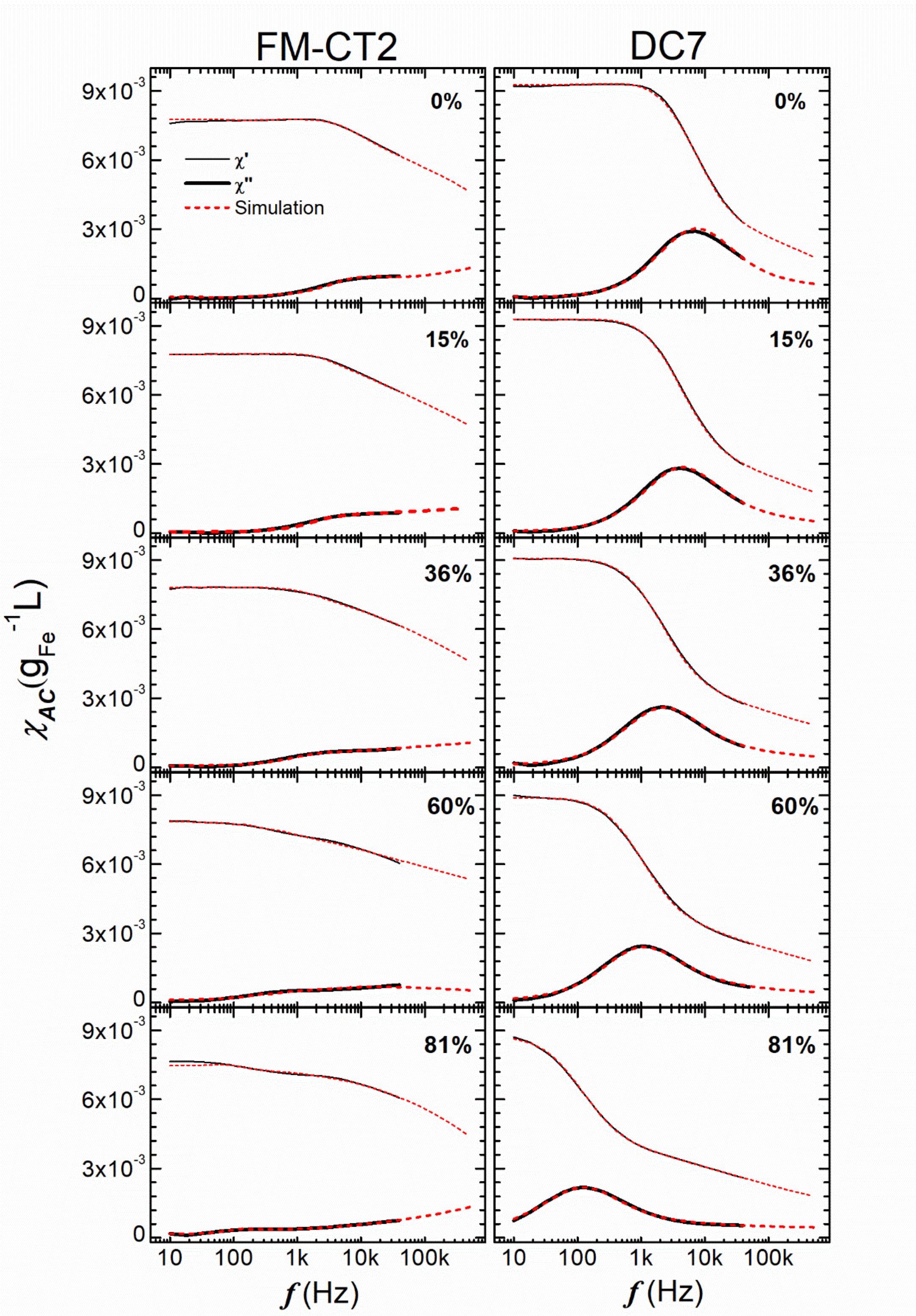

Figure 5.14. Extended experimental and simulated AC susceptibility data at increasing hydrodynamic size (D_H) and inside cells of FM-CT2 and DC7 samples. Numbers inserted in graph correspond to experimental z-average values.

The assumptions employed for modeling ACM and ACS results -*i.e.* variations in V_H and K_{eff}, the later mediated by magnetic dipole-dipole interactions- lead to a good agreement of numerical simulations with the experimental results. It is worth to note the influence of the IONP aggregation increase on the dynamical magnetic response depending on the prevalent relaxation mechanism. The simulations point out that the increase of V_H mainly influences the magnetic response of the larger (21nm) IONPs via the Brownian relaxation time, which is highly sensible to changes in the hydrodynamic size. Otherwise, the variation of K_{eff} -related to magnetic dipole-dipole interactions- is required to model the aggregation dependence of ACS results for both IONP sizes (see Table 5.3). Additionally, the fitting parameter related to the size polydispersity index (PDI) of the aggregates increased in a similar way to the experimental values determined by DLS.

According to previous studies,[9,60] the role intra-aggregate magnetic dipole-dipole interaction on the dynamical hysteresis loops of IONPs was found to be highly dependent on the spatial arrangement of the nanoparticles inside the aggregate. Most of these studies correlate random MNP aggregates arrangements[100] with demagnetizing effects. This provides a qualitative explanation for the effects of aggregate size on the intra-aggregate interacting phenomena, and consequently on the K_{eff} value. At the limit of a high values of D_H, the number of local particle neighbors per aggregate increases, leading to no intrinsic preferential direction of the magnetic anisotropy to align with field orientation. Therefore, a decrease of energy barrier takes place, allowing that a part of the particle magnetic moments of the aggregate follows the external AC magnetic field. This results in the decrease of the area of the hysteresis loop and the lowering of the SAR. Besides, the number of local particle neighbors per aggregate at the limit of a low values of D_H is lower and hence, an intrinsic preferential direction of the magnetic anisotropy appears favored by its particular spatial arrangement.[101] Noticeably, cellular TEM images (Fig. 5.2 be) corroborates a random IONP intracellular agglomeration inside cells vesicles, reinforcing our hypothesis.

5.5. Conclusions

We investigated the influence of cell uptake of IONPs on their dynamical magnetic response by ACS and ACM. We set a suitable methodology for testing the influence of biological environments on the dynamical magnetic response, including magnetic heat losses of magnetic nanostructures based on viscosity and aggregation studies. The comparison of these measurements of IONPs between colloidally dispersed and in inside live cells point out that the intracellular IONP clustering favoring magnetic dipolar interactions provides the major contribution to the intracellular variation of the studied IONPs magnetic response rather than the immobilization. Indeed, AC magnetometry can probe the magnetic heat losses of IONPs inside live cells without affecting their viability. Furthermore, ACS measurements reveal that the influence of the cell internalization on dynamic magnetic response of IONPs depends on their size, environmental viscosity, and aggregation state. Numerical simulations support the conclusion that magnetic dipolar interactions taking place within randomly ordered IONP clusters, play a central role in the 50% decrease of magnetic heating losses observed when the 21nm IONPs were aggregated inside live cells. Understanding the phenomenology related to the intracellular nanoparticle transit and their effects on the MNPs response will allow the design of novel nanostructures whose dynamical magnetic response (i.e. magnetic heating losses and MPI signal) will remain invariable in any biological environments. Such achievement will favor the transfer of magnetic hyperthermia mediated by MNPs and MPI to clinics.

5.6. Methods

For IONPs aggregation studies, hydrodynamic size (D_H) raise were induced through the addition of increasing fractions of Fetal Bovine Serum (FBS) to the dispersion (See Table 5.3 for used FBS volume fractions). During the magnetic measurements, the hydrodynamic size of these dispersions was monitored in a Zetasizer 3000 using a quartz cuvette at a final concentration of $0.02g_{Fe}/L$.

Iron quantification

Iron quantification of IONP concentration in aqueous and cell dispersions were performed with ICP-OES and ICP-MS at Instituto de Ciencia de Materiales-CSIC, Ciudad Universitaria de Cantoblanco, Madrid (Spain). 25µL of iron oxide nanoparticles were digested in aqua regia (HNO3 + 3HCl) at room temperature under sonication and diluted 1:1000 in water. Cells were digested in acid media 36.6-38% HCl (Sigma) for 30 minutes under sonication at 40˚C. Afterwards, they were kept at room temperature overnight and finally diluted 1:1000 in water.

Cell culture experiments

Figure 15 presents a graphical summary of the experiments performed with cells is shown in. Around 1.5 million MCF-7 (HTB-22) breast cancer cells, purchased from the LGC Standards (Middlesex, UK); were seeded in T175 flasks DMEM (Sigma)supplemented with 10% FBS, 100 IU/ml penicillin and 100g/L streptomycin (Lonza) and 2 mM L-Glutamine (Lonza) was used as cell culture media. The cells were incubated at 37˚C in air atmosphere with 5% CO2. After 48 hours, the culture media were substituted for a suspension of 0.1g_{Fe}/L IONPs in fresh media for 24 hours. At this point, the cells were washed with PBS (Sigma) five times to remove all non-internalized IONPs, detached with trypsin (Lonza), pelletized and resuspended in 200 µL of supplemented media.

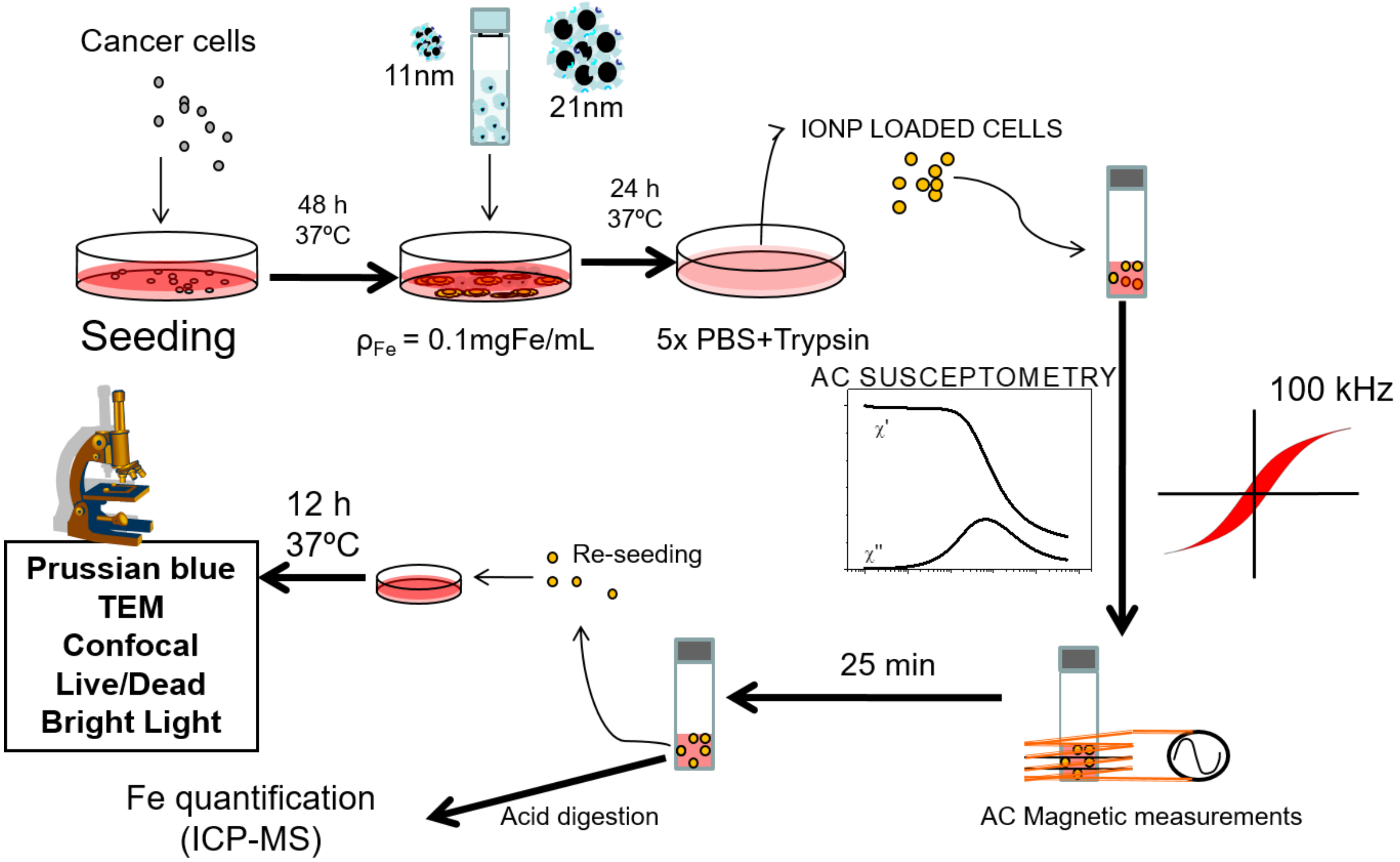

Figure 5.15. Graphical summary of the employed methodology for experiments with cells.

AC measurements (susceptometry and magnetometry) were performed immediately after. Once the measurements were finished, one fifth of the cell pellet was reseeded onto P35 plates, onto glass cover slide and directly onto 24-multiwell plates. After 12 hours, the cells became adherent and they were separated in 5 sets for microscopy studies. The rest of the cell suspensions were digested to quantify the iron content.

Prussian Blue Staining

Cells were fixed on 24-multiwell incubating with methanol for 15 minutes at room temperature. Next, the fixative was removed and the cultures were washed twice with ddH_2O. Then, the wells were treated with solutions of 20% aqueous solution of hydrochloric acid (v/v) and 10% of potassium ferrocyanide (w/v) (Sigma) for 20 minutes at room temperature. The washing step was repeated and the cell monolayers were treated with Nuclear Fast Red (Sigma) for 5 minutes. Finally, the wells were washed three times with ddH_2O and observed under inverted microscope (EVO) with bright field configuration. For staining-free cells, only fixation procedure was performed.

Confocal microscopies

Cells were fixed onto 24-wells cover slips via incubation with cold ethanol during 5 minutes at-20˚C. Next, the coverslips were washed twice with PBS and stained first with ActinRed® (Molecular Probes) and DAPI. Finally, the cover slips were mounted onto microscope slides and vertical micrographs sections with a 300nm step were taken with Olympus U-TBI 90 Microscope. For cell viability, cover slips with were treated with LIVE/DEAD® calcein AM/ethidium homodimer-1 viability/cytotoxicity kit (Molecular Probes™), mounted onto microscope slides and sealed with nail varnish.

Transmision Electron Microscopy

Transmission Electron Microscopy images of cell cultures were performed in Servicio de Microscopía Electrónica del Centro de Biología Molecular "Severo Ochoa" in a Jeol JEM-1010 microscope equipped with a CMOS 4K x 4K , F416 de TVIPS camera. Cells were fixed on P35 Petri dishes with 2% glutaraldehyde (Sigma) in PBS for two hours at room temperature. Once the fixation was finished, the fixative was retired and the dishes were rinsed with PBS three times. Next, the cultures were treated sequentially with a solution of 1% sodium tetraoxide plus 1% of potassium ferrocyanide in ddH_2O for 1 hour; 0.15% of tannic acid in 1M phosphate buffer pH 7.4 for 1 minute and 2% of Uranyl Acetate in ddH2O for 1 hour. Finally, the samples were dehydrated with EtOH in various steps with crescent concentration and infiltrated with TAAB 812 epoxy resin. After the polymerization is finished, ultrafine slides (60-70nm) were made with ultramicrotome Leica Ultracut, placed on Cu/Pd grides and dyed with 2% uranyl acetate and plumb citrate.

Magnetic characterization

Dynamical conditions: AC hysteresis loops were traced with a home-made inductive magnetometer based on the one described by Connord et al[64], operating at room temperature. The magnetic field are generated by a Litz wire solenoid, inside which two counterwise-wounded compensated with the same diameter and number of turns collect the induction signal of the sample. The AC magnetisation signal was normalized to the mass of magnetic material. Cells are exposed to magnetic hyperthermia field for a short period of time (< 5 s) and kept at 25 º C for 5 minutes, resulting in non-appreciable effect in cell viability after their reseeding 12 h after the experiment.

AC magnetic susceptibility: ACS was measured in a home-made AC susceptometer on 200 µl of the sample at 37°C. An oscillating magnetic field ($H_{max}\sim 0.4\ kA/m$) was applied from 10 Hz to 520 kHz and the induction signal was monitored via two counter-wise pick-up coil. After a background subtraction, the real and the imaginary part of the susceptibility is calculated for every frequency. In order to preserve the cell integrity, all the susceptibility measurements were performed at 37 ˚C. Due to the IONP induction signal fall provoked by physiological media and cells in some IONPs, the measurements study were limited up to 40 kHz. Determination of specific absorption rate: The specific absorption rate (SAR) on the studied IONPs was determined as follows: AC hysteresis loops were measured three times and averaged. Afterwards, area was extracted from the averaged curve and SAR value was calculated accordingly to SAR= $A\cdot f$,[102] where f is field frequency

Influence of MNP-biomolecules interaction on the dynamical magnetic response of MNPs

6

Chapter

6. Influence of MNP-biomolecules interaction on the dynamical magnetic response of MNPs

6.1. Introduction

In this chapter, we assess the effects of nanoparticle-biomolecules interaction on the magnetic response of MNPs by AC magnetometry measurements. When MNPs are dispersed in a liquid containing biomolecules, MNPs composition[103] and surface properties such hydrophilicity or net surface charge[104-109] dictate the extent on how MNP surface will interact with proteins. These unspecific interactions between MNP surface and proteins are generally ruled by electrostatic and/or steric interactions [108,110,111] and drive the colloidal stability of MNPs in protein rich media, which influences their magnetic response[49,65]. Due to the effects of these unspecific interactions between MNPs and biomolecules on the magnetic response of MNPs, understanding the mechanisms involved in the changes of the intrinsic magnetic properties is of high relevance for insuring its preservation when MNPs are intravenously injected into animal models. On the whole, such MNP-protein interaction can lead to changes in the MNPs colloidal state[112,113] and , indirectly, modify their dynamical magnetic response.

Considering the afore-mentioned aspects, herein we will assess the colloidal properties (hydrodynamic size, $D_{H,}$ and zeta-potential, ζ) of an array of 15 IONP coated with different biocompatible materials in double distillated water (DDW), phosphate buffer saline (PBS) and human blood plasma (HBP).
In addition to monitor colloidal stability by standard characterization techniques (DLS,ELS), we also perform a magnetic characterization by AC magnetometry in order to correlate magnetic and colloidal changes. Finally, we evaluated the translation of this AC magnetic-based methodology to disclose specific interactions between MNPs and target biomolecules. This would ultimately have a strong impact in the field of biosensing, thanks to the previously-mentioned advantages of AC magnetometry. Indeed, the functionalization of MNPs with recognition ligands for selective interaction with target biomolecules (i.e. analyte) has shown to yield different magnetic methodologies for detecting biomarkers [114-116]. Hence, we will also study the variation

of the dynamical magnetic response (i.e. AC hysteresis loops) after specifically interacting with functionalized MNPs and which are the effects of the related parameters (i.e. MNP size, composition, ligand-analyte affinity, field conditions, analyte multivalence, etc.).

6.2. MNPs colloidal properties in biological fluids

Figure 6.1 shows the colloidal parameters (i.e. ζ and D_H) from 14 commercial and 1 non-commercial IONP with different coatings (see Table 6.1) dispersed in DDW, PBS, and HBP and incubated for 1 hour at 37ºC. ζ and D_H of a given coated-IONPs strongly depend on the dispersion media as shown in Figure 6.1ab. Concerning the net surface charge of IONP dispersed in DDW, we grouped the studied IONPs depending on the sign of ζ : positive (red shadow), negative (blue shadow) and quasi-neutral (white shadow). These measured values of ζ can be related to the expected chemical groups present on the surface. Whereas amine or chitosan yield to positive surface charge values, dextran or dimercaptosuccinic acid (DMSA) yield to negative surface charge values. However, IONPs coated with PEG300 molecules with -COOH or -NH_2 attached onto dextran molecules (nanomag®-D-spio-PEG-COOH and -NH_2) yielded quasi-neutral ζ values (< ±10 mV, white zone). In this sense, note that the quantification of the -NH_2 groups onto the surfaces of nanomag®-D-spio-PEG-NH_2 (5 μmol/g Fe) and fluidMAG-PEG-Amine (25 μmol/g Fe) explains the observation of different ζ values (-3 mV and + 44 mV, respectively). Finally, the relatively low negative ζ value observed for fluidMAG-D is characteristic of starch coating.

Values measured in DDW dispersions significantly change when IONPs are dispersed in PBS. On one hand, most of the ζ values are negatives for all IONPs coatings except for DEAE (see Figure 6.1a). On the other hand, the extent of negative charge value in PBS is tightly related to the ζ value in DDW. In the case of the positively charged IONPs in DDW, we observed similar negative values of ζ (~ -32 mV). In the case of the negatively charged IONP in DDW dispersions, the values of ζ in PBS become more negative for IONPs coatings with larger negative charge values (in DDW). However, in the case of neutral or low negatively charged coatings, low negative ζ values were observed (< -15 mV). When IONPs are dispersed in HBP, the values of ζ from IONP behave differently than in PBS and DDW. At a first glance, we observed that the ζ values after incubation in HBP are rather similar (~ -25 mV) independently of the coating, in agreement with recent observations.[107,108,117] We assign this to the formation of a protein corona onto the nanoparticle surface, which occur independently of the pristine net IONP surface charge in DDW dispersions.

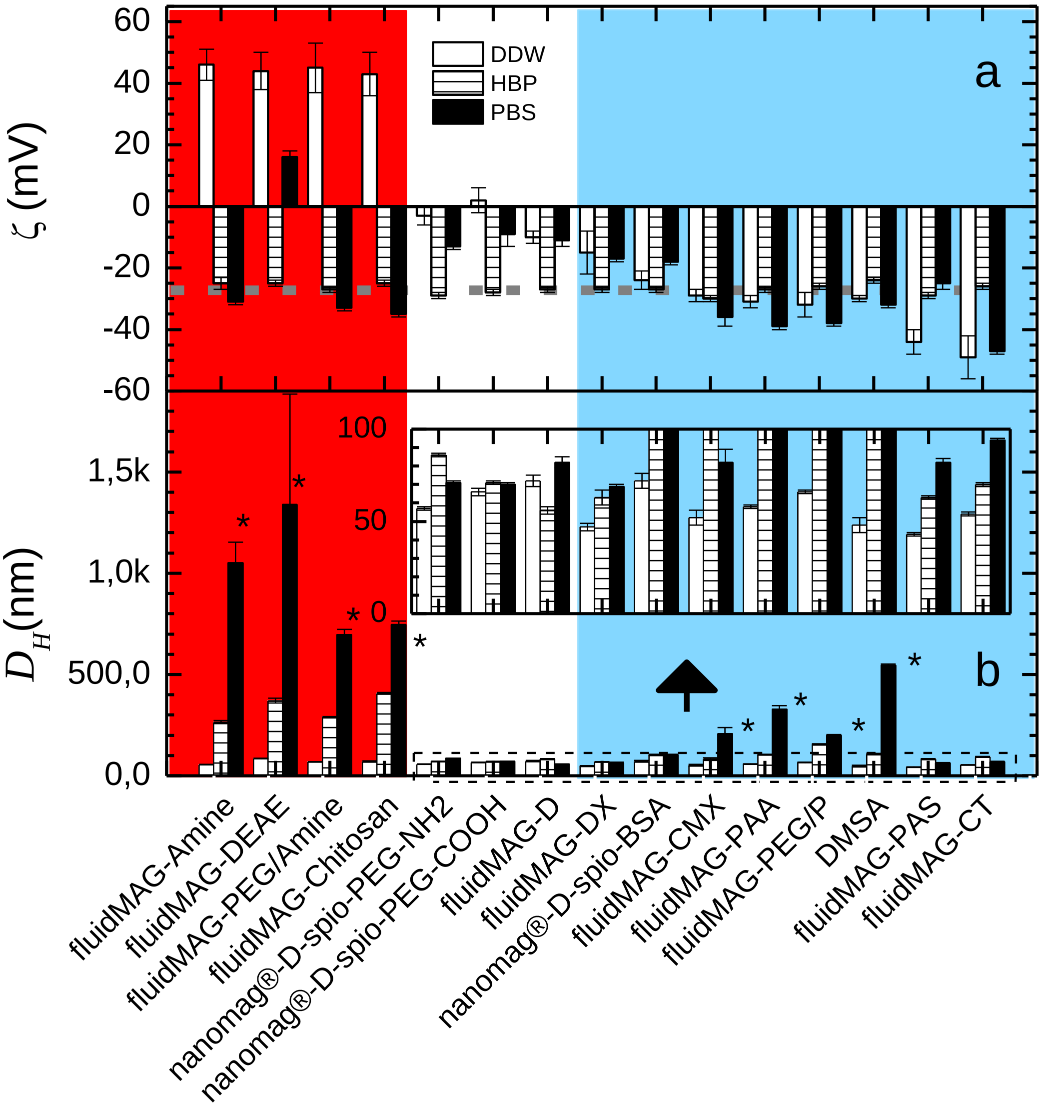

Figure 6.1. a) Zeta potential of the different IONP dispersed in DDW (empty column), PBS (patterned column) and HBP (solid column). Dashed line corresponds to ζ = -27 ±1 mV related to HBP proteins diluted in DDW dispersions as indicated in Methods Section, b) Hydrodynamics size of the different IONP dispersed in DDW (empty column), PBS (patterned column) and HBP (solid column) dispersions, Blue, red and white colors respectively arrange negatively, positively and neutral charge IONP. Symbol (*) refers to the precipitation of IONP after incubation in PBS dispersions.

The similar ζ value of net surface charge observed for all IONPs in HBP dispersions is the same than the net charge of the HBP dispersion that we measured, reflecting the contribution of the proteins to the ζ values of IONP dispersed in HBP (ζ = -27 ±1 mV, see dot line in Figure 6.1a). The variation of IONP values of ζ in HBP is highly related to their ζ values in DDW. Indeed, the strongest variations of ζ were observed for positively charged coatings in DDW dispersions due to the sign inversion of the net surface charge resulting after protein corona formation. For neutrally charged coatings in DDW dispersions, ζ reach negative values (~ -25 mV) as reflected in the significant increase of their IONP net surface charge. Finally, for negatively charged IONP in DDW dispersions, the variation of ζ values in HBP with respect to DDW is the smallest among all IONP incubated in HBP dispersions.

Table 6.1. Coating and core size of the studied IONP.

IONP	Coating	*d* (nm)
fluidMAG-Amine	Amine Silane	14±4
fluidMAG-DEAE	Diethylamine ethyl	14±4
fluidMAG-PEG/Amine	Polyethylene glycol α-Methoxy-ω-amine	12±4
fluidMAG-Chitosan	Chitosan	14±4
nanomag®-D-spio-PEG-NH$_2$	Polyethylene glycol with amine groups on dextran	7±2
nanomag®-D-spio-PEG-COOH	Polyethylene glycol with carboxylic groups on dextran	7±2
fluidMAG-D	Starch	7±2
fluidMAG-DX	Dextran	10±3
nanomag®-D-spio-BSA	Albumin on dextran	7±2
fluidMAG-CMX	Carboxymethyldextran	15±4
fluidMAG-PAA	Polyaspartic acid	13±4
fluidMAG-PEG/P	Polyethylene glycol α-, ω-diphosphate	12±3
DMSA	meso-2,3-dimercaptosuccinic acid	21±3
fluidMAG-PAS	Polyacrylic acid	13±3
fluidMAG-CT	Citric acid	13±4

As expected, the evolution of ζ from IONP dispersed in PBS and HBP with respect to values in DDW has strong consequences on the hydrodynamic sizes of the different IONP studied (Figure 6.1b). This is most significant when a sign inversion of net surface charge is involved. Thus, positively charged IONP dispersed in DDW showed a remarkable increase of D_H in biological fluids: up to 30-fold in PBS or up to 6-fold in HBP with respect to the values in DDW. Neutrally or negatively charged IONP generally showed much lower increase in D_H than positively charged IONP. In PBS, D_H values generally maintained the value in DDW, except for some particular cases (all positively and some negatively charged IONP: fluidMAG-PAA, fluidMAG-CMX, fluidMAG-PEG/P and DMSA) where D_H reached values of few hundreds of nm (< 600 nm). It is worth noting that there is a correlation of the colloidal stability in PBS and HBP. Thus, when the value of D_H from IONP dispersed in PBS varies with respect to DDW dispersions, changes of D_H are also observed in HBP. But the changes of D_H are generally more pronounced in PBS. The colloidal stability of IONP dispersed in a protein-rich or ion-rich media is mainly governed by the net surface charge, type of functional surfaces group, hydrophilicity, and amount of the IONP coating. Indeed, the variation of D_H in PBS dispersions for IONP with similar net negative charge (in DDW dispersions) was different. For example, different IONP coatings (fluidMAG-CMX, fluidMAG-PAA, fluidMAG-PEG/P and DMSA) but with comparable values of ζ (ranging from -28 to -34 mV) show different values of D_H ranging from 80 to 550 nm. Such behavior of D_H cannot just be explained by the net IONP surface charge, but it may be related to the distinct hydrophilicity of the different coating molecules considering their chemical composition: carboxymethyldextran (CMX) coating is more hydrophilic than dimercaptosuccinic acid (DMSA), which shows the largest D_H value. Even though all tested IONP are hydrophilic, small differences of D_H are significantly appreciated under conditions of similar net surface charge. Thus, the higher hydrophilicity of coating leads to higher colloidal stability when net surface charge is relatively low. Also, functional surface groups, such us hydroxyl groups (highly present in CMX coating), differently behave in ion rich media than other functional groups such as carboxylic acid (highly present in PAA and DMSA coatings) or phosphate groups (highly present in PEG/P coating). Therefore, colloidal stability in aqueous media strongly depends on the chemical groups active on IONP surface coating[118], the supplied net surface charge, and hydrophilicity. Similarly, in BSA coated IONP all these effects will play a role in their stability, but the contribution of the different elements is harder to analyze because of the chemical diversity of the protein.

Correlation of MNPs colloidal properties with their dynamical magnetic response in HBP

As shown in Figure 6.1, the resulting protein adsorption onto MNPs after dispersion in HBP leads to variations in the hydrodynamic volume, which vary with the distinct coating material. Consequently, such variations of DH may modify the magnetic response of the related IONPs when exposed to an external AMF.[29,60] To visualize the correlation between D_H, ζ and the IONPs dynamical magnetic response, we assessed the evolution of those parameters when the % HBP in DDW solutions is varied (i.e. the protein concentration). For that purpose, we select fluidMAG-Chitosan nanoparticles, whose intrinsic parameters (like size) allow to evidence dipolar interaction phenomena in case these particles aggregate. Figure 6.2 shows the evolution of D_H and ζ with HBP fraction of such positively charged IONPs. Low % HBP (≤1 %) led to significant variations of ζ from +43 mV (at 0 % HBP) to +11 mV (at 0.2 % HBP) and −9 mV (at 1 % HBP). Then, the negative values of ζ progressively increased up to −21 mV, which is roughly constant beyond 5 % HBP. We attribute such constant ζ value to the formation of a protein corona onto the IONP surface.

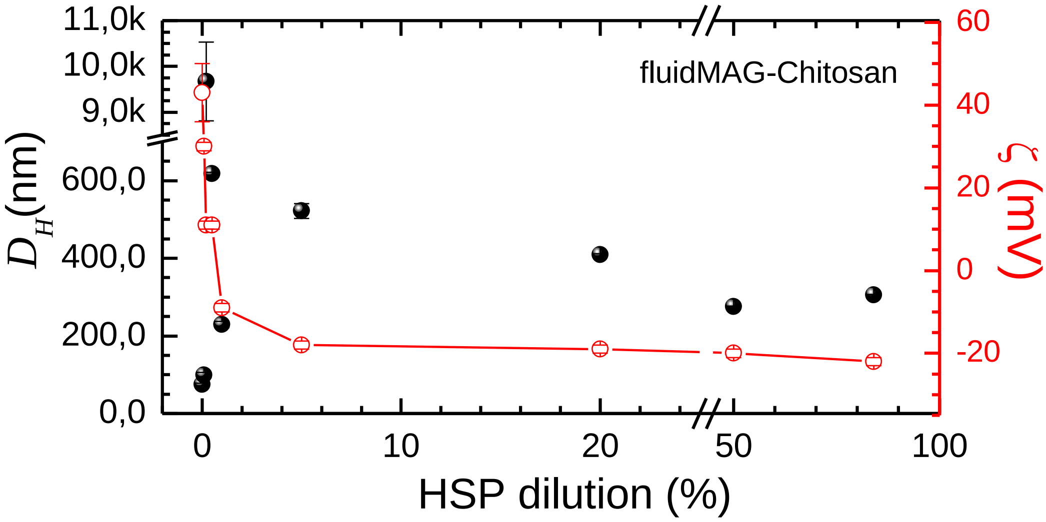

Figure 6.2. Evolution of hydrodynamic size (solid circles) and zeta potential (empty circles and lines) in a) fluidMAG-Chitosan, b) nanomag®-d-spio-PEG-COOH, and c) fluidMAG-CT dispersed in DDW solutions with different % HBP fractions after incubation at 37 °C for 1 hour.

Otherwise, variations ζ strongly influences D_H, especially when ζ values approach zero. Under such circumstances, D_H changed dramatically from 50 nm (at 0 % HBP) to 9.8 µm (at 0.2 % HBP). Then, it progressively decreased to 305 nm (at 84 % HBP). From the behavior of D_H and ζ with the % HBP, we stress the relevance of the net charge inversion (i.e. from positive to negative) on the change of D_H, according to the well-known relationship between net surface charge and aggregation state of nanoparticles. In order to evaluate whether this increase in D_H is somehow evidenced in the magnetic response of IONPs, we measured the AC hysteresis loops of fluidMAG-Chitosan dispersed in PBS with four different human blood plasma volume fractions (0, 0.2, 5, 83%) at 100 kHz and 25 kA m^{-1} (Figure 6.3).

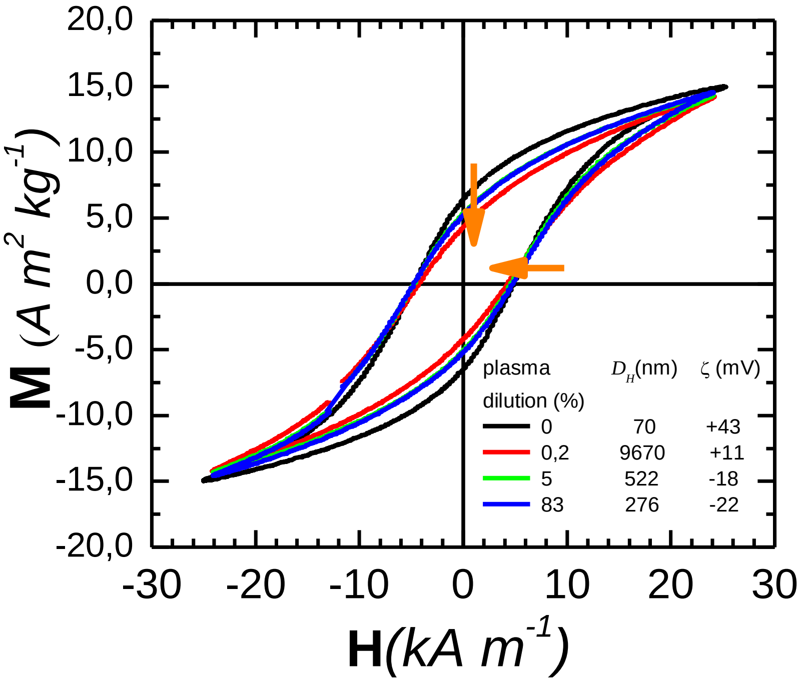

Figure 6.3. AC hysteresis loop of fluidMAG-Chitosan dispersed in PBS at increasing human blood plasma volume fractions. f =100 kHz; H_{MAX} = 30 kA m^{-1}; ρ_{Fe}= 1g$_{Fe}$/L. Arrows indicate the decrease of M_R and H_C upon the addition of HBP to the dispersion.

Indeed, AC Hysteresis loops presented important variations when D_H increase. Hereby, the hysteretic area *(A)* reduced from 563 mJ kg^{-1} in blank dispersion (i.e. without HBP) to 490 mJ kg^{-1} at the maximum HBP fraction added (83 %). The shape of AC hysteresis loops also seems to be highly influenced by the addition of HBP, losing its sigmoidal shape due to the decrease of M_R – from 6.4 A m^2 kg^{-1} when measured in DDW to 4.95 A m^2 kg^{-1} at 0.2% of HBP (%v_{HBP}/v where v_{HBP} is the HBP volume and v is the total dispersion volume). M_{MAX} and H_C instead does not present important changes when HSP volume fraction increases, exhibiting only a tiny decrease in the hysteresis loop measured at 0.2% of HBP. In addition, the evolution of the hysteresis loops is not linear with the addition of HBP to the dispersion: AC hysteresis loops of fluidMAG-Chitosan measured 0.2% of HBP yielded the lowest hysteretic area (A) values (434 mJ kg^{-1}) of the series and presents the major losses of sigmoidallity. That said, it is important to note that below 1% of HSP, D_H showed their larger variability (Figure 6.3). The largest D_H value in addition was observed at a concentration of 0.2% of HBP, giving consistency to the significant changes in the hysteresis loops measured at similar HBP concentration. The variations of AC hysteresis loops at different %v_{HBP}/v are related to the D_H value due to the enhancement of IONP agglomeration, as recently reported[60]. Indeed, such increase of IONP clustering leads to an increase of intra-aggregate magnetic dipolar interactions, which results in substantial variations of AC hysteresis loops. All these results give rise to a relevant fact: the unspecific adsorption of proteins onto the MNPs surfaces induces significant changes in the colloidal properties (i.e. ζ and consequently D_H), which are reflected on the dynamical magnetic response of MNPs (i.e. AC hysteresis loops). This fact turns out the interest of AC magnetometry to probe the effects of specific interactions between MNP surface and biomolecules on the MNP magnetic response. In next sections, we will study a novel biodetection magnetic methodology based on the variation of the AC hysteresis loop signal of functionalized MNPs after their specific interaction with an analyte. For that purpose, we assess the influence of several parameters (MNP size and composition, valence of the system, ligand-analyte affinity) on the detection sensitivity.

6.3. Unveiling specific MNP-biomolecule interaction by AC magnetometry: towards a biosensing platform

Recent studies have proposed the use of MNPs as magnetic transducer for sensing biomarkers related to distinct diseases and pathological conditions. Thus, *Mezger et al.*[119] proposed the detection of biomolecules by magnetic nanoparticles employing a magneto-optical set-up, disclosing the identification of bacteria from urine samples based on padlock probe recognition followed by two cycles of rolling circle amplification (RCA). *Wang et al.*[116] reported on the detection of DNA by a Giant Magneto Resistance (GMR) sensor using MNPs with sizes ranging from 10 to 100 nm. *Fornara et al.*[23] described a high sensitivity magnetic detection method based on changes in the magnetic susceptibility under an alternating magnetic field. Besides, *Gandhi et al.*[120] discloses the detection of cancer-specific proteases by a magnetic particle spectrometer (MPS) relying only on the magnetic relaxation mechanisms of functionalized nanoparticles. In spite of some of these magnetic methodologies are extremely sensitive to low analyte concentrations, the acquisition times for analyte recognition are longer than several tens of minutes or the measurements require exhaustive sample preparation. In overall, these issues hinder an easy-going to reach clinical use.

Here we studied the potential of a novel detection method based on AC magnetometry for displaying specific MNPs-biomolecule interactions. The advantages of the AC magnetometry mainly rely on two aspects: i) fast measurement times (<5 s) and ii) the negligible contribution of the biological media where MNPs are dispersed to the magnetic measurement, enabling to measure the MNP signal straight in biological fluids. Eventually, such issues represent substantial improvements with respect to the above-mentioned magnetic methods.

Another relevant fact for the proposed detection methodology is the use of MNPs functionalized with recognition ligands, which favor the specific interaction with an analyte. In this manner, interaction between MNP and analyte leads to the analyte absorption on the surface and eventually MNP-analyte cross-linking, whose extent depends on the valence of the system. This results in strong variations of the magnetic response of the functionalized MNPs with respect to the case in absence of analyte.

Transducers were obtained in the frame of a collaboration with Prof. Aitziber L. Cortajarena (CICbiomaGUNE, and iMdea Nanociencia). Dr. Antonio Aires working as a postdoctoral fellow at Cortajarena's group prepared MNPs functionalized with analytes of different valence: mono-, di-and tetravalence, schematized in Figure 6.4 according to their recognition sites valence. Larger valences provide an additional parameter that may define the sensitivity of our system, in addition to the standard analyte-ligand affinity.

The different MNP-analyte assembly configurations resulting from the MNP-analyte interactions tightly depends on different parameters such the number of ligands attached onto MNP, analyte valence and MNPs concentrations. In monovalent systems, an analyte can be only attached to one ligand, leading to variations of the hydrodynamic volume (V_H) in the colloid (See **Figure 6.1**) solely derived from the analyte adsorption onto the surface MNP. In multivalent systems instead a single analyte can interact with several MNPs, resulting in a cross-linking configuration that remarkably enhance the MNP agglomeration. Indeed, MNP-ligand-analyte assembling results in the decrease of MNPs interparticle distances, which at the end results into the enhancement of the magnetic dipolar interactions, variations of the MNP effective magnetic anisotropy (K_{eff}) and consequently, changes in the dynamical magnetization response with respect to the case of the MNP signal in absence of analytes.

In previous chapters, it was shown that MNPs magnetic response is influenced by V_H and K_{eff} in a different manner depending on the magnetic relaxation mechanism (i.e. *Néel* or *Brown*), which governs the magnetic response of the MNPs. *Fornara et al.*[23] show that AC magnetic susceptibility measurements of the transducer (i.e. functionalized MNP) clearly reflect the alteration of magnetic relaxation process in absence or in presence of the analyte. For that reason, MNP composition and sizes are also parameters that may influence the sensitivity of this novel magnetic detection approach. In addition, results shown in Chapter 4 underline the influence of field conditions to modulate the influence of parameters as viscosity on the magnetic relaxation mechanism, and therefore, the AC magnetization response. In overall, this novel sensing methodology has a larger potential for magnetic detection thanks to the different mechanisms (analyte-ligand affinity, system valence, MNP composition and size, field conditions, analyte and MNP concentrations) for tuning the detection sensitivity with respect to traditional detection technologies.

Next, we will present the results obtained for different transducers based on two different composition and size MNPs, functionalized with ligands that interacts with analytes accordingly three valence schemes: mono-, di-, and tetravalent. In monovalent and divalent system, magnetic nanoparticles (MNPs) were functionalized with the tetratricopeptide (TPR), whose sequence MEEVF is specifically recognized by the VSP-TPR2-MMY repeat domain (analyte). Nonetheless, repeat domains which take the role of analyte in these experiments provides one recognition site in the case of monovalent system (VSP$_{monomer}$-TPR2-MMY), whereas in the divalent system the analyte (VSP$_{dimerr}$-TPR2-MMY) contributes with two recognition sites.

In case of tetravalent system, MNPs nanoparticles were functionalized with a GST fusion to the peptide Acceptor peptide (AP) sequence GLNDIFEAQKIEWHE that is biotinylated in the K position (AP-biotin). Biotin is specifically recognized by the tetravalent protein avidin (analyte), which supplies four recognition positions (See methods section for further MNPs functionalization details).

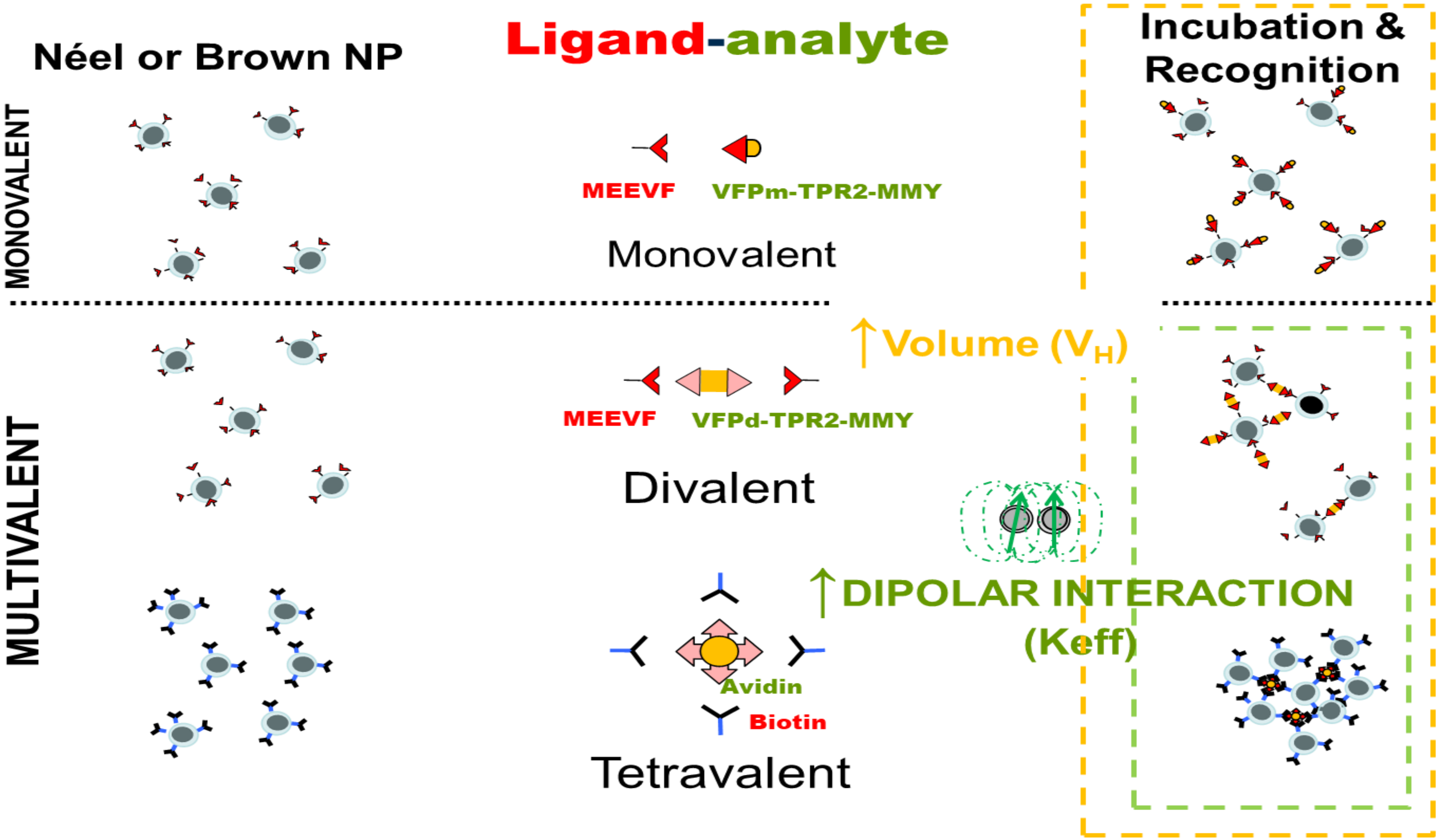

Figure 6.4. Schematic illustration of the MNPs-ligand-analyte systems employed for assessing the feasibility of AC magnetometry to sense MNPs-biomolecules specific interactions

The employed MNPs were commercially available 12 nm DMSA coated iron oxide nanoparticles (MF66), in which Néel relaxation mechanism prevails, and 21 nm PMAO coated cobalt ferrite nanoparticles (SA94), with predominant Brownian magnetic relaxation mechanism. The later was kindly supplied by the group led by Dr. Teresa Pellegrino from Istituto Italiano di Tecnolgia (Genoa, Italy).

Monovalent system

First, we appraised the viability of monitoring the interaction of a monovalent analyte (VFPm-TPR2-MMY) with two different core size (12 and 21 nm) functionalized MNPs by AC magnetometry measurements. Thus, after its corresponding ligand functionalization (see methods section), both MNPs were incubated 60 minutes for 1 h at 37ºC in PBS with different concentrations(ρ_{Analyte}) of analyte (VFP$_m$-TPR2-MMY). Immediately after, we measured AC hysteresis loops of the dispersions. Figure 6.5 shows AC hysteresis loops (f = 50 kHz; H_{MAX} = 20 kA m^{-1}) of ligand–functionalized SA94 sample (SA94-GST-MEEVF onwards) measured in PBS dispersions at increasing analyte (VFPm-TPR2-MMY) concentration.

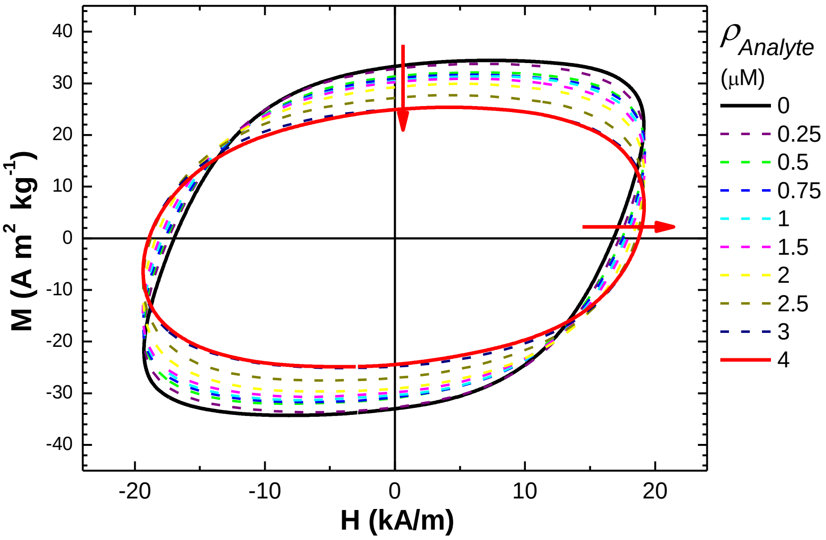

Figure 6.5. AC hysteresis loops of SA94-GST-MEEVF nanoparticles measured in PBS dispersions with increasing analyte (VFPm-TPR2-MMY) molarity. f = 50 kHz; ρ_{Fe}= 1g$_{\mathrm{Fe}}$/L; H_{MAX} = 20 kA m^{-1}. Arrows indicates variations of M_R and H_C with the addition of analyte to the dispersion.

SA94-GST-MEEVF measured in PBS displayed a wide-open cycle, similar to those obtained in Chapter 4. However, AC hysteresis loops displayed significant modifications from the initial state as when SA94-GST-MEEVF were incubated at raising $\rho_{analyte}$:

remanence (M_R) decreased, shrinking from 33 Am^2 kg^{-1} when measured in PBS without analyte to finally reach 25 Am^2 kg^{-1} when $\rho_{analyte}$= 4 µM. In contrast, coercivity (H_C) followed the opposite trend, increasing from H_c = 17 kA m^{-1} when measured solely in PBS to extend up to H_c = 19 kA m^{-1} at the maximum studied analyte concentration (4 µM). These changes in the hysteresis loops, which collectively leads to the flattening and elipsization of the AC hysteresis loop, leads to significant variations in the area enclosed inside the loops, as shown in Figure 6.6.

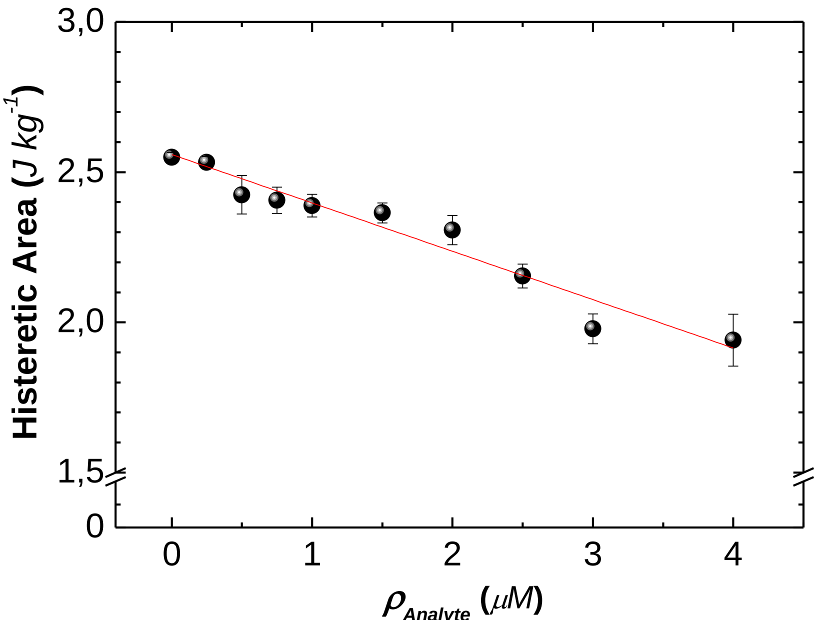

Figure 6.6. AC hysteresis loops of SA94-GST-MEEVF nanoparticles dispersed in PBS at increasing analyte (VFPm-TPR2-MMY) concentration. f = 50 kHz; H_{MAX} = 20 kA m^{-1}; ρ_{Fe}= 1g$_{Fe}$/L. Red line is a guide-to-eye to indicate a linear trend.

Here one can appreciate good linear correlation between the hysteresis area and analyte concentration, depicting a dose-dependence decrease of the hysteretic area. Such linear trend of SA94-GST-MEEVF dynamical magnetic response with $\rho_{Analyte}$ is consequence of the selective attachment of the analytes to the recognition ligands anchored to SA94-GST-MEEVF surface. Certainly, that specific interaction among analyte and transducer results in a tiny increase of the hydrodynamic volume (V_H), that significantly alters the predominant Brownian magnetic relaxation mechanisms of SA94 nanoparticles ($\tau_B = \frac{3\eta V_H}{k_B T}$) and therefore, the AC hysteresis loop. According to the Brownian time expression, variations related to V_H similarly influence τ_B than viscosity. Considering that SA94 sample showed AC hysteresis loops (see Figure 4.1.) extremely sensitive to viscosity, it can be understood that small changes of V_H may result in significant variations of AC hysteresis loops. Hence, the monovalent transducer is not expected to induce aggregation after interaction with analyte due to the monovalent nature of the ligand.

In this regard, the AC magnetic measurements of functionalized MF-66 nanoparticle, where Néel magnetic relaxation mechanisms prevails, allows to shed light on our assumptions. Figure 6.7 shows AC hysteresis loops (f = 100 kHz; H_{MAX} = 30 kA m-1) of ligand-functionalized MF-66 MNPs (MF66-GST-MEEVF onwards), measured in PBS dispersions without analyte and at the maximum $\rho_{Analyte}$ that the dispersion admits previously its destabilization ($\rho_{Analyte}$ = 4 μM).

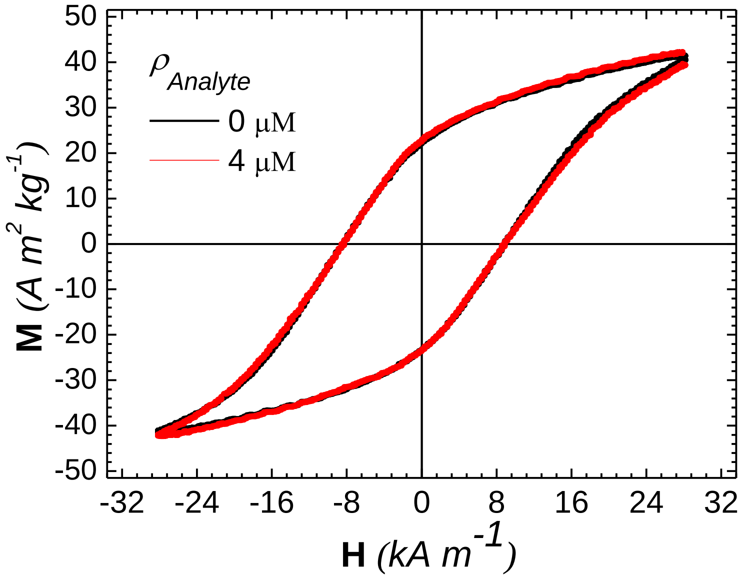

Figure 6.7. AC hysteresis loops of MF66-GST-MEEVF nanoparticles dispersed in PBS with 0 and 4 μM of analyte (VFP_m-TPR2-MMY). f =100 kHz, H_{MAX} = 30 kA m^{-1}; ρ_{Fe}= 1g_{Fe}/L. Hysteresis loops at $\rho_{analyte}$ = 0 and 4 μM are highlighted for a better visualization

Hysteresis loops do not depict any remarkable change when the analyte is added to the dispersion even at the highest $\rho_{Analyte}$ employed in Figure 6.2. The AC hysteresis of the monovalent transducer does not depend on the analyte presence More in detail, the hysteretic area (A) values extracted for both analyte concentration values (0 and 4 μM) are statistically indistinguishable (Figure 6.8), underlying the relevance of the magnetic relaxation processes on the liability to detect monovalent analytes: transducers characterized by Brownian relaxation proccess lead to variation of AC hysteresis loops, but not those characterized by Néel relaxation. The laters are unable to magnetically tranduce and display the ligand-analyte recognition.

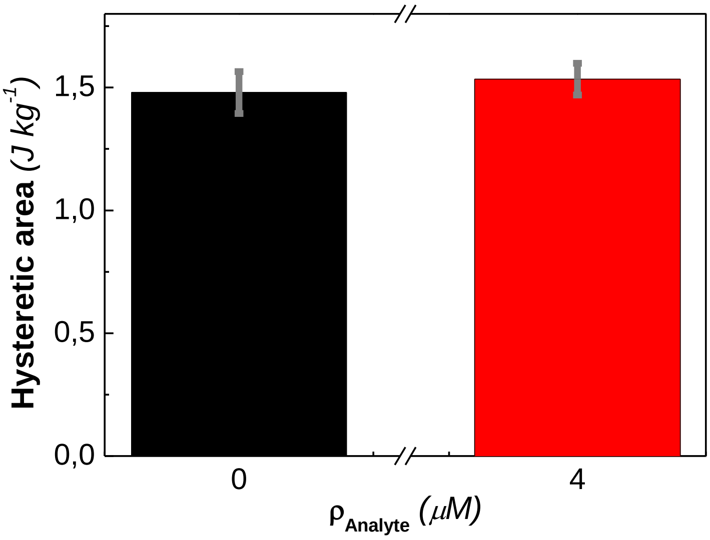

Figure 6.8. Hysteretic area (A) extracted from AC hysteresis loops of MF66-GST-MEEVF samples dispersed in PBS with analyte content concentrations of 0 and 4 µM. *f* =100 kHz, H_{MAX} = 30 kA m^{-1}; ρ_{Fe}= 1g$_{Fe}$/L.

We understand such lack of detection sensitivity of the system to the prevalence of the Néel relaxation mechanism in MF66 nanoparticles. Indeed, Néel relaxation time ($\tau_N = \frac{\sqrt{\pi}}{2\sqrt{K_{eff}V/k_BT}}\tau_0 e^{-K_{eff}V/k_BT}$) is strongly modulated by variation of the effective magnetic anisotropy (K_{eff}), which happens when aggregation increase and intra-aggregate dipolar interactions raise up, as shown in Chapter 3 and 5. Nonetheless, this generalized MNPs aggregative scenario is likely in multivalent but not in monovalent systems.

Divalent system

The addition of valences to the transducer provides the capability to induce cross-linking assembly after specific interaction between MNP and analyte, as schematically represented in Figure 6.1. Under those conditions, MNPs characterized by both magnetic relaxation processes (Brownian and Néel) are expected to display variations of their dynamical magnetic response after the analyte-ligand interaction. In order to prove that assumption, we performed AC magnetometry measurements of MF66-GST-MEEVF nanoparticles but adding a divalent analyte (VFPd-TPR2-MMY) to the dispersion for, in this manner, inducing the MNPs agglomeration once the analyte recognition takes place. Figure 6.9 shows AC hysteresis loops of MF66-GST-MEEVF nanoparticles after incubation of MNPs at given concentration ($1g_{Fe}$/L), and at increasing analyte (VFPd-TPR2-MMY) concentrations for 1 h at 37°C in PBS.

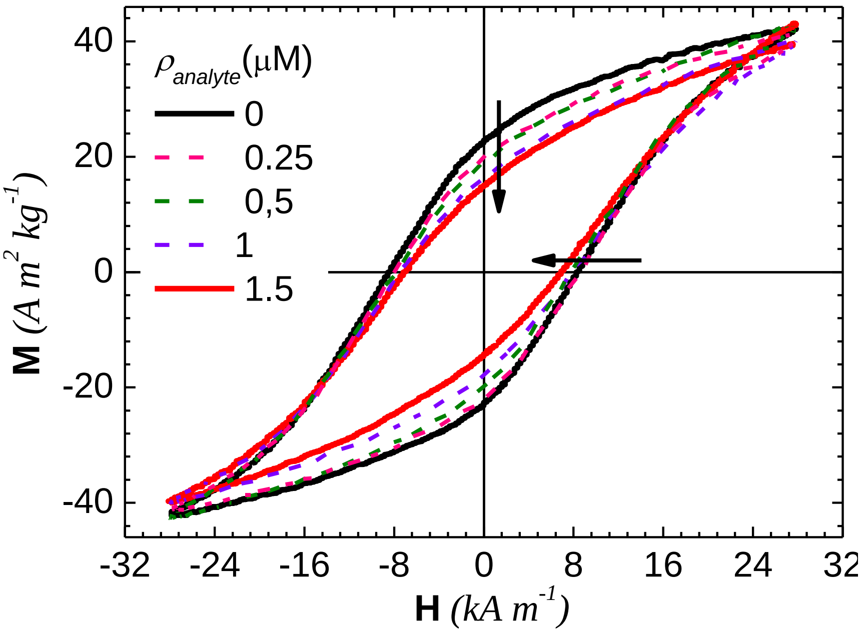

Figure 6.9. Hysteretic area (A) extracted from AC hysteresis loops of MF66-GST-MEEVF samples dispersed in PBS with increasing divalent analyte concentration. f =100 kHz; ρ_{Fe}= $1g_{Fe}$/L; H_{MAX} = 30 kA m^{-1}. Arrows highlight the decrease of H_C and M_R at larger analyte concentrations. Hysteresis loops at $\rho_{analyte}$ = 0 and 1.5 µM are highlighted for a better visualization.

In contrast with the MF66 monovalent picture, we can observe that the characteristic sigmoidal curve obtained in PBS is softened as the analyte concentrations rises. Mainly, those variations are due to the decrease of remanence (M_R) – from 22.8 Am^2 kg^{-1} when MNPs are measured solely in PBS to 18 Am^2 kg^{-1} when $\rho_{analyte}$= 4 mM – and to lesser extent, coercive field (H_C) – from 8.4 kA m^{-1} in absence of analyte to 6.8 kA m^{-1} at maximum $\rho_{analyte}$.

In consequence, hysteretic area (A) also depicts a considerable variability as $\rho_{Analyte}$ raises, as shown in Figure 6.10. Here we can appreciate how the presence of the analyte molecule (VFP$_d$-TPR2-MMY) caused a dose-dependent decrease in the hysteresis loop area of the MF66-GST-MEEVF. As in the case of SA94-GST-MEEVF nanoparticles with a monovalent analyte (VFP$_m$-TPR2-MMY), area dropped following a linear behavior when increasing the MMY peptide concentration in the range from 0.25 to 1.5 µM.

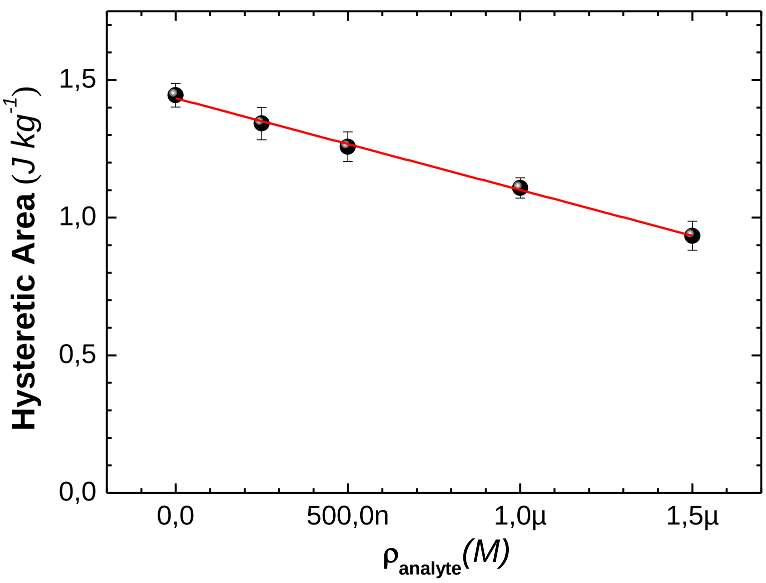

Figure 6.10. Hysteretic area (A) extracted from AC hysteresis loops of MF66-GST-MEEVF samples dispersed in PBS with different analyte molarity. f =100 kHz; H_{MAX} = 30 kA m^{-1}; ρ_{Fe}= 1g$_{Fe}$/L. Red line is a guide-to-eye to indicate a linear trend.

Thus, we understand the reduction of A upon the addition of analyte to the dispersion as due to the effect of magnetic dipolar interactions, favored by the increase of MNP agglomeration induced by the divalent analyte (VFP$_d$-TPR2-MMY) specific interaction with MF66-GST-MEEVF nanoparticles. Indeed, MNP-ligand-analyte interaction benefits the enhancement of the MNPs aggregation state, which results in variation of V_H and favors magnetic dipolar interactions (i.e. variations of K_{eff}). Therefore, the effective magnetic anisotropy (K_{eff}) of MNPs and its dependent relaxation mechanisms (i.e. Néel relaxation mechanisms) are modified. Finally, the analyte divalence benefits the MNP cross-linking assembly induced by specific MNP-analyte interactions. Such cross-linking results in a significant enhancement of V_H and MNP agglomeration, which is expected to result in more significant changes of AC hysteresis loops than in the case of monovalent analytes.

Tetravalent system

As mentioned above, raising the analyte valence from mono- to divalent has shown a benefit for the magnetic detection of MNPs, independently of their intrinsic dynamical magnetic properties. Indeed, greater valences of the system would favour stronger MNPs aggregation phenomena, deriving in major variations in the hydrodynamic volume and/or intra-aggregate magnetic dipolar interaction at low analyte concentrations. To experimentally evaluate the implications of increasing the recognition sites on the sensitivity of the magnetic detection approach, we used SA94 and MF66 MNPs functionalized with a GST fusion to the peptide Acceptor Peptide (AP) sequence GLNDIFEAQ**K**IEWHE that is biotinylated in the **K** position (AP-biotin). As previously mentioned, biotin is specifically recognized by the protein avidin (analyte), providing four recognition centers, i.e. tetravalent analyte.

After incubating at given concentration (1g_{Fe}/L) in PBS 1 h at 37°C with different avidin concentrations (i.e. ρ_{Analyte}), we measured the AC magnetic response of functionalized SA94 and MF66 nanoparticles. Figure 6.11 displays the AC hysteresis loops of biotin functionalized SA94 samples (SA94-MNP-GST-AP-Biotin onwards) measured in PBS dispersions while raising avidin concentration. Again, the hysteresis loops measured in absence of analyte (Figure 6.11 – black straight line) strongly vary by the addition avidin to the dispersion, converging to a more flattened curve at the largest avidin concentration (Figure 6.11 – red straight line). However, the final shape of the AC hysteresis loops is still far from becoming an ellipse, contrasting with the effect observed in the SA94 monovalent (see Figure 4.1.). Comparing the results shown in Figure 6.11 (tetravalent case) with those in Figure 6.5 (monovalent case), one observes similarly reduction of remanence values (M_R) while increasing avidin concentration, but distinct coercivity (H_C) behavior. Now, H_C also shrinks its value from 17.7 kA m^{-1} (at $\rho_{analyte}$ = 0) to 16.9 kA m^{-1} (at $\rho_{analyte}$ = 4 μM), contrary to the trend observed for the monovalent counterpart. We attribute those different behaviors of the dynamical magnetic response of SA94 MNPs to the disctinct nature of the variations occurred in the MNPs colloidal stateafter the specific MNP-analyte interactions. Hence, in monovalent system, the transducer signal corresponds to individual MNP with few analytes attached onto its suface. Conversely, MNPs are agglomerated in tetravalent system, tailoring magnetic dipolar interactions and consequently resulting in a totally different AC hysteresis loop.

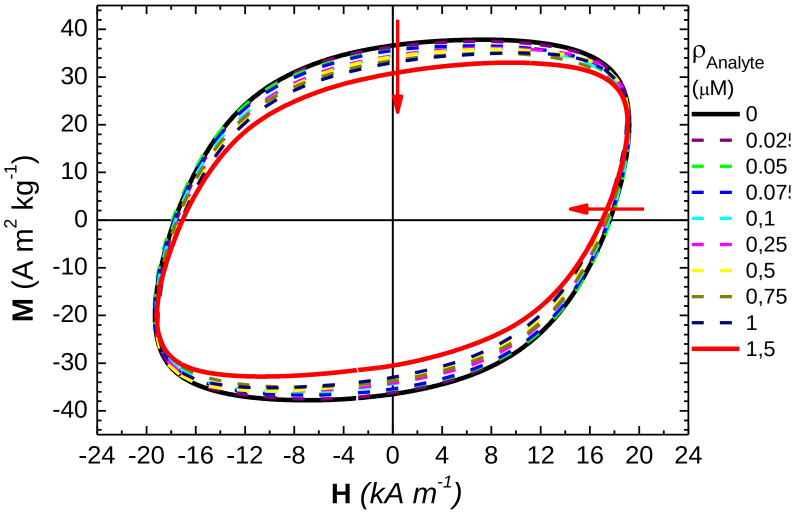

Figure 6.11. AC hysteresis loops of SA94-GST-AP-Biotin nanoparticles measured in PBS dispersions with increasing analyte (avidin) concentration. f = 50 kHz; ρ_{Fe}= 1g_{Fe}/L. H_{MAX} = 20 kA m^{-1}. Arrows highlight the variations of M_R and H_C upon the addition of the analyte to the dispersion. Hysteresis loops at $\rho_{analyte}$ = 0 and 4 μM are highlighted for a better visualization.

Moreover, we also found that the analyte concentration dependence of the hysteretic area (A) of SA94-GST-AP-Biotin reflects the existence of differently steep linear behavior at different analyte concentration ranges. Figure 6.12 displays the analyte concentration dependence of *A* extracted from Figure 6.12. It is worth noting three analyte concentration regions with distinct linear behavior, being steeper at the lowest analyte concentration range (from 0 to 10nM), softer for analyte concentration values larger than 1μM (close to sedimentation), and intermediate-slope at intermediate concentrations.

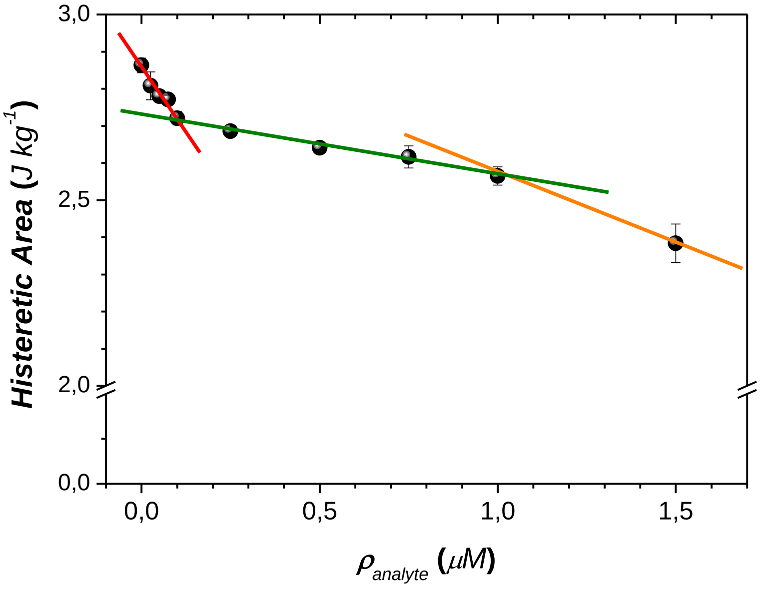

Figure 6.12. Hysteretic area (A) extracted from AC hysteresis loops of SA94-GST-AP-Biotin samples measured in PBS dispersions with increasing analyte (avidin) molarity. *f* = 50 kHz; H_{MAX} = 20 kA m^{-1}. Coloured straight lines are guide-to-eyes to indicate three different linear regions.

This variability of the *A* linear behavior can be understood in terms of the distinct magnetic behavior originated from different MNP assemblies at distinct analyte concentration ranges. Similar behavior was observed for transducers based on MF66 MNPs. Figure 6.13 shows AC hysteresis loops of biotin functionalized MF66 particles (MF66-MNP-GST-AP-Biotin onwards) dispersed in PBS at variable avidin concentration. In a similar manner than in case of divalent MF66 system or the SA94 tetravalent system, the AC hysteresis loops looses its sigmoidality as the analyte concentration increases. Such lost of sigmoidality relies on the simultaneous variation of H_C (from 7.8 kA m^{-1} at $\rho_{analyte}$ = 0 to 6.9 kA m^{-1} at $\rho_{analyte}$ = 1.6 μM) and M_R (from 15.9 A m^2 kg^{-1} at $\rho_{analyte}$ = 0 to 11.00 A m^2 kg^{-1} at $\rho_{analyte}$ = 1.6 μM). M_{MAX} also showed a evident decrease for the largest $\rho_{analyte}$.

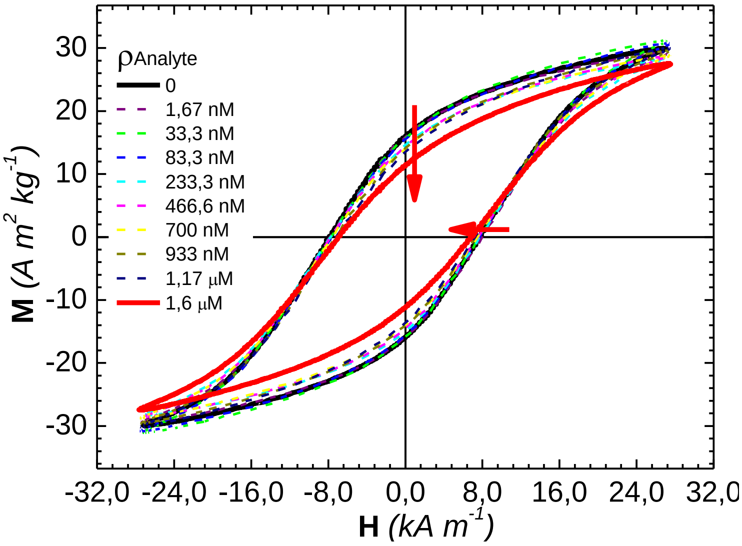

Figure 6.13. AC hysteresis loops of MF66-GST-AP-Biotin nanoparticles dispersed in PBS with different analyte (avidin) analyte molarity. *f* =100 kHz; H_{MAX} = 30 kA m^{-1}; ρ_{Fe}= 1g$_{Fe}$/L. Arrows indicated the reduction of M_R and H_C by the adding of analyte to the dispersion. Hysteresis loops at $\rho_{analyte}$ = 0 and 1.6 μM are highlighted for a better visualization.

Interestingly, the behavior of *A* at variable analyte concentration for transducers based on MF66, functionalized to specifically interact with the tetravalent analyte, also shows three distinct linear regimes (dashed colored lines) similarly than SA94 as shown in Figure 6.14-(black dots).

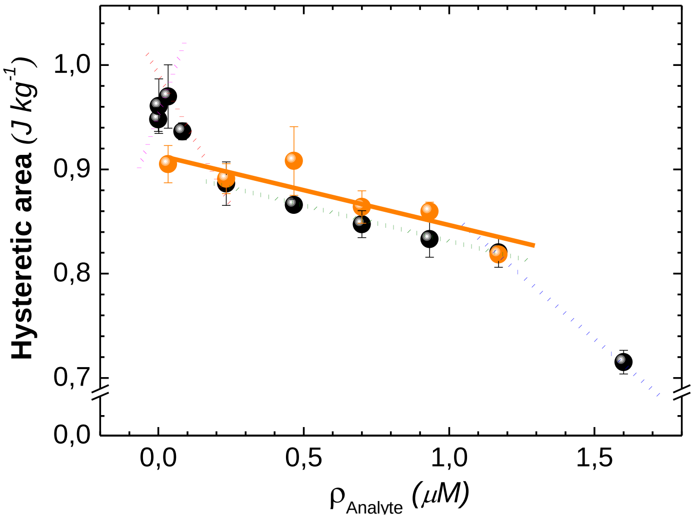

Figure 6.14. Hysteretic area (A) extracted from AC hysteresis loops of MF66-GST-AP-Biotin samples measured in PBS dispersions (black dots) and Human Serum Plasma (orange dots) with increasing analyte (avidin) concentration. f =100 kHz; H_{MAX} = 30 kA m^{-1}; ρ_{Fe}= 1 g_{Fe}/L. Coloured dotted lines indicate different slopes found in the measurements. Dashed colored lines are guide-to-eye that indicates linear correlations found in PBS measurements. Orange straight line are guide-to-eye that indicates the linear correlation found when analyte and transducer are dispersed in HBP.

To explain such phenomenology of *A* for both types of MNPs at different analyte ranges, we hypothesize the existence of three different scenarios in which the MNP assembly tightly depends on the avidin concentration (Figure 6.15). First, the interaction between avidin and MNP considerably favors the MNP clustering at low $\rho_{analyte}$. In this regard, most of functionalized MNPs are available to interact with the analyte and to form assemblies of large V_H. Consequently, such MNP clustering, which changes AC hysteresis loops via the final average value of V_H or K_{eff}, control the dynamical magnetic response of SA94 and MF66 nanoparticles (Brownian or Néel, respectively). Nevertheless, such clustering effects become more inefficient when analyte concentration increases, since an important fraction of the nanoparticles are already located in aggregates. Also, larger aggregates tend to be less compacted, reducing the strength of the magnetic dipolar interactions and consequently, the changes of the AC hysteresis loops are less significant in such analyte concentration range.

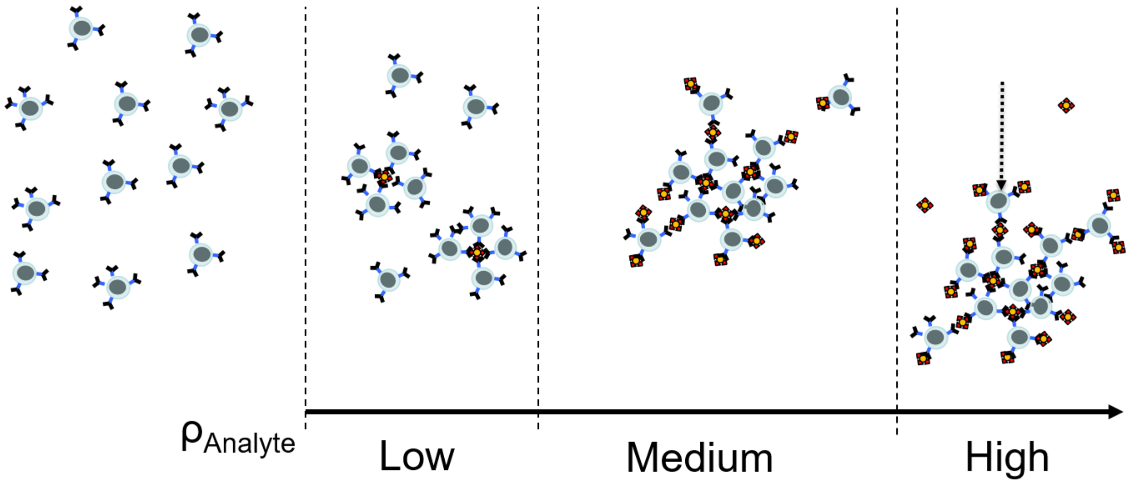

Figure 6.15. Schematic representation of the MNPs-GST-AP-Biotin clustering mediated by the specific avidin-MNP interaction at different avidin concentration ranges.

Finally, larger avidin concentrations lead to MNP aggregates of high V_H values and the saturation of the dispersion medium, favoring the destabilization of the colloid and provoking the sedimentation of the MNPs. This its-self decrease in the opening of the magnetic response of the MNPs in a more significant manner than in the previous $\rho_{analyte}$ range.

Besides, the proof of concept of this novel magnetic detection methodology has been checked for the MF66-MNP-GST-AP-Biotin dispersed in Human Blood Plasma measuring AC hysteresis loops (*f* =100 kHz) while increasing avidin concentration. (Figure 6.16).

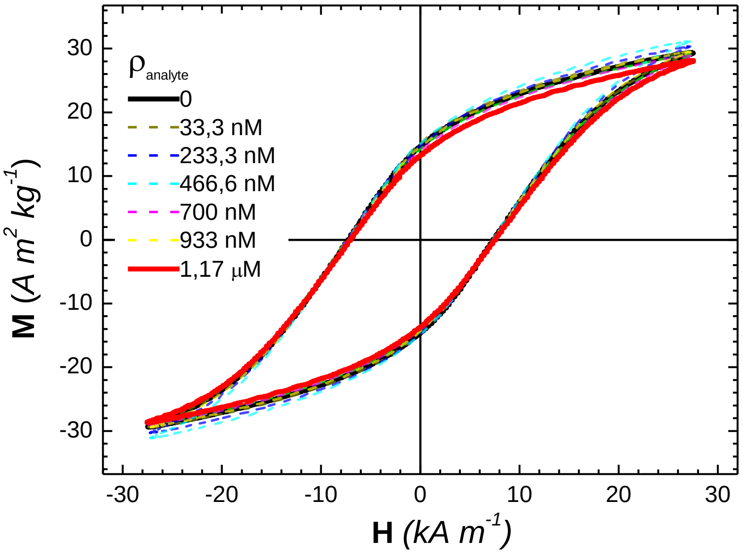

Figure 6.16. AC hysteresis loops of MF66-GST-Biotin nanoparticles measured in Human Serum Plasma with different analyte (avidin) molarity. *f* =100 kHz; ρ_{Fe}= $1g_{Fe}$/L.

In spite of the fact the DMSA coated MNPs are not intentionally designed for minimizing unspecific interactions with serum proteins, we manage to appreciate changes of the hysteretic area while increasing the analyte concentration. It is worth noting that the changes of the hysteresis loops MF66-GST-AP-Biotin after specific interactions are less pronounced. This can be understood as unspecific serum protein adsorption (see Figure 6.1). Nonetheless, a more recognizable trend is observed when plotting *A* concentration dependence (see Figure 6.14, orange dots). Indeed, similar *A* values are observed in the intermediated $\rho_{analyte}$ range and also the concentration dependence of *A* is kept linear. The only differences between measurements in PBS and HBP are observed at the low $\rho_{analyte}$ range where *A* values are reduced. Indeed, the linear dependence is less steeper in HBP than in PBS, which we understand in terms of the increase of V_H at zero $\rho_{analyte}$ due to unspecific serum protein adsorption onto DMSA surface (see Figure 6.4) resulting in larger V_H and consequenty, closer AC hysteresis loop. However, it is worthy to remark that the hysteretic area when measured in HBP show a slope similar to this found when dispersed PBS in the $\rho_{Analyte}$ = 0.23–1.77 μM region (Figure 6.14 – orange green dashed line). In last term, the presence of these similar slopes suggests that the sensitivity of the tetravalent system based on MF66 MNPs is comparable in this analyte concentration region, in PBS and HBP. This is an important hint towards the validation of this novel methodology to detect biomolecules located in protein-loaded biological fluids media.

Assessing parameters influencing the sensitivity of the proposed magnetic detection.

For the sake of comparing the sensitivity of the different transducers studied, we proceed to seek an analysis based on the normalization of *A* to the value obtained at the lowest analyte concentration. Figure 6.17 shows the concentration dependence of the normalized hysteretic for transducers based on SA94 functionalized with recognition ligands for specific interactions with monovalent (Figure 6.17-black dots) or tetravalent (Figure 6.17-red dots) analytes. The *A* normalization to the *A* value at $\rho_{Analyte}$ =0 allows to clearly visualize the sensitivity performance of the distinct studied detection methodologies. Hence, SA94-GST-AP-Biotin (i.e. tetravalent system) normalized hysteretic area evolution shows more pronounced slopes in comparison with SA94-GST-MEEVF plus VFP$_m$-TPR2-MMY (i.e. monovalent system) along the $\rho_{Analyte}$ = 0-1.5 μM range, backing the principle of a stronger sensitivity at larger valences when Brownian relaxation mechanisms dominates.

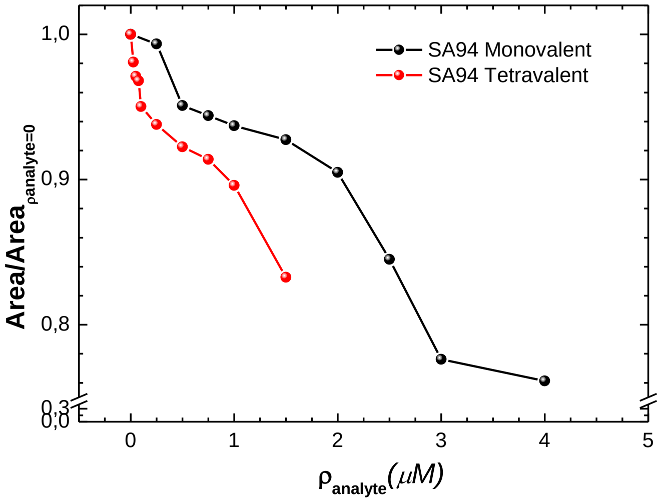

Figure 6.17 Normalized hysteretic area (A/A$\rho_{analyte}$=0) extracted from AC hysteresis loops of SA94-based systems classified according to their valence (monovalence-black dots, tetravalence-red dots) plotted while increasing analyte concentrations.

Indeed, the magnetic response of these SA94 nanoparticles are mostly determined by the hydrodynamic volume (V_H). Hence, the more MNPs aggregation is generated by the ligand-analyte recognition, the larger changes can be expected in the AC hysteresis loop and their enclosed area. Since the multivalence leads to higher MNP entanglement, the larger sensitivity of SA94 based transducer is consistent.

Contrarily, the scenario is sensibly different for the MNPs where Néel relaxation mechanisms prevails (i.e. MF66). Figure 6.18 shows A$\rho_{Analyte=0}$ normalized hysteretic area upon the increase of analyte concentration for transducers based on MF66, classified according to the analyte valence.

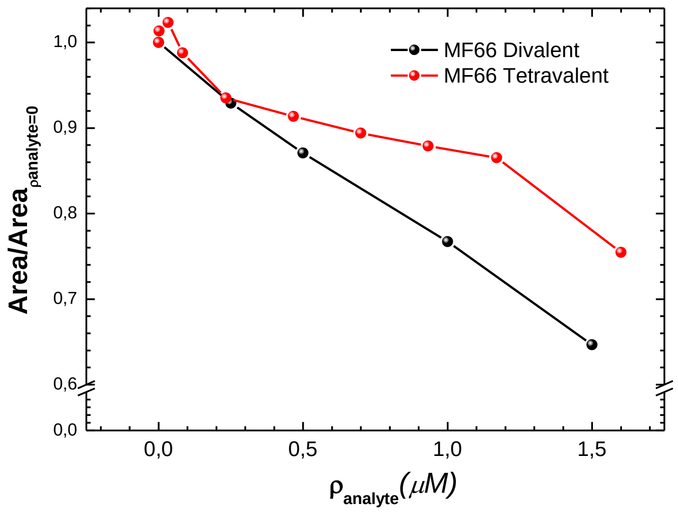

Figure 6.18. Normalized hysteretic area ($A/A_{\rho analyte=0}$) extracted from AC hysteresis loops of MF66-based systems, classified according to their valence (divalent: black dots, tetravalent: red dots) and plotted at increasing concentration of their respective analytes.

At low concentration of each respective analyte ($\rho_{analyte}$ = 0 - 0.23µM), the tetravalent case (Figure 6.18 - red dots) exhibits non-monotonic behavior of the slopes with respect to the divalent case, evidencing a better sensitivity for larger valences in this analyte concentration range. However, divalent MF66-based system shows a better sensitivity beyond $\rho_{analyte}$ = 0.23 µM and prior to the precipitation of both colloids, as the slope of the trend are steeper than its multivalent counterpart. As previously mentioned, the dynamical magnetic response of these particles is highly modulated by the intra-aggregates magnetic dipolar interactions and how those varies the effective magnetic anisotropy (K_{eff}). Hence, the spatial arrangement of the particles into the agglomerate becomes a key parameter since, as shown in Chapter 3, strongly determines the magnetizing or demagnetizing character of the dipole-dipole interaction. Unfortunately, this intra-aggregate spatial distribution of MNP is difficult to be experimentally verified, requiring the use of relatively advance microscopy techniques, such as cryo-TEM.[9] In any case, we can conclude that for the studied MF66 concentration (1 g_{Fe}/mL), the ligand-analyte recognition benefits from large relative variation of V_H values at analyte concentration lower than 200 nm. Other MNP concentration will lead to different scenario where sensitivity may vary.

6.4. Conclusions

Here, we have assessed the colloidal properties of 15 differently coated IONP by analyzing their ζ and D_H when dispersed in DDW, PBS and HBP. We observed that colloidal stability of the tested IONP coatings depends on the dispersion media observing similar behavior in HBP and PBS, where the changes of D_H are generally more pronounced in PBS. We have also assessed that the formation of the protein corona takes place for all tested coatings independently of their net surface charge but at different extent. Indeed, larger protein adsorption appeared when net charge value is large, independently of its sign. Interestingly, the formation of the protein corona onto IONP surface supplies a similar negative net charge for all tested IONP coatings. Besides, hydrophilicity influences the colloidal stability of IONP dispersed on ionic media. In addition, we found that the dynamical magnetic response of MNPs unveiled MNPs-biomolecule unspecific interaction phenomena, as long as that their magnetic relaxation mechanism (Néel or Brown) are indirectly altered by the protein adsorption.

Based on those results, we also demonstrated the suitability of using AC magnetometry to detect MNPs-biomolecule specific interactions. We found variations in the hysteresis loops of two core size ligand-functionalized MNPs (MF66 and SA94) upon the addition of a target analyte in both PBS and biological fluids (Human Blood Plasma). We disclosed that the sensitivity of this approach mainly lies on the following parameters: i) the magnetic relaxation mechanisms that prevails in the MNPs, ii) the valence of the ligand-analyte system, iii) the analyte concentration and iv) the AMF conditions. Our findings encourage further investigation towards the engineering of more complex MNPs nanostructures which, ultimately, will enable a more efficient magnetic detection of clinical biomarkers based on AC magnetometry and multivalent recognition ligands.

6.5. Methods

Materials

All reagents were commercially available and used as received without further purification. Human serum plasma was obtained from Biowest (Human Plasma Pooled Ref.: FT.S4180an).

Quantification of iron content in the magnetic colloids

The Fe concentration in the MNPs colloids was determined by measuring the Fe content by inductively coupled plasma mass spectrometry in ICP-MS NexION 300XX (PerkinElmer).

MNPs samples

Different types of iron oxide nanoparticles were investigated: 1) commercially available ferrofluids were obtained from Chemicell GmbH (magnetite core size indicated in Table 1, D_H=50 nm) with different coatings (fluidMAG-Amine, fluidMAG-DEAE, fluidMAG-PEG/Amine, fluidMAG-Chitosan, fluidMAG-D, fluidMAG-DX, fluidMAG-CMX, fluidMAG-PAA, fluidMAG-PEG/P, fluidMAG-PAS, fluidMAG-CT), from micromod Partikeltechnologie GmbH (iron oxide core size indicated in Table 1 D_H=50–70 nm) with different coatings (nanomag®-d-spio-BSA, nanomag®-d-spio-PEG-NH2, nanomag®-d-spio-PEG-COOH); 2)MF66 sample is maghemite IONPs coated with *meso*-2.3-dimercaptosuccinic acid (DMSA) were synthesized by Liquid Research Ltd in the frame of FP7 European project (MultiFun GA 262943) using a coprecipitation method [121] with controlled growth conditions giving a narrow size distribution. The particles are nominally Fe_3O_4 but the exact composition will lie between Fe_3O_4 and Fe_2O_3; 3) maghemite IONPs synthesized by a modified thermal decomposition method of an iron precursor. The resulting hydrophobic IONP were subsequently transferred to aqueous media after a ligand substitution procedure with *meso*-2.3-dimercaptosuccinic acid (DMSA)[46] . SA94 sample is $Co_{0.7}Fe_{2.3}O_4$ nanocubes 21 ± 2 nm size, from which Further details are provided in Annex I.[90]

Incubation of IONP in water, phosphate buffered saline, and human plasma

The studied IONP with different coatings were incubated at 2 $mg_{Fe}\ mL^{-1}$ in 1000 µL of DDW, PBS, and HBP for 1 h at 37 °C.

Colloidal characterization

The hydrodynamic size of the different IONP that is presented in the distinct media was obtained using a photocorrelation spectrometer (PCS) Brookhaven 90 plus (Zetasizer Nano from Malvern Instrument) from a dilute suspension of the IONP at 0.05 mg_{Fe} mL^{-1} in double distilled water pH 5.5 after incubation of IONP at 2 mg_{Fe} mL^{-1} for 1 h in double distilled water, PBS, or human plasma. The 40-fold dilution prior to the DLS measurements ensured that there was no contribution of any unbounded plasma protein. In all the cases the DLS measurements showed a unique size population corresponding to the IONP. The surface charge of IONP was determined after IONP incubation in the different media by measuring the zeta potential from a dilute suspension of the IONP at 0.05 mg_{Fe} mL^{-1} in double distilled water 0.01 m of KNO_3. The pH of the dilution was adjusted to 5.5 before the measurements. The zeta potential value of human plasma was determined from a 5 % dilute dispersion of HBP in DDW pH 5.5. The intensity size distributions were used for extracting D_H, and the pH value was adjusted to 5.5 for all DLS measurements.

MNPs functionalization

Monovalent system

1 mL of MF-66 or SA94 nanoparticles at 1.5 mg Fe/mL were incubated 1 hour at room temperature with 150 µmol of EDC/g Fe and 75 µmol of NHS/g Fe. Then, the samples was washed by cycles of centrifugation and redispersion in milliQ 10 mM sodium phosphate buffer pH 7.4 (PB buffer) at least 3 times. Later, glutathione S-transferase (GST)-MEEVF was reacted with the activated MF66 or SA94 MNPs. This pre-activated MNPs were incubated with 200 µl of GST-MEEVF at 7.5 µM in sodium phosphate buffer 10 mM (PB buffer), 4 h at room temperature and overnight at 4°C. After that, the MNPs functionalized with GST-MEEVF was purified by filtration thought a sepharose 6 CLB column using PB buffer. Samples of supernatants before and after the immobilization process were extracted and measured using Bradford assay. The number of GST-MEEVF molecules immobilized per MF66-MNP or SA94-MNP was 10 molecules (calculated considering the diameter of one MF66 MNP 12nm or SA94 MNP 21 nm, as measured by TEM using a JEOL JEM-1010. The amount of bound GST-MEEVF was determined as the difference between the remaining GST-MEEVF concentration in the supernatant at

ending of the immobilization process and the GST-MEEVF concentration at the beginning of the immobilization process (µmol GST-MEEVF/mgFe).

Divalent system

1 mL of MF-66 at 1.5 mg Fe/mL were incubated 1 hour at room temperature with 150 µmol of EDC/g Fe and 75 µmol of NHS/g Fe. Then, the sample was washed by cycles of centrifugation and redispersion in milliQ 10 mM sodium phosphate buffer pH 7.4 (PB buffer) at least 3 times. Then, glutathione S-transferase (GST)-MEEVF was reacted with the activated DMSA-MNP. This pre-activated DMSA-MNP were incubated with 200 µl of GST-MEEVF at 7.5 µM in sodium phosphate buffer 10 mM (PB buffer), 4 h at room temperature and overnight at 4°C. After that, the DMSA-MNP functionalized with GST-MEEVF was purified by filtration through a sepharose 6 CLB column using PB buffer. Samples of supernatants before and after the immobilization process were extracted and measured using Bradford assay. The number of GST-MEEVF molecules immobilized per DMSA-MNP was 10 molecules (calculated considering the diameter of one DMSA-MNP 12 nm, as measured by TEM (JEOL JEM-1010). The amount of bound GST-MEEVF was determined as the difference between the remaining GST-MEEVF concentration in the supernatant at ending of the immobilization process and the GST-MEEVF concentration at the beginning of the immobilization process (µmol GST-MEEVF/mgFe).

Tetravalent system

1 mL of MF66 or SA94 at 1.5 mg Fe/mL were incubated 1 hour at room temperature with 150 µmol of EDC/g Fe and 75 µmol of NHS/g Fe. Then, the sample was washed by cycles of centrifugation and redispersion in milliQ 10 mM sodium phosphate buffer pH 7.4 (PB buffer) at least 3 times.

Then, GST-AP-Biotin was reacted with the activated MF66 or SA94. The pre-activated MNPs were incubated with 200 µl of GST-AP-biotin at 7.5 µM in sodium phosphate buffer 10 mM (PB buffer), 4 h at room temperature and overnight at 4°C. After that, the MF66 or SA94 functionalized with GST-AP-biotin were purified by filtration through a sepharose 6 CLB column using PB buffer. Samples of supernatants before and after the immobilization process were extracted and measured using Bradford assay. The amount of bound GST-MEEVF was determined as the difference between the remaining GST-AP-biotin concentration in the supernatant at ending of the immobilization process and the GST-AP-biotin concentration at the beginning of the immobilization process (µmol GST-AP-biotin/mg Fe). The number of GST-AP-Biotin molecules immobilized per MF66 or SA94 MNP was 10 molecules (calculated considering 12 and 21 nm as the diameter of MF66 or SA94, respectively, measured by TEM (JEOL JEM-1010).

Ligand-functionalized MNPs incubation

Monovalent and divalent analyte systems

In monovalent system, 55 µl of MF66-GST-MEEVF or SA94-GST-MEEVF were incubated 60 minutes at 37ºC with 0, 0.25, 0.5, 0.75, 1.0, 1.5, 2.0, 2.5, 3 and 4 µM of VFP_m -TPR2-MMY in PBS. In divalent system, 55 µl of MF66-GST-MEEVF were incubated 60 minutes at 37ºC with 0, 0.25, 0.50, 1.0, and 1.5 µM of VFP_d -TPR2-MMY in PBS.

Multivalent system

55 µl of MF66-GST-AP-Biotin were incubated 60 minutes at 37ºC with 0, 0.083, 0.233, 0.466, 0.70, 0.93 1.17 and 1.6 µM of avidin in PBS. Also, 55 µl of SA94-GST-AP-Biotin were incubated 60 minutes at 37ºC with 0, 0.025, 0.050, 0.075, 0.100, 0.250, 0.500, 0.750, 1.000 and 1.500 µM of avidin in PBS.

For the magnetic measurements in biological fluids, 55 µl of MF66-GST-AP-Biotin were incubated 30 minutes at 37ºC with 0, 0.233, 0.70, 0.93, 1.17 and 1.6 µM of avidin in HBP.

General Conclusions

Conclusiones Generales

7

Chapter

7. General conclusions - *Conclusiones generales*

In the present work, we have studied the influence of different parameters on the dynamical magnetic response of magnetic nanoparticles for their use in biomedical applications. In order to evaluate the MNPs magnetic performance, their dynamical magnetic response was initially tested under biological-mimicking conditions to, finally, address the studies after interacting with live cells and biomolecules. We developed a home-made AC magnetometer in order to accomplish the proposed magnetic studies under alternating field conditions. This apparatus allowed us to perform AC hysteresis measurements of MNPs in colloidal dispersions (including ion- and protein-rich media), and inside live cells.

Once the prototype was tested, we studied the interacting phenomena on MNPs by AC magnetometry and calorimetry measurements. Thus, we examined the impact of inter and intra-aggregate magnetic dipolar interactions on the MNPs magnetic response, seeing the different phenomenology related to both types of magnetic dipolar interactions. Additionally, we experimentally presented other parameters that can modulate the magnetic dipolar interactions in MNPs colloids, such as the external field intensity (H_{MAX} and f) and the particle volume.

Later, we evaluated the role of the environmental viscosity on the dynamical magnetic response of MNPs colloids. We performed AC magnetometry, susceptometry and calorimetry measurements from selected MNPs of different barrier anisotropy values (i.e. distinct K and V) dispersed in increasingly viscous media. Our results provided conclusive evidences on the balance between those parameters determining the dominant magnetic relaxation process -namely size, size distribution, H_{MAX}, f and K- eventually define the viscosity sensitivity of the dynamical magnetic response of MNPs. We also proved the correlation between the AC hysteresis area to that of the SAR. In addition, we demonstrated the crucial role of the field conditions (field frequency and intensity) to modulate the magnetic relaxation mechanism.

After evaluating the aggregation and viscosity effects on the dynamical magnetic response of MNPs, we investigated how the interaction of MNPs with live cells and biomolecules affects their nanomagnetism. First, we investigated the influence of IONP cell internalization on their dynamical magnetic response by AC magnetometry and susceptometry. For understanding the results, we probed the viscosity and aggregation effects on MNP colloids by AC magnetic measurements. For that purpose, we employed viscosity and hydrodynamic size values similar to those of the subcellular vesicles. The comparison between these results obtained from MNPs inside live cells and in colloidal dispersions, with different viscosity and MNP aggregation degrees, pointed out that the intracellular MNPs clustering provides the major contribution to the studied MNPs magnetic response. Indeed, MNP clustering benefit magnetic dipolar interactions, favored by the large MNP agglomeration into subcellular vesicles (early and late endosome, and lysosomes).

Finally, we assessed the effects of dispersing MNPs in biological fluids on their magnetic response. We studied the colloidal properties of 15 differently coated IONP by dispersed in DDW, PBS and HBP. Colloidal parameters (D_H and ζ-) of the tested IONP coatings vary with the dispersion media observing similar trends of D_H and ζ in HBP and PBS, but changes of D_H are generally more pronounced in PBS. We found that the AC magnetometry of MNPs shed light on the nature of the changes of D_H thanks to its sensitivity to magnetic dipolar interactions. The unspecific interactions between MNP surface and serum proteins leads to the protein corona formation, which may modify the net surface charge. Such structure formation results in variation of D_H, favoring of magnetic dipolar interactions and consequently, changes of the AC hysteresis loops. Derived from these results, we also showed the suitability of AC magnetometry to unveil specific MNPs-biomarker interactions even in biological fluids (Human Blood Plasma), suggesting future applications of the AC magnetometry as displayer inside a biosensing platform for biomarkers detection. Parameters such as MNP composition and analyte multivalence have been tested for probing their influence on the sensitivity of these novel magnetic detection methodology.

Most of our experimental finding were theoretically supported by magnetic simulations performed by different collaborating groups. In a general manner, our results remark the importance of understanding the phenomenology related to the interaction of MNPs with biological entities and how this alter their magnetic response under AMF conditions. The know-how outcome of this thesis work will allow the design of novel nanostructures whose magnetic losses (i.e. magnetic hyperthermia efficiency) will remain non-influenced by viscosity and aggregation effects related to biological environments. Moreover, our findings encourage further investigation towards the engineering of more complex functionalized MNPs which, ultimately, will allow conception of an effective biomarkers sensing platform based on the use of AC magnetometer.

En el presente trabajo, hemos estudiado la influencia de diferentes parámetros en la respuesta magnética dinámica de nanopartículas magnéticas (NPM) cuyo uso se encuentra orientado a las aplicaciones biomédicas. Con el fin de evaluar su rendimiento, su respuesta magnética dinámica se testeó inicialmente en condiciones que imitaban diverso entorno biológico. Posteriormente, llevamos a cabo similares estudios una vez estas nanopartículas interaccionan con células vivas y biomoléculas.

Desarrollamos un magnetómetro de corriente alterna (CA) a fin de lograr los estudios magnéticos propuestos. Este aparato nos permitió realizar medidas de histéresis en CA de NPM en dispersiones coloidales (incluyendo medios ricos en iones y proteínas), así como dentro de células vivas.
Una vez puesto a punto el prototipo, estudiamos los fenómenos de interacción en NPM mediante magnetometría de CA y medidas de calorimetría bajo campos magnéticos CA (H_{CA})*. Examinamos el impacto de las interacciones dipolares magnéticas inter e intra-agregadas en la respuesta magnética de NPM, encontrando diferentes fenomenologías relacionadas con ambas tipologías de interacciones dipolares magnéticas. Junto a esto, evaluamos otros parámetros que presumiblemente modulan las interacciones dipolares magnéticas en los coloides MNP, como la intensidad del campo externo* (H_{MAX}) *y el volumen de las NPM.*

A continuación, evaluamos el papel de la viscosidad del medio de dispersión de las NPM en su respuesta magnética dinámica. Realizamos medidas de magnetometría CA, susceptometría CA y calorimetría de NPM seleccionadas según distintos valores de barrera de anisotropía (es decir, distintos K y V) dispersas en medios con viscosidad creciente. Nuestros resultados proporcionaron conclusiones sobre el equilibrio entre los parámetros que determinan el proceso de relajación magnética dominante -es decir, tamaño, distribución de tamaños, H_{MAX}*, frecuencia (f) y K- que finalmente definen la sensibilidad a la viscosidad de la respuesta magnética dinámica de las NPM. Demostramos la correlación entre el área de histéresis de los ciclos en CA y la tasa de absorción específica (TAE). Por otra parte, también demostramos el papel crucial que las* *condiciones de campo (H_{MAX} y f) juegan en la modulación de los mecanismos de relajación magnética.*

Conocidos los efectos que la viscosidad del medio y la agregación de las NPM ejercen sobre su respuesta magnética, investigamos como la interacción de las NPM con células vivas y biomoléculas afecta a su nanomagnetismo. Inicialmente, investigamos el efecto producido por la internalización de nanopartículas de óxido de hierro (NPOH) en células cancerígenas a su respuesta magnética dinámica, valiéndonos de magnetometría de CA y susceptometría de CA. Para una mejor interpretación de los resultados, llevamos también a cabo medidas magnéticas en CA de las NPOH variando la viscosidad y su estado de agregación, en rangos similares a los que se pueden encontrar cuando las NPOH ocupan las vesículas intracelulares. La confrontación entre los resultados obtenidos dentro de células vivas y en dispersiones coloidales, modificadas de acuerdo con distintas magnitudes de viscosidad y grados de agregación de las NPOH, señaló que la "clusterización" intracelular de las NPOH contribuye mayoritariamente a la variación de la respuesta magnética de NPOH. Tal hecho tiene lugar debido al incremento de las interacciones dipolares magnéticas (endosoma temprano y tardío, y lisosomas).

Finalmente, evaluamos la respuesta magnética dinámica de las NPOH cuando son dispersadas en fluidos biológicos. Estudiamos en primer lugar las propiedades coloidales de 15 NPOH, recubiertas con distintos recubrimientos, dispersas en agua de doble destilación (ADD), tampón fosfato salino (TFS) y plasma sanguíneo humano (PSH). Los parámetros coloidales (D_H y ζ) de las NPOH varían según los medios en los que son dispersadas, observando tendencias similares en ambos parámetros en PSH y TFS, si bien los cambios de D_H son generalmente más pronunciados en TFS. Descubrimos por otra parte que la magnetometría de CA arroja luz sobre la naturaleza de los cambios de D_H, gracias a su sensibilidad a las interacciones dipolares magnéticas y a cambios en el volumen hidrodinámico (V_H). Las interacciones inespecíficas entre la superficie de MNP y las proteínas del suero conducen a la formación de una corona de proteínas, la cual puede modificar la carga neta superficial. Dicha formación de estructura da como resultado una variación de D_H, favoreciendo las interacciones dipolares magnéticas y, en *consecuencia, provocando cambios en los ciclos de histéresis de CA. También demostramos la idoneidad de la magnetometría de CA para revelar interacciones específicas de biomarcadores de NPM incluso en fluidos biológicos (PSH), sugiriendo aplicaciones futuras de la magnetometría de CA como visualizador dentro de una plataforma de detección de biomarcadores. En relación con esto, parámetros como la composición de NPM y valencia del analito han sido probados por su influencia en la sensibilidad de esta novedosa metodología de detección magnética.*

La mayoría de nuestros hallazgos experimentales fueron apoyados teóricamente por simulaciones magnéticas realizadas por diferentes grupos colaboradores. De una forma general, nuestros resultados remarcan la importancia de entender los fenómenos derivados de la interacción de las NPM con entidades biológicas, y como esta interacción modifica la respuesta magnética de las NPM una vez expuestas a condiciones H_{CA}.

Los resultados de este trabajo de tesis permitirán el diseño de nuevas nanoestructuras cuyas pérdidas magnéticas (i.e. eficiencia en la hipertermia magnética) se mantendrá invariable a los cambios en la viscosidad del entorno de las NPM y a su estado de agregación que tiene lugar en entidades biológicas. Por otra parte, nuestros hallazgos animan a potenciar una mayor investigación de NPM funcionalizadas que, ulteriormente, permitirán la concepción de una plataforma sensórica de biomarcadores basada en el uso de magnetometría de CA.

ANNEX I – Magnetic nanoparticles samples

G54, G31 and R26

G and *R* series are DMSA coated iron oxide nanoparticles prepared by a modified thermal decomposition of iron organic precursors previously reported[46] by Dr. Gorka Salas' group. **Figure A1** shows a TEM micrograph of G54, G31 and R26. G54 and G31 present faceted shape, whereas R26 present a more rounded morphology. D_H = 56 nm and a polydispersity index (PDI) equal to 0.2.

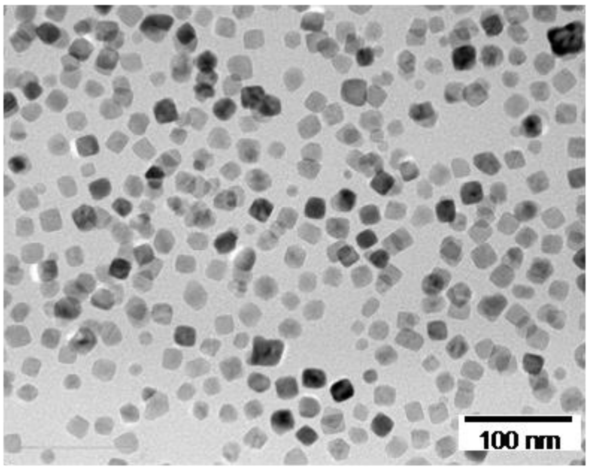
a)

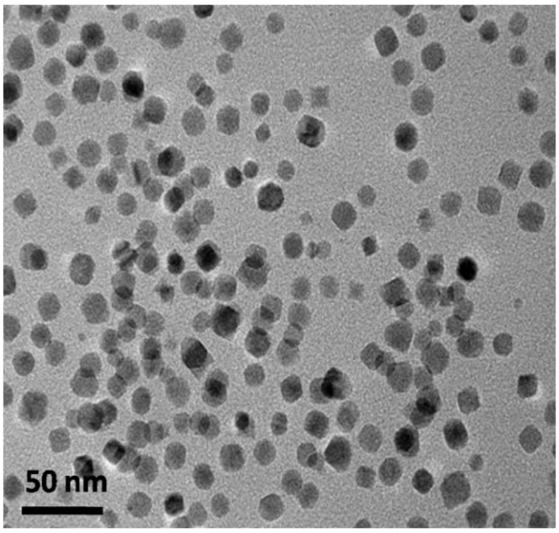
b)

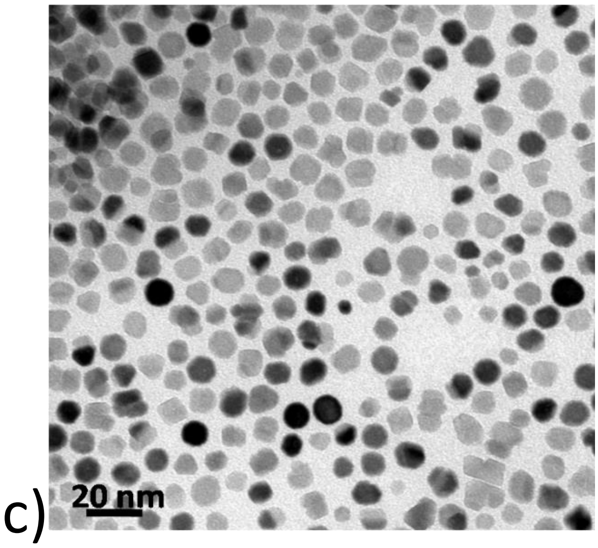

Figure A1. Selected TEM micrograph of a)G54, b)G31 and c)R26 sample.

In **Figure A2**, core size distribution of G54 sample extracted from TEM images and hydrodynamic size in water dynamic is presented. Referring to core size, a value of 20 ± 3 nm was determined (Fig.2a). Otherwise, hydrodynamic size measurements yielded a value *D_H* = 56 nm and polydispersity index (PDI) equal to 0.2 (Fig. 1b) when water dispersed.

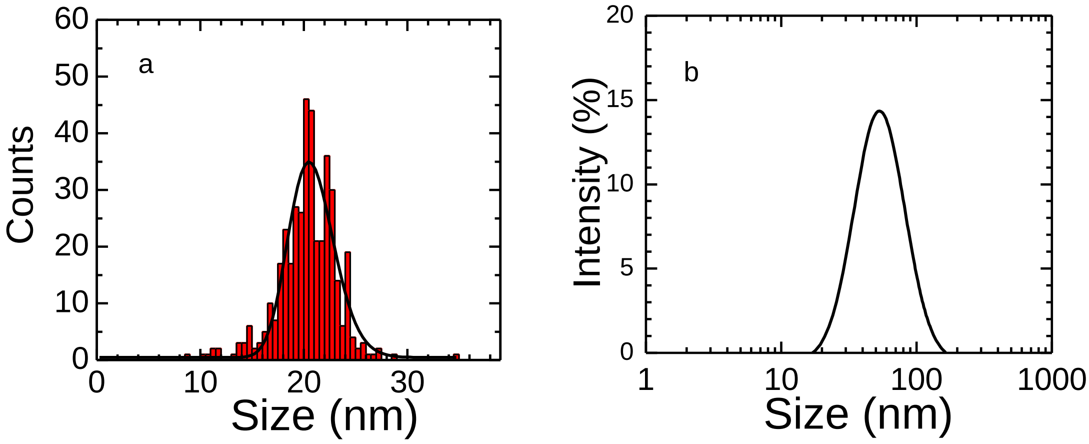

Figure A2. Histograms of G54 IONP a) core size distribution and b) hydrodynamic size in water.

Figure A3 shows core and hydrodynamic size distribution for R26 and G31 samples. In this case, core sizes of 19 ± 3 nm for R26 and 12 ± 1 nm were found for R26 and G31 samples, respectively. Referring to hydrodynamic size, both IONPs yield comparable values in water – D_H = 48nm and PDI= 0.2 for R26; D_H = 49 nm and PDI = 0.22 for G31.

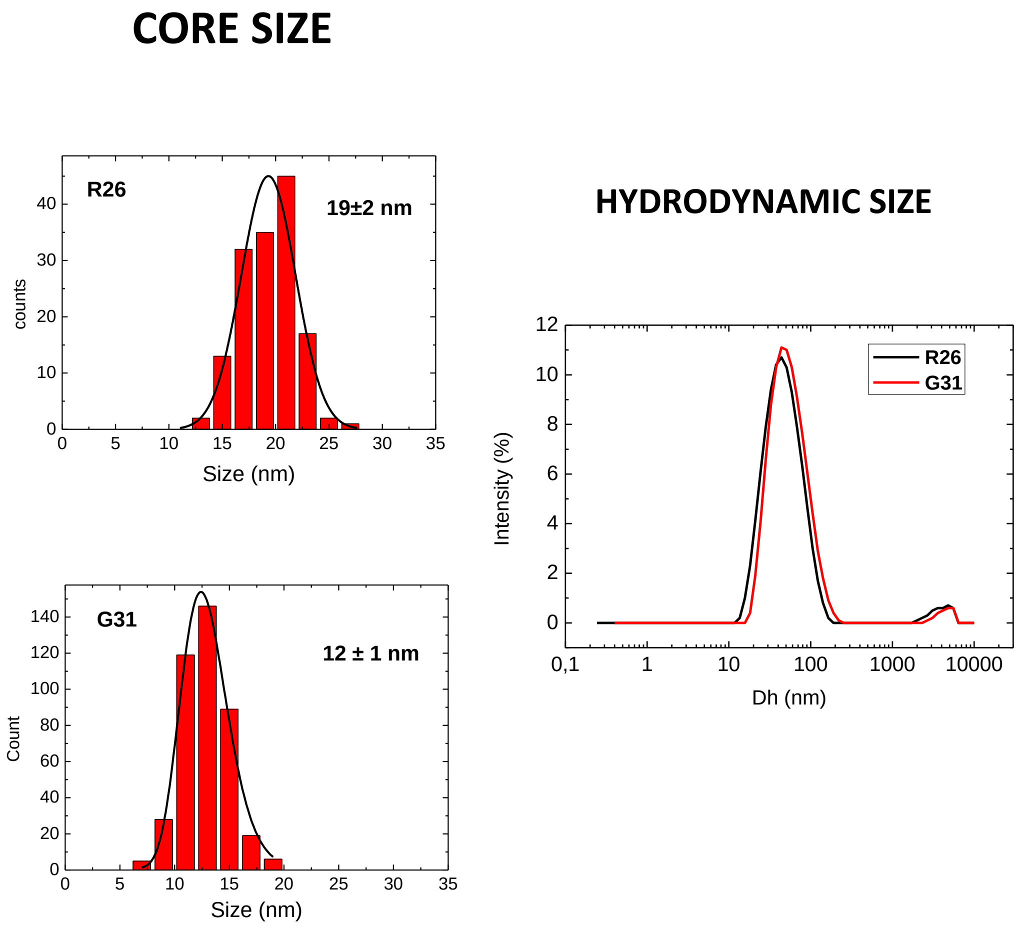

Figure A3. R26 and G31 IONPs core size distribution and hydrodynamic size diagrams.

Magnetisation under quasi-static conditions

Magnetization curves of G54 dispersed in water were measured in VSM at T = 5 and 250 K (**Figure A4**). M_S shows values close to 60 A m^2 kg^{-1} are reached beyond H = ±2.4 MA m^{-1} near room temperature. At the same time, M_S values are slightly sensitive to temperature increasing by 8% when lowering temperature from 250 to 5 K. Besides, coercive fields (H_C) and remanent magnetization (M_R) values are negligible at 250 K, underlying the superparamagnetic-like behaviour of the studied G54 sample at near room temperature.

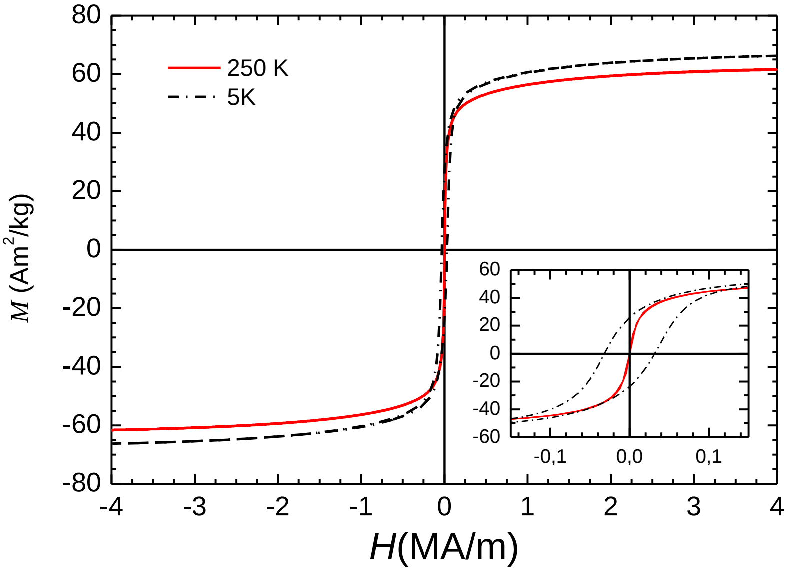

Figure A4. Iron oxide mass-normalized magnetization cycles of sample G54 at 5 K (dashed line) and 250 K (solid line). Insets: details of the magnetization curves at low magnetic fields.

In the case of R26 and G31 IONPs, DC loops measured at near room temperature (250 K) show again superparmagnetic-like behavior since coercive field (H_C) and remanent magnetization (M_R) values are near to zero (**Fig. A5**). Remarkably, both samples reach comparable magnetisation saturation values (M_S) despite of their different magnetic core size volume – 68 A m^2 kg^{-1} for R26 sample and 66 A m^2 kg^{-1} for G31 sample.

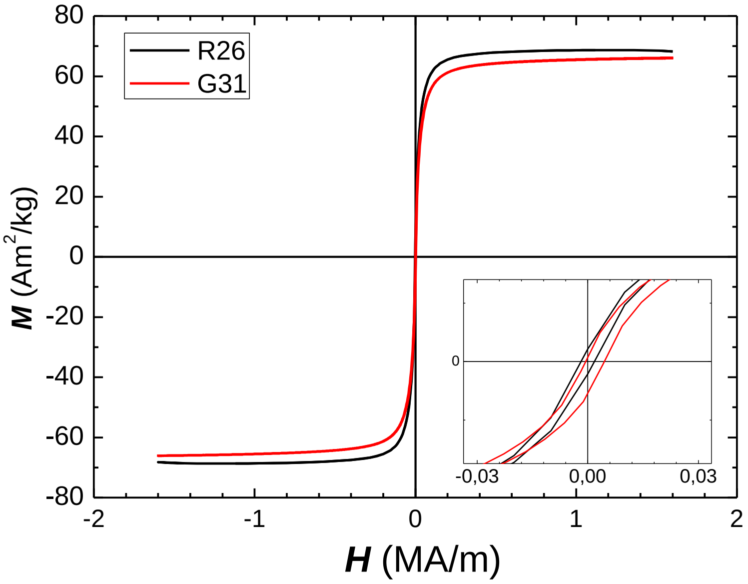

Figure A5. Iron oxide mass normalized loops of R26 and G31 samples at 250 K. Insets: details of the magnetization curves at low magnetic fields.

M195, M221 and SA94

M series samples consist of Iron Oxide Nanocubes (IONCs) with edge sizes, extracted from TEM images (**Figure A6**), of 14 ± 2 and 24 ± 4 nm were synthesized by thermal decomposition method as described elsewhere[16,17] by Dr. Teresa Pellegrino's group. Briefly, to obtain Fe_3O_4 nanocubes of 14 nm size, 0.353 g (1 mmol) of iron(III) acetylacetonate with 1.04 g (6 mmol) decanoic acid and 15 mL dibenzyl ether were dissolved in 10 mL squalane in a 50 mL three-neck flask. After degassing for 120 min at 65 °C, the mixture was heated up to 200 °C (3 °C/min) and kept at this value for 2.5 h. Finally, the temperature was increased at a heating rate of 7 °C/min up to 310 °C or reflux temperature and maintained at this value for 1 h. After cooling down to room temperature, 60 mL acetone was added, and the whole solution was centrifuged at 8500 rpm. After removing the supernatant, the black precipitate was dispersed in 2–3 mL chloroform, and the washing procedure was repeated at least two more times. Finally, the collected particles were dispersed in 15 mL chloroform. Fe_3O_4 nanocubes with 24 nm edge size were obtained following the same protocol but using 4 instead of 6 mmol decanoic acid.

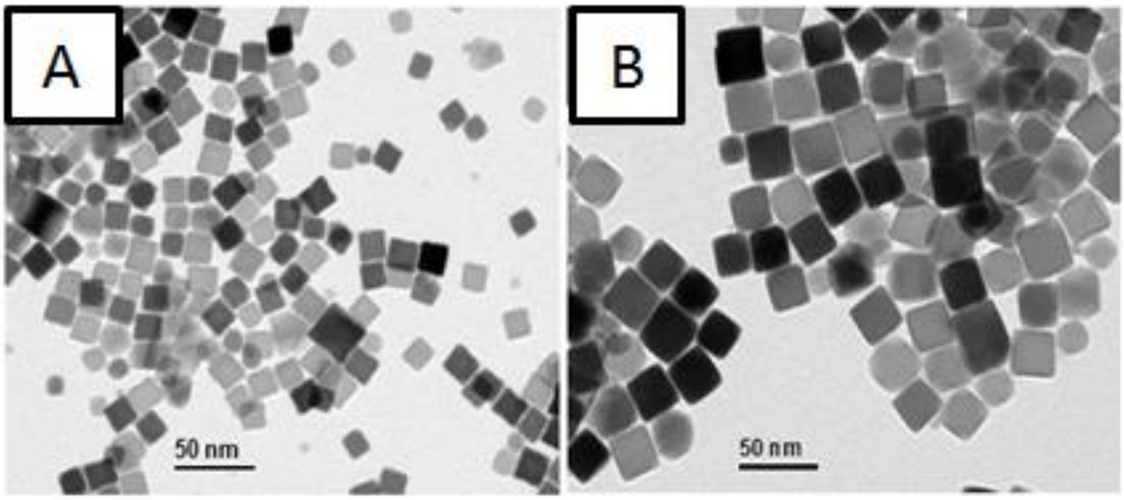

Figure A6. Selected TEM micrograph of a)M195 and b)M221 extracted from ref. [61]

Transfer of IONCs to water

IONCs were transferred into water by exchanging their surfactant molecules with gallic acid PEG ligand (GA-PEG) as described elsewhere.[17] Briefly, at the end of the IONCs synthesis after reducing the temperature of the reaction mixture from 310 to 70 °C, 15 mL GA-PEG solution (0.1 M in chloroform containing 1 mL triethylamine) was injected and the resulting mixture was stirred overnight at constant temperature. Then, the mixture was allowed to cool to room temperature and was transferred to a separating funnel. 10 mL de-ionized water was added, resulting in the formation of two phases. After emulsification by means of shaking, the phases were allowed to separate and the aqueous phase containing the IONCs bearing GA-PEG was collected. This step was repeated until all nanocubes were transferred into water. Then, the solution was concentrated under reduced pressure at 40 °C to a final volume of about 50 mL and the excess of GA-PEG was removed by dialysis versus 5L de-ionized water, using cellulose membrane tubing with a pore size of 50 kDa. The sample was dialyzed overnight at room temperature. This step was repeated five times. Finally, the IONCs solution was concentrated by centrifugation with a centrifuge filter (molecular cut-off point 100 kDa). The IONCs dispersed in aqueous media were employed for structural, colloidal and magnetic studies.

SA94 series consists of $Co_xFe_{3-x}O_4$ nanocubes with edge sizes, extracted from TEM images (**Figure A7**), of 21 ± 2 nm and cobalt fraction of x=0.7 were synthesized by thermal decomposition, following a procedure described elsewhere,[122] by Dr. Teresa Pellegrino's group. In a three-neck flask connected to a standard Schlenk line, 0.71 mmol (183 mg) $Co(acac)_2$, 0.84 mmol (297 mg) $Fe(acac)_3$, and 6 mmol (1.04 g) decanoic acid were dissolved in a mixture of 7 mL squalane and 18 mL benzyl ether. The resulting deep red solution was degassed at 65 °C for 2 h under reduced pressure of 50 mTorr. Under N_2 flow, the mixture temperature was increased to 200 °C at the rate of 5 °C/min and kept at 200 °C for 2 h. The reaction temperature was increased to 305 °C at the rate of 7.5 °C/min, and then the mixture was kept at reflux for 1 h. The flask was cooled down to room temperature under inert atmosphere. The black colloidal solution was washed three times with excess amount of isopropanol (10 mL) and acetone (30 mL) mixture and centrifuged at 4500 rpm for 10 min. The final particles were dispersed in chloroform (8 mL) for further measurements.

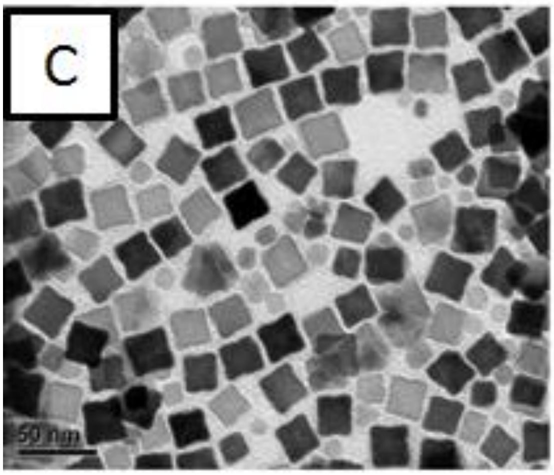

Figure A7. Representative TEM micrographs SA94 MNP extracted from ref. [61]

Transfer of CoFeNCs to water

The as-synthesized, hydrophobic CoFeNCs were transferred into water by using poly(maleic anhydride-alt-1-octadecene) following a protocol described previously.[122-124] Initially, 21 nm size nanocubes (3 mL with Co and Fe concentrations of 4.3 and 8.3 g/L) were diluted with excess amount of chloroform (200 mL) and sonicated for 10 min. A specific amount of poly(maleic anhydride-alt-1-octadecene) solution in chloroform (137 mM, concentration referred to the monomer unit) was added by fixing 500 molecules of monomer unit per each nm^2 of nanocube surface, and the solvent was evaporated under reduced pressure (fixed at 460 mbar) until complete solvent evaporation. The sample was then resuspended in 20 mL of borate buffer and was shaken overnight at 65 °C. The well-dispersed sample was concentrated to nearly 2 mL with centrifuge filters (Amicon ultra, with 100 kDa in molecular weight cut off) by sequential centrifugation steps at room temperature (RT) and 1500 rpm for 10 min per each cycle. Subsequently, the nanocubes were separated from the free polymer by ultracentrifugation at 30000 rpm for 60 min on sucrose gradient (2 mL of 20%, 4 mL of 40%, and 3 mL of 60% in a ultracentrifuge tube, from top to bottom). Excessive polymer (visible under ultraviolet (UV) lamp) at the 20% sucrose was removed by syringe aspiration, and the nanocubes were usually found in the fraction at 40−60% of the sucrose gradient. The collected sample was washed further with a borate buffer solution (pH 9) several times to remove the excess of sucrose, and finally it was dispersed in buffer solution. The CoFeNCs dispersed in aqueous media were employed for structural, colloidal and magnetic studies.

Magnetisation under quasi-static conditions

Field dependent magnetic measurements under quasi-static conditions were performed by Teresa Pellegrino’s group. Measurements were carried out at 260 K in an ever-cooled Magnetic Property Measurement System (*MPMS-XL*, Quantum Design) on nanoparticle dispersion volumes of 100μL at concentration of 2 g_{Fe}/L. The nanoparticles were physically blocked by slowly cooling the sample from room temperature to 260 K. The magnetization signal was normalized to the mass of magnetic material (i.e. magnetite or cobalt ferrite). As easily appreciated in their DC magnetization loops (**Figure A8**), M-samples showed superparamagnetic-like behavior at room temperature. SA94 samples instead presents a considerable coercivity, evidencing its blocking character at room temperature.

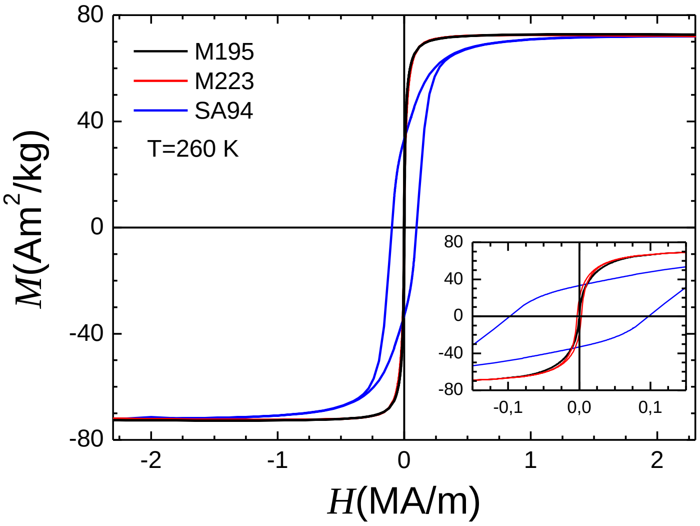

Figure A8. Mass-normalized magnetization cycles measured at 260 K for 14 nm IONCs (black line), 24 nm IONCs (red line), and 21 nm CoFeNCs(blue line) dispersed in water.

FM2-CT

The 11nm core size magnetite IONPs, coated with citrate, are commercial IONPs (fluidMAG-CT, product number: 4122-5, hydrodynamic diameter 50nm) produced by Chemicell GmbH, Berlin (Germany). Core size were determi

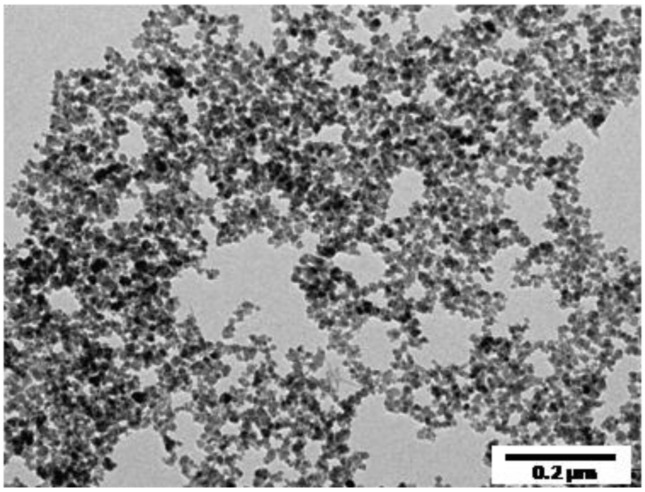

Figure A9. Representative TEM micrographs FM2-CT sample.

DC7

DC7 sample were prepared from commercial maghemite iron oxide powder (Iron(III) oxide, <50nm particle size, sigma reference 544884-25G) produced and distributed by at Sigma-Aldrich Corporation, Saint Louis, USA. From the original powder state, these IONPs were coated with citrate according to *Răcicu et al.* protocol.[125]

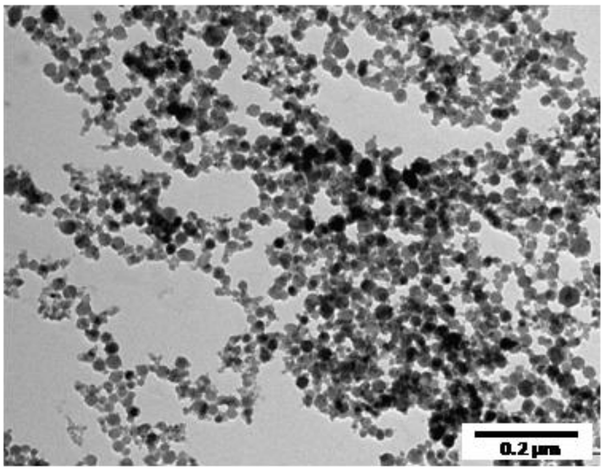

Figure A10. Representative TEM micrographs DC7 sample.

References

1 Di Corato, R. *et al.* Magnetic hyperthermia efficiency in the cellular environment for different nanoparticle designs. *Biomaterials* **35**, 6400-6411, doi:http://dx.doi.org/10.1016/j.biomaterials.2014.04.036 (2014).

2 Kuimova, M. K., Yahioglu, G., Levitt, J. A. & Suhling, K. Molecular rotor measures viscosity of live cells via fluorescence lifetime imaging. *Journal of the American Chemical Society* **130**, 6672-6673, doi:10.1021/ja800570d (2008).

3 Lévy, M., Gazeau, F., Bacri, J.-C., Wilhelm, C. & Devaud, M. Modeling magnetic nanoparticle dipole-dipole interactions inside living cells. *Physical Review B* **84**, 075480 (2011).

4 Levy, M. *et al.* Nanomagnetism reveals the intracellular clustering of iron oxide nanoparticles in the organism. *Nanoscale* **3**, 4402-4410, doi:10.1039/c1nr10778j (2011).

5 Chiappi, M. *et al.* Cryo-soft X-ray tomography as a quantitative three-dimensional tool to model nanoparticle:cell interaction. *Journal of Nanobiotechnology* **14**, 15, doi:10.1186/s12951-016-0170-4 (2016).

6 Coral, D. F. *et al.* On the effect of nanoclustering and dipolar interactions in heat generation for magnetic hyperthermia. *Langmuir*, doi:10.1021/acs.langmuir.5b03559 (2016).

7 Materia, M. E. *et al.* Mesoscale Assemblies of Iron Oxide Nanocubes as Heat Mediators and Image Contrast Agents. *Langmuir* **31**, 808-816, doi:10.1021/la503930s (2015).

8 Aslibeiki, B., Kameli, P. & Salamati, H. The effect of dipole-dipole interactions on coercivity, anisotropy constant, and blocking temperature of MnFe2O4 nanoparticles. *Journal of Applied Physics* **119**, 063901, doi:doi:http://dx.doi.org/10.1063/1.4941388 (2016).

9 Etheridge, M. L. *et al.* Accounting for biological aggregation in heating and imaging of magnetic nanoparticles. *TECHNOLOGY* **02**, 214-228, doi:10.1142/s2339547814500198 (2014).

10 Rudolf, H., Silvio, D. & Michael, R. Effects of size distribution on hysteresis losses of magnetic nanoparticles for hyperthermia. *Journal of Physics: Condensed Matter* **20**, 385214 (2008).

11 Vergés, M. A. *et al.* Uniform and water stable magnetite nanoparticles with diameters around the monodomain–multidomain limit. *Journal of Physics D: Applied Physics* **41**, 134003 (2008).

12 Périgo, E. A. *et al.* Fundamentals and advances in magnetic hyperthermia. *Applied Physics Reviews* **2**, 041302, doi:doi:http://dx.doi.org/10.1063/1.4935688 (2015).

13 Maier-Hauff, K. *et al.* Efficacy and safety of intratumoral thermotherapy using magnetic iron-oxide nanoparticles combined with external beam radiotherapy

on patients with recurrent glioblastoma multiforme. *Journal of Neuro-Oncology* **103**, 317-324, doi:10.1007/s11060-010-0389-0 (2011).

14 Johannsen, M. *et al.* Clinical hyperthermia of prostate cancer using magnetic nanoparticles: Presentation of a new interstitial technique. *International Journal of Hyperthermia* **21**, 637-647, doi:10.1080/02656730500158360 (2005).

15 Salas, G. *et al.* Modulation of Magnetic Heating via Dipolar Magnetic Interactions in Monodisperse and Crystalline Iron Oxide Nanoparticles. *The Journal of Physical Chemistry C* **118**, 19985-19994, doi:10.1021/jp5041234 (2014).

16 Guardia, P. *et al.* Water-Soluble Iron Oxide Nanocubes with High Values of Specific Absorption Rate for Cancer Cell Hyperthermia Treatment. *ACS Nano* **6**, 3080-3091, doi:10.1021/nn2048137 (2012).

17 Guardia, P. *et al.* One pot synthesis of monodisperse water soluble iron oxide nanocrystals with high values of the specific absorption rate. *Journal of Materials Chemistry B* **2**, 4426-4434, doi:10.1039/c4tb00061g (2014).

18 Arami, H., Khandhar, A., Liggitt, D. & Krishnan, K. M. In vivo delivery, pharmacokinetics, biodistribution and toxicity of iron oxide nanoparticles. *Chemical Society Reviews* **44**, 8576-8607, doi:10.1039/c5cs00541h (2015).

19 Pankhurst, Q., Connolly, J., Jones, S. & Dobson, J. Applications of magnetic nanoparticles in biomedicine. *J Phys D Appl Phys* **36**, R167 (2003).

20 Martinez-Boubeta, C. *et al.* Adjustable Hyperthermia Response of Self-Assembled Ferromagnetic Fe-MgO Core–Shell Nanoparticles by Tuning Dipole–Dipole Interactions. *Advanced Functional Materials* **22**, 3737-3744, doi:10.1002/adfm.201200307 (2012).

21 Latorre, A., Couleaud, P., Aires, A., Cortajarena, A. L. & Somoza, Á. Multifunctionalization of magnetic nanoparticles for controlled drug release: A general approach. *European Journal of Medicinal Chemistry* **82**, 355-362, doi:https://doi.org/10.1016/j.ejmech.2014.05.078 (2014).

22 Bauer, L. M., Situ, S. F., Griswold, M. A. & Samia, A. C. S. Magnetic Particle Imaging Tracers: State-of-the-Art and Future Directions. *The Journal of Physical Chemistry Letters* **6**, 2509-2517, doi:10.1021/acs.jpclett.5b00610 (2015).

23 Fornara, A. *et al.* Tailored Magnetic Nanoparticles for Direct and Sensitive Detection of Biomolecules in Biological Samples. *Nano Letters* **8**, 3423-3428, doi:10.1021/nl8022498 (2008).

24 Lévy, M., Wilhelm, C., Devaud, M., Levitz, P. & Gazeau, F. How cellular processing of superparamagnetic nanoparticles affects their magnetic behavior and NMR relaxivity. *Contrast Media & Molecular Imaging* **7**, 373-383, doi:10.1002/cmmi.504 (2012).

25 Amiri, H. *et al.* Protein corona affects the relaxivity and MRI contrast efficiency of magnetic nanoparticles. *Nanoscale* **5**, 8656-8665, doi:10.1039/c3nr00345k (2013).

26 Fortin, J.-P., Gazeau, F. & Wilhelm, C. Intracellular heating of living cells through Néel relaxation of magnetic nanoparticles. *European Biophysics Journal* **37**, 223-228, doi:10.1007/s00249-007-0197-4 (2008).

27 Shen, H., Tong, S., Bao, G. & Wang, B. Structural responses of cells to intracellular magnetic force induced by superparamagnetic iron oxide nanoparticles. *Physical Chemistry Chemical Physics* **16**, 1914-1920, doi:10.1039/c3cp51435h (2014).

28 Fortin, J.-P. *et al.* Size-Sorted Anionic Iron Oxide Nanomagnets as Colloidal Mediators for Magnetic Hyperthermia. *Journal of the American Chemical Society* **129**, 2628-2635, doi:10.1021/ja067457e (2007).

29 Soukup, D., Moise, S., Céspedes, E., Dobson, J. & Telling, N. D. In Situ Measurement of Magnetization Relaxation of Internalized Nanoparticles in Live Cells. *ACS Nano* **9**, 231-240, doi:10.1021/nn503888j (2015).

30 Coey, J. M. D. *Magnetism and magnetic materials*. (2010).

31 Hernando, A. & Rojo, J. M. *Física de los Materiales Magnéticos*. (2001).

32 Wohlfarth, E. P. Relations between Different Modes of Acquisition of the Remanent Magnetization of Ferromagnetic Particles. *Journal of Applied Physics* **29**, 595-596, doi:doi:http://dx.doi.org/10.1063/1.1723232 (1958).

33 Brown, W. F. Thermal Fluctuations of a Single-Domain Particle. *Physical Review* **130**, 1677-1686 (1963).

34 Coffey, W. T. & Kalmykov, Y. P. Thermal fluctuations of magnetic nanoparticles: Fifty years after Brown. *Journal of Applied Physics* **112**, doi:10.1063/1.4754272 (2012).

35 Néel, L. Théorie du traînage magnétique des ferromagnétiques en grains fins avec application aux terres cuites. *Annales de Géophysique* **5**, 99-136 (1949).

36 Rosensweig, R. E. Heating magnetic fluid with alternating magnetic field. *Journal of Magnetism and Magnetic Materials* **252**, 370-374, doi:10.1016/s0304-8853(02)00706-0 (2002).

37 Ruta, S., Chantrell, R. & Hovorka, O. Unified model of hyperthermia via hysteresis heating in systems of interacting magnetic nanoparticles. *Scientific Reports* **5**, doi:10.1038/srep09090 (2015).

38 Mehdaoui, B. *et al.* Optimal Size of Nanoparticles for Magnetic Hyperthermia: A Combined Theoretical and Experimental Study. *Advanced Functional Materials* **21**, 4573-4581, doi:10.1002/adfm.201101243 (2011).

39 Usov, N. A. & Liubimov, B. Y. Dynamics of magnetic nanoparticle in a viscous liquid: Application to magnetic nanoparticle hyperthermia. *Journal of Applied Physics* **112**, 023901, doi:doi:http://dx.doi.org/10.1063/1.4737126 (2012).

40 Takashi, Y. & Keiji, E. Simulation and Quantitative Clarification of AC Susceptibility of Magnetic Fluid in Nonlinear Brownian Relaxation Region. *Japanese Journal of Applied Physics* **48**, 127002 (2009).

41 Mamiya, H. & Jeyadevan, B. Hyperthermic effects of dissipative structures of magnetic nanoparticles in large alternating magnetic fields. *Scientific Reports* **1**, 157, doi:10.1038/srep00157

http://www.nature.com/articles/srep00157#supplementary-information (2011).

42 Carrey, J., Mehdaoui, B. & Respaud, M. Simple models for dynamic hysteresis loop calculations of magnetic single-domain nanoparticles: Application to magnetic hyperthermia optimization. *Journal of Applied Physics* **109**, 083921, doi:doi:http://dx.doi.org/10.1063/1.3551582 (2011).

43 Braunschweig, T. U. C.-W. z. <http://www.emg.ing.tu-bs.de/forschung/material/magmat_d.html> (

44 Kharisov, B. I. *et al.* Solubilization, dispersion and stabilization of magnetic nanoparticles in water and non-aqueous solvents: recent trends. *RSC Advances* **4**, 45354-45381, doi:10.1039/C4RA06902A (2014).

45 Yallapu, M. M., Foy, S. P., Jain, T. K. & Labhasetwar, V. PEG-Functionalized Magnetic Nanoparticles for Drug Delivery and Magnetic Resonance Imaging Applications. *Pharmaceutical research* **27**, 2283-2295, doi:10.1007/s11095-010-0260-1 (2010).

46 Salas, G. *et al.* Controlled synthesis of uniform magnetite nanocrystals with high-quality properties for biomedical applications. *Journal of Materials Chemistry* **22**, 21065-21075, doi:10.1039/C2JM34402E (2012).

47 Rose, P. A. *et al.* Drug Embedded PVP Coated Magnetic Nanoparticles for Targeted Killing of Breast Cancer Cells. *Technology in Cancer Research & Treatment* **12**, 463-472, doi:10.7785/tcrt.2012.500333 (2013).

48 Blanco-Andujar, C. *et al.* Real-time tracking of delayed-onset cellular apoptosis induced by intracellular magnetic hyperthermia. *Nanomedicine* **11**, 121-136, doi:10.2217/nnm.15.185 (2015).

49 Aires, A., Cabrera, D., Alonso-Pardo, L. C., Cortajarena, A. L. & Teran, F. J. Elucidation of the Physicochemical Properties Ruling the Colloidal Stability of Iron Oxide Nanoparticles under Physiological Conditions. *ChemNanoMat* **3**, 183-189, doi:10.1002/cnma.201600333 (2017).

50 Kuimova, M. K. *et al.* Imaging intracellular viscosity of a single cell during photoinduced cell death. *Nat Chem* **1**, 69-73, doi:http://www.nature.com/nchem/journal/v1/n1/suppinfo/nchem.120_S1.html (2009).

51 Andreu, I. & Natividad, E. Accuracy of available methods for quantifying the heat power generation of nanoparticles for magnetic hyperthermia. *International Journal of Hyperthermia* **29**, 739-751, doi:10.3109/02656736.2013.826825 (2013).

52 Moise, S. *et al.* The cellular magnetic response and biocompatibility of biogenic zinc- and cobalt-doped magnetite nanoparticles. *Scientific Reports* **7**, doi:10.1038/srep39922 (2017).

53 Foner, S. Versatile and Sensitive Vibrating-Sample Magnetometer. *Review of Scientific Instruments* **30**, 548-557, doi:10.1063/1.1716679 (1959).

54 Romani, G. L., Williamson, S. J. & Kaufman, L. Biomagnetic instrumentation. *Review of Scientific Instruments* **53**, 1815-1845, doi:10.1063/1.1136907 (1982).

55 Bannunah, A. M., Vllasaliu, D., Lord, J. & Stolnik, S. Mechanisms of Nanoparticle Internalization and Transport Across an Intestinal Epithelial Cell Model: Effect of Size and Surface Charge. *Molecular Pharmaceutics* **11**, 4363-4373, doi:10.1021/mp500439c (2014).

56 Oh, N. & Park, J.-H. Endocytosis and exocytosis of nanoparticles in mammalian cells. *International Journal of Nanomedicine* **9**, 51-63, doi:10.2147/IJN.S26592 (2014).

57 Ocampo, S. M. *et al.* g-force induced giant efficiency of nanoparticles internalization into living cells. *Scientific Reports* **5**, 15160, doi:10.1038/srep15160

https://www.nature.com/articles/srep15160#supplementary-information (2015).

58 Chen, C.-C. V. *et al.* Simple SPION Incubation as an Efficient Intracellular Labeling Method for Tracking Neural Progenitor Cells Using MRI. *PLOS ONE* **8**, e56125, doi:10.1371/journal.pone.0056125 (2013).

59 Calero, M. *et al.* Efficient and safe internalization of magnetic iron oxide nanoparticles: Two fundamental requirements for biomedical applications. *Nanomedicine: Nanotechnology, Biology and Medicine* **10**, 733-743, doi:10.1016/j.nano.2013.11.010.

60 Ovejero, J. G. *et al.* Effects of inter- and intra-aggregate magnetic dipolar interactions on the magnetic heating efficiency of iron oxide nanoparticles. *Physical Chemistry Chemical Physics* **18**, 10954-10963, doi:10.1039/c6cp00468g (2016).

61 Cabrera, D. *et al.* Unraveling viscosity effects on the hysteresis losses of magnetic nanocubes. *Nanoscale* **9**, 5094-5101, doi:10.1039/c7nr00810d (2017).

62 Teran, F. J. *et al.* Accurate determination of the specific absorption rate in superparamagnetic nanoparticles under non-adiabatic conditions. *Applied Physics Letters* **101**, 062413, doi:10.1063/1.4742918 (2012).

63 Garaio, E., Collantes, J M., Plazaola, F., Garcia, J A. & Castellanos-Rubio, I. A multifrequency eletromagnetic applicator with an integrated AC magnetometer for magnetic hyperthermia experiments. *Measurement Science and Technology* **25**, 115702 (2014).

64 Connord, V., Mehdaoui, B., Tan, R. P., Carrey, J. & Respaud, M. An air-cooled Litz wire coil for measuring the high frequency hysteresis loops of magnetic samples—A useful setup for magnetic hyperthermia applications. *Review of Scientific Instruments* **85**, 093904, doi:doi:http://dx.doi.org/10.1063/1.4895656 (2014).

65 Aires, A. *et al.* BSA-coated magnetic nanoparticles for improved therapeutic properties. *Journal of Materials Chemistry B* **3**, 6239-6247, doi:10.1039/C5TB00833F (2015).

66 Garaio, E., Collantes, J.-M., Garcia, J. A., Plazaola, F. & Sandre, O. Harmonic phases of the nanoparticle magnetization: An intrinsic temperature probe. *Applied Physics Letters* **107**, 123103, doi:10.1063/1.4931457 (2015).

67 Cabrera, D., Camarero, J., Ortega, D. & Teran, F. J. Influence of the aggregation, concentration, and viscosity on the nanomagnetism of iron oxide nanoparticle colloids for magnetic hyperthermia. *Journal of Nanoparticle Research* **17**, 121, doi:10.1007/s11051-015-2921-9 (2015).

68 Conde-Leboran, I. *et al.* A Single Picture Explains Diversity of Hyperthermia Response of Magnetic Nanoparticles. *The Journal of Physical Chemistry C* **119**, 15698-15706, doi:10.1021/acs.jpcc.5b02555 (2015).

69 Ruta, S., Chantrell, R. & Hovorka, O. Unified model of hyperthermia via hysteresis heating in systems of interacting magnetic nanoparticles. *Scientific Reports* **5**, 9090, doi:10.1038/srep09090 (2015).

70 Pineiro-Redondo, Y. *et al.* The influence of colloidal parameters on the specific power absorption of PAA-coated magnetite nanoparticles. *Nanoscale Research Letters* **6**, 383 (2011).

71 Urtizberea, A., Natividad, E., Arizaga, A., Castro, M. & Mediano, A. Specific Absorption Rates and Magnetic Properties of Ferrofluids with Interaction Effects at Low Concentrations. *The Journal of Physical Chemistry C* **114**, 4916-4922, doi:10.1021/jp912076f (2010).

72 Landi, G. T. Role of dipolar interaction in magnetic hyperthermia. *Physical Review B* **89**, 014403 (2014).

73 Tan, R. P., Carrey, J. & Respaud, M. Magnetic hyperthermia properties of nanoparticles inside lysosomes using kinetic Monte Carlo simulations: Influence of key parameters and dipolar interactions, and evidence for strong spatial variation of heating power. *Physical Review B* **90**, 214421 (2014).

74 Zhang, W. in *Nanomaterial* Vol. 811 *Advances in Experimental Medicine and Biology* (eds David G. Capco & Yongsheng Chen) Ch. 2, 19-43 (Springer Netherlands, 2014).

75 Ota, S., Kitaguchi, R., Takeda, R., Yamada, T. & Takemura, Y. Rotation of Magnetization Derived from Brownian Relaxation in Magnetic Fluids of Different Viscosity Evaluated by Dynamic Hysteresis Measurements over a Wide Frequency Range. *Nanomaterials* **6**, 170 (2016).

76 Kechrakos, D. & Trohidou, K. N. Magnetic properties of dipolar interacting single-domain particles. *Physical Review B* **58**, 12169-12177 (1998).

77 Varón, M. *et al.* Dipolar Magnetism in Ordered and Disordered Low-Dimensional Nanoparticle Assemblies. *Scientific Reports* **3**, 1234, doi:10.1038/srep01234 (2013).

78 Rosensweig, R. Heating magnetic fluid with alternating magnetic field. *J Magn Magn Mater* **252**, 370 (2002).

79 Mehdaoui, B. *et al.* Influence of a transverse static magnetic field on the magnetic hyperthermia properties and high-frequency hysteresis loops of ferromagnetic FeCo nanoparticles. *Applied Physics Letters* **100**, -, doi:doi:http://dx.doi.org/10.1063/1.3681361 (2012).

80 Mehdaoui, B. *et al.* Increase of magnetic hyperthermia efficiency due to dipolar interactions in low-anisotropy magnetic nanoparticles: Theoretical and experimental results. *Physical Review B* **87**, 174419 (2013).

81 Serantes, D. *et al.* Influence of dipolar interactions on hyperthermia properties of ferromagnetic particles. *Journal of Applied Physics* **108**, 073918, doi:doi:http://dx.doi.org/10.1063/1.3488881 (2010).

82 Jordan, A. *et al.* Inductive heating of ferrimagnetic particles and magnetic fluids: Physical evaluation of their potential for hyperthermia. *International Journal of Hyperthermia* **9**, 51-68, doi:10.3109/02656739309061478 (1993).

83 Mehdaoui, B. *et al.* Influence of a transverse static magnetic field on the magnetic hyperthermia properties and high-frequency hysteresis loops of ferromagnetic FeCo nanoparticles. *Applied Physics Letters* **100**, doi:10.1063/1.3681361 (2012).

84 Wang, S. Y., Huang, S. & Borca-Tasciuc, D. A. Potential Sources of Errors in Measuring and Evaluating the Specific Loss Power of Magnetic Nanoparticles in an Alternating Magnetic Field. *IEEE Transactions on Magnetics* **49**, 255-262, doi:10.1109/tmag.2012.2224648 (2013).

85 Wildeboer, R. R., Southern, P. & Pankhurst, Q. A. On the reliable measurement of specific absorption rates and intrinsic loss parameters in magnetic hyperthermia materials. *Journal of Physics D: Applied Physics* **47**, 495003 (2014).

86 Coey, J. M. *Magnetism and magnetic materials*. (Cambridge University Press, 2010).

87 Oyarzún, S., Tamion, A., Tournus, F., Dupuis, V. & Hillenkamp, M. Size effects in the magnetic anisotropy of embedded cobalt nanoparticles: from shape to surface. *Scientific Reports* **5**, 14749, doi:10.1038/srep14749

http://www.nature.com/articles/srep14749#supplementary-information (2015).

88 Dieckhoff, J., Eberbeck, D., Schilling, M. & Ludwig, F. Magnetic-field dependence of Brownian and Néel relaxation times. *Journal of Applied Physics* **119**, 043903, doi:doi:http://dx.doi.org/10.1063/1.4940724 (2016).

89 Dieckhoff, J., Schilling, M. & Ludwig, F. Fluxgate based detection of magnetic nanoparticle dynamics in a rotating magnetic field. *Applied Physics Letters* **99**, 112501, doi:doi:http://dx.doi.org/10.1063/1.3639276 (2011).

90 Sanz, B. *et al.* In Silico before In Vivo: how to Predict the Heating Efficiency of Magnetic Nanoparticles within the Intracellular Space. *Scientific Reports* **6**, 38733, doi:10.1038/srep38733

http://www.nature.com/articles/srep38733#supplementary-information (2016).

91 Maldonado-Camargo, L., Torres-Díaz, I., Chiu-Lam, A., Hernández, M. & Rinaldi, C. Estimating the contribution of Brownian and Néel relaxation in a magnetic fluid through dynamic magnetic susceptibility measurements. *Journal of Magnetism and Magnetic Materials* **412**, 223-233, doi:https://doi.org/10.1016/j.jmmm.2016.03.087 (2016).

92 Creixell, M., Bohórquez, A. C., Torres-Lugo, M. & Rinaldi, C. EGFR-Targeted Magnetic Nanoparticle Heaters Kill Cancer Cells without a Perceptible Temperature Rise. *ACS Nano* **5**, 7124-7129, doi:10.1021/nn201822b (2011).

93 Connord, V. *et al.* Real-Time Analysis of Magnetic Hyperthermia Experiments on Living Cells under a Confocal Microscope. *Small* **11**, 2437-2445, doi:10.1002/smll.201402669 (2015).

94 Kim, D.-H. *et al.* Biofunctionalized magnetic-vortex microdiscs for targeted cancer-cell destruction. *Nat Mater* **9**, 165-171, doi:http://www.nature.com/nmat/journal/v9/n2/abs/nmat2591.html#supplementary-information (2010).

95 Etoc, F. *et al.* Magnetogenetic Control of Protein Gradients Inside Living Cells with High Spatial and Temporal Resolution. *Nano Letters* **15**, 3487-3494, doi:10.1021/acs.nanolett.5b00851 (2015).

96 Leliaert, J., Vansteenkiste, A., Coene, A., Dupré, L. & Van Waeyenberge, B. Vinamax: a macrospin simulation tool for magnetic nanoparticles. *Medical & Biological Engineering & Computing* **53**, 309-317, doi:10.1007/s11517-014-1239-6 (2015).

97 Ludwig, F. *et al.* Self-consistent magnetic properties of magnetite tracers optimized for magnetic particle imaging measured by ac susceptometry, magnetorelaxometry and magnetic particle spectroscopy. *Journal of Magnetism and Magnetic Materials* **360**, 169-173, doi:https://doi.org/10.1016/j.jmmm.2014.02.020 (2014).

98 Shah, S. A., Reeves, D. B., Ferguson, R. M., Weaver, J. B. & Krishnan, K. M. Mixed Brownian alignment and N\'eel rotations in superparamagnetic iron oxide nanoparticle suspensions driven by an ac field. *Physical Review B* **92**, 094438 (2015).

99 Gehrke, N. *et al.* Magnetic Characterization of Clustered Core Magnetic Nanoparticles for MPI. *IEEE Transactions on Magnetics* **51**, 1-4, doi:10.1109/TMAG.2014.2358275 (2015).

100 Serantes, D. *et al.* Multiplying Magnetic Hyperthermia Response by Nanoparticle Assembling. *The Journal of Physical Chemistry C* **118**, 5927-5934, doi:10.1021/jp410717m (2014).

101 Hovorka, O. Thermal activation in statistical clusters of magnetic nanoparticles. *Journal of Physics D: Applied Physics* **50**, 044004 (2017).

102 Mehdaoui, B. *et al.* Influence of a transverse static magnetic field on the magnetic hyperthermia properties and high-frequency hysteresis loops of ferromagnetic FeCo nanoparticles. *Applied Physics Letters* **100**, 052403, doi:doi:http://dx.doi.org/10.1063/1.3681361 (2012).

103 Aggarwal, P., Hall, J. B., McLeland, C. B., Dobrovolskaia, M. A. & McNeil, S. E. Nanoparticle interaction with plasma proteins as it relates to particle biodistribution, biocompatibility and therapeutic efficacy. *Advanced Drug Delivery Reviews* **61**, 428-437, doi:http://dx.doi.org/10.1016/j.addr.2009.03.009 (2009).

104 Hühn, D. *et al.* Polymer-Coated Nanoparticles Interacting with Proteins and Cells: Focusing on the Sign of the Net Charge. *ACS Nano* **7**, 3253-3263, doi:10.1021/nn3059295 (2013).

105 Lee YK, Choi EJ, Webster TJ, Kim SH & D, K. Effect of the protein corona on nanoparticles for modulating cytotoxicity and immunotoxicity. *International Journal of Nanomedicine »* **10**, 7, doi:10.2147/IJN.S72998 (2014).

106 Sakulkhu, U. *et al.* Significance of surface charge and shell material of superparamagnetic iron oxide nanoparticle (SPION) based core/shell nanoparticles on the composition of the protein corona. *Biomaterials Science* **3**, 265-278, doi:10.1039/c4bm00264d (2015).

107 Gräfe, C. *et al.* Intentional formation of a protein corona on nanoparticles: Serum concentration affects protein corona mass, surface charge, and nanoparticle–cell interaction. *The International Journal of Biochemistry & Cell Biology* **75**, 196-202, doi:http://dx.doi.org/10.1016/j.biocel.2015.11.005 (2016).

108 Calatayud, M. P. *et al.* The effect of surface charge of functionalized Fe3O4 nanoparticles on protein adsorption and cell uptake. *Biomaterials* **35**, 6389-6399, doi:http://dx.doi.org/10.1016/j.biomaterials.2014.04.009 (2014).

109 Docter, D. *et al.* Quantitative profiling of the protein coronas that form around nanoparticles. *Nat. Protocols* **9**, 2030-2044, doi:10.1038/nprot.2014.139

http://www.nature.com/nprot/journal/v9/n9/abs/nprot.2014.139.html#supplementary-information (2014).

110 Hirsch, V. *et al.* Surface charge of polymer coated SPIONs influences the serum protein adsorption, colloidal stability and subsequent cell interaction in vitro. *Nanoscale* **5**, 3723-3732, doi:10.1039/c2nr33134a (2013).

111 Adair, J. H., Suvaci, E. & Sindel, J. in *In Encyclopedia of Materials: Science and Technology , The Netherlands ,* 8996-9006. (Elsevier Publishing, 2001).

112 Gebauer, J. S. *et al.* Impact of the Nanoparticle–Protein Corona on Colloidal Stability and Protein Structure. *Langmuir* **28**, 9673-9679, doi:10.1021/la301104a (2012).

113 Landgraf, L. *et al.* Anti-oxidative effects and harmlessness of asymmetric Au@Fe3O4 Janus particles on human blood cells. *Biomaterials* **35**, 6986-6997, doi:http://dx.doi.org/10.1016/j.biomaterials.2014.04.111 (2014).

114 Tian, B., Bejhed, R. S., Svedlindh, P. & Strömberg, M. Blu-ray optomagnetic measurement based competitive immunoassay for Salmonella detection. *Biosensors and Bioelectronics* **77**, 32-39, doi:https://doi.org/10.1016/j.bios.2015.08.070 (2016).

115 Ludwig, F., Balceris, C., Jonasson, C. & Johansson, C. Analysis of AC Susceptibility Spectra for the Characterization of Magnetic Nanoparticles. *IEEE Transactions on Magnetics* **53**, 1-4, doi:10.1109/TMAG.2017.2693420 (2017).

116 Wang, W. *et al.* Magnetoresistive performance and comparison of supermagnetic nanoparticles on giant magnetoresistive sensor-based detection system. *Scientific Reports* **4**, 5716, doi:10.1038/srep05716

https://www.nature.com/articles/srep05716#supplementary-information (2014).

117 Jurašin, D. D. *et al.* Surface coating affects behavior of metallic nanoparticles in a biological environment. *Beilstein Journal of Nanotechnology* **7**, 246-262 (2016).

118 Sperling, R. A. & Parak, W. J. Surface modification, functionalization and bioconjugation of colloidal inorganic nanoparticles. *Philosophical Transactions of the Royal Society A: Mathematical, Physical and Engineering Sciences* **368**, 1333-1383, doi:10.1098/rsta.2009.0273 (2010).

119 Mezger, A. *et al.* Scalable DNA-Based Magnetic Nanoparticle Agglutination Assay for Bacterial Detection in Patient Samples. *ACS Nano* **9**, 7374-7382, doi:10.1021/acsnano.5b02379 (2015).

120 Gandhi, S., Arami, H. & Krishnan, K. M. Detection of Cancer-Specific Proteases Using Magnetic Relaxation of Peptide-Conjugated Nanoparticles in Biological Environment. *Nano Letters* **16**, 3668-3674, doi:10.1021/acs.nanolett.6b00867 (2016).

121 Khalafalla, S. E. & Reimers, G. W. Preparation of dilution-stable aqueous magnetic fluids. *IEEE Transactions on Magnetics* **16**, 178-183, doi:10.1109/TMAG.1980.1060578 (1980).

122 Sathya, A. *et al.* CoxFe3–xO4 Nanocubes for Theranostic Applications: Effect of Cobalt Content and Particle Size. *Chemistry of Materials* **28**, 1769-1780, doi:10.1021/acs.chemmater.5b04780 (2016).

123 Di Corato, R. *et al.* Water solubilization of hydrophobic nanocrystals by means of poly(maleic anhydride-alt-1-octadecene). *Journal of Materials Chemistry* **18**, 1991-1996, doi:10.1039/b717801h (2008).

124 Pellegrino, T. *et al.* Hydrophobic Nanocrystals Coated with an Amphiphilic Polymer Shell: A General Route to Water Soluble Nanocrystals. *Nano Letters* **4**, 703-707, doi:10.1021/nl035172j (2004).

125 Răcuciu, M., Creangă, D. E. & Airinei, A. Citric-acid-coated magnetite nanoparticles for biological applications. *The European Physical Journal E* **21**, 117-121, doi:10.1140/epje/i2006-10051-y (2006).

List of publications

"Dynamical magnetic response of iron oxide nanoparticles in live cells"

D. Cabrera, A. Coene, J. Leliaert, Emilio J. Artés-Ibañez, L. Dupré, N. D. Telling and F. J. Terán.

Journal: ACS Nano, *under minor corrections* **Year:** 2018

"Optomagnetic Nanoplatforms for In Situ Controlled Hyperthermia"

Dirk H. Ortgies, Francisco J. Teran, Uéslen Rocha, Leonor de la Cueva, Gorka Salas, **David Cabrera**, Alexander S. Vanetsev, Mihkel Rähn, Väino Sammelselg, Yurii V. Orlovskii, Daniel Jaque.

Journal: Advanced Functional Materials **Year:** 2018

DOI: 10.1002/adfm.201704434

"Emergence of the Stoner-Wohlfarth astroid in thin films at dynamic regime"

Cuñado, J.L.F., Bollero, A., Pérez-Castañeda, T., Perna, P., Ajejas, F., Pedrosa, J., Gudín, A., Maldonado, A., Niño, M.A., Guerrero, R., **Cabrera, D.**, Terán, F.J., Miranda, R., Camarero, J.

Journal: Scientific Reports , 2017 , 7 **Year:** 2017

DOI: 10.1038/s41598-017-13854-7

"Unraveling viscosity effects on the hysteresis losses of magnetic nanocubes"

D. Cabrera, A. Lak, T. Yoshida, M.E. Materia, D. Ortega, F. Ludwig, P. Guardia, A. Sathya, T. Pellegrino, and F. J. Teran.

Journal: Nanoscale 9(16) **Year:** 2017

DOI: 10.1039/C7NR00810D

"Elucidation of the Physicochemical Properties Ruling the Colloidal Stability of Iron Oxide Nanoparticles under Physiological Conditions"

Antonio Aires, **David Cabrera**, Laura C. Alonso-Pardo, Aitziber L. Cortajarena, and Francisco J. Teran.

Journal: ChemNanoMat **Year:** 2017

DOI: 10.1002/cnma.201600333 (SELECTED FOR JOURNAL COVER)

"Effects of inter- and intra-aggregate magnetic dipolar interactions on the magnetic heating efficiency of iron oxide nanoparticles"

J. G. Ovejero, **D. Cabrera**, J. Carrey, T. Valdivielso, G. Salas and F. J. Teran.

Journal: Physical Chemistry Chemical Physics 18(16):10954 **Year:** 2016
DOI: 10.1039/C6CP00468G

"*In Vivo Deep Tissue Fluorescence and Magnetic Imaging Employing Hybrid Nanostructures*"

Ortgies, D.H., De La Cueva, L., Del Rosal, B., Sanz-Rodríguez, F., Fernández, N., Iglesias-De La Cruz, M.C., Salas, G., **Cabrera, D.**, Teran, F.J., Jaque, D., Martín Rodríguez, E.

ACS Applied Materials and Interfaces, 8 (2), pp. 1406-1414. **Year:** 2015

DOI: 10.1021/acsami.5b10617

"*BSA-coated magnetic nanoparticles for improved therapeutic properties"*

A. Aires, S. M. Ocampo, **D. Cabrera**, L. de la Cueva, G. Salas, F. J. Teran, and A. L. Cortajarena.

Journal: The Journal of Materials Chemistry B, 3 (30), pp. 6239-6247 **Year:** 2015

DOI: 10.1039/C5TB00833F

"A Single Picture Explains Diversity of Hyperthermia Response of Magnetic Nanoparticles"

Conde-Leboran, D. Baldomir, C. Martinez-Boubeta, O. Chubykalo-Fesenko, M.P. Morales, G. Salas, **D. Cabrera**, J. Camarero, F.J. Teran, and D. Serantes.

Journal: The Journal of Physical Chemistry C, 119 (27), pp. 15698-15706 **Year:** 2015

DOI: 10.1021/acs.jpcc.5b02555

"Influence of the aggregation, concentration, and viscosity on the nanomagnetism of iron oxide nanoparticle colloids for magnetic hyperthermia"

David Cabrera, Julio Camarero, Daniel Ortega, Francisco J. Terán.

Journal: *Journal of Nanoparticles Research 17:121* **Year:** 2015

"Modulation of Magnetic Heating via Dipolar Magnetic Interactions in Monodisperse and Crystalline Iron Oxide Nanoparticles"

Gorka Salas, Julio Camarero, **David Cabrera**, Heléne Takacs, María Varela, Robert Ludwig, Heidi Dahring, Ingrid Hilger, Rodolfo Miranda, María del Puerto Morales, and Francisco José Teran.

Journal: *The Journal of Physical Chemistry C. 118, 19985* **Year:** 2014